

UC Santa Barbara

UC Santa Barbara Electronic Theses and Dissertations

Title

Engineering, Control, and Integration of 2D Based Quantum Defects for Integrated Quantum Photonics

Permalink

<https://escholarship.org/uc/item/37n1w979>

Author

Partoandazan Poor, Kamyar

Publication Date

2024

Peer reviewed|Thesis/dissertation

University of California
Santa Barbara

Engineering, Control, and Integration of 2D Based Quantum Defects for Integrated Quantum Photonics

A dissertation submitted in partial satisfaction
of the requirements for the degree

Doctor of Philosophy
in
Electrical and Computer Engineering

by

Kamyar Parto

Committee in charge:

Professor Galan Moody, Co-Chair
Professor Kaustav Banerjee, Co-Chair
Professor Chris G. Van de Walle
Professor Jon Schuller
Professor Bolin Liao

September 2024

The Dissertation of Kamyar Parto is approved.

Professor Chris G. Van de Walle

Professor Jon Schuller

Professor Bolin Liao

Professor Kaustav Banerjee, Committee Co-Chair

Professor Galan Moody, Committee Co-Chair

May 2024

Engineering, Control, and Integration of 2D Based Quantum Defects for Integrated
Quantum Photonics

Copyright © 2024

by

Kamyar Parto

Dedicated to Nika

Acknowledgements

During the past several years, I have had the privilege of working with many great scientists, colleagues, and mentors. First, I would like to thank my advisors, Professor Kaustav Banerjee and Professor Galan Moody, for their outstanding support, mentorship, and advice during my time at UCSB. I am also deeply grateful to my committee members, Professor Chris Van der Walle, Professor Jon Schuller, and Professor Bolin Liao, for their guidance and valuable feedback throughout my research journey.

I also appreciate the invaluable contributions of my collaborators, particularly Professor Chris Van der Walle, Dr. Mark Turianski, Dr. Han Htoon, and Prof. Stephen Wilson, whose expertise and insights have significantly enhanced the quality of my work.

I feel grateful to have so many friends and lab mates who have supported me through the highs and lows of graduate school. A special thanks to Sahil Patel, Josh Castro, Nick Lewis, Shaimaa Azzam, Lillian Thiel, Kunjesh Agashiwalla, Arnab Pal, Aditya Raj, Wei Cao, and Junkai Jiang. Your camaraderie and support have made this journey enjoyable and fulfilling.

To my parents, Jamal and Badri, your unwavering love and encouragement have been the foundation of my success. I am forever grateful for your sacrifices and belief in me. To my partner, Alexis, thank you for your patience, understanding, and constant support. Your presence has been my anchor through this challenging yet rewarding experience.

Curriculum Vitæ

Kamyar Parto

Education

- 2024 Ph.D. in Electrical and Computer Engineering, University of California, Santa Barbara.
- 2017 Bachelor of Engineering Science, University of Tehran, Tehran, Iran

Professional Employment

- 5/2024 R&D Photonic Experimentalist, PsiQuantum, Palo Alto, CA
- 7/2017 - 4/2024 Graduate Student Researcher, Electrical and Computer Engineering Department, University of California, Santa Barbara, CA

Selected Awards

1. Frontiers in Optics Jean Bennett Memorial Award, Winter 2022
2. Frontiers in Optics Emil Wolf Best Student Paper Award Finalist, Winter 2023
3. DOE SCGSR Award, Fall 2021
4. NSF Quantum Foundry Fellowship, Winter 2021
5. IEEE-IEDM Outstanding Student Paper Award, Winter 2021
6. IEEE S3S-3D Best Student Paper Award, Spring 2018
7. UC Santa Barbara ECE Department, Outstanding TA Award, 2018-2021
8. IAESTE Fellowship, 2016
9. Faculty of Engineering Student of the Year Award, 2015-2016

Publications

1. Patel, S. D., **Parto, K.**, Choquer, M., Lewis, N., Umezawa, S., Hellman, L., & Moody, G. (2024). Surface Acoustic Wave Cavity Optomechanics with Atomically Thin h-BN and WSe₂ Single-Photon Emitters. *PRX Quantum*, 5(1), 010330.
2. Turiansky, M. E., **Parto, K.**, Moody, G., & Van de Walle, C. G. (2024). Rational Design of Efficient Defect-Based Quantum Emitters. *arXiv preprint arXiv:2402.08257*.
3. Moody, G., & **Parto, K.** Integrated quantum photonics with atomically thin materials. In *Active Photonic Platforms (APP) 2023* (p. PC126470C). SPIE.
4. Kumar, A., Pal, A., **Parto, K.**, Cao, W., & Banerjee, K. (2023, June). Exploration and Exploitation of Strain Engineering in 2D-FETs. In *2023 Device Research Conference (DRC)* (pp. 1-2). IEEE.

5. Patel, S. D., **Parto, K.**, Choquer, M., Umezawa, S., Hellman, L., Polishchuk, D., & Moody, G. (2023, May). Cavity Optomechanics with WSe₂ Single Photon Emitters. In *CLEO: Fundamental Science* (pp. FW3J-2). Optica Publishing Group.
6. **Parto, K.**, Azzam, S., Lewis, N., Patel, S., Umezawa, S., Watanabe, K., ... & Moody, G. (2023, May). Cavity-Enhanced 2D Quantum Emitters Deterministically Integrated with Silicon Nitride Microresonators. In *CLEO: Fundamental Science* (pp. FTh1A-3). Optica Publishing Group.
7. Azzam, S. I., **Parto, K.**, & Moody, G. (2023). Purcell enhancement and polarization control of single-photon emitters in monolayer WSe₂ using dielectric nanoantennas. *Nanophotonics*, *12*(3), 477-484.
8. Patel, S., **Parto, K.**, Choquer, M., Umezawa, S., Hellman, L., Polishchuk, D., & Moody, G. (2023). Quantum Emitter Optomechanics in a Hybrid WSe₂-LiNbO₃ Surface Acoustic Wave Resonator. In *APS March Meeting Abstracts* (Vol. 2023, pp. Y67-011). .
9. **Parto, K.**, Azzam, S. I., Lewis, N., Patel, S. D., Umezawa, S., Watanabe, K., ... & Moody, G. (2022). Cavity-enhanced 2D material quantum emitters deterministically integrated with silicon nitride microresonators. *Nano Letters*, *22*(23), 9748-9756.
10. **Parto, K.**, Azzam, S., Lewis, N., Patel, S., Umezawa, S., Watanabe, K., & Moody, G. (2022, October). Room Temperature Quantum Emitters Deterministically Integrated with Silicon Nitride Microresonators. In *Frontiers in Optics* (pp. FTh3E-5). Optica Publishing Group.
11. Azzam, S. I., **Parto, K.**, & Moody, G. (2022, May). Control of single-photon emitters in two-dimensional materials using dielectric nanoantennas. In *CLEO: Science and Innovations* (pp. SM3H-4). Optica Publishing Group.
12. Azzam, S., **Parto, K.**, Lewis, N., & Moody, G. (2022). On-chip integration of site controlled hBN quantum emitters in a low-emission silicon nitride platform. In *APS March Meeting Abstracts* (Vol. 2022, pp. Y72-005).
13. **Parto, K.**, Pal, A., Chavan, T., Agashiwala, K., Yeh, C. H., Cao, W., & Banerjee, K. (2021). One-Dimensional Edge Contacts to Two-Dimensional Transition-Metal Dichalcogenides: Uncovering the Role of Schottky-Barrier Anisotropy in Charge Transport across Mo S₂/Metal Interfaces. *Physical Review Applied*, *15*(6), 064068.
14. Azzam, S. I., **Parto, K.**, & Moody, G. (2021). Prospects and challenges of quantum emitters in 2D materials. *Applied Physics Letters*, *118*(24).
15. **Parto, K.**, Azzam, S. I., Banerjee, K., & Moody, G. (2021). Defect and strain engineering of monolayer WSe₂ enables site-controlled single-photon emission up to 150 K. *Nature communications*, *12*(1), 3585.
16. **Parto, K.**, Banerjee, K., & Moody, G. (2021, May). Defect and strain engineering of monolayer WSe₂ for site-controlled single-photon emission up to 150k. In *CLEO: QELS-Fundamental Science* (pp. FTh4M-8). Optica Publishing Group.

17. Agashiwala, K., Jiang, J., **Parto, K.**, Zhang, D., Yeh, C. H., & Banerjee, K. (2021). Demonstration of CMOS-compatible multi-level graphene interconnects with metal vias. *IEEE Transactions on Electron Devices*, 68(4), 2083-2091.
18. **Parto, K.**, Banerjee, K., & Moody, G. (2020, September). Irradiation of Nanostrained Monolayer WSe₂ for Site-Controlled Single-Photon Emission up to 150K. In *Frontiers in Optics* (pp. FW1C-3). Optica Publishing Group.
19. Cao, W., Chu, J. H., **Parto, K.**, & Banerjee, K. (2021). A mode-balanced reconfigurable logic gate built in a van der Waals strata. *npj 2D Materials and Applications*, 5(1), 20.
20. **Parto, K.**, Banerjee, K., & Moody, G. (2021). Defect Engineering Enables Site-Controlled Single-Photon Generation in Monolayer WSe₂ up to 150 K. In *APS March Meeting Abstracts* (Vol. 2021, pp. S51-002).
21. Agashiwala, K., Jiang, J., Yeh, C. H., **Parto, K.**, Zhang, D., & Banerjee, K. (2020, December). Reliability and performance of CMOS-compatible multi-level graphene interconnects incorporating vias. In *2020 IEEE International Electron Devices Meeting (IEDM)* (pp. 31-1). IEEE.
22. Cao, W., Huang, M., Yeh, C. H., **Parto, K.**, & Banerjee, K. (2020). Impact of transport anisotropy on the performance of van der Waals materials-based electron devices. *IEEE Transactions on Electron Devices*, 67(3), 1310-1316.
23. Yeh, C. H., Cao, W., Pal, A., **Parto, K.**, & Banerjee, K. (2019, December). Area-selective-CVD technology enabled top-gated and scalable 2D-heterojunction transistors with dynamically tunable Schottky barrier. In *2019 IEEE International Electron Devices Meeting (IEDM)* (pp. 23-4). IEEE.
24. Pal, A., **Parto, K.**, Agashiwala, K., Cao, W., & Banerjee, K. (2019, December). Computational study of spin injection in 2D materials. In *2019 IEEE International Electron Devices Meeting (IEDM)* (pp. 24-2). IEEE.
25. Jiang, J., **Parto, K.**, Cao, W., & Banerjee, K. (2019). Ultimate monolithic-3D integration with 2D materials: rationale, prospects, and challenges. *IEEE Journal of the Electron Devices Society*, 7, 878-887.
26. Matsuura, K., Hamada, M., Hamada, T., Tanigawa, H., Sakamoto, T., Cao, W., & Wakabayashi, H. (2019, June). Normally-Off Sputtered-MoS₂ nMISFETs with MoSi₂ Contact by Sulfur Powder Annealing and ALD Al₂O₃ Gate Dielectric for Chip Level Integration. In *2019 19th International Workshop on Junction Technology (IWJT)* (pp. 1-4). IEEE.
27. **Parto, K.**, Pal, A., Xie, X., Cao, W., & Banerjee, K. (2018, December). Interfacial thermal conductivity of 2D layered materials: An atomistic approach. In *2018 IEEE International Electron Devices Meeting (IEDM)* (pp. 24-1). IEEE.
28. Jiang, J., **Parto, K.**, Cao, W., & Banerjee, K. (2018, October). Monolithic-3D integration with 2D materials: Toward ultimate vertically-scaled 3D-ICs. In *2018*

IEEE SOI-3D-Subthreshold Microelectronics Technology Unified Conference (S3S)
(pp. 1-3). IEEE.

Presentations

1. Integrated quantum photonics with atomically thin materials, SPIE 2023, San Diego, August 2023, Invited Talk.
2. Engineering, Control, and Integration of 2D Based Quantum Defects for Integrated Quantum Photonics, ACS Northwest Meeting Montana State University, June 2023, Invited Talk.
3. Cavity-Enhanced 2D Quantum Emitters Deterministically Integrated with Silicon Nitride Microresonators, CLEO: Fundamental Science, San Jose, May 2023.
4. Room Temperature Quantum Emitters Deterministically Integrated with Silicon Nitride Microresonators. In *Frontiers in Optics*, Rochester, October 2022.
5. Photonic Integration of Quantum Emitters in 2D Materials, Columbia Programmable Quantum Materials Center, Columbia University, New York, May 2022, Invited Talk.
6. Defect and strain engineering of monolayer WSe₂ for site-controlled single-photon emission up to 150K. *CLEO Fundamental Science*, May 2021, Virtual Conference.
7. Defect Engineering Enables Site-Controlled Single-Photon Generation in Monolayer WSe₂ up to 150 K. *APS March Meeting*, March 2021, Virtual Conference.
8. Irradiation of Nanostrained Monolayer WSe₂ for Site-Controlled Single-Photon Emission up to 150K. *Frontiers in Optics* 2020. October 2020, Virtual Conference.
9. Interfacial thermal conductivity of 2D layered materials: An atomistic approach. IEEE International Electron Devices Meeting (IEDM), December 2018.

Abstract

Engineering, Control, and Integration of 2D Based Quantum Defects for Integrated
Quantum Photonics

by

Kamyar Parto

Solid-state quantum emitters are an indispensable resource for quantum photonic technologies including optical quantum processors, transceivers for secure communications and networking, and random number generation. These technologies can be made into compact and efficient modules by leveraging the mature silicon photonics ecosystem; however, suitable quantum emitters have not yet been demonstrated in silicon-based photonics. The development of CMOS-compatible, high-quality quantum emitters capable of on-demand single-photon generation could revolutionize the field of quantum information in the same way the laser has transformed global communications and high-speed data networks.

Two key requirements are necessary to address this challenge: (1) identification of emitters capable of high purity, high indistinguishability, and bright single-photon generation, and (2) the deterministic integration and alignment of such emitters with silicon-based photonic microcavities to achieve efficient on-chip emission. Many platforms have been developed to address the first challenge, including quantum dots, diamond color centers, and defects in two-dimensional materials. The second challenge has been more difficult to overcome and calls for a hetero-integrated approach that integrates materials hosting high-quality emitters into the silicon-photonic fabrication flow.

In recent years, the discovery of defect-based single quantum emitters (SQEs) in 2D materials (2DMs), most notably WSe_2 and h-BN, has given a boost to this effort. In this

thesis, I present our experiments that shed light on the origins of SQEs in 2DMs and practical methods to site-specifically engineer SQEs in 2D materials with 50 nm spatial resolution, near unity yield, over 95% purity, and record-breaking working temperatures—an achievement exclusive to 2D material platforms. I will present several advances in photonic integration of these emitters that resulted in a development of a 2D-compatible photonic integration platform. The first is the growth of high-quality, non-stoichiometric silicon nitride, which eliminates the auto-fluorescence background in stoichiometric Si_3N_4 films. The second is the process to embed emitters within the photonic waveguiding layer, enabling efficient coupling to a single guided optical mode and the third is the alignment of the emitter position and optical dipole moment with the cavity mode, resulting in $> 46\%$ on-chip single-photon collection efficiency and $> 95\%$ single-photon purity at room temperature. This is the first demonstration of microcavity integration of quantum emitters in two-dimensional material emitters with silicon-based photonics, which improved the on-chip coupling efficiency by an order-of-magnitude over previous demonstrations.

Finally, I will present an outlook to the future of this platform and specifically our progress to integrate our cavity-coupled SQEs into diode structures enabling electrical triggering of single-photons and prototyping the first on-chip quantum light emitting device (qLED).

Contents

Curriculum Vitae	vi
Abstract	x
List of Figures	xv
List of Tables	xxvii
1 Introduction	1
1.1 Thesis Outline	5
1.2 Permissions and Attributions	6
Bibliography	8
2 Background	11
2.1 Quantum Technology Platforms	11
2.2 Qubits, Quantum Algorithms, Quantum Photonics Approaches	11
2.3 Ideal Single Photon Source Metrics	22
2.4 Types of Single-Photon Sources	26
2.5 2D Family	29
2.6 Transition Metal Dichalcogenides	31
2.7 Exciton in Low Dimensional Materials	33
2.8 Hexagonal Boron Nitride	36
2.9 Quantum Defects in 2D-Materials for Single Photon Emission	37
Bibliography	41
3 Experimental Methods	45
3.1 2D Exfoliation Methods	45
3.2 2D Dry Viscoelastic Transfer	50
3.3 Inexpensive 2D Transfer Station	51
3.4 Cryogenic Photoluminescence Microscopy	52

3.5	Life-time measurements	58
3.6	Second-order Auto-correlation Measurements	59
Bibliography		65
4	Physics, Characterization, and Engineering of Quantum Emitters in 1L-WSe₂	66
4.1	Strain Engineering of WSe ₂ Emitters	70
4.2	Photoluminescence Spectroscopy of Strained WSe ₂ on Nanopillars	71
4.3	Photoluminescence spectroscopy of electron-beam irradiated WSe ₂	78
4.4	Photoluminescence spectroscopy of strained and electron-beam Irradiated WSe ₂	79
4.5	Observation of biexciton emission cascade	82
4.6	Temperature dependent properties of the engineered single-photon emitters	86
4.7	Discussion	90
Bibliography		95
5	Photonic Integration of Quantum Emitters in 2D Materials	99
5.1	Rationale for 2D Integrated Quantum Light Sources	99
5.2	Previous Integration Demonstrations for 2D Quantum Emitters	102
5.3	The Ideal Integration Platform for 2D Materials	103
5.4	Engineering quantum defects in hBN	105
5.5	On-chip cavities for efficient on-chip coupling	111
5.6	Low fluorescence 2D-compatible SiN development	118
5.7	Microring Resonator Theory	121
5.8	Microring Resonator Design	125
5.9	Photonic Component Simulations	127
5.10	Integration Strategies	131
5.11	Fabrication Process Flow	134
5.12	Experimental Setup Overview	138
5.13	Microring Resonator Characterization	140
5.14	Integrated System Results	144
5.15	Spectral Purcell Factor	147
5.16	System Efficiency Calibration	148
5.17	Spectral Purcell Factor and Coupling Factor Estimates	149
5.18	Conclusion and Outlook	152
Bibliography		153

6 Outlook for Turnkey Quantum Diodes	157
6.1 Figure of Merit for Cavity-Emitter Systems	158
6.2 Cavity Requirements for useful 2D SQEs	162
6.3 The Need for Electrical Excitation for Scalable On-chip Sources	165
6.4 Distinctions Between Electrical and Optical Excitation Method	167
6.5 Lateral Tunable P-I-N Geometry for Simultaneous Electrical and on-chip Integration	169
6.6 Full Diode Fabrication Flow and Contact Engineering	171
6.7 Preliminary Result of Fabrication Prior to Integration	173
6.8 Discussion	173
Bibliography	177
7 Outro	180
Bibliography	184

List of Figures

1.1	Quantum information technology platforms.	3
1.2	Illustration of a quantum photonics chip	5
2.1	Schematic of a Mach-Zender Interferometer with a tunable phase shifter.	13
2.2	KLM protocol. a) Conditional non-linear sign shift gate. Note that the boxes demonstrate a beam-splitter operation with unitary matrix of $\begin{bmatrix} \cos(\theta) & \sin(\theta) \\ \sin(\theta) & \cos(\theta) \end{bmatrix}$. The top left 180° box is only a phase shifter. b) Configuration of a conditional controlled-Z gate utilizing two non-linear sign shift gates. Figures are reproduced here under the Creative Commons CC BY license from Knill et al., [4].	18
2.3	Circuit Diagram for single-qubit operation in cluster-state measurement.	21
2.4	An Ideal Single-Photon Emitter. An ideal SPE source is excited from an electrical pulse of a clock with t_P and a period of t_d . Single photons are generated with probability Q_e (internal quantum efficiency). This photon is collected into a single optical mode with probability η , resulting in brightness $Q\eta/T_1$. The Hanbury Brown and Twiss (HBT) setup is used to quantify the single-photon purity. A Hong-Ou-Mandel (HOM) interferometer is used to determine the indistinguishability ξ of subsequently emitted photons, which is determined by the lifetime T_1 and coherence time T_2	22
2.5	Bandstructure of MoS_2 as function of number of layers. Density-functional theory prediction of MoS_2 as function of layers. Reproduced with permission from Kumar et al., [32] (2012). Copyright 2012 Springer Nature . . .	33

2.6	Spin-resolved bandstructure of TMDs. Both Conduction and Valence band are spin-polarized due to spin-orbit coupling. The sign of splitting is much larger in Valence band compared to Conduction band, hence, we only represent the top spin-polarized band of the Valence band. However, as discussed. the sign of spin-orbit splitting can change in the conduction band for different TMDs, giving rise to two unique electronic bandstructure spin configuration. In the first case, the ground-state transition is spin-allowed and allows for radiative transitions, giving rise to a bright exciton. In the second case, the ground-state transition is spin-forbidden, allowing for formation of dark excitons.	36
2.7	Modes of excitation of quantum defects. (a) In simplest case, an electron from ground state of the defect can be promoted to excited state through either resonant excitation or phonon-assisted non-resonant excitation. (b) Defect interactions with band-edges can provide further pathways for excitation of the defect. For example, the defect can go to excited state by trapping a hole and an electron from Valence and Conduction band respectively.	39
3.1	VdW 2D Materials are held together by weak VdW forces in the out-of-plane direction and strong covalent bonds in the in-plane direction. This anisotropy allows 2D materials to have an "onion-like" structure and allow different layers to be peeled off each other, giving them a unique modular engineering ability, much like Legos.	46
3.2	Exfoliation and transfer process of WSe ₂ . Step-1 demonstrates the size of bulk crystal. In step-2, using nitto-tape, WSe ₂ is thinned down via mechanical exfoliation. In step-3, WSe ₂ is transferred from nitto tape to PDMS. In step-4, through optical imaging, a monolayer WSe ₂ can be identified on the PDMS. In step-5, PDMS is loaded on a glass slide in cantilever-like configuration. In step-6, while monitoring the position of the flake using optical microscope and micropositioners, WSe ₂ is stamped on a deterministic position on the substrate. In step-7 and 8, the PDMS stamp is slowly lifted off of the substrate, leaving the WSe ₂ behind. . . .	48
3.3	a) Completed transfer station. b) Transfer station during transfer process	52

3.4	Photoluminescence (PL) spectroscopy setup. Four different laser lines can be selected via flip mirrors and be sent to the optical axis of the measurement apparatus. In the current drawing, only the green laser line is allowed to pass to the setup. Both room temperature and cryogenic module are illustrated in the setup. For spectroscopy, the spectrometer and a visible silicon CCD can be used to take spectral images of the collected light. For quantum optics experiments, the spectrometer can be used as a monochromatic and the filtered light exits through the side-slit for either second-order auto-correlation measurements, time-resolved PL spectroscopy, or stroboscopic measurement.	53
3.5	Image of the PL setup.	55
3.6	Example of Time-resolved Photoluminescence Measurement. Blue dots demonstrate life-time of a WSe ₂ single-photon emitter. Green dots demonstrate life-time of Purcell-enhanced WSe ₂ single-photon emitters [10] with much smaller life-time. Red line demonstrates the instrument response time.	60
3.7	Statistical classification of light.	61
4.1	a) Cryogenic PL map of WSe ₂ . Localized spots show emission below the free exciton of WSe ₂ . b) Representative spectrum of a localized emission spot. Sharp emission lines below free-exciton resemble quantum-dot like features. The left inset shows that the sharp emission line consists of a doublet structure indicative of fine-structure splitting. The right inset demonstrates the delocalized exciton emission c) Representative second-order auto-correlation function of a localized sharp emission line in WSe ₂ . The dip below 0.5 at time zero evidences the single-photon emission nature of the light. Panels (a)(c): Reproduced with permission from He <i>et al.</i> , Nat. Nanotechnol. 10, 497502 (2015). Copyright 2015 Springer Nature .	67
4.2	Suspected mechanism of single-photon emitters in WSe ₂ a) top band-diagram illustrates the spatial variation of the bandgap (valence band), and subsequently the excitonic levels (bright exciton as blue line and dark-exciton as black dashed line) due to strain profile of the pillar. Bottom inset represents an illustration of WSe ₂ on nanopillar. b) band-structure representation of the WSe ₂ . Here, we have denoted the spin-orbit splitted conduction band as Dark (spin-forbidden radiative transition) and Bright (spin-allowed radiative transition) band to represent the excitonic picture in the same momentum-space representation of band-diagram. The localized defect is represented as a straight line in the momentum space. If exciton in the Dark band can efficiently hybridize with the localized defect, the valley symmetry is broken and electrons in the bound-exciton can efficiently recombine through the defect, leading to bright single-photon emission	69

4.3	Overview of the fabrication process a) HSQ resist is spun on SiO ₂ /Si chips to yield resist with thickness of 200 nm. b) Electron beam lithography is used to define nanopillars with diameter of 150 nm and height of 200 nm. c) Rapid thermal annealing at 1000 °C turns HSQ into SiO ₂ . d) Bottom h-BN with roughly 5 nm thickness is transferred on the nanopillars. e) Top WSe ₂ /h-BN stack is then transferred on top of the previous h-BN layer. f) Electron beam lithography is used to create defects in the 2D monolayer	70
4.4	PL Spectra of WSe ₂ On and Off Nanopillars. a) Darkfield image of a representative stack on top of the nanopillars b) PL Spectra of WSe ₂ off pillar (solid line) in a pristine unstrained region and WSe ₂ on the pillar (dashed line) is presented. Only slight shift in free exciton (X) and trion (X ⁻) is observed which is within the sample to sample uncertainty. No sharp peaks that can be associated with single-photon emitters are observed.	73
4.5	Calculated strain profile at the nanopillar from classical continuum model.	74
4.6	Finite excitation spot size corrections for nanopillar strain profile a) Excitation spot with FWHM of 1 μ m. b) Horizontal line cut of simulated strain profile of a 150 nm diameter nano-pillar. Note that line-cut travels through the center of the pillar. c) Intrinsic PL response in unstrained regions obtained from fitting a gaussian with 10 meV FWHM to the experimental results. d) Predicted PL response with strain. The main observed peak is from the unstrained neutral exciton. Note that P2 and P1 correspond to the strained neutral exciton at nano-pillar positions. P1 is the peak corresponding to the maximum strain at the edge of the pillar and P1 peak is attributed to the top of the pillar where the strain relaxes to some extent.	76
4.7	Finite excitation spot size corrections for a linear strain profile a) Excitation spot with FWHM of 1 μ m. b) Simulated strain profile that has a residual strain corresponding to a redshift of -0.03 eV which linearly increases to 0.06 eV at the center. c) Intrinsic PL response in unstrained regions obtained from fitting a gaussian with 10 meV FWHM to the experimental results. d) Predicted PL response. The PL signal is redshifted by 56 meV and its linewidth is broadened to 15 meV. The redshift is proportional to the average of strain per length, while the broadening corresponds to the linear slope of the strain profile	77
4.8	PL Spectra of e-beam engineered defects in WSe ₂ a) Illustration of the e-beam induced crystal damages that mostly result in creation of Chalcogen vacancies. b) Intensity of the defect band as function of irradiation dosage for a 100 keV beam. N ₁ dosage corresponds to 10 ⁵ electron/ μ m ² and N ₂ corresponds to 10 ⁶ electron/ μ m ²	78

4.9	PL Spectra of e-beam engineered defects in WSe ₂ a) Statistics of number of emitters per site with irradiation dosage of 10 ⁵ electron/ μm^2 . b) Statistics of number of emitters per site with irradiation dosage of 10 ⁶ electron/ μm^2 . c) PL map of six irradiated sites with the 10 ⁶ electron/ μm^2 dosage. PL map demonstrates the integrated intensity of collected light with wavelengths above 775 nm. The localized emission spots are the position of the pillars. Some sites demonstrate more than one emitter and saturate the detector over the exposure period. d) PL Spectra of three pillars seen in (c). Excitation power is set at 1 μW . Sharp emission lines appear in pairs, pointing to possible creation of biexciton-like complexes.	80
4.10	Statistics of the Engineered Emitters a) Distribution of $g^2(0)$ with average purity of 92%. b) Distribution of homogeneous linewidth with average of 75 μeV . c) Distribution of zero-field doublet-splitting. Horizontal dashed lines denote the average of measurements. Error bars denote the standard deviation from fitting the data.	81
4.11	Second-order auto-correlation measurement $g^2(t)$ for exciton-like (X) and biexciton-like (XX) observed features. Both lines demonstrate purity over 90%, indicating quantum nature.	82
4.12	Exciton and Biexcitons a) An illustration of configuration of bright exciton (one electron and one hole with the same spin) and biexciton (two electron and two holes). b) Energy level structure for the biexciton radiative cascade in absence of strain- and defect- dependent fine-structure splitting. Polarization-entangled photon pair can be generated in this case with circularly polarized basis. Here, E_b denotes the biexciton binding energy. c) Energy level structure for a biexciton-exciton radiative cascade in presence of fine-structure splitting which breaks the degeneracy of the intermediate transition, mixing the circularly polarized basis and resulting in linear polarization emission of photons that are separated by the zero-field splitting energy	83

4.13	Optical spectroscopy of biexcitonic-like Features a) High resolution polarization-resolved PL spectrum of a biexcitonic (XX) and excitonic (X) feature. Each pair consist of two doublets with cross-linear polarization, however the sign of the polarization is reversed in each pair. b) PL intensity as function of excitation power. Exciton intensity increases sub-linearly with power and shows saturation at very high powers. Biexciton however, grows super-linearly with excitation power as expected for a two-level system. Dashed lines are linear fit $\log(P_{int}) = x\log(P_{exc})$ to the data with extracted slopes of 0.96 for exciton (X) and 1.587 for biexciton (XX), respectively. c) Time-resolved photoluminescence measurement of the exciton-like (X) and biexcitonic-like (XX) feature. Data are fit with a bi-exponential function with decay times $T_1 = 6.12$ ns for the exciton and $T_1 = 4.01$ ns for the biexciton features, in line with the expected dynamics of an exciton-biexciton pair. d) Time-trace of the spectral diffusion of the exciton and biexciton features. Each row represents a 10s integration time over a total 5 minute measurement window. Almost no spectral diffusion on the order of 10s was observed. Small jitter at around $t=250$ s is correlated on both exciton and biexciton lines, further hinting at their correlated nature.	85
4.14	Temperature dependence of the single photon emitters up to 150 K a) Temperature evolution of a representative single-photon emitter from 5 K to 150 K. b) Single-photon energy as a function of temperature. Single-photon is redshifted due to decrease in bandgap energy which follows the Varshni's empirical equation. c) Second-order auto-correlation function at 5 K for the emitter seen in (a) d) Homogenous linewidth of the emitter as function of temperature. e) Arrhenius plot of the integrated intensity of the emitter as function of temperature . A quenching behaviour is observed at $T= 215$ K. Shaded region in b, e, and e demonstrate the range of recorded parameters for an ensemble of emitters. Open circles demonstrate measured data for a single emitter in the ensemble and the solid black lines are theoretical fit to the data. f) Second-order auto-correlation function at 150 K for the emitter seen in (a)	86
4.15	Estimated activation energy (E_A) of reported TMD-based single photon emitters as function of energy difference between defect emission and free-exciton. Quenching temperatures are color coded. Chakraborty et al. refers to reference [4], He <i>et al.</i> [21], Luo <i>et al.</i> [26], Klein <i>et al.</i> [27], and Arora <i>et al.</i> [28]	90
4.16	Statistics of single emitters across the ensemble a) Percentage of probed sites containing 0-5 emitters. b) Second-order correlation function, $g_2(0)$, measured at 5 K (blue) and 150 K (red). c) Homogeneous linewidth (γ) at 5 K (blue) and 150 K (red).	91

4.17	DFT Calculations of strained defect bandstructure a) Simulated strain profile at the nanopillar location. b) Bandgap variation as a function of applied biaxial tensile strain. The inset band diagram qualitatively illustrates the movements of the conduction band (E_C), valence band (E_V), and Fermi level (E_F) under strain. Notably, the conduction band exhibits a larger shift compared to the valence band. c) Evolution of the band diagram for a selenium vacancy under strain. E_D and the corresponding blue bands represent the localized defect levels. As strain is applied, the conduction band (E_C) and defect level (E_D) draw closer to each other. d) Evolution of the band diagram for the WSe_6 pore complex under strain. With strain, the energy gap between the conduction band and the nearest defect level diminishes. It is important to note that the Fermi level's position varies depending on the supercell size.	94
5.1	Universal platform for precision integration of 2D quantum emitters in silicon nitride photonics. a) The family of 2D materials , including hBN emitters at UV [7, 12] and visible [13] wavelengths, TMD emitters [9, 14, 15], and TMD heterostructures [16, 17] , exhibiting a rich spectrum of quantum emitters spanning the ultraviolet-to-telecommunications wavelength transparency window of silicon nitride photonics. Height of each bar corresponds to reported intensity of each class of emitters. Grey data ports are brightness corrected for the objective extraction efficiency, whereas blue data points are reported at the detector. b) Our ideal platform for deterministic integration of 2D quantum emitters. Single-photon emitters embedded in silicon nitride micro-ring resonators with precise positional and dipole alignment accuracy to achieve high Purcell enhancement. . .	103
5.2	Red emitters in hBN. a) Representative PL spectra of plasma treated and thermally annealed activated red single-photon emitters in hBN. b) Representative second-order autocorrelation function g^2 of red-emitters demonstrating dip below 0.5 at zero time delay, evidencing single-photon emission.	106
5.3	Nanopore engineering of visible hBN emitters. a) hBN flakes are exfoliated on SiO_2/Si chips. b) PMMA photoresist is spun on the substrate. c) Using electron beam lithography, nanometer array of pores are patterned in the PMMA. d) Inductively Coupled Plasma (ICP) etch using CHF_3/O_2 chemistry was utilized to etch pores into the hBN. e) A 1-nm carbon film can be deposited on the resist and the pores. Note that this step can be complimentary. f) After lift-off and photoresist strip, a thermal annealing step can be used to optically stabilize active emitters.	107

5.4	Nanopore engineering of visible hBN emitters results. a) Optical image of a processed hBN flake. Note that only the three largest rows of nanopores are visible withing the image. b) Represenative PL spectra of one of the engineered emitters. c) Position of measured single-photon emitters relative to the nanopores. Red dots denote the position of the pores and green dots are the position of the emitters.	109
5.5	Electron beam engineering of blue emitters in hBN. a) Optical image of an irradiated hBN flake. The dark rings form around the center of irradiation and are only visible in SEM image. The SEM is centered on an irradiation spot. b) Represenative PL spectra of one of the engineered emitters. . .	110
5.6	a) A two-level system with radiative rate of W_{free} and broadening (homogenous and inhomogenous) rate of γ^* will have an experimental linewidth larger than the intrinsic linewidth. b) A two-level system placed inside a cavity with Purcell Factor of F , will have total emission rate of $(1 + F)W_{free}$, the radiative linewidth is broadened while the broadening terms (γ^*) remain constant. Therefore, the experimental linewidth becomes closer to the intrinsic linewidth, demonstrating enhancement in the indistinguishability.	116
5.7	PL Spectra of visible hBN emitters under stoichiometric PECVD nitride.	118
5.8	Non-stoichiometric SiN charactrization. a) Background emssion of silicon nitride as funtion of silane/ammonia ratio (R). At $R = 20$, the background emission is suppressed, enabling high-purty measurments of hBN quantum emitters. b) Refractive index of silicon nitride as function of R	119
5.9	Non-stoichiometric SiN anneal at 1000 °C for 20 minutes . a) Background emission pre-anneal. b) Background emission post annealing.	120
5.10	PL Spectra of visible hBN emitter before (red line) and after (blue line) integration with annealed non-stoichiometric nitrogen-rich nitride.	121
5.11	Schematic of an add-drop and all-pass ring resonator. The relevant coupling and transmission coefficients for an all-pass ring resonator are shown in the central panel. The different coupling regimes are illustrated in the simulated transmission spectra of an all-pass ring resonator that is 10x undercoupled, critically coupled, and 10x overcoupled.	122
5.12	a) Mode effective index as function of width of the waveguide. Waveguide height is set at 100 nm. The bottom of Y-axis is set at SiO ₂ refractive index. It can be seen that for waveguide width below 620 nm only the fundamental modes can propagate. b) Cross-sectional mode intensity profile of the fundamental TE mode for a waveguide with 600 nm width and 100 nm thickness	128
5.13	Calculated bend loss of the waveguide.	129

5.14	Final design of the ring resonator, bus-waveguide, and the edge taper. Waveguide width is set at 600 nm, coupling distance between waveguide and ring is 3 μm in this design. Distance between ring and the waveguide is fixed at 150 nm and only the coupling length is varied to tune the coupling coefficient of the system. Taper is 120 μm wide considering both the taper region and the fixed extension which was added to allow for error in dicing step. Width of the taper is 150 nm (Note that the value of 150 nm was chosen so that experimentally the taper width achieved 110 nm width. The optimized electron beam dose that yields the correct 150 nm gap for the waveguide and ring cross-section underexposes the tapered region and slightly wider taper was implemented in the design to achieve the design value.)	130
5.15	Simulated waveguide-emitter coupling efficiency (β) for 2D quantum emitters on top, within, or below the straight waveguide. A maximum of up to 40% coupling efficiency (summed over both waveguide propagation directions) is possible for each type of emitter.	132
5.16	Emitter-waveguide coupling efficiency as a function of emitter misalignment from the center of the waveguide	133
5.17	Photonic integration fabrication process flow. a) To position the flake with respect to the photonic structure, thin hBN flakes are exfoliated on PECVD SiN films with optional thickness (t_{opt}) that is either equal to full or one-half of the designed thickness of the waveguide for top or embedded flakes, respectively. Alternatively, to position the flake on bottom of the waveguide, hBN can be exfoliated directly on the SiO ₂ substrate. Gold alignment markers are patterned with electron-beam lithography in close proximity to the flake. b) The position and dipole orientation of quantum emitters are determined by high numerical-aperture polarization-resolved microscopy and raster scanning the sample. c) Thin-film PECVD SiO ₂ for protecting TMD flakes from damage during SiN PECVD. d) Deposition of remaining SiN, if necessary, to complete the photonic layer. e) Electron-beam lithography and ICP-RIE etching are used to define the photonic circuits. f) Final PECVD SiO ₂ for the cladding layer.	134
5.18	Optical images of the alignment process. a) Optical image during the re-identification process. The green laser spot denotes the SQE location. Note that the laser is attenuated using an additional notch filter, while the blue-light imaging is achieved by passing a white light source through a dichroic mirror. The camera is centered on the flake with the alignment marks in the field of view of the image. b) Processed image with corrections. The reference pattern of the alignment marks (dashed orange lines) is now overlaid with the alignment bars. The location of the defect with respect to the center of the first pattern is read and displayed on the image.	136

5.19	Alignment process. a) Optical image of a sample after fine-alignment mark array deposition. b) Alignment of the corrected optical image and the layout of the resonator. c) Final fabricated device. d) PL Spectra of the emitter before and after integration. e) Measured emission dipole of the emitter. f) Second-order auto-correlation function of the emitter after all the fabrication steps.	138
5.20	Optical Setup Schematic	139
5.21	Microring resonator characterization. a) Optical image of a device under test. The input port is used to launch a broadband superluminescent diode into the waveguide. Light is collected from the output port. b) Dashed black line is the scattered light from the waveguide when objective is centered on the input waveguide. The dashed black line represents the SLED spectrum. The blue line represents scattered light from the ring-resonator. c) The transmission spectrum of the superluminescent diode collected from the top waveguide is indicated by the blue curve, and the raw spectrum of the superluminescent diode is shown by the orange curve for reference. Dips in the transmission correspond to the resonances of the microresonator. The normalized microresonator transmission and reference spectra are fit using the presented theoretical model to determine the microresonator response.	141
5.22	Fit to the theoretical model. a) Coupling coefficient (K) extracted from fitting the normalized transmission plots with under-coupled and over-coupled assumptions of the theoretical model. The undercoupled fit closely matches the designed coupling coefficient extracted from the Lumerical simulations. b) Extracted coupling and intrinsic quality factors with the under-coupled assumption. The coupling quality factor average is $Q_c = 9690$ with a standard deviation of 1834. The intrinsic quality factor average is $Q_i = 3560$ with standard deviation of 393.	143
5.23	ZPL of the emitter observed from the output port of the waveguide using an aligned fiber array (blue line) and from the top collection (red line). A factor of ten reduction of the ZPL linewidth is observed (from 7.2 nm down to 0.72 nm) as expected from the bandwidth of the microresonator. The peak intensity of the ZPL is misaligned from the nearest cavity resonance by ~ 0.35 nm.	145

5.24	a) Illustration of the step in the ring due to the presence of the hBN underneath. b) Visible camera image of scattering of the 638 nm superluminescent diode. The edge of the flake is denoted by the dashed black lines. Increased scattering is observed from the edge of the flake under the ring waveguide. c) Theoretical (lines) and experimental (points) resonator quality factor as a function of the integrated hBN flake thickness. It is assumed the flake covers 25% of the ring in the simulations. The Black dashed line represents the theoretical simulations, which do not consider the intrinsic loss due to the flake and absorption in the guiding medium. The Blue dashed line represents the theoretical simulations corrected with the experimental intrinsic quality factor.	146
5.25	Coupling efficiency and Purcell factor estimation as a function of objective collection efficiency. The error bound has been extracted from the standard deviation in the Q_c values. The red region represents the estimated objective extraction efficiencies using Lumerical for hBN (610 nm). . . .	150
5.26	a) PL Spectra of the WS_2 integrated microring resonator measured from the output of the bus-waveguide. b-c) Coupling efficiency and Purcell factor estimation as a function of objective collection efficiency. The error bound has been extracted from the standard deviation in the Q_c values. The red region represents the estimated objective extraction efficiencies using Lumerical for WS_2 (640 nm)	151
6.1	System efficiency η (emission of photons into the bus waveguide), indistinguishability (V), and system efficiency indistinguishability product ($\eta \times V$) as a function of the loaded quality factor of the cavity and the cavity volume normalized by the mode volume.	164
6.2	a) Total system efficiency-indistinguishability figure of merit $\eta \times V$ as a function of loaded Q at the minimum achievable mode volume for hBN and WSe_2 emitters in the visible wavelength. The intrinsic linewidth and total dephasing rate are taken from previous resonant fluorescence studies to be 50 MHz and 150 MHz (for hBN [11]) and 100 MHz and 2 GHz (for WSe_2 monolayers [12]), respectively. b) Maximum figure of merit $\eta_{max} \times V$ achievable for each class of emitters as function of the intrinsic quality factor of the SiN platform	165
6.3	Illustration of arrays of on-chip cavity-coupled 2D-based single-photon emitters.	166
6.4	Excitation modalities of quantum defects. a) Sub-bandgap optical excitation through phonon-assisted absorption. b) Above-bandgap optical excitation. c) Above-bandgap electrical excitation. Excess carriers are injected near the defect in a p-i-n junction and radiatively recombine . . .	168

6.5	Band diagram of a tunable P-I-N single-photon emitter diode. a) Architecture of the proposed single-photon emitter. b) Band-diagram of the device.	169
6.6	Overview of diode-only SPE device.	171
6.7	Optical and scanning electron microscope of fabricated devices. a) Dark-field image of the nanopillar array at the intrinsic region of the diode. b) Bottom gate structure before 2D integration. c) Fully fabricated diode after monolayer WSe ₂ transfer and top contact deposition. d) Scanning electron microscope image of the monolayer WSe ₂ at the intrinsic region of the device. Monolayer WSe ₂ can be seen draping over the nanopillar.	172
6.8	Preliminary results of the fabricated diodes. a) Characterization of gate dielectric leakage current for a 400 μm^2 capacitor. b) PL Spectra of the intrinsic region of the device at a nano-pillar location displaying sharp features.	174
6.9	Benchmarking procedure for defect-based single-photon diodes	175

List of Tables

2.1	Benchmark of Three Single-photon Emitter Platforms.	25
3.1	Part-list used to build our customized transfer station.	51
6.1	Material properties and parameters used in the calculation of single photon extraction efficiency as a function of the cavity's loaded quality factor, and the cavity volume normalized by the modal volume. Where λ_0 represents the free-space wavelength of the emitter, τ represents the emitter lifetime, η_Q represents the quantum efficiency, n_d represents the material's refractive index, and Q_i representing the intrinsic quality factor.	163

Chapter 1

Introduction

With the advent of quantum algorithms such as Shor's (1995) [1] and Grover's (1996) [2], the untapped potential and promise of quantum computing technologies became evident to the world. Quantum algorithms can potentially provide exponential speedups to classically hard problems by leveraging interference between the complex probability amplitudes of qubits. As researchers continued exploring the application space of quantum algorithms, experimentalists focused on building the necessary hardware and components for quantum computers. Fueled by investments from both public and private sectors, multiple quantum information platforms have emerged at the forefront of quantum information technologies. The most notable platforms include superconducting qubits, neutral atoms and ions, electrostatically defined spin qubits, and linear optical quantum systems. Each platform presents its own set of advantages and challenges in terms of benchmarks important for quantum computing.

Superconducting qubits [3], consisting of transmon qubits formed in Josephson junctions, have achieved modest coherence times up to milliseconds and impressive qubit gate fidelities up to 99%. Spearheaded by Google Quantum AI, superconducting qubits were the first to claim quantum advantage over classical algorithms [4]. However, these

qubits are limited to operation at millikelvin temperatures and require substantial cryogenic overhead. The increased complexity and connectivity requirements of adding each additional qubit make these systems challenging to scale. Ion-trap-based quantum computers [5] are known for their ultra-long coherence times and high gate fidelities [6]; however, such systems require bulk optics, significantly adding to the size and cost of scaling.

The emphasis on commercial scalability is a hard-learned lesson from decades of progress in the semiconductor chip industry. The scalability requirement becomes even more critical in quantum information technologies because qubits are prone to phase errors and decoherence. To make a "useful" quantum processor, tens of thousands of logically error-corrected qubits are required, which translates to platforms capable of hosting millions of qubits. Therefore, an ideal platform should arguably be compatible with or leverage the mature CMOS industry to achieve commercial viability. Another major requirement is "connectivity". Transferring and routing electrical signals in classical semiconductor chips is taken for granted. However, for quantum information, given that the no-cloning theorem makes it impossible to create copies of the same qubits, this is a major problem. This is especially true for matter-based quantum computing platforms, where information is encoded in some properties of a local particle or system. While it may be possible to "shuffle" the qubits by applying local gate operations on neighboring qubits and teleporting the quantum information to a different position on the chip, routing quantum information over longer distances requires quantum transduction [7]. This involves imprinting the encoded information from a matter-based basis onto the property of a single photon to be delivered across a network. Unsurprisingly, quantum transduction is also not an easy task, and state-of-the-art demonstrations have not yet achieved high-enough conversion efficiency with low-enough added noise.

Considering the requirements for scalability and connectivity, quantum photonic plat-

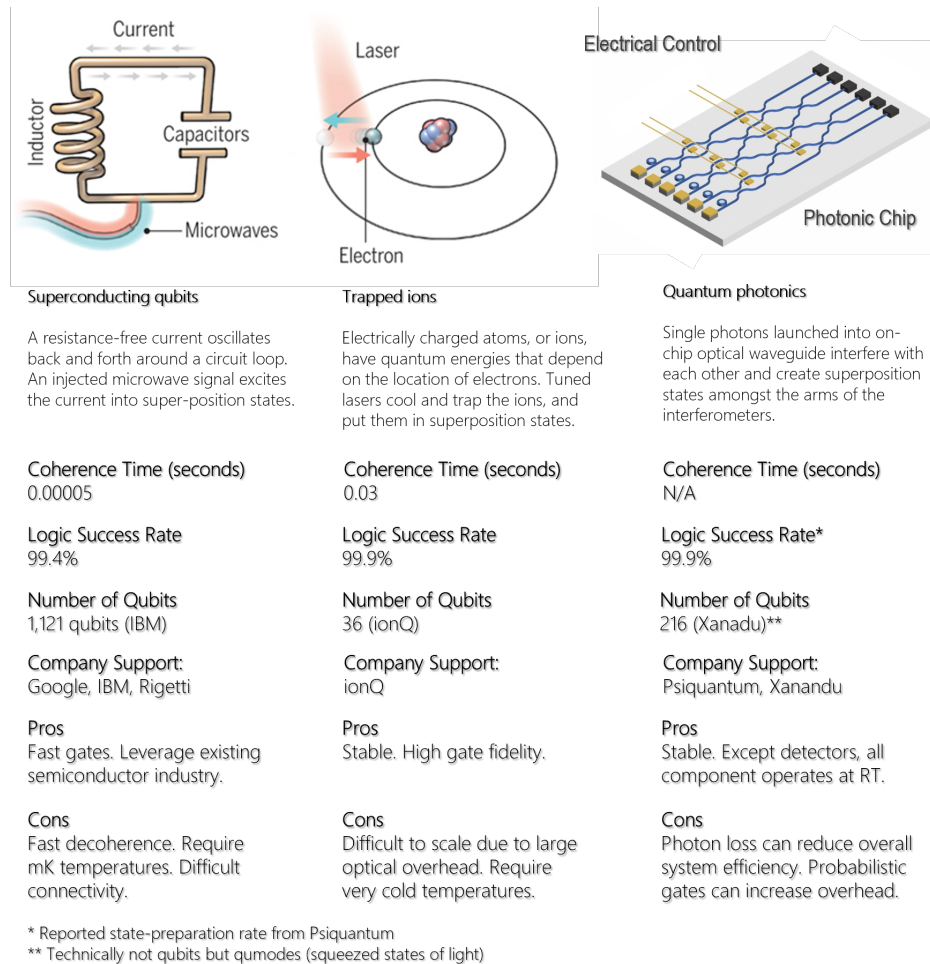


Figure 1.1: Quantum information technology platforms.

forms demonstrate significant advantages over matter-based approaches. First, they can leverage decades-long progress in classical semiconductor photonic processing to achieve commercial viability and scalability [8–10]. Second, quantum information processing with photons naturally circumvents the need for quantum transduction. Photons can be efficiently coupled in and out of photonic chips and transferred via mature photonic fibers with low loss to other network nodes [11]. These two essential advantages have made quantum photonic platforms one of the leading candidates for the future of quantum information processing.

In the last decades, multiple milestones have been achieved in quantum photonics. On the experimental side, quantum photonics leveraging bulk optics was fundamental to verification of many foundational quantum concepts such as violation of Bell’s inequality [12], Hong, Ou, and Mandel’s interference [13], quantum cryptograpy [14], quantum teleportation [15], and entanglement swapping [16]. On the theoretical side, Knill, Laflamme, and Milburn solved the long-standing problem of demonstrating entangling gates by proposing using ancilla-photons and probabilistic non-linear photonic circuits to create probabilistic CZ and CNOT gates [17]. Followed by advancements in one-way measurement based quantum computing [18, 19], efficient and practical photonic quantum computers became a theoretical possibility. This was shortly followed by experimental realization of CNOT gates [20], first-integrated quantum photonic circuitry [21], on-chip boson sampling [22], and finally culminated in demonstrating quantum advantage with quantum photonic [23].

At the moment, a huge endeavor has been placed on miniaturization of bulk optics components for demonstration of efficient and scalable on-chip quantum photonic computers. A quantum photonic chip can be broadly categorized to three main components as seen in Figure 1.2. First, the quantum light source responsible for efficient and on-demand creation of the single-photons in optical waveguides. Next, a low-loss and tunable quantum photonic circuitry, responsible for choreographing an interference pattern amongst the photons and finally, an efficient single photon detector array, responsible for measuring the final state of the circuit. Each of these sub-sections of quantum photonics chips can be considered a field of their own and require exploration of new materials, new conceptual devices, and new physics to meet the strict component benchmarks for a useful quantum photonic chip. The focus of this thesis is to develop a novel and scalable on-chip quantum light source by utilizing the properties of isolated atomic defects in two-dimensional materials.

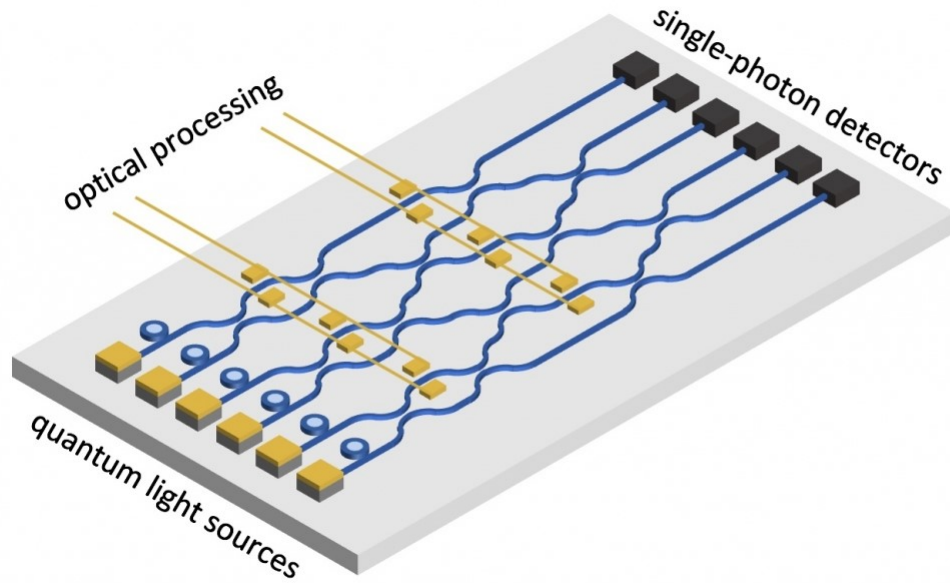


Figure 1.2: Illustration of a quantum photonics chip

1.1 Thesis Outline

This thesis is organized into seven main chapters. Chapter. 1 serves as a introduction to the thesis. Chapter. 2 provides theoretical background necessary to discuss the future chapters of the thesis. These include a brief introduction to quantum photonics, benchmarks of ideal single photon sources and various types of single-photon emitters. Then we focus on solid-state based single-photon sources in the context of 2D materials which is the main focus of this thesis. 2D material family are introduces with a focus on their excitonic properties such as dark and localized exciton which will set the stage for the future chapters of the thesis.

In Chapter 3, we will discuss the experimental procedures used in thesis. This chapter can be devided to two general categories. First, the experimental process to prepare 2D samples, such as 2D exfoliation methods, 2D layer identification method, and 2D dry viscoelastic transfer methods are introduced. In the next part of this chapter, we will

discuss the optical setups used to perform routing optical experiments utilized in the thesis. These include introduction to cryogenic photoluminescence spectroscopy and its setup, time-resolved photoluminescence spectroscopy, and second-order auto-correlation measurements.

In Chapter 4, we will focus on our efforts in understanding microscopic mechanism of single-photon emission in WSe_2 in the framework of defect-bound excitons, through which, we engineer a novel method to engineer site-specific single-photon emitters with sub-100 nm spatial accuracy, high purity, and record-breaking working temperature operations. In Chapter 5, we shift our engineering efforts from engineering emitters to integrating 2D-based quantum emitters in a scalable photonic platform. In this chapter, we develop a CMOS compatible low-autofluorescence 2D-compatible SiN photonic material and put forward a novel technique that allows for efficient integration of 2D materials with photonic waveguides via integration with microring resonators.

Chapter 6, focuses on the modeling the emitter-cavity system and projecting the required system metrics that would enable us to achieve a competitive and useful deterministic single-photon system. Furthermore, we discuss our progress in simultaneous integration of 2D-based single-photon emitters with on-chip cavities and tunable P-I-N junction diodes for electrical injection.

Finally, Chapter 7 provides a summary of this thesis and concludes the work.

1.2 Permissions and Attributions

1. The content of Chapter 2 has previously appeared in the journal Applied Physics Letters [24]. It is reproduced here under the Creative Commons CC BY license.
2. The content of Chapter 4 has previously appeared in the open access journal Nature Communications [25]. It is reproduced here under the Creative Commons

Attribution 4.0 International.

3. The content of Chapter 5 and Chapter 6 have previously appeared in the open access journal Nanoletters [26]. It is reproduced here under the Creative Commons CC BY license.

Bibliography

- [1] P. W. Shor, *Polynomial-time algorithms for prime factorization and discrete logarithms on a quantum computer*, *SIAM review* **41** (1999), no. 2 303–332.
- [2] L. K. Grover, *A fast quantum mechanical algorithm for database search*, in *Proceedings of the twenty-eighth annual ACM symposium on Theory of computing*, pp. 212–219, 1996.
- [3] M. H. Devoret and R. J. Schoelkopf, *Superconducting circuits for quantum information: an outlook*, *Science* **339** (2013), no. 6124 1169–1174.
- [4] F. Arute, K. Arya, R. Babbush, *et. al.*, *Quantum supremacy using a programmable superconducting processor*, *Nature* **574** (2019), no. 7779 505–510.
- [5] J. I. Cirac and P. Zoller, *Quantum computations with cold trapped ions*, *Physical review letters* **74** (1995), no. 20 4091.
- [6] C. D. Bruzewicz, J. Chiaverini, R. McConnell, and J. M. Sage, *Trapped-ion quantum computing: Progress and challenges*, *Applied Physics Reviews* **6** (2019), no. 2.
- [7] A. Alkauskas, C. E. Dreyer, J. L. Lyons, and C. G. Van de Walle, *Role of excited states in shockley-read-hall recombination in wide-band-gap semiconductors*, *Physical Review B* **93** (2016), no. 20 201304.
- [8] J. L. O’Brien, A. Furusawa, and J. Vučković, *Photonic quantum technologies*, *Nature Photonics* **3** (2009), no. 12 687–695.
- [9] S. Slussarenko and G. J. Pryde, *Photonic quantum information processing: A concise review*, *Applied Physics Reviews* **6** (2019), no. 4.
- [10] G. Moody, V. J. Sorger, D. J. Blumenthal, *et. al.*, *2022 roadmap on integrated quantum photonics*, *Journal of Physics: Photonics* **4** (2022), no. 1 012501.
- [11] K. Alexander, A. Bahgat, A. Benyamini, *et. al.*, *A manufacturable platform for photonic quantum computing*, *arXiv preprint arXiv:2404.17570* (2024).

BIBLIOGRAPHY

- [12] A. Aspect, P. Grangier, and G. Roger, *Experimental realization of einstein-podolsky-rosen-bohm gedankenexperiment: a new violation of bell's inequalities*, *Physical review letters* **49** (1982), no. 2 91.
- [13] C.-K. Hong, Z.-Y. Ou, and L. Mandel, *Measurement of subpicosecond time intervals between two photons by interference*, *Physical review letters* **59** (1987), no. 18 2044.
- [14] C. H. Bennett, F. Bessette, G. Brassard, *et. al.*, *Experimental quantum cryptography*, *Journal of cryptology* **5** (1992) 3–28.
- [15] D. Bouwmeester, J.-W. Pan, K. Mattle, *et. al.*, *Experimental quantum teleportation*, *Nature* **390** (1997), no. 6660 575–579.
- [16] J.-W. Pan, D. Bouwmeester, H. Weinfurter, and A. Zeilinger, *Experimental entanglement swapping: entangling photons that never interacted*, *Physical review letters* **80** (1998), no. 18 3891.
- [17] E. Knill, R. Laflamme, and G. J. Milburn, *A scheme for efficient quantum computation with linear optics*, *nature* **409** (2001), no. 6816 46–52.
- [18] R. Raussendorf and H. J. Briegel, *A one-way quantum computer*, *Physical review letters* **86** (2001), no. 22 5188.
- [19] M. A. Nielsen, *Cluster-state quantum computation*, *Reports on Mathematical Physics* **57** (2006), no. 1 147–161.
- [20] J. L. O'Brien, G. J. Pryde, A. G. White, *et. al.*, *Demonstration of an all-optical quantum controlled-not gate*, *Nature* **426** (2003), no. 6964 264–267.
- [21] A. Politi, M. J. Cryan, J. G. Rarity, *et. al.*, *Silica-on-silicon waveguide quantum circuits*, *Science* **320** (2008), no. 5876 646–649.
- [22] J. B. Spring, B. J. Metcalf, P. C. Humphreys, *et. al.*, *Boson sampling on a photonic chip*, *Science* **339** (2013), no. 6121 798–801.
- [23] H.-S. Zhong, H. Wang, Y.-H. Deng, *et. al.*, *Quantum computational advantage using photons*, *Science* **370** (2020), no. 6523 1460–1463.
- [24] S. I. Azzam, K. Parto, and G. Moody, *Prospects and challenges of quantum emitters in 2d materials*, *Applied Physics Letters* **118** (2021), no. 24.
- [25] K. Parto, S. I. Azzam, K. Banerjee, and G. Moody, *Defect and strain engineering of monolayer wse₂ enables site-controlled single-photon emission up to 150 k*, *Nature communications* **12** (2021), no. 1 3585.

BIBLIOGRAPHY

- [26] K. Parto, S. I. Azzam, N. Lewis, *et. al.*, *Cavity-enhanced 2d material quantum emitters deterministically integrated with silicon nitride microresonators*, *Nano Letters* **22** (2022), no. 23 9748–9756.

Chapter 2

Background

2.1 Quantum Technology Platforms

In the following chapter, we will discuss quantum information processing with photons in more depth and introduce the concept of the ideal single-photon source, arguably the most essential component in quantum photonic technologies. Next, we will explore various approaches to engineering an ideal single-photon source and set the stage for the required physics knowledge necessary to discuss our approach to creating single-photon emitters based on solid-state defects in 2D materials, which are covered in the following chapters.

2.2 Qubits, Quantum Algorithms, Quantum Photonics Approaches

In this section, we will discuss the fundamental ideas of encoding quantum information with single photons [1, 2] using integrated quantum photonic platforms. A single photon propagating in a unique spatiotemporal mode of a waveguide can naturally give rise to a

quantum state. Single photons can be represented in Fock (number) states by utilizing the creation operator a^\dagger on the ground-state of the quantized electromagnetic mode:

$$a^\dagger |0\rangle = |1\rangle. \quad (2.1)$$

Mathematically, the creation operator serves as our ideal photon source, where by deterministically applying it to a an empty optical mode, generates a single excitation. The photon can then propagate to a 50:50 beamsplitter, which allows us to encode the quantum information onto the path that the photon traverses. Given that a photon is a quantum particle, the probability amplitude of the photon propagates along both outputs of the splitter. Here, if we represent the existence of the photon in upper output as state $|u\rangle$ and existence of the photon in the lower output as state $|l\rangle$, the wavefunction of the system after the splitter can be represented as an equal superposition of the two possible states, defining our qubit in the so called "dual rail" configuration.

$$|\psi\rangle = \frac{1}{\sqrt{2}} |u\rangle + \frac{1}{\sqrt{2}} |l\rangle \quad (2.2)$$

The splitter can be arbitrarily engineered to control the probability amplitude of both arms. However, after introducing the concept of Mach-Zender Interferometers (MZIs) with active phase-shifters, dynamically tunable devices can be used to create any arbitrary qubit superposition. For simplicity of notations, from this point onwards, I will denote the $|u\rangle$ and $|l\rangle$ as $|1\rangle$ and $|0\rangle$, as shown in Fig. 2.1. Note that the kets no longer represent Fock-state eigenvectors in this notation and instead represent the arms of the waveguides.

To perform single-qubit gate operations, an MZI structure can be utilized. The MZI consists of two perfect directional coupler with one phase shifter embedded in one arm. First let us discuss the unitary matrix representation of a directional coupler [3].

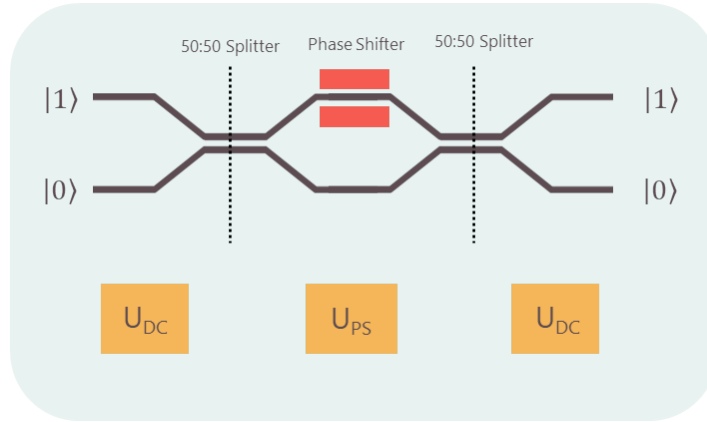


Figure 2.1: Schematic of a Mach-Zender Interferometer with a tunable phase shifter.

Assuming a dual rail photonic qubit is operated upon by a perfect 50:50 directional coupler as seen in Figure 2.1, two outcomes are possible. In first case, assuming the photon enters the top rail, then 50% of the photon probability amplitude is transmitted and 50% is scattered to the bottom output port. The state can be represented as:

$$\frac{1}{\sqrt{2}}(|1\rangle + i|0\rangle). \quad (2.3)$$

Similarly, if the photon was initially in the bottom port, the state transform as follows:

$$\frac{1}{\sqrt{2}}(|0\rangle + i|1\rangle). \quad (2.4)$$

Note that the imaginary sign is due to the phase shift from the evanescent coupling of the modes at the directional coupler. Therefore, the following unitary matrix can be composed:

$$U_{DC} = \frac{1}{\sqrt{2}} \begin{bmatrix} 1 & i \\ i & 1 \end{bmatrix} \quad (2.5)$$

Note that, in the case of dual rail representation, this unitary matrix is equivalent to

Hadamard gate (H) up to only σ_z rotations following:

$$U_{DC} = iR_z\left(\frac{\pi}{2}\right)HR_z\left(\frac{\pi}{2}\right) \quad (2.6)$$

where $R_z(\theta)$ denotes:

$$R_z(\theta) = \begin{bmatrix} e^{-i\frac{\theta}{2}} & 0 \\ 0 & e^{i\frac{\theta}{2}} \end{bmatrix} \quad (2.7)$$

Furthermore, an ideal phase shifter unitary matrix in dual rail can be represented as:

$$U_{PS} = \begin{bmatrix} e^{i\phi} & 0 \\ 0 & 1 \end{bmatrix} \quad (2.8)$$

where the phase shift is only applied to the photon in the top rail. On a side note, Z-gate can be constructed by placing the phase shifter on the bottom rail (in a structure without an MZI) and setting $\phi = \pi$,

$$U_{PS}^{down} = \begin{bmatrix} 1 & 0 \\ 0 & -1 \end{bmatrix} = Z \quad (2.9)$$

representing a Pauli-Z gate.

When two directional coupler are placed back to back, as represented in Fig. 2.1, the following expression would describe the system:

$$U_{DC} = -R_z\left(\frac{\pi}{2}\right)HR_z(\pi)HR_z\left(\frac{\pi}{2}\right) \quad (2.10)$$

Note that, $R_z(\pi)$ can also be expressed as:

$$R_z(\pi) = e^{i\frac{\pi}{2}} \begin{bmatrix} e^{-i\pi} & 0 \\ 0 & 1 \end{bmatrix} \quad (2.11)$$

which is just a global phase shift in addition to phase shift of $-\pi$ on the top arm. We can now add the phase shifter to the top rail in the MZI, merging the additional incurred phase due to use of directional coupler in the phase term of the phase shifter. Therefore:

$$U_{MZI} = U_{DC} \times U_{PS} \times U_{DC} = -iR_z\left(\frac{\pi}{2}\right)HU_{PS}(\pi + \phi)HR_z\left(\frac{\pi}{2}\right) \quad (2.12)$$

Note that similar to previous step, the extra local R_z rotations can also be translate to a global phase and a phase shift on one arm of the input and output which can either be accounted for in the calculation or be compensated by using extra phase shifter. Therefore, for simplicity we disregard these terms. Furthermore, we assume that $\pi + \phi \rightarrow \phi'$:

Note that for $\phi' = 0$, this would represent identity. Photon will exit the same arm it entered.

$$U_{MZI} = U_{DC} \times U_{PS} \times U_{DC} = HU_{PS}(\phi')H \quad (2.13)$$

Knowing the unitary matrix representation of each individual component, the MZI operator can be written as:

$$U_{MZI} = H \times U_{PS} \times H = \frac{1}{2} \begin{bmatrix} e^{i\phi'} + 1 & e^{i\phi'} - 1 \\ e^{i\phi'} - 1 & e^{i\phi'} + 1 \end{bmatrix} \quad (2.14)$$

For $\phi' = \pi$, the U_{MZI} becomes:

$$U_{\phi'=\pi} = - \begin{bmatrix} 0 & 1 \\ 1 & 0 \end{bmatrix} \quad (2.15)$$

In this case, the MZI acts as a Pauli-X gate with an additional π rotation. Finally, the Pauli Y-gate can be created by having two phase-shifter with $\phi = \pi/2$ on each rail and then operating a Pauli X and Z gate.

$$U_Y = U_{PS\pi/2}^{up} \times U_{PS\pi/2}^{down} \times U_X \times U_Z = \begin{bmatrix} i & 0 \\ 0 & 1 \end{bmatrix} \begin{bmatrix} 1 & 0 \\ 0 & i \end{bmatrix} \begin{bmatrix} 0 & 1 \\ 1 & 0 \end{bmatrix} \begin{bmatrix} 1 & 0 \\ 0 & -1 \end{bmatrix} = \begin{bmatrix} 0 & -i \\ i & 0 \end{bmatrix} \quad (2.16)$$

With the Pauli Gates and Phase Gate implemented, the only requirement of the photonic circuit to become capable of universal quantum computing is the demonstration of an entangling gate. The CZ gate is a two-qubit gate that induces a qubit phase flip on the first (target) qubit depending on the state of the second (control) qubit. Two-qubit gates have been the Achilles heel of photonic quantum computing since it inherently requires interactions of two particles. The bosonic nature of photons does not allow two photons to interact with each other easily, at least without a sufficiently strong nonlinearity; however, in 2001, a landmark paper by Knill, Laflamme, and Milburn [4] introduced the KLM protocol, which by leveraging the bosonic symmetry, ancilla photons, and post selection, the probabilistic demonstration of two-qubit photonic gates became possible.

The first step in the KLM protocol is to create a probabilistic non-linear sign shift

gate. Here, we denote this gate by NS_{-1} . The NS_{-1} acts on the Fock state modes of a waveguide with state $|\psi\rangle$:

$$|\psi\rangle = \alpha_0 |0\rangle + \alpha_1 |1\rangle + \alpha_2 |2\rangle \quad (2.17)$$

and transforms them as follows:

$$NS_{-1} |\psi\rangle = \alpha_0 |0\rangle + \alpha_1 |1\rangle - \alpha_2 |2\rangle \quad (2.18)$$

The sign flip on biphoton state is the signature function of this gate. Unfortunately, given the bosonic nature of photons, it can be proven that this gate cannot be constructed with only passive linear optics elements [5]. However, this gate can be probabilistically realized using a three by three circuit that can be defined with the following unitary matrix:

$$\begin{bmatrix} 1 - \sqrt{2} & 2^{-\frac{1}{4}} & \sqrt{\frac{3}{\sqrt{2}} - 2} \\ 2^{-\frac{1}{4}} & \frac{1}{2} & \frac{1}{2} - \frac{1}{\sqrt{2}} \\ \sqrt{\frac{3}{\sqrt{2}} - 2} & \frac{1}{2} - \frac{1}{\sqrt{2}} & \sqrt{2} - \frac{1}{2} \end{bmatrix} \quad (2.19)$$

Here, the first port of the circuit is state $|\psi\rangle$, and the other ports are ancilla photons, where on the second port we have one single photon (state $|1\rangle$) and vacuum on the final port (state $|0\rangle$). Figure 2.2a represents the circuit diagram. It can be proven that if two detectors are placed on the outputs of port two and port three, in the cases where there is one detection event on port two and no detection event on port three, the first output would transform as $NS_{-1} |\psi\rangle$. The proof of the unitary matrix representation

of the NS_{-1} can be found in reference [6] and furthermore this unitary matrix can be constructed following the theory put forward by Reck et al. [7] that allows for procedural construction of any N-by-N unitary matrix using beam-splitters and phase shifters. Note that, the NS_{-1} gate only works quarter of the time.

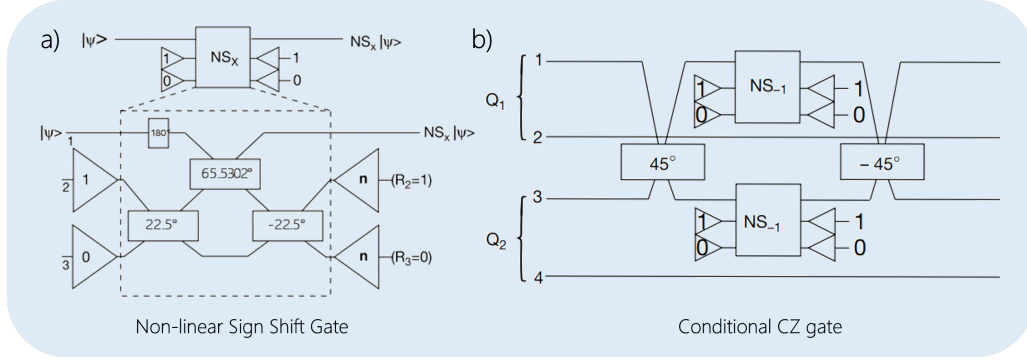


Figure 2.2: KLM protocol. a) Conditional non-linear sign shift gate. Note that the boxes demonstrate a beam-splitter operation with unitary matrix of $\begin{bmatrix} \cos(\theta) & \sin(\theta) \\ \sin(\theta) & \cos(\theta) \end{bmatrix}$. The top left 180° box is only a phase shifter. b) Configuration of a conditional controlled-Z gate utilizing two non-linear sign shift gates. Figures are reproduced here under the Creative Commons CC BY license from Knill et al., [4].

Finally, a probabilistic controlled-Z gate can be realized by utilizing two NS_{-1} gates in the configuration presented in Figure 2.2b. Verifying operation of the total circuit is relatively straightforward. Let us assume one out of the sixteen cases where both NS_{-1} gates act as intended. Note that, the NS_{-1} gate is equal to identity unless there is a probability that input $|\psi\rangle$ contains a biphoton mode. For the three cases of $|00\rangle$ (both photons on each qubit in the bottom rail), $|01\rangle$, and $|10\rangle$, at no point two photons enter the beam-splitters together. Therefore, in these three cases, there is no probability of having a biphoton mode at the entrance of the NS_{-1} gates. Hence, the two beam-splitters act back to back as $H \times H = I$, and the state of the circuit is identical to the input at the output.

However, situation is different for $|11\rangle$ case. Here, after the first beam-splitter the

state can be represented and evolved as:

$$\begin{aligned}
|11\rangle &= a_1^\dagger a_3^\dagger |vac\rangle \\
a_1^\dagger &\xrightarrow{BS_1} \frac{1}{\sqrt{2}}(a_1^\dagger + a_3^\dagger) \\
a_3^\dagger &\xrightarrow{BS_3} \frac{1}{\sqrt{2}}(a_1^\dagger - a_3^\dagger) \\
|11\rangle &\xrightarrow{BS_1 \& BS_3} = \frac{1}{2}(a_1^\dagger + a_3^\dagger)(a_1^\dagger - a_3^\dagger) |vac\rangle \\
&= \frac{1}{\sqrt{2}}\left(\frac{1}{\sqrt{2}}(a_1^\dagger)^2 - \frac{1}{\sqrt{2}}(a_3^\dagger)^2\right) |vac\rangle
\end{aligned}$$

Applying the NS_{-1} gates, will only change the sign before the creation operators. Therefore:

$$\begin{aligned}
|11\rangle &\xrightarrow{BS_1 \& BS_3 \& NS_{-1}^1 \& NS_{-1}^3} = \frac{1}{\sqrt{2}}\left(-\frac{1}{\sqrt{2}}(a_1^\dagger)^2 + \frac{1}{\sqrt{2}}(a_3^\dagger)^2\right) |vac\rangle \\
&= \frac{1}{2}(a_3^\dagger + a_1^\dagger)(a_3^\dagger - a_1^\dagger) |vac\rangle
\end{aligned}$$

Finally, applying the last two beam-splitters:

$$\begin{aligned}
|11\rangle &\rightarrow \frac{1}{2}\left[\frac{1}{\sqrt{2}}(a_1^\dagger - a_3^\dagger) + \frac{1}{\sqrt{2}}(a_1^\dagger + a_3^\dagger)\right]\left[\frac{1}{\sqrt{2}}(a_1^\dagger - a_3^\dagger) - \frac{1}{\sqrt{2}}(a_1^\dagger + a_3^\dagger)\right] |vac\rangle \\
&= -a_1^\dagger a_3^\dagger |vac\rangle = -|11\rangle
\end{aligned}$$

Leading to the desired outcome of the controlled-Z gate with probability of one out of sixteen. In their seminal paper [4], Knill, Laflamme, and Milburn further demonstrate that the probabilistic CZ gate success rate can be increased to 0.25 by utilizing quantum teleportation. The first experimental demonstration of KLM CZ gate was carried out by

O'Brien et al. [8]. However, the probabilistic nature of these gates creates an unscalable overhead for all-optical gate-based quantum computing. Although more successful and efficient gates can be implemented, the non-unity fidelity of two-qubit gates exponentially decreases the fidelity of the total system.

The next milestone that addressed this problem came with the advancements in measurement-based one-way quantum computing in cluster-state approaches [9]. It was shown that starting with a large entangled cluster state, it is possible to translate any qubit gate operation, even multi-qubit gates, to a series of one-qubit gate operations whose results affect the operation of future gates in a feed-forward manner [10].

Figure 2.3 represents a simple example of single-qubit measurement in cluster state approach. Figure 2.3a represents the circuit diagram for single-qubit teleportation. Here, state $|\Psi\rangle$ undergoes a Controlled-X gate with an ancilla qubit in state $|0\rangle$. After entangling with the ancilla qubit, a Hadamard gate is applied to initial state and it is measured. Knowing the measurement outcome of the initial state, the initial state can be 'teleported' to the ancilla qubit by applying a conditional Z gate (applying identity if $m=0$ and apply Z gate if $m=1$). Given that CX gate can be translated to a CZ gate by implementing two extra Hadamard gate as shown in Figure 2.3b, the overall circuit can be rewritten as Figure 2.3c. Finally, let's assume that an arbitrary rotation around Z-axis was applied to our initial state. Since single qubit rotation commutes with the CZ gate, the final circuit diagram can be represented in Figure 2.3d. This final circuit is the foundational identity circuit behind cluster-state quantum computing. Note that via performing single-qubit operation on two entangled qubits and feed-forwarding the result of the measurement on the initial state, we have now transformed the ancilla qubit to our desired qubit operation on the initial state. It can be further shown that by using more ancilla qubits, initial state can be mapped to any other point on the Bloch-sphere and more importantly, applying only single-qubit operations on a set of entangled qubits, can mimic the operation of

multi-qubit gates [10].

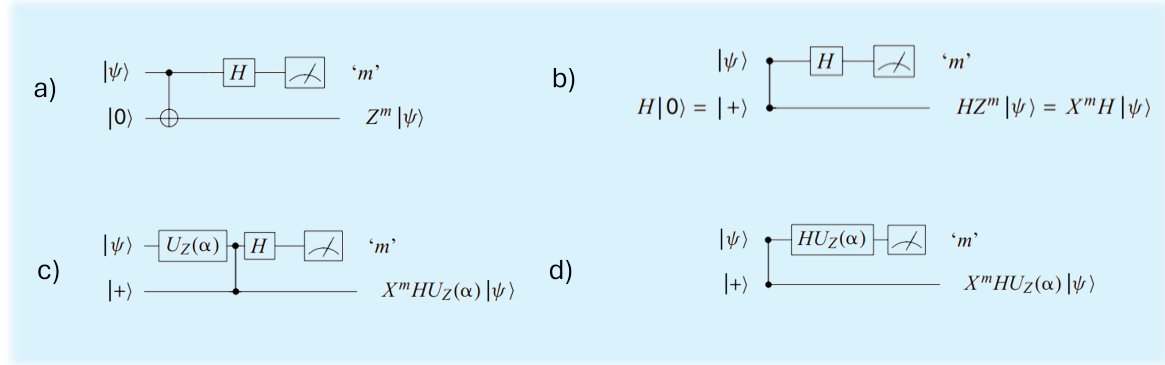


Figure 2.3: Circuit Diagram for single-qubit operation in cluster-state measurement.

This approach essentially removes the need for probabilistic optical two-qubit gates on the front-end of the operation if the entanglement is already established by the cluster-state generation in the first place, i.e. probabilistic gates are only required in the beginning of an operation to generate large cluster states. This approach essentially decouples the cluster-state generation part of the chip from the processor unit. One can imagine many probabilistic chips are running simultaneously to generate large cluster states, although at a much longer time scale, but once the cluster state is produced, it can be transmitted to the optical processing unit for deterministic operation.

With demonstrations of probabilistic two-qubit gates, the cluster-state approach relying on fusion operations [11] to create large dimensional clusters, a clear path forward for photonic quantum computing to demonstrate universal quantum computers is paved.

The three main components of this system will be an ideal-single photon source to feed into the cluster-state generator, low-loss and ultra-fast passive and the switch photonic circuitry, and an ideal single-photon detector. Each of these components are being developed and continually improved in parallel beginning several decades ago. Here, we turn our focus to the ideal single-photon source, which is the subject of this thesis.

2.3 Ideal Single Photon Source Metrics

In this section, we define the ideal metrics of a single-photon emitter. While different applications of quantum information technologies may require different specifications for quantum light sources, generally five important metrics are essential: brightness, purity, indistinguishability, system efficiency, and scalability. Here, we briefly discuss each of these metrics in the context of actual experimental settings.

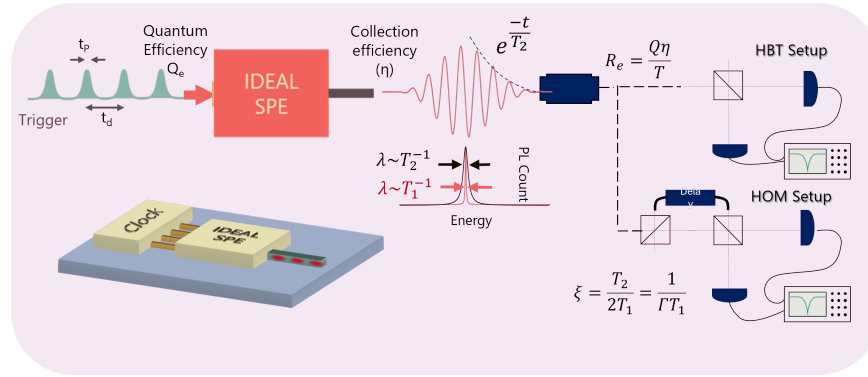


Figure 2.4: An Ideal Single-Photon Emitter. An ideal SPE source is excited from an electrical pulse of a clock with t_p and a period of t_d . Single photons are generated with probability Q_e (internal quantum efficiency). This photon is collected into a single optical mode with probability η , resulting in brightness $Q\eta/T_1$. The Hanbury Brown and Twiss (HBT) setup is used to quantify the single-photon purity. A Hong-Ou-Mandel (HOM) interferometer is used to determine the indistinguishability ξ of subsequently emitted photons, which is determined by the lifetime T_1 and coherence time T_2 .

- **System Efficiency:** Figure 2.4 represents the schematic of an experiment for single-photon generation. Here, we represent the single-photon generator as an ideal black box. To trigger single-photon generation, an electrical or an optical pulse needs to excite the SPE. The width of this pulse would determine the timing precision of the overall circuit, and in order to be able to synchronize the interference of the wave functions of many different photons, the pulse width must be ideally orders of magnitude smaller than the lifetime of the single-photon emission process, which in turn determines the spatial extent of the wave function. Next, it is critical

that with each pulse, only one photon is generated. The probability of generation of a single photon with a given pulse is denoted as quantum efficiency Q . Next, it is imperative for each photon to be emitted into the same spatiotemporal mode so the subsequent photons emitted from the source are all indistinguishable with respect to each other. For many sources, this process depends on how well the light from source is collimated or coupled to a unique optical mode and is usually represented as collection efficiency η . Therefore, we can define the system-wide efficiency as the probability of having a single photon at the defined output mode of the source as $\eta \times Q$. A fully deterministic source has $\eta \times Q = 1$.

- **Brightness:** In a quantum photonic circuit, the generation rate of the photons serves a similar function to that of the electrical clock in integrated logic circuits. The overall generation rate of the photons depends on the trigger frequency (f_p). However, the trigger cannot be faster than the average time for the single-photon emitter to generate the photon. For the case of two-level systems, this timescale can be regarded as the lifetime of the two-level optical transition (T_1). Therefore, the maximum rate of the system will have an upper limit of $\frac{\eta Q}{T_1}$. To achieve high brightness, ideally at gigahertz rates or higher, the lifetime of the photon has to be small and on the order of 100-1000 *ps*. In many systems, this is limited by the inherent physical properties of the optical transition; however, it is possible to engineer lifetime by utilizing optical cavities. This process will be discussed in depth in Chapters 5-7.
- **Purity:** Now we focus on the properties of the generated light itself. Purity is a measure of a sub-Poissonian characteristic and the "one at a time" behavior of the quantum light. The purity is generally measured as the value of the second-order autocorrelation function at zero time delay ($g^2(0)$) through Hanbury Brown and

Twiss interferometry as shown in Fig. 2.4. A well-spaced train of antibunched single photons incident on a beamsplitter will never result in measured coincidence counts on two different detectors at the outputs of the beamsplitter. Purity is not only a measure of "quantumness" of light, but it also contains valuable information about the uncorrelated optical background emission that could be present in the system. An ideal sub-Poissonian emitter in the presence of background photons will yield non-zero $g^2(0)$. Presence of unwanted photons from environment can cause $g^2(0) > 0$ and result in unexpected counts on detectors, lowering the fidelity of the optical gates. Therefore, for quantum information experiments, experimental $g^2(0)$ values are fundamental and should not be corrected for background in a real experimental setting. Finally, achieving both high brightness and high purity is essential to decrease the probability amplitude of the vacuum component of the electromagnetic field.

- **Indistinguishability:** Indistinguishability (ξ) is a measure of how strongly two photons generated from the different emitters (or the same emitter at different times) can interfere with each other. Indistinguishability can be measured through Hong-Ou-Mandel interferometry, as seen in Figure 2.4. Two identical photons incident on a perfect 50:50 beamsplitter will exit the same port of the beamsplitter together, leading to zero coincidence counts on the detectors. For two photons to be indistinguishable, it is critical for them to not only be emitted in the same spatiotemporal optical mode, but also for the phase of the wavefunctions to be matched. Physical mechanisms that lead to the alteration of the phase of the photon can be categorized as homogeneous (elastic carrier-carrier and carrier-phonon scattering or pure dephasing) and inhomogeneous broadening factors (such as spectral wandering due to stark shift) and result in the coherence time of the photon

(T_2) to become larger than the limit set by the lifetime ($2T_1$) [12]. Experimentally, the measured linewidth becomes larger than the Fourier-limited linewidth of the transition, and the visibility of the interference is decreased. In order to achieve the strongest interference, the source must be Fourier-limited.

- **Scalability:** An ideal single-photon source must be scalable, in the sense that it would be both technologically and financially viable to create millions of such components reliably and with a small footprint on-chip and directly integrated into single-mode waveguides with near-unity efficiency. Sources that leverage material systems and processes that are compatible or can become compatible with CMOS process flow are advantageous. Furthermore, it is preferable that the single-photon emit in wavelengths compatible with current infrastructure of optical communication, ideally C-band (1530-1565 nm).

To date, no SPE technology has satisfied all of these requirements at once, and achieving this ideal black box has become the "holy grail" of quantum photonic technologies. Table 2.1 represents a series of benchmarks for each of these metrics for various quantum applications. In the next section, we discuss common approaches to creating single-photon emitters with respect to these metrics.

	Nonlinear Crystals	III-V Quantum Dots	h-BN
Operating Temperature	4-300	<5 K	Room Temperature
Photon Generation Efficiency	Probabilistic, 10^3 Hz	On-Demand, 10^7 Hz	On-Demand, 10^6 Hz
Efficiency	1%	80%	45 %
Purity	> 99.9%	>99%	>95%
Indistinguishability	Intrinsically	Up to 20 photons	Fourier-limited demonstrated
Scalability	Integrated Photonics	Limited to single QDs	Integrated Photonic
Commercial Availability	Available \$	Available \$\$\$	N/A

Table 2.1: Benchmark of Three Single-photon Emitter Platforms.

2.4 Types of Single-Photon Sources

Single-photon sources can be divided into two main categories: probabilistic sources based on nonlinear optical processes and deterministic sources based on fluorescence from an isolated two-level system. First, we will briefly discuss the probabilistic nonlinear sources.

Probabilistic sources typically utilize either spontaneous parametric downconversion or spontaneous four-wave mixing to generate single and entangled photons [13]. In parametric downconversion, relying on materials with a $\chi^{(2)}$ nonlinearity due to broken inversion symmetry, a pump photon interacts with the nonlinear polarization of the crystal and, with some probability under the correct energy and momentum conservation conditions, undergoes annihilation to create two photons at lower frequencies. Similarly, in spontaneous four-wave mixing, relying on the $\chi^{(3)}$ third-order nonlinearity, two pump photons interact with a nonlinear medium, annihilate, and create a signal and idler photon at higher and lower energies relative to the pump photon energy. The inherent low probability that the laser pump undergoes the nonlinear processes makes them valuable for single-photon generation, to the point that in the rare occurrence of a nonlinear event, only a single signal and an idler photon are generated. While it is possible to increase the generation rate of the single photons by increasing the pump laser intensity, the purity and brightness of nonlinear sources are tied together. For instance, one can increase the pulse intensity so that at least one signal and idler are generated in the cycle. However, this comes at the cost of having observable multi-photon events that decrease the single photon purity.

To circumvent this problem, it is possible to use multiple nonlinear single-photon sources in parallel and use a high-speed optical switch to route the photon of the source that successfully undergoes a nonlinear process [14]. However, these approaches substan-

tially increase the system's overhead and require significant advances in optical switch and optical memory technologies to become practical. While the probabilistic nature of nonlinear sources is their most crucial disadvantage, one of the critical advantages of these sources is their high indistinguishability. As we will discuss shortly, deterministic sources that rely on the radiative decay of electrons typically suffer from high linewidth broadening and low indistinguishability. The charged electron can strongly interact with its local environment, enabling many mechanisms that can cause broadening before its decay. All these processes imprint their effect on the phase of the emitter photons, leading to low indistinguishability. However, the photons barely interact with the medium in nonlinear processes due to their bosonic nature. Therefore, photons generated in parametric down-conversion or spontaneous-four-wave mixing can be highly indistinguishable—a feat that is very difficult to achieve for deterministic sources.

The second type of single-photon source, which is the type that is studied in this thesis, is based on fluorescence from isolated two-level systems [15]. An isolated two-level system, such as a single atom, quantum dot, or quantum defect, can be a natural rate-limiting system. If an optical pump pulse incident on a two-level system, it can only excite a single electron into a state with a higher quantum number; the excited electron will prohibit further excitation to the same quantum state due to the Pauli exclusion principle. The excited electron can then radiate via decay to the ground state within the lifetime of the transition and generate a single photon with the same energy as the transition. The system can then undergo another excitation event, resulting in the single-photon source's overall one-at-a-time behavior. In these types of sources, the brightness is decoupled from purity. The overall system efficiency will be dependent on multiple factors [16]. First, the excitation efficiency is heavily dependent on the type of excitation mechanism, such as phonon-assisted non-resonant excitation, free carriers from band edges (for quantum dots and defects), or resonant excitation.

Furthermore, the dipole strength and scattering cross-section would also affect the excitation efficiency. Once the system is excited, the electron can return to the ground state through radiative transition and non-radiative decay paths such as phonon emission. The dipole orientation and available photonic density of states sets the radiation pattern of the system. Finally, the collection efficiency depends on the engineering of the experiments; for instance, in free-space-based experiments, the collection efficiency is mainly set by the numerical aperture of the objective lens. While many of these mechanisms relate to the inherent properties of the isolated system, it is possible to boost these efficiencies by leveraging another mechanism; for instance, resonance fluorescence in tandem with integration with optical cavities can theoretically bring the overall system efficiency to unity.

The state-of-the-art deterministic single-photon sources are considered to be the III-V InAs quantum dots. Heterogeneous quantum dots are typically grown using Molecular Beam Epitaxy (MBE) during the deposition of InAs on a substrate of GaAs [17]. Given the lattice mismatch between the crystal structure of InAs and GaAs, as the material is deposited, an intrinsic strain is also built up in the interface and the InAs layers. Once this strain reaches a critical point, the interface bonding is broken, and the InAs atoms fuse to form islands of InAs on the GaAs surface in a process known as Stranski-Krastanov [18] self assembly. Next, a capping layer of GaAs with a higher bandgap is grown on the quantum dots to create the three-dimensional confinement potential. The three-dimensional band-alignment of the InAs islands with their surroundings leads to a wholly confined potential that gives rise to an atomic-like density of states. While indistinguishability of quantum dots is typically limited by pure dephasing and inhomogeneous broadening due to stray electric fields caused by free carriers and nearby charge traps [19, 20], resonant excitation along with integration with micropillar cavity [21] and reverse biased PN junctions has tremendously helped diminish these effects and indistinguishable pho-

tons from these sources have been reported in the literature [22]. The primary challenge associated with quantum dot single-photon emitters is the probabilistic nature of their growth process. During the release of stress, the formation of quantum dots becomes almost a completely random stochastic process. While the density of the dots can be controlled in the Stranski-Krastanov method, it is impossible to control their positioning site precisely. This has been an obstacle in the large-scale production of single-photon devices based on III-V quantum dots. While some techniques, such as pre-growth strain engineering, have been explored to realize deterministic positioning, such methods have nearly always proved detrimental to the emitter's single-photon properties. Thus far, no scalable site-specific method that can create quantum emitters generating high-purity and indistinguishable photons has been demonstrated in any material platform.

Finally, we turn our attention to defect-based single-photon emitters, specifically single-photon emitters in 2D materials, as an alternative method to create on-demand single-photon emitters. The main advantage of these single-photon emitters over III-V quantum dots is their ability to be site-specifically engineered through various methods. In the following sections, we briefly introduce 2D materials with a focus on Transition Metal Dichalcogenides and their optical properties that lead to the observation of 2D-based single-photon emitters, setting the stage for the future chapters of this thesis.

2.5 2D Family

2D materials [23–25], are a class of layered materials that are distinguished by being held together with strong covalent bonds in the in-plane direction and having complete, dangling bond-free interfaces in an out-of-plane direction. This effectively results in atomically thin sheets of materials that can be stacked on top of each other. However, once stacked, the different layers are not bonded together and only interact with each

other through weak Van der Waals (VdW) forces. This layered structure of 2D materials results in many different distinct properties. First, it allows 2D materials to be mechanically exfoliated. Flakes from bulk 2D material crystals, either grown in the lab or found in nature, can be peeled off each other, much like an onion-like structure, using various exfoliation methods, some of which we will discuss in the next chapter. This ability to thin down 2D materials from many layers (bulk) to a few layers, trilayer, bilayer, and finally monolayer, allows for a vast tunability of properties of 2D materials. For instance, in the case of Transition Metal Dichalcogenides (TMDs), as the material is thin down from bulk to monolayer, the confinement potential is increased, and the out-of-plane VdW orbital interactions are reduced, resulting in an increase of the bandgap of the material as well as a transition from indirect to direct semiconductors [26]. These strongly affect the electrical and optoelectronic properties of this material, and having the ability to control the number of layers in the material through simple mechanical exfoliation techniques is an unprecedented capability unique to the 2D family.

Another advantage of layered materials is their ability to transfer to other substrates or structures. It is possible to mechanically peel off a layer of 2D materials and transfer it to a foreign substrate without being restrained by the conventional lattice-matching constraints of traditional three-dimensional semiconductors. This arises from the fact that 2D materials only interact with weak VdW forces in the out-of-plane direction. Therefore, 2D materials have become an incredibly versatile platform to showcase various 2D-2D and 2D-3D heterostructures, leading to proof-of-concept of many novel electronics [27], optoelectronic [28], spintronic [29], and valleytronic devices [30]. Finally, another consequence of having no covalent bonds in the out-of-plane direction results in pristine, is the dangling-bond-free interfaces of 2D materials which is devoid of any interface states. Any traditional semiconductor would inevitably have interface states at the boundaries of the material due to termination of the periodicity of the lattice. For many quantum

information and quantum sensing technologies [31], it is critical to have functional interfaces that are as close to the material's surface as possible to maximize any potential electronic or magnetic dipole coupling; however, the existence of interface states typically causes too many unwanted interactions that prohibit the isolated quantum defects from functioning correctly. 2D materials are again excellent in this domain since defects in 2D can exist on the material's surface without being surrounded by any potential interface states.

Having discussed the main advantages of 2D materials, let us discuss the properties of two critical 2D materials, specifically the TMD WSe₂ and hexagonal boron nitride (h-BN), that will be discussed throughout this thesis.

2.6 Transition Metal Dichalcogenides

Following the successful exfoliation of graphite to monolayer graphene, the scientific community turned its attention to identifying other van der Waals materials. Transition metal dichalcogenides (MX₂, M denotes the transition metal and X denotes the chalcogen) emerged as top candidates, with some TMDs like molybdenite (MoS₂) standing out due to their naturally occurring mineral crystals and unique layered hexagonal crystal structure. These layers, bound together by van der Waals forces, give MoS₂ extremely low friction properties, making molybdenite a widely used solid lubricant in high-temperature and high-pressure applications.

A breakthrough in the 2000s was the realization that the TMDs can also be exfoliated down to a few layers and even monolayer using simple scotch tape methods while retaining high crystallinity. Bulk TMDs typically have an indirect bandgap with the top of the valence band at the Γ point and the bottom of the conduction band at the K point in the first Brillouin zone. The valence band orbital composition at the Γ point mainly

consists of a combination of p_z orbitals of sulfur atoms and d_{z^2} orbitals on molybdenum atoms. These orbitals are delocalized in nature and arise due to anti-bonding interaction. Once the interlayer coupling is weakened as the crystal is thinned down to the monolayer limit, the energy of these states is reduced significantly. At the same time, the orbital composition of valence and conduction band at the K points is mostly a combination of localized in-plane orbitals, which remains undisturbed by the change in interlayer coupling separation. The culmination of these effects is that the top of the valence band at the Γ point is significantly lowered in energy, and the material undergoes an indirect-to-direct transition with the new bandgap located at almost unaltered K points as seen in Figure 2.5 [32]. In addition to decreasing the Coulomb interaction between charges in the monolayer sheet due to reduced dielectric screening, this effect also allows for the realization of two-dimensional excitons with extremely high binding energies in monolayer TMDs. As a result, monolayer TMDs have vastly different optoelectronic properties compared to bilayer, few-layer, and bulk TMDs. Retaining high quantum efficiency and absorption in monolayer TMDs has made them exciting candidates for many optoelectronic devices such as light emitting diodes (LEDs), photodetectors, and modulators. From a purely electronic perspective, monolayer TMDs are also extremely interesting given that their pristine dangling bond-free interfaces, in conjunction with the reduced dielectric screening, allow them to retain very high electron mobilities at atomic thickness limits that are theoretically impossible for other 3D semiconductors [33]. This is a tremendous advantage for 2D semiconductors, given that for highly scaled field-effect transistors, as channel length continues to shrink, the channel thickness should also become thinner to mitigate short-channel effects [34]. 2D-based electronic devices such as highly scaled transistors, memories, and memristors have become an active area of research in recent decades by industry and academia.

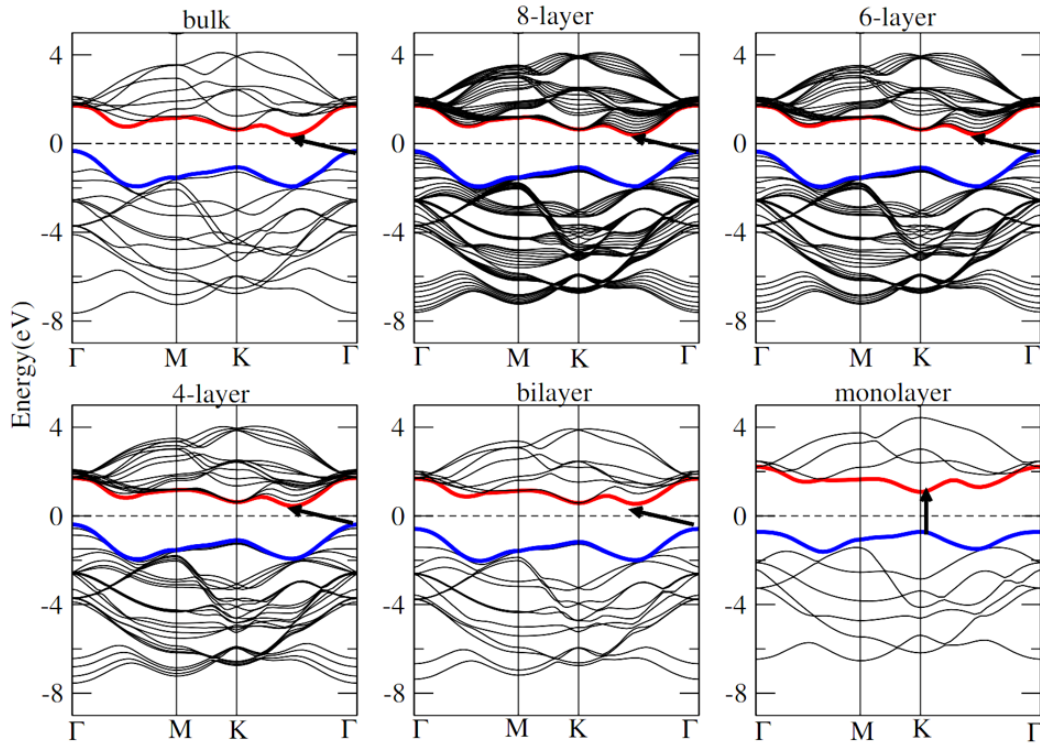


Figure 2.5: Bandstructure of MoS₂ as function of number of layers. Density-functional theory prediction of MoS₂ as function of layers. Reproduced with permission from Kumar et al., [32] (2012). Copyright 2012 Springer Nature

2.7 Exciton in Low Dimensional Materials

In this section, we discuss the excitonic properties of transition metal dichalcogenides in more detail before introducing the concept of defect-based single photon emitters.

After excitation of a semiconductor with the above band-gap photons, a non-equilibrium density of free carriers in the conduction band and valence band is created, which then relaxes to the bottom of the conduction band and top of the valence band through acoustic phonon emission on the timescale of femtoseconds. The timescale of the decay of this population depends on the time constants of the radiative and non-radiative recombination pathways, but are generally on the timescale of tens of picoseconds to nanoseconds. During this time, a free electron-hole pair in the semiconductor can attract to each other

through Coloumb interactions and lower their overall energy by forming a hydrogen-like state, creating a bosonic quasi-particle called an exciton [35]. The bosonic nature of excitons allows many pairs of electron and holes to retain the same energy state, and effectively, the optical properties of the semiconductor during this timeframe are dominated by the properties of the excitonic state. The binding energy of the exciton relates directly to the probability of exciton formations/annihilation. It depends on factors such as the extent of Coulomb interaction, the level of quantum confinement in the material, the strength of electric field screening by other carriers in the materials, and temperature. For instance, in bulk GaAs and GaN, excitons have binding energy on the order of 4-5 meV and 20-25 meV.

After successfully demonstrating monolayer TMDs, their excitonic properties were experimentally studied. Surprisingly, the excitonic binding energies in this system can reach values as high as 300-500 meV [36]. Furthermore, the Rydberg series of these excitonic states shows an apparent deviation from typical excitons in three-dimensional materials. In monolayer 2D materials, free electrons and holes are entirely confined to a two-dimensional sheet of material, eliminating any potential screening of the fringe electric fields of the two charges in an out-of-plane direction. Furthermore, for a suspended sheet of 2D material, the effective dielectric constant above the sheet is determined by the dielectric constant of either air or vacuum, leading to a further enhancement of fringe electric field extending outside of the material and changing the functional form of the column potential between the two charges [37]. This effect leads to the high observed excitonic binding energies and the change of the Rydberg series of these excitons from a hydrogenic 3D system to a theoretical 2D hydrogen-like state. Given the strength of exciton binding energy in TMDs, acoustic phonons typically cannot destroy the excitonic state at room temperature, and most photoluminescence, absorption, and optoelectronic signatures of TMDs at room temperature are dominated by their excitonic properties [36].

The next important characteristic of 2D-TMDs is their significant spin-orbit coupling, which results in spin-polarized band structure. The transition metals in TMDs cause a large spin-orbit coupling near the top of the valence band of the TMDs, which, as mentioned before, are mostly dominated by d_{z^2} orbitals of the transition metal with a total angular momentum of two, resulting in up to 450 meV of splitting between the spin-up and spin-down configuration at K and $-K$ points. The spin-orbit coupling effect is not limited to the top of the Valence band and can be also seen at the bottom of the conduction band. At the conduction band minimum, the orbital composition is a mixture of the transition metal d_0 orbitals and p orbitals of the chalcogen atoms. Interestingly, the sign of spin-orbit coupling contribution from the second-order effects of d_0 orbitals and p orbitals are opposite of each other and for different transition metal and chalcogen configuration, the overall sign of spin-orbit coupling at the conduction band can be either positive or negative. This gives rise to a very interesting band structure possibility in monolayer TMDs. For materials such as MoSe_2 and MoS_2 , the sign of spin-orbit coupling in the valence band maximum and conduction band minimum is the same. This means that the ground-state direct optical transition between excitons in either K or $-K$ momentums are the same and spin-allowed, resulting in typical observation of bright excitons as seen in Figure 2.6. However, for materials such as WS_2 , WSe_2 , and MoTe_2 , the sign of spin-orbit coupling in the conduction and valence band is opposite. This results in a spin-forbidden transition for the ground-state exciton and the creation of a dark-exciton band. In these materials, after optical excitation, although excitons form with high probability, these excitons cannot decay radiatively due to momentum-conservation principle, and specially at low-temperature where the population of bright excitons are exponentially lower, photoluminescence response of these 'dark' TMDs, are surprisingly dim. The implications of dark excitons and their contribution to single-photon generation in TMDs are significant and will be discussed in detail in future chapters, underscoring

the potential impact of our research.

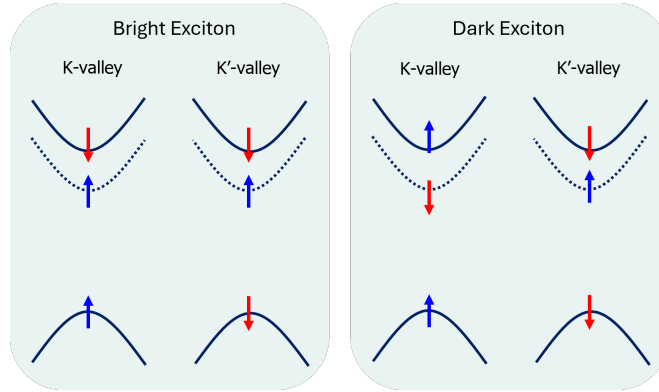


Figure 2.6: Spin-resolved bandstructure of TMDs. Both Conduction and Valence band are spin-polarized due to spin-orbit coupling. The sign of splitting is much larger in Valence band compared to Conduction band, hence, we only represent the top spin-polarized band of the Valence band. However, as discussed, the sign of spin-orbit splitting can change in the conduction band for different TMDs, giving rise to two unique electronic bandstructure spin configuration. In the first case, the ground-state transition is spin-allowed and allows for radiative transitions, giving rise to a bright exciton. In the second case, the ground-state transition is spin-forbidden, allowing for formation of dark excitons.

2.8 Hexagonal Boron Nitride

Another widely used material in 2D-family is boron nitride. Boron nitride has several possible phases, including cubic, wurtzite, amorphous, and hexagonal boron nitride. In its hexagonal form, boron nitride has a layered structure similar to graphite where each layer is composed of in-plane covalently bonded nitrogen and boron pairs arranged in a hexagonal lattice and different layers only interact with each other through weak van der Waals forces, allowing h-BN to be exfoliatable [38]. h-BN possesses a very large bandgap energy (5.955-5.97 eV) with a strong cathodoluminescence response at UV wavelength (215 nm), making it a strong candidate for light-emitting application in the UV region. Interestingly, though, the band structure of hBN was a debated topic until recently. The cathodoluminescence experiments [38] suggest a direct-band gap energy as well as a large

Wannier-type exciton with a binding energy of up to 130 meV. However, the ab-initio calculation suggested that h-BN may have an indirect bandgap [39, 40] between the K-M points in the band diagram. In 2016, Cassabois et al., [41], through phonon-assisted photoluminescence and absorption and two-photon excitation spectroscopy, experimentally verified that hBN is indirect bandgap material and its optoelectronic behavior is heavily dominated by phonon-assisted recombinations.

The wide bandgap of hBN makes it a near-perfect electrical insulator. The lack of intrinsic dangling bonds at the h-BN interface, in conjunction with relatively high breakdown fields and its compatibility with exfoliation and transfer techniques, has made hBN the most popular choice of gate dielectric for experiments involving 2D materials. Furthermore, the minimal surface roughness due to its atomically flat interface has allowed hBN to also serve as a perfect substrate for electrical or optical characterization of other 2D materials. In our experiments, we are most interested in optical properties of isolated defects in hBN. Over the years, several classes of luminescent defects have been observed in hBN, and several of them was able to demonstrate single-photon emission. In the next section, we will discuss microscopic dynamics that can lead to single-photon emission from an atomic defect and classes of hBN emitters are formally introduced in Chapter 5.

2.9 Quantum Defects in 2D-Materials for Single Photon Emission

Finally, we turn our attention to quantum defects in 2D materials. Point defects in semiconductors are imperfections of the crystal lattice. They can be categorized by a variety of types, such as vacancy (removal of an atom from the lattice), interstitials (extra or foreign atoms positioned at sites that are not lattice vertices), and substitutional

defects (extra or foreign atoms replacing the default atom at the lattice sites). In almost all of these cases, a point defect results in insufficient or excess electrons that do not participate in the regular bonding structure of the crystal lattice. Such dangling bonds alter the distribution of the lattice potential in their vicinity and, due to their atomic sizes, naturally give rise to a highly confined potential distribution overlaid on the broader potential of the lattice. Depending on the arrangement of the dangling bonds, this confined potential creates its own discrete atomic-like electronic states, which can be occupied by the excess charges that do not participate in lattice bonding. In a sense, the dangling bonds resulting from atomic defects in the crystal behave very much like artificial atoms and molecules, and electrons trapped in localized states of the defect, based on the arrangement of the dangling bonds, may absorb or emit photons by going to higher or lower energy states.

Figure 2.7a represents a simplified single-particle picture of the electronic configuration of a hypothetical isolated defect within the bandgap of a semiconductor. Note that the discrete electronic states of the defect extend to the conduction band and valence band; however, the only relevant electronic states are states closest to the Fermi level of the semiconductor, so we focus on two states within the bandgap. The possible optoelectronic interaction of the defect can be categorized into two broad categories: first, inter-defect interactions. For instance, an electron residing in the ground state of the defect can be excited via a resonant laser or a phonon-assisted non-resonant excitation into the excited state of the defect. This electron can return to its lower energy via radiative or non-radiative recombination. In the case of defects with allowed radiative transitions and high quantum efficiencies, this results in a bright single photon emitter. Most known single photon emitters, such as nitrogen-vacancy centers in diamond or boron vacancies in hBN, belong to this class of emitters. The second set of possible interactions are the defect interactions with the band edges. The defect can act as an intermediary between valence

and conduction bands. For instance, an electron in the conduction band can relax into the excited state of the defect, and then the defect returns to its groundstate by receiving a hole from valence band and emitting a photon in the process (Fig. 2.7b). Similarly, the defect can trap a hole or an electron, and an electron/hole from the conduction/valence band can directly relax into the defect by radiating a single photon (not shown in the figure). Such interactions can be even more complicated considering that 2D-TMDs with high excitonic binding energy, free electrons, and free holes interact with the defect as an excitonic complex. These complexes are known as a localized defect-bound exciton. The exciton pair can also be attracted to the point-defect through coulomb interaction, creating a three-body complex of an exciton and bounded electron/hole, further altering the electronic configuration of the defect.

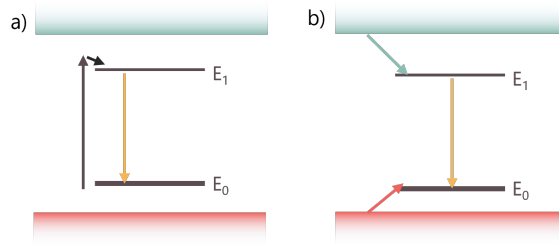


Figure 2.7: Modes of excitation of quantum defects. (a) In simplest case, an electron from ground state of the defect can be promoted to excited state through either resonant excitation or phonon-assisted non-resonant excitation. (b) Defect interactions with band-edges can provide further pathways for excitation of the defect. For example, the defect can go to excited state by trapping a hole and an electron from Valence and Conduction band respectively.

TMDs capable of hosting dark excitons are a unique platform for observing localized-bound excitons. At cryogenic temperatures, the photoluminescence intensity of the bright exciton in TMDs, such as WS_2 and WSe_2 decreases with temperature since the bose-einstein population of the dark exciton ground state increases with respect to the bright exciton. Ideally, the dark TMDs should not display any photoluminescence response as temperature reaches near absolute zero. This creates the perfect opportunity

to observe defect-bound dark excitons in TMDs, as seen in pioneering experiments of low-temperature photoluminescence spectroscopy of TMDs. Various sharp photoluminescence peaks can be seen from localized spots on the TMD crystals with energies much below the excitonic transition of TMDs, attributed to defect-bound dark excitons.

In the following chapters, we will discuss the microscopic process of defect-bound excitons TMDs and how they can be utilized for single-photon generation.

Bibliography

- [1] A. M. Fox, *Quantum optics: an introduction*, vol. 15. Oxford University Press, USA, 2006.
- [2] M. A. Nielsen and I. L. Chuang, *Quantum computation and quantum information*. Cambridge university press, 2010.
- [3] A. Politi, J. C. Matthews, M. G. Thompson, and J. L. O’Brien, *Integrated quantum photonics*, *IEEE Journal of Selected Topics in Quantum Electronics* **15** (2009), no. 6 1673–1684.
- [4] E. Knill, R. Laflamme, and G. J. Milburn, *A scheme for efficient quantum computation with linear optics*, *nature* **409** (2001), no. 6816 46–52.
- [5] P. Kok and B. W. Lovett, *Introduction to optical quantum information processing*. Cambridge university press, 2010.
- [6] S. Stanisic, *Universal quantum computation by linear optics*, 2015.
- [7] M. Reck, A. Zeilinger, H. J. Bernstein, and P. Bertani, *Experimental realization of any discrete unitary operator*, *Physical review letters* **73** (1994), no. 1 58.
- [8] J. L. O’Brien, G. J. Pryde, A. G. White, *et. al.*, *Demonstration of an all-optical quantum controlled-not gate*, *Nature* **426** (2003), no. 6964 264–267.
- [9] R. Raussendorf and H. J. Briegel, *A one-way quantum computer*, *Physical review letters* **86** (2001), no. 22 5188.
- [10] M. A. Nielsen, *Cluster-state quantum computation*, *Reports on Mathematical Physics* **57** (2006), no. 1 147–161.
- [11] S. Bartolucci, P. Birchall, H. Bombin, *et. al.*, *Fusion-based quantum computation*, *Nature Communications* **14** (2023), no. 1 912.
- [12] G. Grynberg, A. Aspect, and C. Fabre, *Introduction to quantum optics: from the semi-classical approach to quantized light*. Cambridge university press, 2010.

BIBLIOGRAPHY

- [13] R. W. Boyd, A. L. Gaeta, and E. Giese, *Nonlinear optics*, in *Springer Handbook of Atomic, Molecular, and Optical Physics*, pp. 1097–1110. Springer, 2008.
- [14] K. Alexander, A. Bahgat, A. Benyamini, *et. al.*, *A manufacturable platform for photonic quantum computing*, *arXiv preprint arXiv:2404.17570* (2024).
- [15] I. Aharonovich, D. Englund, and M. Toth, *Solid-state single-photon emitters*, *Nature photonics* **10** (2016), no. 10 631–641.
- [16] S. I. Azzam, K. Parto, and G. Moody, *Prospects and challenges of quantum emitters in 2d materials*, *Applied Physics Letters* **118** (2021), no. 24.
- [17] K. Y. K. Yamaguchi, K. Y. K. Yujobo, and T. K. T. Kaizu, *Stranski-krastanov growth of inas quantum dots with narrow size distribution*, *Japanese journal of applied physics* **39** (2000), no. 12A L1245.
- [18] I. N. Stransski and L. Krastanow, *On the theory of oriented precipitation of ionic crystals on each other*, *Monthly Journal of Chemistry and Related Sciences* **71** (1937) 351–364.
- [19] Y. Arakawa and M. J. Holmes, *Progress in quantum-dot single photon sources for quantum information technologies: A broad spectrum overview*, *Applied Physics Reviews* **7** (2020), no. 2.
- [20] P. Senellart, G. Solomon, and A. White, *High-performance semiconductor quantum-dot single-photon sources*, *Nature nanotechnology* **12** (2017), no. 11 1026–1039.
- [21] C. Santori, D. Fattal, J. Vučković, *et. al.*, *Indistinguishable photons from a single-photon device*, *nature* **419** (2002), no. 6907 594–597.
- [22] N. Somaschi, V. Giesz, L. De Santis, *et. al.*, *Near-optimal single-photon sources in the solid state*, *Nature Photonics* **10** (2016), no. 5 340–345.
- [23] S. Z. Butler, S. M. Hollen, L. Cao, *et. al.*, *Progress, challenges, and opportunities in two-dimensional materials beyond graphene*, *ACS nano* **7** (2013), no. 4 2898–2926.
- [24] K. S. Novoselov, A. Mishchenko, A. Carvalho, and A. Castro Neto, *2d materials and van der waals heterostructures*, *Science* **353** (2016), no. 6298 aac9439.
- [25] P. Ajayan, P. Kim, and K. Banerjee, *Two-dimensional van der waals materials*, *Physics Today* **69** (2016), no. 9 38–44.
- [26] K. F. Mak, C. Lee, J. Hone, *et. al.*, *Atomically thin mos 2: a new direct-gap semiconductor*, *Physical review letters* **105** (2010), no. 13 136805.

BIBLIOGRAPHY

- [27] G. Fiori, F. Bonaccorso, G. Iannaccone, *et. al.*, *Electronics based on two-dimensional materials*, *Nature nanotechnology* **9** (2014), no. 10 768–779.
- [28] T. Tan, X. Jiang, C. Wang, *et. al.*, *2d material optoelectronics for information functional device applications: status and challenges*, *Advanced Science* **7** (2020), no. 11 2000058.
- [29] E. C. Ahn, *2d materials for spintronic devices*, *npj 2D Materials and Applications* **4** (2020), no. 1 17.
- [30] J. R. Schaibley, H. Yu, G. Clark, *et. al.*, *Valleytronics in 2d materials*, *Nature Reviews Materials* **1** (2016), no. 11 1–15.
- [31] C. L. Degen, F. Reinhard, and P. Cappellaro, *Quantum sensing*, *Reviews of modern physics* **89** (2017), no. 3 035002.
- [32] A. Kumar and P. Ahluwalia, *Electronic structure of transition metal dichalcogenides monolayers $1h-mx_2$ ($m = mo, w; x = s, se, te$) from ab-initio theory: new direct band gap semiconductors*, *The European Physical Journal B* **85** (2012) 1–7.
- [33] W. Cao, H. Bu, M. Vinet, *et. al.*, *The future transistors*, *Nature* **620** (2023), no. 7974 501–515.
- [34] W. Cao, J. Kang, D. Sarkar, *et. al.*, *2d semiconductor fets projections and design for sub-10 nm vlsi*, *IEEE transactions on electron devices* **62** (2015), no. 11 3459–3469.
- [35] M. Fox, *Optical properties of solids*, vol. 3. Oxford university press, 2010.
- [36] M. Koperski, M. R. Molas, A. Arora, *et. al.*, *Optical properties of atomically thin transition metal dichalcogenides: observations and puzzles*, *Nanophotonics* **6** (2017), no. 6 1289–1308.
- [37] A. Chernikov, T. C. Berkelbach, H. M. Hill, *et. al.*, *Exciton binding energy and nonhydrogenic rydberg series in monolayer ws_2* , *Physical review letters* **113** (2014), no. 7 076802.
- [38] Y. Kubota, K. Watanabe, O. Tsuda, and T. Taniguchi, *Deep ultraviolet light-emitting hexagonal boron nitride synthesized at atmospheric pressure*, *Science* **317** (2007), no. 5840 932–934.
- [39] Y.-N. Xu and W. Ching, *Calculation of ground-state and optical properties of boron nitrides in the hexagonal, cubic, and wurtzite structures*, *Physical review B* **44** (1991), no. 15 7787.

BIBLIOGRAPHY

- [40] J. Furthmüller, J. Hafner, and G. Kresse, *Ab initio calculation of the structural and electronic properties of carbon and boron nitride using ultrasoft pseudopotentials*, *Physical review B* **50** (1994), no. 21 15606.
- [41] G. Cassabois, P. Valvin, and B. Gil, *Hexagonal boron nitride is an indirect bandgap semiconductor*, *Nature photonics* **10** (2016), no. 4 262–266.

Chapter 3

Experimental Methods

In this Chapter, we will discuss the experimental methods utilized throughout this thesis. This Chapter will describe our 2D material device preparation techniques, specifically our 2D exfoliation and transfer methods. Then, we will thoroughly discuss the main optical and quantum optics measurements that are used to characterize the optoelectronic properties of 2D materials.

3.1 2D Exfoliation Methods

One of the most intriguing properties of 2D materials is their ability to be thinned down using exfoliation methods. By definition, atoms in 2D materials are only bonded in in-plane direction with pristine surfaces devoid of dangling bonds. Therefore, in bulk 2D materials, the layers are held together with weak Van der Waals interactions, facilitating their exfoliation [1]. Through upward force, the "onion-like" structure of 2D bulk flakes can be peeled off each other to create thinner flakes down to monolayer thickness. As discussed in the previous chapter, the 2D materials' electronic and optoelectronic properties can be drastically changed by controlling the number of layers. The ability to do

so in a reliable and inexpensive manner is one of the significant factors in the explosive nature of 2D research in the past two decades.

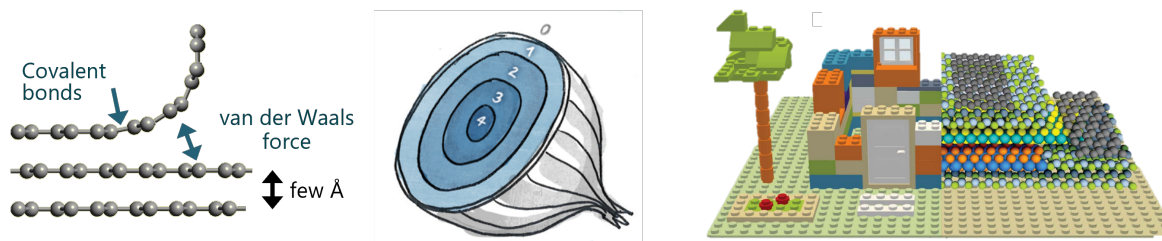


Figure 3.1: VdW 2D Materials are held together by weak VdW forces in the out-of-plane direction and strong covalent bonds in the in-plane direction. This anisotropy allows 2D materials to have an "onion-like" structure and allow different layers to be peeled off each other, giving them a unique modular engineering ability, much like Legos.

This section focuses on exfoliation techniques pertaining mostly to WSe_2 , which has been extensively used throughout this thesis. However, the methods described can also be applied to other 2D materials, albeit some adjustments and optimization is required when switching between materials with different properties.

Throughout the years, many exfoliation methods have been developed to prepare 2D materials [2], from simple methods such as scotch-tape exfoliation to liquid-based exfoliation [3] and more sophisticated and time-consuming methods such as gold-assisted exfoliation [4]. The most critical metrics and benchmarks for exfoliation techniques are the yield of the method, accessibility and time-cost, size of the flake, and quality and cleanliness of the final flakes. There are always trade-offs in choosing the proper exfoliation method for a specific project; for instance, if large area monolayer flakes ($>10000 \mu\text{m}^2$) are needed, one has to opt for an exfoliation method relying on gold-assisted or PVA-assisted exfoliation [5]. In our projects, given that there was no considerable constraint on the size of the flakes needed (up to $1000 \mu\text{m}^2$), we relied on the mechanical exfoliation method as described below. We suggest the following articles for a review of

other exfoliation methods [2, 6].

WSe₂ bulk flakes were obtained from either 2D semiconductors or HQ graphene vendors. In our experience, HQ graphene bulk flakes were considerably larger in size, with crystals up to 1×2 cm, which is a very important criterion for obtaining large-area monolayer flakes, as will be described shortly.

In the first exfoliation step, a low-residue blue Nitto tape (SPV224 procured from Amazon) is secured on a glass slide. The bulk WSe₂ flake is laid on top of the Nitto tape and is gently pushed to the tape with cotton swabs. Next, the WSe₂ bulk flake is peeled off the Nitto tape using a sharp metal tweezer. This is a critical step which depends on the operator's experience. Removing all of the bulk flake is essential while leaving a very thin but large layer on the Nitto tape. If this step is done successfully, a replica of the bulk flake, but considerably thinner, would remain on the Nitto tape; we will call this tape the "mother tape" from here onwards.

In the following steps, smaller nitto tape pieces are prepared to further thin down the flake on mother-tape via subsequent exfoliation steps. Each time, a tape is laid slowly on top of the mother tape so it would adhere to it without leaving any air bubbles. Next, the tape is peeled off very slowly to thin down the flake further. Each time an exfoliation step is repeated, it results in thinner flakes and breaking of the 2D flakes, hence smaller flakes. Peeling the Nitto tape as slowly as possible by securing one side of the tape on a micropositioner helps reduce the breaking and cracking. In our experience, repeating this step about five to seven times can guarantee achieving a monolayer with sizes up to $500 \mu m^2$ per stamp in later stages. Since each step reduces the size of the flakes, it is also essential to begin the process with a very large flake.

After 5-7 repeats of Nitto tape exfoliation, we will prepare the final stamp. Polydimethylsiloxane (PDMS) gels are used as an intermediate transfer medium. We used PDMS gels cut from GELPAK trays procured from Ted Pella (AD-11C-00-X0). In our

experience, X0 gelpaks with the highest thickness provide the best results for later transfer steps. The PDMS gel is cut with a surgical scalpel in a rectangular shape ($1 \times 2 \text{ cm}$) and is placed on a glass slide. Next, the exfoliated blue tape is pressed on the PDMS stamp. Gentle swabbing ensures no air bubbles between the PDMS and the Nitto tape.

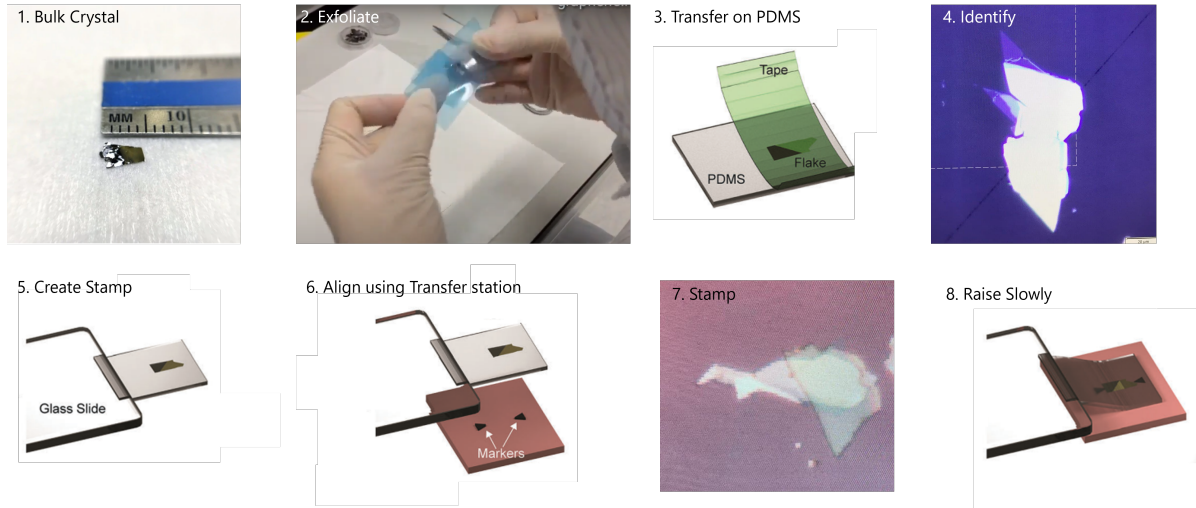


Figure 3.2: Exfoliation and transfer process of WSe_2 . Step-1 demonstrates the size of bulk crystal. In step-2, using nitto-tape, WSe_2 is thinned down via mechanical exfoliation. In step-3, WSe_2 is transferred from nitto tape to PDMS. In step-4, through optical imaging, a monolayer WSe_2 can be identified on the PDMS. In step-5, PDMS is loaded on a glass slide in cantilever-like configuration. In step-6, while monitoring the position of the flake using optical microscope and micropositioners, WSe_2 is stamped on a deterministic position on the substrate. In step-7 and 8, the PDMS stamp is slowly lifted off of the substrate, leaving the WSe_2 behind.

We typically place a weight (0.5 kg) on the PDMS and Nitto tape for 10 minutes to ensure more flakes are adhered to the PDMS. The next step is to remove the Nitto tape from the stamp. This is the most critical step in the exfoliation process. PDMS behaves as an elastic solid on fast time scales and a viscous fluid on slow time scales. This is the essential advantage of PDMS, allowing it to serve as the intermediary medium. If the Nitto tape is peeled off very fast, a lot of flakes would be adhering to the PDMS; however, removing the tape very fast also causes a lot of cracking of the flakes and results in tiny flakes.

Similarly, removing the tape too slowly does not allow the PDMS to maintain enough adhesion level to retain any nitto tape flakes. Therefore, the operator has to dial the optimal speed through trial and error. We suggest using slow speeds at first, and if the ideal results were not achieved in the first run, to increase the speed on the subsequent runs.

After exfoliation on the PDMS stamp, optical microscopy is used to identify possible monolayer flakes. Monolayer WSe₂ on PDMS under a brightfield microscope would have a very transparent look, as seen in Figure 3.2. Optical images were taken using a CMOS camera mounted on a MOTIC BA310MET microscope. To identify the number of layers, ideally Photoluminescence (PL) spectroscopy or reflection measurements are necessary to distinguish between monolayer, bilayer, and trilayer and accurately distinguish the layer number. However, contrast measurement can also provide a speedy and straightforward method to distinguish the layer numbers for most cases. An optical image was captured on the 50x objective on MOTIC BA310MET with standard halogen lamp epi-illumination to perform optical contrast measurements. The image is then processed in PowerPoint. First the image saturation is set to zero. Then using the eyedropper function, we extract the HSL (Hue, Saturation, Luminescence) color code of the PDMS background next to the flake. We note the value of Luminescence. Next, we extract the flake's HSL color code as well. Typically for monolayers the difference between Luminescence score of the background and flake is 10-20. For values between 20-30 the flake is bilayer and for above 30, the flake is multi-layer. Note that while this method is fast, it is heavily dependent on the microscope camera setting and intensity of the lamp, so it is advised that the optical values for Luminescence number for monolayers to be first calibrated first either via Atomic Force Microscopy or PL Spectroscopy.

3.2 2D Dry Viscoelastic Transfer

Next, the PDMS stamps with monolayer are prepared for transfer. Here, we utilize the cantilever transfer method introduced by Castellanos-Gomez [7, 8] *et al.* The PDMS stamp is moved to the edge of the glass very slowly, so the region containing the monolayer would hang from the side of the glass for about ~ 1 cm. It is ideal for the flake to be at the outer edge of the stamp, further away from the glass slide. Therefore, depending on the position of the flake, it might be necessary to cut an additional piece of the PDMS using scalpels. Once the PDMS is in position, it is secured to the glass slide using scotch tape.

In the meantime, the target chip is loaded on the XY positioner using double-sided scotch tape or a vacuum seal. The zoom camera is used to image the target location of the flake on the chip. Next, the transfer stamp is flipped, with the monolayer side facing the bottom of the stage, and mounted on the XYZ positioner so that the flake on the PDMS stamp is roughly over the target location on the chip. The zoom lens is then moved upward to image the surface of the PDMS. The PDMS stamp is scanned by moving the X and Y linear stages until the monolayer flake is found. Next, the PDMS stamp is lowered very slowly toward the sample stage.

By iteratively switching between the focus of the PDMS and the sample while slowly lowering the PDMS stage, alignment accuracy down to $5\mu m$ can be maintained in this approach. The main advantage of the cantilever approach is that the tilted side of the PDMS is the first place to make contact with the chip. Once this occurs, an air "seal line" is created between the PDMS and the chip, which then propagates from the left (the side that makes contact first) to the right of the chip very fast. In the cantilever approach, the seal line moves uniformly, and the tension in the cantilever, in addition to the adhesive force between the chip and the PDMS, allows the whole PDMS chip to make

contact with the chip without any trapped air bubbles between the chip and the PDMS. In the traditional method, where the PDMS film is entirely on the glass slides, the seal is created in part of the chip, and it is usually challenging to achieve a complete seal all over the chip, which reduces the overall yield of the transfer. Figure 3.2 demonstrates an example of a transfer process using this method.

Part Description	Purchase Link	Quantity	Total Price .
Zoom Camera with Epi-light	Amazon	1	\$248
CMOS C-mount Camera	Amazon	1	\$117
Metal Arm Holder	Amazon	1	\$127
Stainless Steel Optical Breadboard	Amazon	1	\$198
300mm Post Base	Thorlabs	1	\$69
Mounting Post Base	Thorlabs	1	\$28
XYZ Translation Stage	Amazon	1	\$125
XY Translation Stage	Amazon	1	\$75
N52 Magnets (10 piece)	Amazon	1	\$13
Total Price			\$1000

Table 3.1: Part-list used to build our customized transfer station.

3.3 Inexpensive 2D Transfer Station

In the previous section, we discussed preparing monolayer TMDs on PDMS stamps and the transfer process. In this section, we will introduce our inexpensive custom-built transfer station. This setup was built on a \$ 1000 budget to serve as a starting prototype station for our group and was inspired by a similar setup in reference [9]. However, its modularity and ease of use has made it our go-to setup for several years.

Our transfer station comprises two micropositioners and a zoom lens mounted on an optical breadboard. The artist and estimated budget per part is listed in the table. The micropositioners are secured to the breadboard with N52 magnets, which allows us to move the positioners to different positions without the need to use set screws. The micropositioner with rotational and linear X-Y stage is used as a sample mount. For

the PC-PPC transfer process, a PID-controlled ceramic heater with a thermocouple can be mounted on the sample stage. The micropositioner with X-Y-Z linear stages is used as the stamp holder. Double-sided M3 adhesive tapes can easily mount the glass slide at this stage. The zoom camera provides sufficient magnification to see flakes in $10\ \mu\text{m}$ sizes. Modular lenses can be installed on the camera to offer more magnification at the expense of working distance, depending on the application. The camera is installed on a mount with coarse and fine adjustment to its vertical distance. The camera holder arm is also mounted on a Thorlabs post-mount, as seen in Figure 3.3.

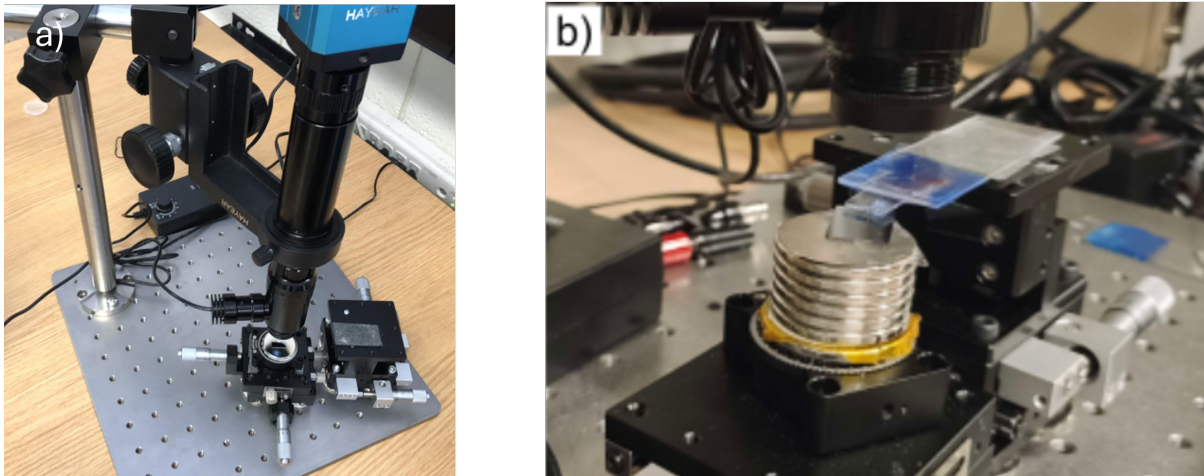


Figure 3.3: a) Completed transfer station. b) Transfer station during transfer process

3.4 Cryogenic Photoluminescence Microscopy

This section will discuss the confocal photoluminescence microscopy techniques widely used throughout this thesis. In a confocal microscopy setup, a collimated laser source is focused at the focal plane of an objective to excite fluorescence from a material. The excited light is then collimated via the same objective and can be sent to a spectrometer for further analysis. Using a pinhole or slit allows only the fluorescence light from the

excitation spot to be analyzed with each measurement, and by scanning the material in X or Y axis, a full fluorescence map of the material can be formed.

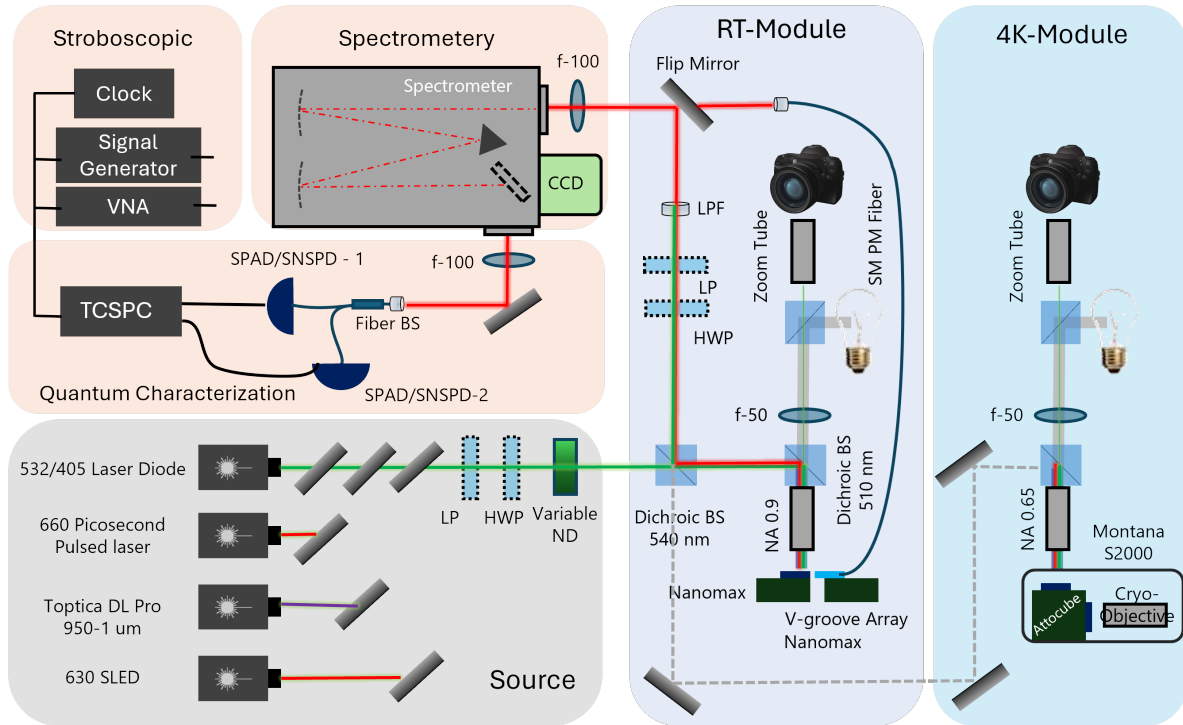


Figure 3.4: Photoluminescence (PL) spectroscopy setup. Four different laser lines can be selected via flip mirrors and be sent to the optical axis of the measurement apparatus. In the current drawing, only the green laser line is allowed to pass to the setup. Both room temperature and cryogenic module are illustrated in the setup. For spectroscopy, the spectrometer and a visible silicon CCD can be used to take spectral images of the collected light. For quantum optics experiments, the spectrometer can be used as a monochromatic and the filtered light exits through the side-slit for either second-order auto-correlation measurements, time-resolved PL spectroscopy, or stroboscopic measurement.

Figure 3.4 demonstrates the optical table configuration for our custom-built PL setup. This setup features both a cryogenic and a room-temperature setup. Here, we describe the main elements in the setup by taking the path of the green laser diode. Other lasers can be introduced to the same setup using a mirror mounted on flip mounts. However, they might require different optics and filters.

The green laser diode is a TO Can DPSS laser diode (DJ532-40 mW- Thorlabs),

which outputs a single-mode laser beam with a slight divergence angle ($\theta_{div} = 12\text{mrad}$) and is mounted into a laser diode mount controller (LDM56- Thorlabs). Next, the light from the laser is collimated based on the divergence angle of the diode. For instance, for DJ532 laser diode with 12 mrad divergence angle, an achromatic doublet with focal length (f_c) of 100 mm can achieve a collimated beam with a diameter of 1.2 mm (calculated using $2\sin(\theta_{div})f_c$). Note that for non-DPSS laser diodes, the divergence angle is usually relatively higher, and an aspheric lens with small focal lengths is favored. Next, the collimated beam is coupled to a single-mode fiber (PM 460-HP) using a fixed collimator package that is NA-matched to the fiber. This is done to ensure the laser diode's mode profile is a perfect fundamental Gaussian mode. While DPSS diode modes usually have a symmetric output profile, most TO can lasers have different divergent angles in directions parallel and perpendicular to the laser's polarization axis. This inevitably results in elliptical beam shapes, which can either be corrected through an anamorphic prism pair or by coupling to a single-mode fiber, albeit at the expense of some loss.

Next, the laser is reintroduced to the system's optical path using another collimation package; the focal length of this package and the Numerical Aperture (NA) of the fiber will determine the collimated beam diameter. We generally use a beam diameter that fits the back aperture of the imaging objective. A 532 nm band-pass filter is used to ensure the diode laser's spectral tail is sufficiently suppressed and does not leak into the setup. The collimated beam reaches a 50:50 beam splitter that sends half of the light through while reflecting the other half. This beam splitter effectively decouples the excitation and collection path. For non-resonant excitation, this beam-splitter can be replaced with a dichroic mirror that either reflects/transmits the 532 nm laser while transmitting/reflecting the longer wavelengths, depending on which setup (cryogenic or room temperature) is being used. However, for polarization-based measurements, the dichroic elements introduce birefringence, and using a beam splitter is preferred. Next,

the light goes through a 3-axis linear stage with a floating optical axis, as seen in Figure 3.5. The design of this linear stage allows the objective to be translated in all three directions while maintaining the optical alignment in the overall system. Finally, the light is introduced into an infinity-corrected imaging setup, which is then focused on the sample plane with an objective.

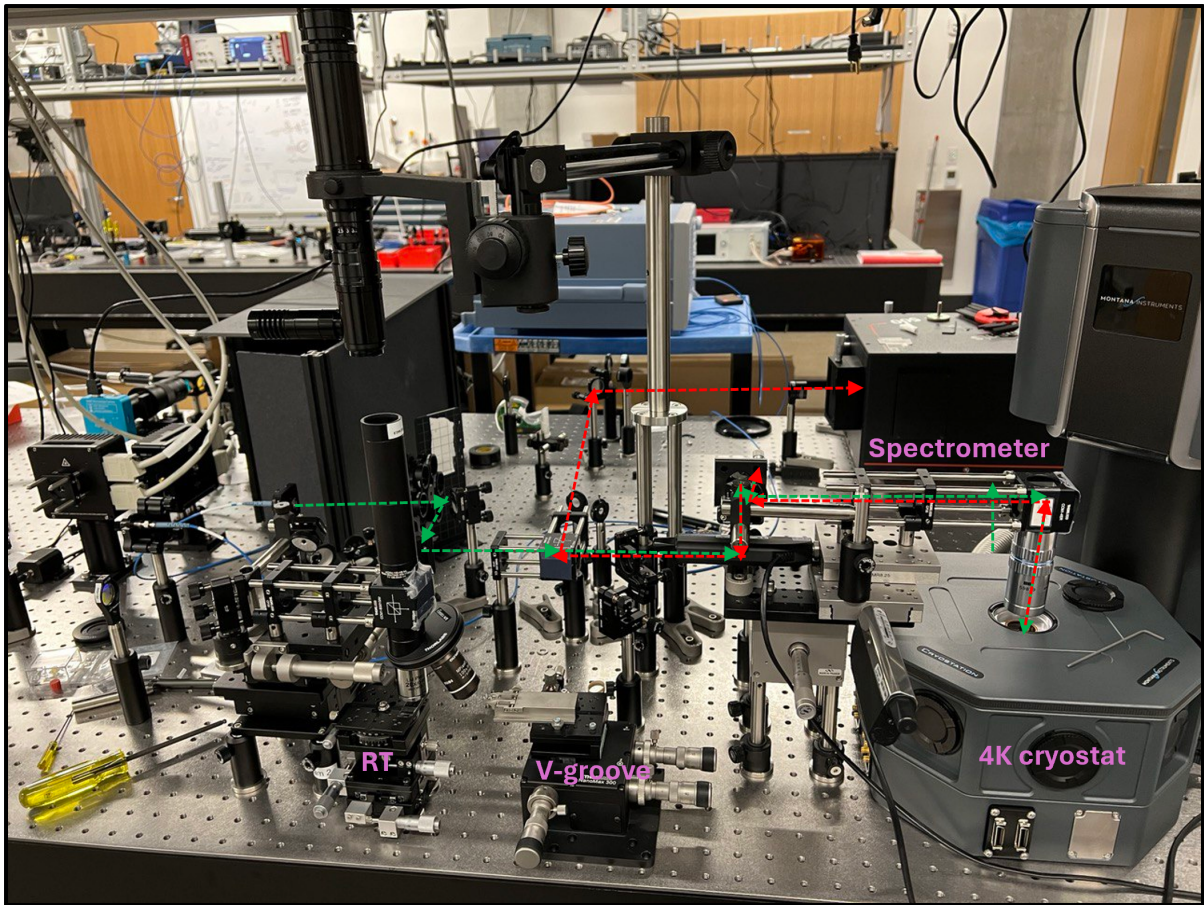


Figure 3.5: Image of the PL setup.

The infinity-corrected imaging setup consists of two back-to-back lenses. In traditional microscopes, the sample is at a point that is further away from the real focal plane of the objective. This design requires a fixed length between the objective and the eye-piece for nominal operation (conventionally 160 mm). This can cause potential problems when further optical elements like polarization filters, beam-splitters for epi-light,

etc, are introduced into the optical path. In the infinity corrected setup, the sample is placed at the focal plane of the objective, and the objective collimates the light from the sample plane and does not form an image plane on its own. A second objective is required to create the image plane. The ratio between the working distance of the image-forming objective and the sample objective determines the magnification of the setup. The advantage of the infinity-corrected system is that the distance between the two objectives can be arbitrary (hence the name infinity-corrected) and that any optical elements can be inserted in between the objectives. We place either a 50:50 beam-splitter or a dichroic here to send the laser beam into the sample. A zoom lens is also placed on top of the imaging objective used for white light imaging in situ with PL spectroscopy, which significantly enhances the system's ease of use and flexibility.

The green laser beam arrives at the back aperture of the objective lens and is focused on the Gaussian diffraction-limited spot size on the sample. The full-width half maxima of this spot will be given by the expression $(4M^2\lambda f/\pi D)$ where M is the beam ideality factor, which quantifies how Gaussian the input beam is, λ is the wavelength, f is the focal length, and D is the back aperture diameter. High NA lenses with minor focal points and large back aperture diameters can achieve a smaller spot size. For a well-collimated 532 nm laser with a 3 mm beam diameter using our objective (Olympus MPLAN FL 100x), this results in an FWHM of 226 nm, which serves as the spatial resolution of the overall system.

The material under the laser spot will absorb the excitation light through many possible light-matter interaction mechanisms (non-linear, Raman, photoluminescence) and scatter backlight either at the same frequency (typical reflection) or at an altered frequency. The scattered light that falls within the collection angle of the objective is collimated again and travels back on the same optical path as the incoming laser back to the initial 50:50 beam-splitter. However, here, the beam-splitter sends roughly half

the scattered light to a unique path, which we call the collection path. A long pass filter is used to reject the scattered light from the laser and allow the luminescent light with a longer wavelength to pass through. Note that this filter can be replaced with a notch filter for Raman spectroscopy to analyze scattered light very close to the laser frequency. The light is then focused on the entrance slit of the spectrometer (Princeton Instruments) and sent for analysis.

Inside the spectrometer, two convex mirrors reflect the light off of a diffraction grating. Diffraction grating will reflect the light at different angles depending on the wavelength of the incident light. The reflected light is then focused on a closed-loop thermo-electrically cooled Charge Coupled Device (CCD) Camera (PIXIS) at the image plane. In a well-calibrated spectrometer, using gas lamps, the grating angle for each specific frequency is calibrated to the position of that light on the CCD. Therefore, the spectrometer based on the illumination intensity at each pixel can create photoluminescence spectra of the input light. A second flip mirror is also placed in front of the CCD plane. For applications, when the spectrometer is required to be used as a tunable filter (monochromator), the flip mirror is activated, which sends the diffracted light into a second slit which is centered at the center frequency of the grating. The slit can then be opened and closed to select the bandwidth of the light that exits the spectrometer.

Two sets of linear polarizers and half-wave plates are typically used in excitation and collection paths for polarization measurements. In the excitation path, the first linear polarizer is placed with a polarization axis linear to the table, which is the same as the polarization of the laser. Next, the half-wave plate is placed in front of the linear polarizer. Rotation of the half-wave plate allows us to tune the polarization of the excitation field and perform emission dipole measurements. First, a half-wave plate is placed on the collection path, and then a linear polarizer with a polarization axis aligned parallel to the table. The linear polarizer alignment can be arbitrary. However, the

spectrometer reflects higher when input polarization is aligned parallel to the table. The half-wave plate rotation can map out the luminescent light's polarization and perform polarization-resolved PL measurements.

3.5 Life-time measurements

Upon excitation of a optoelectronic material with an ultrafast pulse, electrons are promoted to an excited state. As described in the previous chapter, many radiative or non-radiative recombination pathways are available for return of the electrons to the ground-state. Photoluminescence spectra gives us valuable information about the energy of these transitions, however, in order to quantify contributions of different processes involved, it is important to measure the average time the electrons spend in the excited state before returning to ground-state. This information can be obtained through time-resolved photoluminescence. Electrons return to the ground state following a characteristic decay profile, and extracting this characteristic provides further information about the strength of the optical transition and contribution from different decay mechanisms. In order to calculate the decay-time, a histogram of time-intervals between the start of the laser pulse and the first detector click from a photoluminescence photon of the material should be measured.

In order to perform time-resolved photoluminescence measurements, a 660 nm picosecond pulsed laser (Picoquant) is used to excite the sample. The output trigger sync of the laser is connected to a Swabian time-tagger. This trigger sends an electrical pulse to the time tagger at the start of each laser pulse. As discussed in the previous section, the spectrometer is utilized as a monochromator in this experiment. The PL spectra are obtained first, and the grating is centered on the emission line of interest. Then the flip mirror is flipped for light to exit the side slit of the spectrometer. An achromatic

doublet is placed one focal length away from the side slit to collimate the output light. The scattered light is then coupled to a multimode fiber and is sent to a single-photon avalanche detector (SCPM-AQRH-13-FC). The output of the avalanche diode is then connected to another channel of the time-tagger.

The time tagger is programmed to measure the time difference between the clicks from the start of the pulse (laser output trigger sync) and the clicks of the photon's arrival on the single-photon detector. A histogram of the counts is then built. After acquiring enough counts that would yield a fit with a low error bar, the measurement is stopped. The data are fit to an exponential decay model depending on the properties of the emission line, and appropriate lifetimes are extracted as shown in Fig. 3.6. Furthermore, we note that the finite instrument response time due to the finite width of the pulse, the jitter of the detector, and the error of the time tagger can make it challenging to estimate short lifetimes and impossible to estimate lifetimes shorter than the instrument response time. A faint pulsed laser is reflected from a reflective sample to measure the instrument response time. Given that the laser has a very short pulse duration with respect to the detector jitter, the lifetime measured by the system can be approximated as the instrument's lifetime. This value can then be used to estimate the instrument's corrected lifetime by deconvolving the measured lifetimes from the instrument response time.

3.6 Second-order Auto-correlation Measurements

Majority of the light sources in our environment are of classical nature, i.e the light behaves mostly as a classical electromagnetic wave. Within the description of quantum electromagnetic field, classical light can be defined as a superposition of Fock states. However, experimentally distinguishing between classical, coherent, or a single-photon

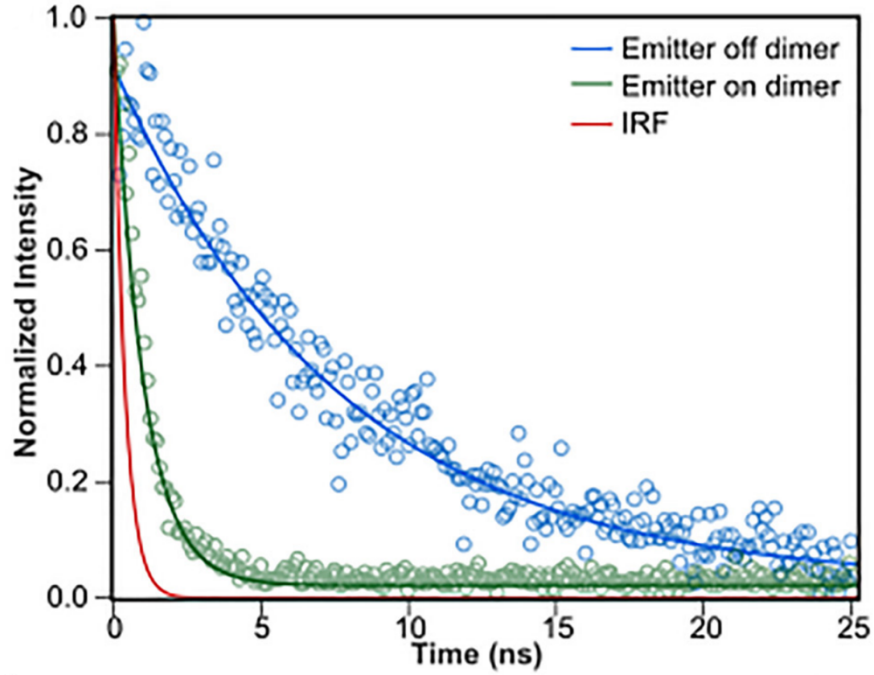


Figure 3.6: Example of Time-resolved Photoluminescence Measurement. Blue dots demonstrate life-time of a WSe₂ single-photon emitter. Green dots demonstrate life-time of Purcell-enhanced WSe₂ single-photon emitters [10] with much smaller life-time. Red line demonstrates the instrument response time.

light can be difficult. Fortunately, second-order auto-correlation function can provide a quantifiable metric to distinguish the nature of the emitted light and provides information about the specific superposition of Fock states that are in a stream of light, determining to what degree the light is classical, coherent, or quantum. Second-order auto-correlation function or $g^2(\tau)$, measures the correlation between intensities of a stream of light at two different times separated by time delay τ . Mathematically we $g^2(\tau)$ is defined as:

$$g^2(\tau) = \frac{\langle n_1(t)n_2(t+\tau) \rangle}{\langle n_1(t) \rangle \langle n_2(t+\tau) \rangle} \quad (3.1)$$

where $n_1(t)$ and $n_2(t)$ are the average photon counts the detector measures at time t . $g^2(\tau)$ can be described as the conditional probability of measuring a photon at time t on one detector and measuring another photon at time $t = \tau$ on the other detector. In

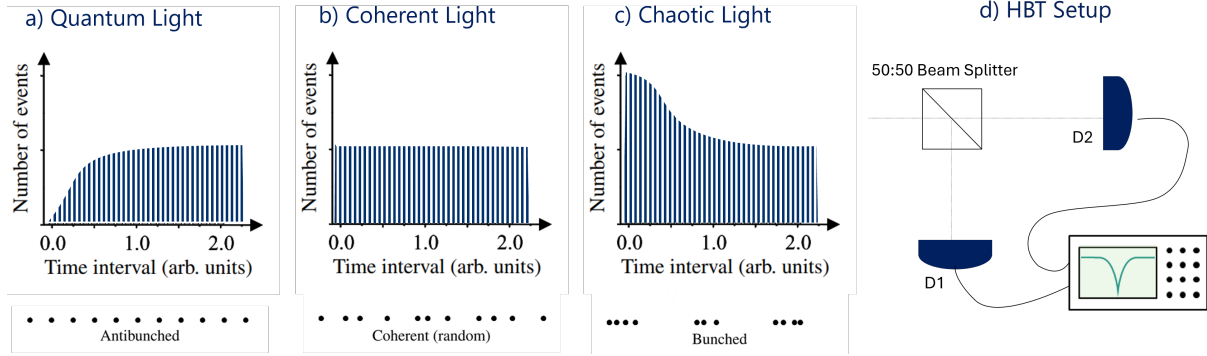


Figure 3.7: Statistical classification of light.

other words, $g^2(\tau)$ tells us how the photons in the light stream are spaced-apart from each-other. To setup a $g^2(\tau)$ experiment, the collimated stream of light is passed through a perfect 50:50 beam-splitter where two single-photon detectors are placed at the end of each arm as seen in Figure 3.7. Detection of a single-photon on one arm starts a timer which only stops when the other arm detects another photon. The measurement is then repeated until a histogram of number of detections versus time-delay τ is built. Based on these histogram, light sources can be classified into three broad category: (1) quantum light or anti-bunched source displaying sub-Poissonian photon statistics; (2) coherent light sources exhibit perfect Poissonian statistics; and (3) bunched or chaotic sources display super-Poissonian statistics. Figure 3.7 demonstrates these three distinct cases.

Single-Photon Sources: For a single-photon source, such as a quantum dot or a single atom, photons are anti-bunched, separated well-spaced in time. In such a scenario, detecting one photon at one arm reduces the probability of detecting a consequent photon immediately at the other arm. In other words, $g^2(0)$ should be zero for an ideal single-photon source, a hallmark of quantum light.

Coherent Light: For a coherent light source, such as a laser operating far above threshold, photons are completely uncorrelated in their timing separation which means that detecting one photon at one arm does not have any effect on probability of detection

of the other arm, indicating perfect Poissonian photon distribution and a normalized $g^2(\tau) = 1$ for all delays τ .

Classical Light Sources: For a classical light source like a thermal source (e.g., a lamp or blackbody radiation), photons are bunched in time, resulting in an increased probability of detection if one of the arms of the beam-splitter measures a detection event. For a perfect chaotic source, $g^2(0) = 2$, indicating bunching behavior.

In our experimental setup, the emission light from the single-photon emitter is redirected to the output slit of the spectrometer for performing the second-order auto-correlation measurements. Here, depending on the wavelength, we can use single-photon avalanche diodes (SCPM-AQRH-13-FC) or superconducting nanowire single-photon detectors (SNSPDs). For SPADs, the light is coupled into a 50:50 multimode beam splitter, and then each arm is connected to an optical circulator, which is then fed into the SPAD. A circulator with silicon-based SPADs is essential given that SPADs themselves, upon detection, can photoluminesce, which can couple back into the fiber and create a strong correlation between the two detectors. To use the SNSPDs, the signal is connected to single-mode fiber (Thorlabs PM-780) and then fed into a 50:50 beam splitter, which is then connected to the input fiber port of the cryostat.

Generally, the output of the detector is an electrical pulse whose width correlates with the detector's timing jitter. Based on the detector used, the output signal of the detector can either be amplified or attenuated using a high-speed amplifier or attenuator to be compatible with the acceptable voltage input range of the time tagger. Next, by setting a voltage threshold on the time-tagger, typically about 70% of the electrical pulse height of the detector, the time-tagger is configured to measure the detection events of the single photons. In our case, we utilize a Swabian time tagger.

Next, the time tagger is configured to measure the time-delay between detection events on each detector. A detection event on either detector would start an internal

timer, which only stops when another detection event on the other detector is recorded. The time difference is then stored, and the measurement is repeated again until a statistically significant histogram is obtained. Next, the histogram is binned into larger time intervals. For example, five recorded time delays corresponding to 10 ps, 120 ps, 150, 210 ps, and 250 ps when mapped with 100 ps bins, translate to one count in the 0-100ps bin, two counts in the 100-200 ps bin, and two counts in the 200-300 ps bin. Since the timing resolution of the time-taggers is extremely fine (in picoseconds) and the rate of coincident counts is much smaller than this range, the time-binning process is necessary to achieve a statistically significant histogram. Note that over-binning the data can lead to substantial convolution errors in $g_2(t)$ measurements, and one should carefully choose the time-bin size so that it is much smaller than the time constants of any temporal feature in the $g_2(t)$. Finally, the histogram can be normalized to the average value of the total counts on long-time delays.

Depending on the type of excitation used, two types of second-order correlation measurements typically exist, either continuous-wave (CW) excitation $g_2(t)$ measurements or pulsed $g_2(t)$. In the CW $g_2(t)$, for a case of an isolated single-photon emitter, a dip in the $g_2(t)$ can be found at a time-delay close to zero. Note that, in the experimental setting, the dip in $g_2(t)$ does not necessarily happen at time zero but at a time delay corresponding to the sum of the optical and electronic delay of the two arms of the detection apparatus.

The normalized data can be fit to the following expression;

$$g^2(t) = 1 - Ae^{-\left|\frac{t-t_{off}}{\gamma}\right|} \quad (3.2)$$

Here, A correlates with the purity of the emitter. t_{off} is the offset from time-delay zero due to unbalanced electronic and optical delay of the arms, and $1/\gamma$ correlates with

the lifetime of the emitter. For a perfectly pure isolated emitter, A is one. However, in presence of uncorrelated background emission, A can take on values less than one. Note that, in some measurements, one may be measuring not a single emitter but an ensemble of emitters that spectrally overlap. In such cases, A takes on the form of $\frac{1}{N}$ where N is the number of emitters in the ensemble. For example, for a two emitter ensemble the minimum observable dip in $g_2(0)$ would be 0.5. It can be difficult to distinguish uncorrelated background emission from possible ensemble-like emission, in such cases, an experimental background emission subtraction can be useful. For experimental background emission, the laser can be spatially off-set from the emitter location and the second-order correlation measurement should be conducted, with the same laser intensity, polarization, monochromator settings for the same duration as the initial $g_2(t)$ measurement. Then the new obtained histogram can be subtracted from previous measurement. In case of uncorrelated background emission, the new $g_2(0)$ should go close to zero. However, for ensemble measurement, the $g_2(0)$ would remain almost the same.

Pulsed $g_2(t)$ measurement is generally easier to interpret in comparison with CW measurement. Experiment setting is identical to CW measurement. However, the final built histogram for pulsed $g_2(t)$ consists of series of peaks spaced apart from each other in time with a delay set by the repetition rate of the laser. For a perfect single-photon emitter, the peak corresponding to the sum of the electronic and optical delay of the arms should be missing from the histogram. The height of this peak, compared to normalized height of the peaks in the histogram would be inversely proportional to the purity of the emitter. Similar to CW $g_2(t)$, for an ensemble of emitters, the minimum dip in the peak takes on the form of $1 - \frac{1}{N}$ and the same background subtraction procedure can be used to distinguish correlated ensemble emission from uncorrelated background emission.

Bibliography

- [1] K. S. Novoselov, A. K. Geim, S. V. Morozov, *et. al.*, *Electric field effect in atomically thin carbon films*, *science* **306** (2004), no. 5696 666–669.
- [2] M. A. Islam, P. Serles, B. Kumral, *et. al.*, *Exfoliation mechanisms of 2d materials and their applications*, *Applied Physics Reviews* **9** (2022), no. 4.
- [3] C. Huo, Z. Yan, X. Song, and H. Zeng, *2d materials via liquid exfoliation: a review on fabrication and applications*, *Science bulletin* **60** (2015), no. 23 1994–2008.
- [4] Y. Huang, Y.-H. Pan, R. Yang, *et. al.*, *Universal mechanical exfoliation of large-area 2d crystals*, *Nature communications* **11** (2020), no. 1 2453.
- [5] Y. Li, S. Weng, R. Niu, *et. al.*, *Poly (vinyl alcohol)-assisted exfoliation of van der waals materials*, *ACS omega* **7** (2022), no. 43 38774–38781.
- [6] Y. Li, G. Kuang, Z. Jiao, *et. al.*, *Recent progress on the mechanical exfoliation of 2d transition metal dichalcogenides*, *Materials Research Express* **9** (2022), no. 12 122001.
- [7] A. Castellanos-Gomez, M. Buscema, R. Molenaar, *et. al.*, *Deterministic transfer of two-dimensional materials by all-dry viscoelastic stamping*, *2D Materials* **1** (2014), no. 1 011002.
- [8] R. Frisenda, E. Navarro-Moratalla, P. Gant, *et. al.*, *Recent progress in the assembly of nanodevices and van der waals heterostructures by deterministic placement of 2d materials*, *Chemical Society Reviews* **47** (2018), no. 1 53–68.
- [9] Q. Zhao, T. Wang, Y. K. Ryu, *et. al.*, *An inexpensive system for the deterministic transfer of 2d materials*, *Journal of Physics: Materials* **3** (2020), no. 1 016001.
- [10] S. I. Azzam, K. Parto, and G. Moody, *Purcell enhancement and polarization control of single-photon emitters in monolayer wse_2 using dielectric nanoantennas*, *Nanophotonics* **12** (2023), no. 3 477–484.

Chapter 4

Physics, Characterization, and Engineering of Quantum Emitters in 1L-WSe₂

The first single-photon emitters (SPEs) in WSe₂ were reported in 2015 simultaneously by five different groups [1–5]. In these experiments, monolayer WSe₂ was exfoliated on SiO₂ substrates, and cryogenic photoluminescence maps (Figure 4.1a) uncovered localized and sharp (< 200 *meV*) spectral features seemingly appearing randomly at a spectral range of 1.5-1.7 eV below the free exciton emission at a certain spot in the sample. A typical spectrum of these features is portrayed in Figure 4.1b. These sharp spectral features displayed lifetimes on the order of 2 ns in time-resolved photoluminescence, they typically appeared in doublets resembling fine-structure emission from semiconductor quantum dots, and they appeared to be linearly polarized. Second-order auto-correlation measurements were used to verify the quantum nature of the single photon emission (Figure 4.1c with $g^2(0)$ below 0.5).

Two main hypotheses were put forward as the likely microscopic nature of these

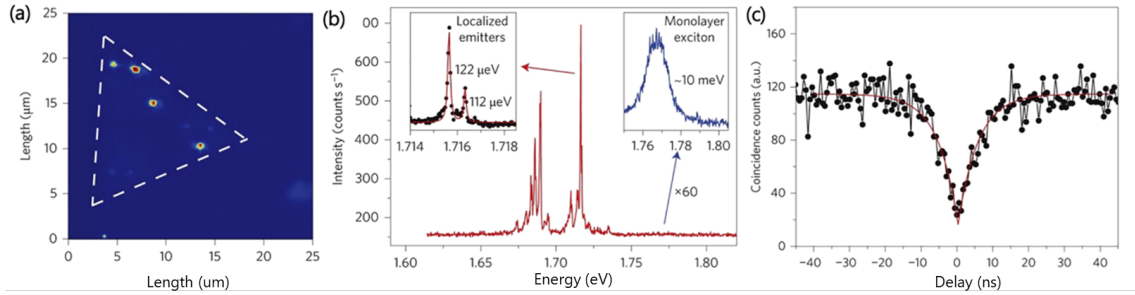


Figure 4.1: a) Cryogenic PL map of WSe₂. Localized spots show emission below the free exciton of WSe₂. b) Representative spectrum of a localized emission spot. Sharp emission lines below free-exciton resemble quantum-dot like features. The left inset shows that the sharp emission line consists of a doublet structure indicative of fine-structure splitting. The right inset demonstrates the delocalized exciton emission c) Representative second-order auto-correlation function of a localized sharp emission line in WSe₂. The dip below 0.5 at time zero evidences the single-photon emission nature of the light. Panels (a)(c): Reproduced with permission from He *et al.*, Nat. Nanotechnol. 10, 497502 (2015). Copyright 2015 Springer Nature

emitters. In the first hypothesis, the emission was attributed to defects in the WSe₂, operating similarly to other quantum defects in wide-bandgap materials. In the second theory, given that these emitters were more likely to be found close to the edges or wrinkles in the TMDs, it was hypothesized that this emission is due to quantized levels arising from the confinement in strain pockets in the material. In the coming years, studies provide evidence supporting each theory. For instance, Kumar *et al.* [6], and Branny *et al.* [7] showed a statistical correlation between regions of high strain and the probability of having an SPE in WSe₂. They also showed that spectral features of WSe₂ emitters are sensitive to the magnitude of the local strain. Kern *et al.* [8] demonstrated the semi-deterministic creation of WSe₂ emitters by draping the WSe₂ over gold nano-rods and creating high-strain regions. This demonstration reached significant milestones when in 2016, Palacios *et al.* [9] and Branny *et al.* [10] demonstrated high-yield site-specific engineering of WSe₂ emitters by deterministic creation of strain in WSe₂ through transferring monolayer TMDs over nanometer scale SiO₂ nanopillar stressors.

Through nanopillar engineering, they achieved yields close to unity in creating an emitter per strain site, displaying purities as high as 95% and high brightness. Following this demonstration, other strain-engineering methods such as metallic nano-cubes [11], AFM nano-indentation [12], and microcantilevers [13] were also used to create single photon emitters in WSe₂.

The success of strain engineering methods unequivocally proved that strain plays a role in the microscopic nature of these emitters. However, other experimental studies also provided evidence that defects in WSe₂ might also play a significant role in the microscopic process of these emitters. At cryogenic temperatures, WSe₂ displays a broadband emission at energies lower than free excitons commonly attributed to defect states [14]. Further experimental studies correlated electron-beam density with the number of induced atomic defects such as single and double selenium vacancies [15, 16]. Interestingly, Rosenberg *et al.* [12], by statistically studying the center spectral frequencies of engineered single-photon emitters, revealed that the spectral histogram of WSe₂ emitters resemble the lineshape of the WSe₂ cryogenic defect band, indicating the possibility that the observed single-photon emitters are isolated atomic-defects in WSe₂. However, the observed SPEs display a surprisingly higher brightness level than the broad defect band, which raises the possibility that if the single-photon emission is indeed from isolated atomic defects, another microscopic process should be present through which the quantum efficiency of the isolated defect is increased significantly. In 2019, a theoretical study by Linhart *et al.* [17] proposed a mechanism for such a possibility in WSe₂ single-photon emission. In regions of high strain, as the bandgap of WSe₂ decreases, the exciton energy levels also decrease (Figure 4.2 a). This could allow for spin-forbidden dark excitons in WSe₂ to lower their energies and come into resonance with localized defects in WSe₂ bandgap to form hybridized defect-bound excitons. The spin-forbidden dark exciton, in the new defect-bound configuration, due to the broken valley symmetry of the defect, can

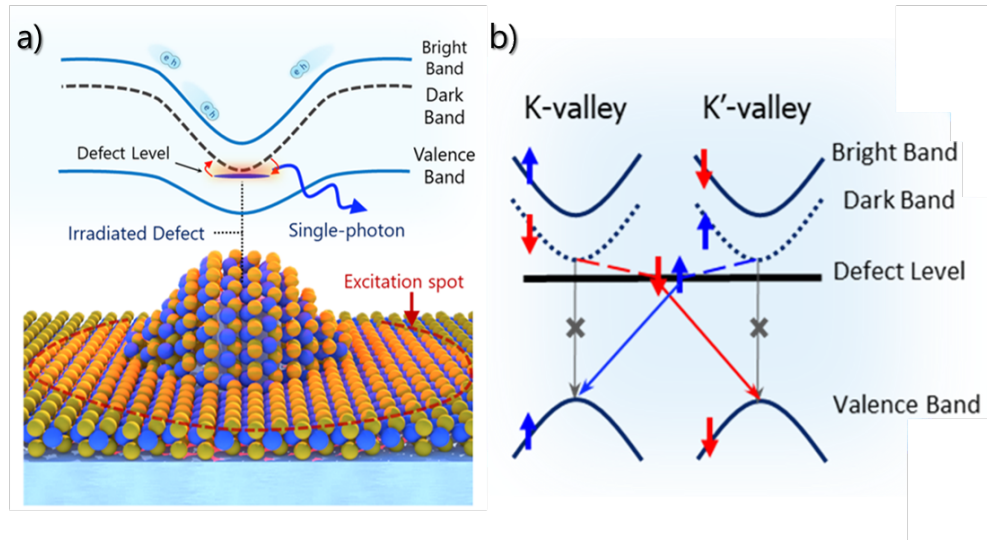


Figure 4.2: Suspected mechanism of single-photon emitters in WSe₂ a) top band-diagram illustrates the spatial variation of the bandgap (valence band), and subsequently the excitonic levels (bright exciton as blue line and dark-exciton as black dashed line) due to strain profile of the pillar. Bottom inset represents an illustration of WSe₂ on nanopillar. b) band-structure representation of the WSe₂. Here, we have denoted the spin-orbit splitted conduction band as Dark (spin-forbidden radiative transition) and Bright (spin-allowed radiative transition) band to represent the excitonic picture in the same momentum-space representation of band-diagram. The localized defect is represented as a straight line in the momentum space. If exciton in the Dark band can efficiently hybridize with the localized defect, the valley symmetry is broken and electrons in the bound-exciton can efficiently recombine through the defect, leading to bright single-photon emission

efficiently radiatively recombine through the defect and give rise to bright single-photon emission (Figure 4.2b).

This hypothesis described the puzzling brightness of the WSe₂ emitter and explained the correlation of the single-photon center wavelength emission with applied electric and magnetic fields. Furthermore, the requirement for both strain and defects corroborated the experimental studies that demonstrated links to single photon emission for both defects and strain. While Moon *et al.* [18] had previously shown that single-photon emitters in WSe₂ correlate with strain and do not appear below the dark-exciton energy of WSe₂, providing evidence for Linhart *et al.* proposal, no studies at the time had

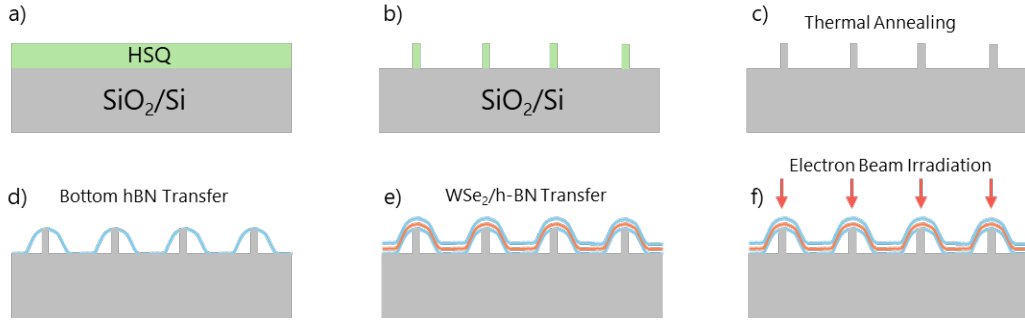


Figure 4.3: Overview of the fabrication process a) HSQ resist is spun on SiO₂/Si chips to yield resist with thickness of 200 nm. b) Electron beam lithography is used to define nanopillars with diameter of 150 nm and height of 200 nm. c) Rapid thermal annealing at 1000 °C turns HSQ into SiO₂. d) Bottom h-BN with roughly 5 nm thickness is transferred on the nanopillars. e) Top WSe₂/h-BN stack is then transferred on top of the previous h-BN layer. f) Electron beam lithography is used to create defects in the 2D monolayer

independently confirmed the need for both defects and strain to create single-photon emission emitters. In this chapter, we shed light on the microscopic nature of these single-photon emitters through independent electron beam-induced defect creation and utilizing SiO₂ nanopillars for inducing strain.

4.1 Strain Engineering of WSe₂ Emitters

In order to create strain in WSe₂, a similar method to Palacios *et al.* [9] and Branny *et al.* [10] was employed. A SiO₂/Si wafer was cleaved into 1 cm² square chips, followed by a conventional solvent clean. Hydrogen Silsesquioxane (HSQ) diluted in Methyl Isobutyl Ketone (MIBK) was spun on the substrates to yield an electron beam resist thickness of 200 nm. A 5-min 90 °C pre-exposure bake followed by electron beam lithography was used to expose nanopillars with a diameter of 150 nm. The sample was developed in 25% Tetramethylammonium Hydroxide (TMAH) for 30s. Rapid thermal annealing at 1000 C was utilized to crystalline the HSQ pillars into SiO₂.

As outlined in Chapter 3, dry viscoelastic transfer was used to create h-BN/WSe₂

heterostructures. First, WSe₂ crystals purchased from 2D semiconductors were exfoliated on SiO₂/Si substrate, and an optical microscope was used to identify monolayers using optical contrast. Next, h-BN flakes are exfoliated on the same stamp, which is then used to pick up the identified monolayer WSe₂ flakes, creating an h-BN/WSe₂ heterostructure. Next, 5 nm h-BN flakes were transferred on nanopillar arrays to protect the WSe₂ from surface adsorbates and also act as a shielding layer which protects the WSe₂ from being punctured or damaged by the nanopillar during the final stamping step. In the final step, the h-BN/WSe₂ heterostructure is transferred on the h-BN/nanopillar arrays to create the encapsulated h-BN/WSe₂/h-BN/pillar heterostructures. Figure 4.3 demonstrates the device fabrication steps.

4.2 Photoluminescence Spectroscopy of Strained WSe₂ on Nanopillars

Figure 4.4a illustrates the darkfield optical image of a representative h-BN/WSe₂/h-BN sample. Chips are then cooled down in a closed-loop cryostat down to 4.2 K temperatures in preparation for cryogenic photoluminescence spectroscopy as outlined in Chapter 3. A non-resonant continuous-wave 633 nm laser with a spot size of 1 μm (0.7 Numerical Aperture) is used to excite the sample for photoluminescence spectroscopy. The collected light is routed to a TE-cooled charge-coupled detector (CCD) with spectral resolution down to 30 μeV . Figure 4.4b shows the PL spectra of the h-bN/WSe₂/h-BN heterostructure in the nanopillar location (strained) and a location away from the nanopillar (unstrained). In our samples, no localized sharp peaks could be detected in the strained or non-strained regions. Only about 1.8 meV and 3.1 meV redshifts for exciton and charged exciton peaks are observed in the strained versus unstrained regions. This redshift was

also within sample-to-sample uncertainty. The linewidth of the neutral exciton also did not show any appreciable broadening. At first glance, our result may seem to conflict with the observations from Branny *et al.* [10] and Palacios *et al.* [9], where they were able to engineer emitters with only the nanopillar strain engineering method. However, our approach is different in two key aspects. First, we utilized a h-BN/WSe₂/h-BN stack compared to transferring monolayers directly on the pillar. In our experience, the bottom h-BN layer was necessary to protect the WSe₂ from trapped surface adsorbates between the pillar and the 2D material and also served as a protective shield that prevented the WSe₂ from being punctured by the pillars. This ensures the transfer process does not create any additional defects within the sample and allows us to decouple the strain engineering aspect from possible defect creation and contaminants. Second, as we will discuss later, our exfoliated 2D sample demonstrated almost no signatures of the WSe₂ cryogenic broad defect band in their photoluminescence spectra, which evidences the high quality of the monolayers. As seen later, the intensity of the defect band directly correlates with the yield and possibility of creating emitters within the strained regions. We should also note that if the bottom layer protective h-BN shield is not used in the process, we can observe single photon emitters within the pillar locations, similar to that of Branny *et al.* [10] and Palacios *et al.* [9].

In order to understand the photoluminescence spectra of the strained only WSe₂ regions, we utilized numerical simulations to predict the expected spectra. Initially, we expected to observe a more pronounced redshift in the strained region; however, as mentioned, only a slight redshift is observed. In Figure 4.6, we performed numerical simulations to predict the strain profile of the WSe₂ on top of the nanopillar. Previously, classical continuum models have been used to predict strain levels of 2D-films draped over nano-stressors [8, 11]. Assuming that the flake rests on top of the nanopillar and starts to bend over only at the edge of the pillar, the height of the flake as a function of

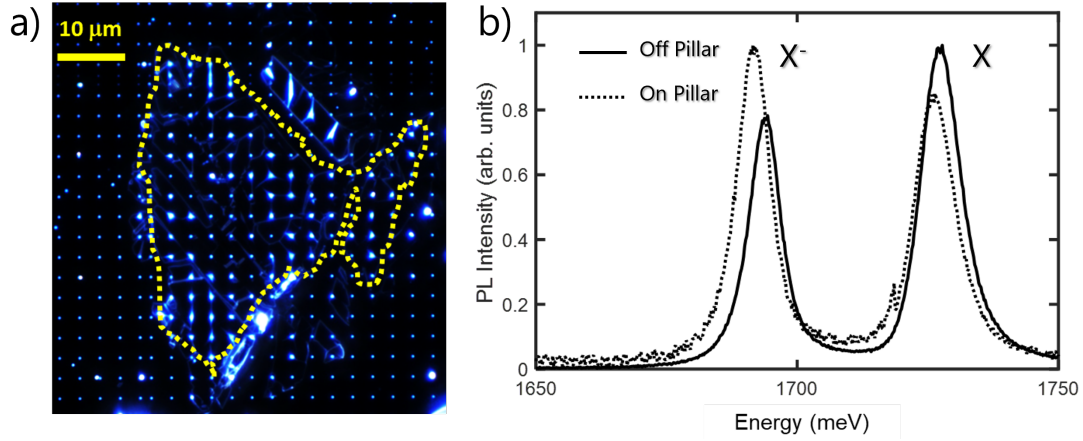


Figure 4.4: PL Spectra of WSe₂ On and Off Nanopillars. a) Darkfield image of a representative stack on top of the nanopillars b) PL Spectra of WSe₂ off pillar (solid line) in a pristine unstrained region and WSe₂ on the pillar (dashed line) is presented. Only slight shift in free exciton (X) and trion (X⁻) is observed which is within the sample to sample uncertainty. No sharp peaks that can be associated with single-photon emitters are observed.

a line-cut through the pillar can be represented as:

$$H(x, y) = \frac{1}{16} H_0 \left[\operatorname{erf} \left(\frac{x+d}{s_x} \right) + 1 \right] \left[\operatorname{erf} \left(\frac{y+d}{s_y} \right) + 1 \right] \quad (4.1)$$

where H_0 is the height of the pillar, d is the diameter of the pillar, s_x and s_y are the depression parameters. Finally, using the height function, assuming the 2D materials as an elastic sheet, the strain map can be calculated using the function:

$$|\epsilon| = \left| \frac{vd}{1-v} \left(\frac{\partial^2 H(x, y)}{\partial x^2} + \frac{\partial^2 H(x, y)}{\partial y^2} \right) \right| \quad (4.2)$$

where v is the Poisson ratio (0.2) and d is the monolayer thickness (0.7 nm).

It can be seen that the strain is maximum in a region of about 20 nm around the perimeter of the pillar where the monolayer drapes over the structure. The maximum strain region is about two orders of magnitude smaller than the full-width half-maxima of the diffraction-limited spot size of the excitation laser beam on the sample. Therefore,

most of the photoluminescence signal, even when the objective is centered on the pillar, originates from the unstrained regions, and the signal from the strained region would be considerably lower in brightness. Tyurnina *et al.* [19] has also reported similar results. Hence, spectroscopic analysis of the strained region would require a near-field method rather than far-field photoluminescence imaging.

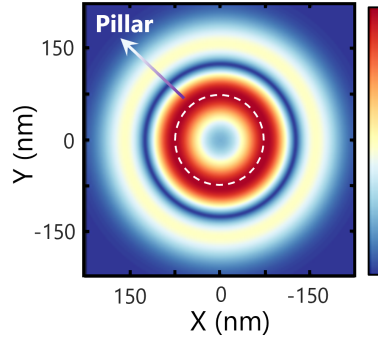


Figure 4.5: Calculated strain profile at the nanopillar from classical continuum model.

In order to quantify the contributions from the unstrained regions, we perform numerical simulations to derive the expected photoluminescence response. We assume that if, at any point in space, the WSe₂ is excited, it would create a Gaussian spectral response with a linewidth of 10 meV following:

$$I_{int}(\lambda) = \exp\left(-\frac{\left(\frac{hc}{\lambda} - \lambda_{zpl}\right)^2}{2(\sigma/2.355)^2}\right) \quad (4.3)$$

where h , c , λ , λ_{zpl} , and σ are Plank's constant, Speed of light, wavelength, the wavelength of the zero-phonon line, and linewidth of the photoluminescence signal.

However, in the strained region, the center frequency of the Gaussian response is redshifted. Given that the maximum strain is localized in the circumference of the pillar, a line cut of the strain map would resemble two peaks separated by the pillar's diameter. We also approximate these two strain peaks as Gaussian functions, and we assume that the maximum spectral redshift of 200 meV would occur due to strain. Hence, the redshift

of the center wavelength as a function of location over the pillar would take the form of:

$$\lambda_{zpl}(x) = -200_{meV} \left[\exp\left(\frac{(-x-d)^2}{2(\sigma_s/2.355)^2}\right) + \exp\left(\frac{(-x+d)^2}{2(\sigma_s/2.355)^2}\right) \right] \quad (4.4)$$

where d is diameter of the pillar and σ_s is the full-width-half-maxima of the strain pocket.

The Gaussian spot of the excitation laser can also be represented as:

$$I_{exc}(x) = \exp\left(-\frac{x^2}{2(\sigma_{exc}/2.355)^2}\right) \quad (4.5)$$

the σ_{exc} is the full-width half maximum of the laser spot size.

Finally, the average response of the system in the strained regions can be calculated by numerically integrating the intrinsic response of the system with the spatial excitation profile of the laser.

$$I_{avg} = \int I_{exc}(x) I_{int}(\lambda_{zpl}(x)) dx \quad (4.6)$$

Figure 4.6a displays the intensity of the excitation spot of the laser with a linewidth of 1 μm . Figure 4.6b shows the simulated center peak redshift due to the strain profile of the nanopillar and Figure 4.6 c shows the response of unstrained regions (center resonance energy at 1.73 eV) obtained from fitting a Gaussian function with 10 meV FWHM to the experimentally obtained PL spectra. Since the lifetime of excitons are on the order of picoseconds and the strain gradient is negligible away from the edge of the pillar, an exciton diffusion/funneling correction ($Dx = 1 \text{ cm}^2/\text{s}$) did not result in any noticeable difference in the calculations. The final predicted PL spectra is presented in Figure 4.6d, as expected, the majority of the signal comes from unstrained regions. The strained regions at the edge and center of the pillar would result in two comparably dim redshifted peaks in the photoluminescence response, accounting for about 1.15 % and 0.85 % of the

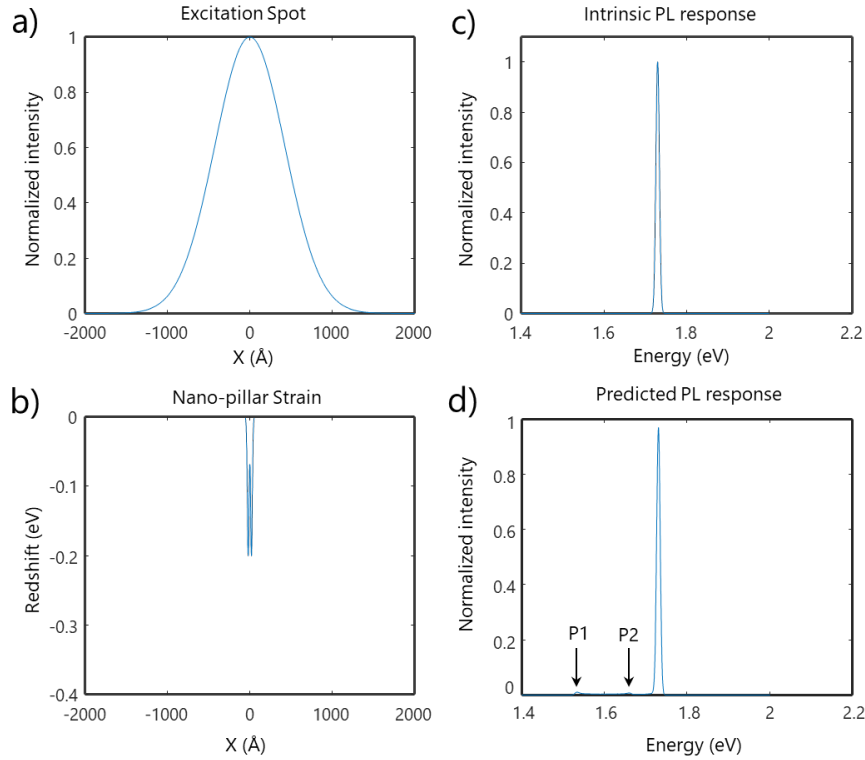


Figure 4.6: Finite excitation spot size corrections for nanopillar strain profile a) Excitation spot with FWHM of 1 μm . b) Horizontal line cut of simulated strain profile of a 150 nm diameter nano-pillar. Note that line-cut travels through the center of the pillar. c) Intrinsic PL response in unstrained regions obtained from fitting a gaussian with 10 meV FWHM to the experimental results. d) Predicted PL response with strain. The main observed peak is from the unstrained neutral exciton. Note that P2 and P1 correspond to the strained neutral exciton at nano-pillar positions. P1 is the peak corresponding to the maximum strain at the edge of the pillar and P1 peak is attributed to the top of the pillar where the strain relaxes to some extent.

intensity of the neutral exciton. We note that in our experiments, we observe, on average, a 3% background emission compared to the neutral exciton. Also, the charged exciton at lower energies practically makes it impossible to see the shifted exciton peaks due to the nanopillar strain pattern in our system. It can be only mapped using near-field imaging methods such as reference [20].

We note that the overall redshift observed in Figure 4.4 can indicate the presence of residual linear strain profile with a scale comparable to the laser's spot size. In order to

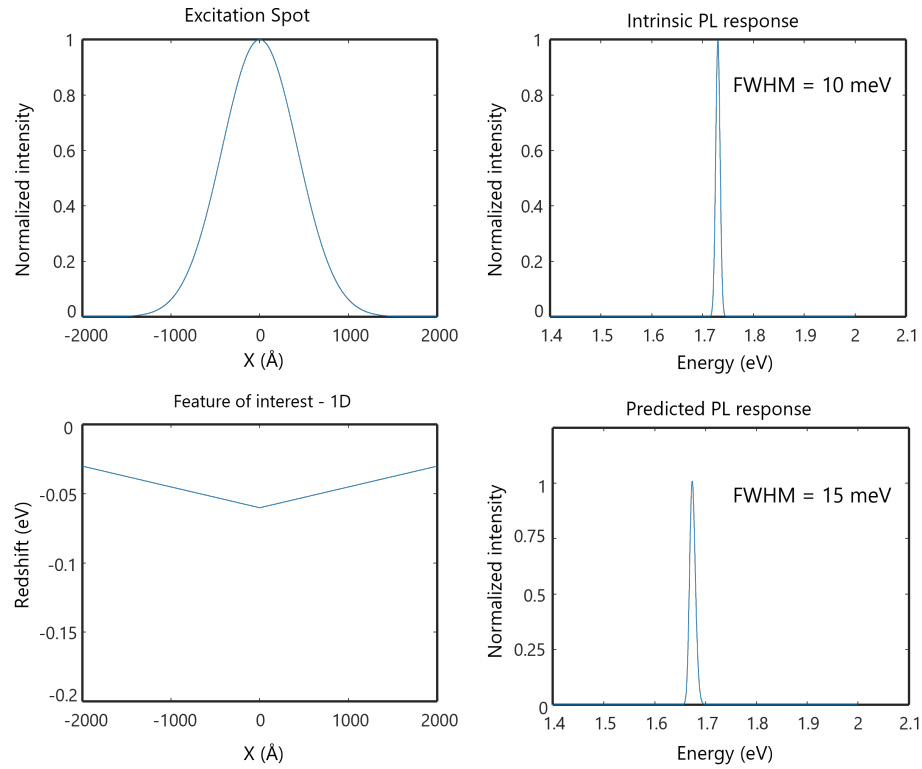


Figure 4.7: Finite excitation spot size corrections for a linear strain profile a) Excitation spot with FWHM of $1\mu\text{m}$. b) Simulated strain profile that has a residual strain corresponding to a redshift of -0.03 eV which linearly increases to 0.06 eV at the center. c) Intrinsic PL response in unstrained regions obtained from fitting a gaussian with 10 meV FWHM to the experimental results. d) Predicted PL response. The PL signal is redshifted by 56 meV and its linewidth is broadened to 15 meV . The redshift is proportional to the average of strain per length, while the broadening corresponds to the linear slope of the strain profile

verify this, we have also simulated the predicted response of the system to a linear strain gradient profile. Figure 4.7c show the simulated redshifted profile of such a strain profile. The strain is simulated to result in a -30 meV redshift $2\mu\text{m}$ away from the center of the laser spot, which linearly increases to -60 meV at the center. Note that the strain is linear all across the FWHM of the excitation spot. Figure 4.7 shows the predicted response of the system calculated through the framework mentioned above. The center energy is shifted overall by -56 meV , and the linewidth is broadened to 15 meV due to the linear slope of the strain. Overall, our results indicate that strain from nanopillars is

hard to observe using far-field PL, and redshift seen in some samples in the pillar location must be arising from residual strain gradients on the order of the excitation spot that has been caused during the stamping process.

4.3 Photoluminescence spectroscopy of electron-beam irradiated WSe₂

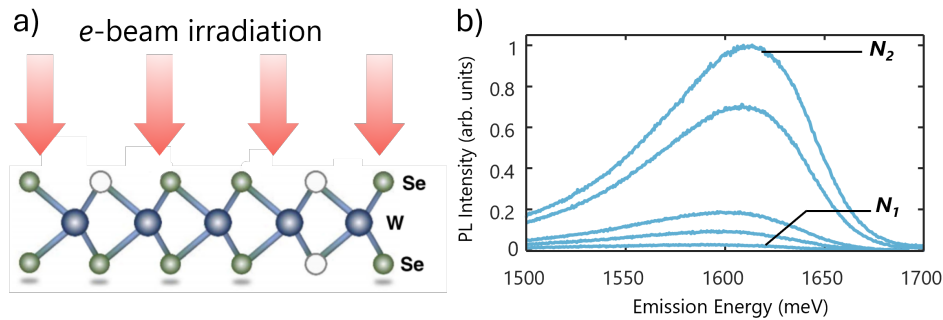


Figure 4.8: PL Spectra of e-beam engineered defects in WSe₂ a) Illustration of the e-beam induced crystal damages that mostly result in creation of Chalcogen vacancies. b) Intensity of the defect band as function of irradiation dosage for a 100 keV beam. N₁ dosage corresponds to 10⁵ electron/ μm^2 and N₂ corresponds to 10⁶ electron/ μm^2

Next, we focus on characterizing WSe₂ samples with higher defect density. Electron-beam irradiation has been previously used to create deterministic defects in 2D materials. High-intensity electron-beam current with sufficiently high accelerating voltage is capable of knocking chalcogen atoms out of the crystal lattice through ballistic displacement scattering due to a large cross-section of chalcogens [15, 16] (Figure 4.8a). Initially, a location away from the pillars is irradiated with a 100 keV electron beam with a focus spot size of (<10 nm) using a JOEL JBX 6300-FS utilizing the fifth lens mode. The spot is held constant with constant current, and the exposure time is changed to achieve different irradiation dosages extending from 10⁵ electron/ μm^2 up to 10⁶ electron/ μm^2 . Figure 4.8b Displays the photoluminescence spectra of the irradiated regions with varied dosages in

the energy range of 1500-1700 meV, well below the exciton and trion peaks. As seen in Figure 4.8, no single isolated peaks that could resemble single-photon emission are seen in any of the dosages. However, a broadband photoluminescence peak with intensity scales sublinearly with $P^{0.7}$ where P excitation power is observed. We attribute the observed defect band to an ensemble of chalcogen vacancies in WSe₂. The defect band retains its qualitative features at different excitation powers with no indication of saturation.

4.4 Photoluminescence spectroscopy of strained and electron-beam Irradiated WSe₂

In order to test the validity of the defect-bound exciton model, in the next step, we irradiated the top of the nanopillar sites with the configuration and dosages specified in the previous section. Dosages below 10^5 electron/ μm^2 did not yield any noticeable changes in the spectra. At around threshold dosage of $> 10^5$ electron/ μm^2 spectra from about 12 % of the sites demonstrated at least one ultra-sharp line indicative of single photon emitter (Figure 4.9a). As the electron-beam dosage increases, the yield and number of single-photon emitters observed per site also increase. At 10^6 electron/ μm^2 , 85% of the sites show at least one single-photon emitter (Figure 4.9b). Figure 4.9c, shows the photoluminescence map of six adjacent sites for the dosage of 10^6 electron/ μm^2 . Spectra of the respective sites are demonstrated in Figure 4.9d. Sharp emission lines attributed to single photon emitters appear in the 1515-1580 meV range, which is roughly 100 meV lower than previous observations of WSe₂ single photon emitters. In the subsequent discussion, we will discuss the implications of the lower energy levels.

Second-order auto-correlation measurements were conducted on the suspected single-photon emitters. Figure 4.10a displays the $g^2(0)$ for 14 spectral lines, displaying the

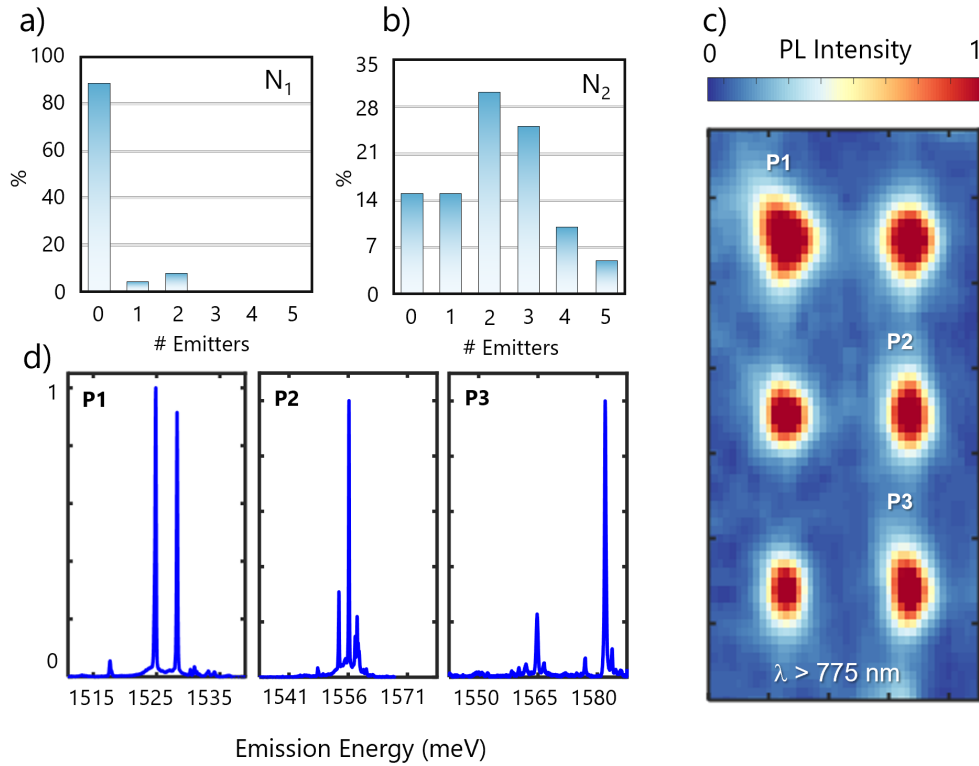


Figure 4.9: PL Spectra of e-beam engineered defects in WSe₂ a) Statistics of number of emitters per site with irradiation dosage of 10^5 electron/ μm^2 . b) Statistics of number of emitters per site with irradiation dosage of 10^6 electron/ μm^2 . c) PL map of six irradiated sites with the 10^6 electron/ μm^2 dosage. PL map demonstrates the integrated intensity of collected light with wavelengths above 775 nm. The localized emission spots are the position of the pillars. Some sites demonstrate more than one emitter and saturate the detector over the exposure period. d) PL Spectra of three pillars seen in (c). Excitation power is set at $1 \mu\text{W}$. Sharp emission lines appear in pairs, pointing to possible creation of biexciton-like complexes.

signature anti-bunching dip at zero-time delay with purity above 85 % and average purity of 92 %. The spectral purity of many emitters reached as high as 95 %, limited by the background emission in the system. The average homogeneous linewidth of the emitters with non-resonant excitation was measured at $75 \mu\text{eV}$ (Figure 4.10b) Upon investigating with finer diffraction grating, each sharp emission line appears as a doublet with cross-linearly polarized emission, evidencing fine-structure splitting. The average zero-field splitting of the doublet is reported in Figure 4.10c. Overall, our method achieved an 85

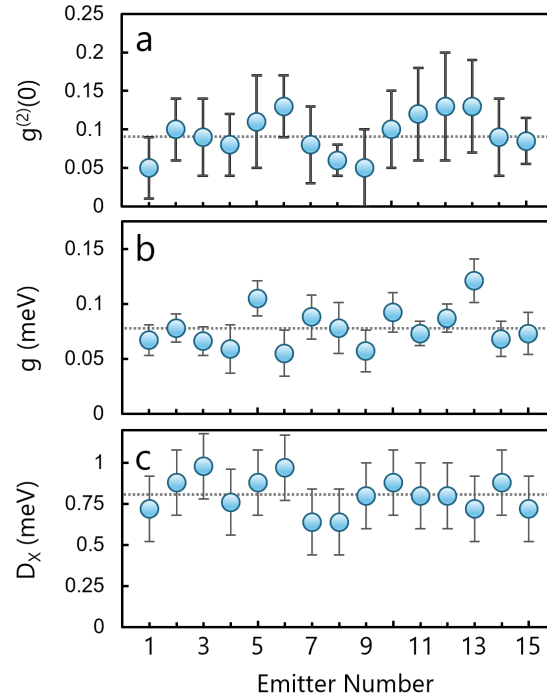


Figure 4.10: Statistics of the Engineered Emitters a) Distribution of $g^2(0)$ with average purity of 92%. b) Distribution of homogeneous linewidth with average of $75 \mu\text{eV}$. c) Distribution of zero-field doublet-splitting. Horizontal dashed lines denote the average of measurements. Error bars denote the standard deviation from fitting the data.

% yield to engineering one emitter per site with spatial resolution down to 100 nm in the spectral range of 1515-1580 meV.

Given that the e-beam irradiation method can be repeated after subsequent measurements, achieving near-unity yield by re-irradiating sites that did not yield single-photon emitters within the first try is possible. We also note that the spectral range at which the emitters are engineered is considerably smaller than in the previous demonstrations. This is a feature of the decoupled defect and strain engineering method. The electron beam creates a defect band within the spectral range of 1.5-1.7 eV, and the nanopillar strain causes the dark exciton to hybridize with the localized defects in certain positions, creating defect-bound excitons. Since the defect band is much wider than the spectral range of the emitters, we hypothesize that the variance seen in the spectral position of the

emitters is due to variance in the engineered strain profiles; other precise strain engineering methods can be potentially useful to reduce this spread. Finally, our experiments strongly suggest that both atomic defects and strain are necessary for the creation of single-photon emitters in WSe₂ and support the hypothesis of defect-bound excitons put forward by Linhart *et al.* [17].

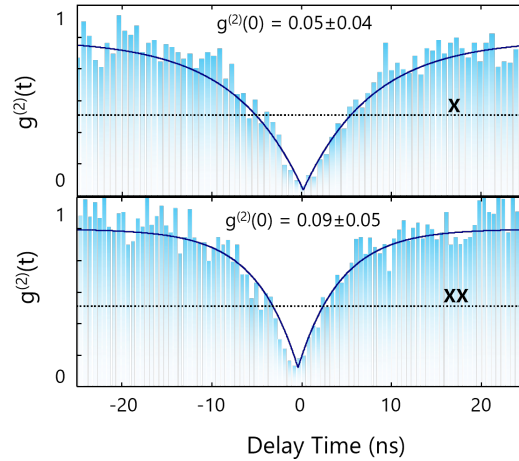


Figure 4.11: Second-order auto-correlation measurement $g^{(2)}(t)$ for exciton-like (X) and biexciton-like (XX) observed features. Both lines demonstrate purity over 90%, indicating quantum nature.

4.5 Observation of biexciton emission cascade

Taking a closer look at the spectra of the single-photons in the nanopillar sites reveals that many of the sharp lines tend to appear in pairs with around 3-5 meV spacing (Figure 4.9d). Each of these sharp lines demonstrates anti-bunching behavior, as seen in Figure 4.11. These features closely resemble the radiative emission cascade of biexcitons in quantum dots that have also been reported for WSe₂ [21]. However, to our knowledge, this is the first work that reports the deterministic creation of such biexcitonic features in WSe₂. Two excitons can bind together to lower their overall energy and form a biexcitonic complex (Figure 4.12 a). The overall energy reduced energy is called

binding energy (E_b). When the biexciton decays, one electron-hole pair with the allowed spin configuration recombines first and emits a photon, returning the overall system to an exciton configuration. Next, after some time, the exciton also recombines at higher energy, and the system decays to a ground state. Given that the Pauli exclusion principle dictates that the sign of spins for the holes and electrons in the biexciton complex have to be different, the polarization of the exciton and biexciton photons are correlated. In the absence of fine-structure splitting, the photons recombine as right and left-hand circularly polarized light with degenerate energy levels, opening up a deterministic pathway to create correlated polarization-entangled photon pairs (Figure 4.12b). However, asymmetry in the confinement potential can lead to large fine-structure splitting (Δ_X) due to electron-hole exchange interaction [22].

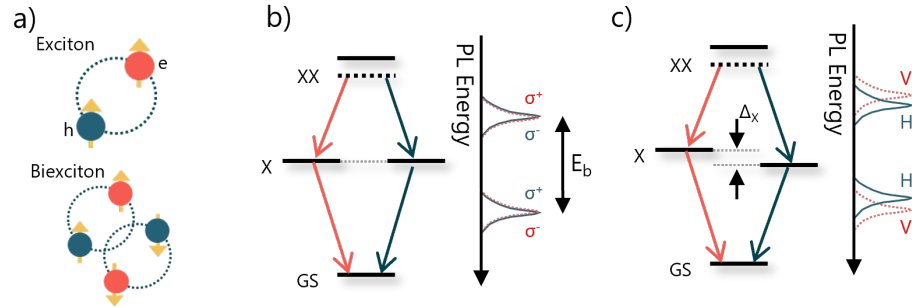


Figure 4.12: Exciton and Biexcitons a) An illustration of configuration of bright exciton (one electron and one hole with the same spin) and biexciton (two electron and two holes). b) Energy level structure for the biexciton radiative cascade in absence of strain- and defect- dependent fine-structure splitting. Polarization-entangled photon pair can be generated in this case with circularly polarized basis. Here, E_b denotes the biexciton binding energy. c) Energy level structure for a biexciton-exciton radiative cascade in presence of fine-structure splitting which breaks the degeneracy of the intermediate transition, mixing the circularly polarized basis and resulting in linear polarization emission of photons that are separated by the zero-field splitting energy

In the presence of fine-structure splitting, the degeneracy between the pair is lifted, and photons recombine as cross-linearly polarized light with distinct zero-field splitting (Figure 4.12c). In this case, the overall wave-function of the correlated photons can be

represented as:

$$|\psi\rangle = \frac{1}{\sqrt{2}}[|H_X H_{XX}\rangle + e^{-i\Delta_X t/\hbar} |V_X V_{XX}\rangle] \quad (4.7)$$

where the zero-field splitting (Δ_X) exponentially reduces the fidelity of the entangled pair, and many methods, such as strain or stark tuning, have been previously employed to erase fine-structure splitting in biexcitonic complexes to enable high-fidelity entangled pair generation.

Figure 4.13a reveals the polarization-resolved photoluminescence of these features. Each sharp line in the pair is consistent with a doublet, attributed to the fine-structure splitting with linear polarization. However, the sign of polarization is reversed in each pair, consistent with the emission cascade of biexcitons (Figure 4.12c). Next, we study the power dependence of the integrated intensity of both excitonic and biexcitonic peaks (Figure 4.13b). The exciton integrated intensity grows sub-linearly with excitation power, whereas the biexciton feature grows super-linearly, which is consistent with previous observations of biexcitonic-like features in WSe₂ [21]. Next, time-resolved photoluminescence measurement is employed using a 635 nm pulsed laser diode which reveals lifetime $T_1 = 6.12$ ns for the exciton-like feature and $T_1 = 4.01$ ns for the biexcitonic-like feature as expected from a biexciton-exciton complex (Figure 4.13c). Figure 4.13d demonstrates the time trace of the spectral diffusion of both peaks during a 5-minute observation window. No appreciable spectral diffusion is seen on long-time scales. The jitter seen at $t=250$ s happens simultaneously on exciton and biexcitonic lines, providing further evidence that the two emissions are correlated. Overall, our experiments verify that the observed doublets are biexcitonic-like features that could potentially be used for deterministic entangled pair generation. However, we note that the physical origin of these observed features is still ambiguous. Biexcitons have been previously studied in the con-

text of quantum dots; however, in our system, biexcitons possibly arise from combining two dark excitons bound to a defect whose properties are not fully understood yet.

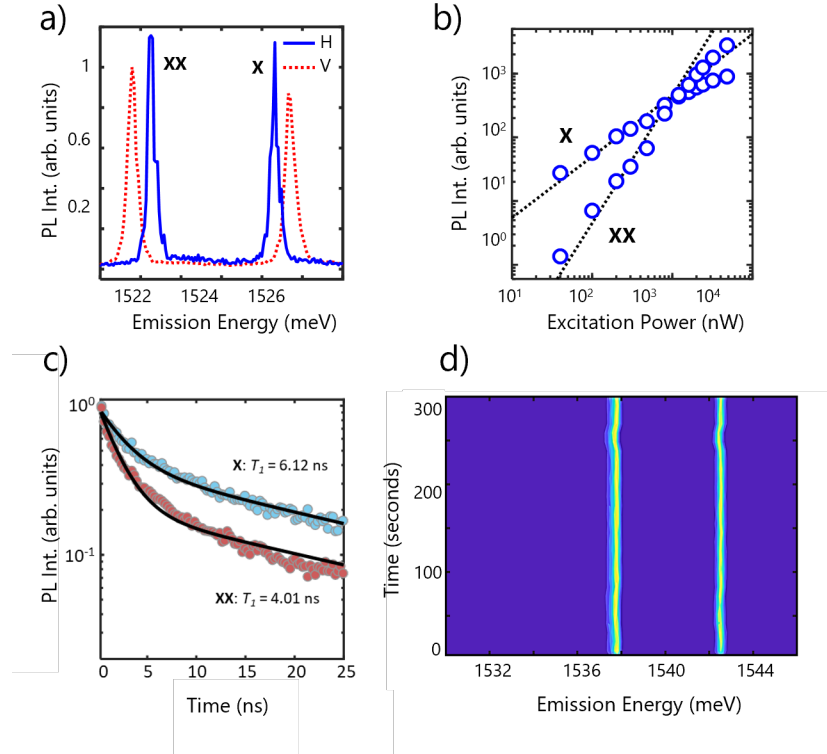


Figure 4.13: Optical spectroscopy of biexcitonic-like Features a) High resolution polarization-resolved PL spectrum of a biexcitonic (XX) and excitonic (X) feature. Each pair consist of two doublets with cross-linear polarization, however the sign of the polarization is reversed in each pair. b) PL intensity as function of excitation power. Exciton intensity increases sub-linearly with power and shows saturation at very high powers. Biexciton however, grows super-linearly with excitation power as expected for a two-level system. Dashed lines are linear fit $\log(P_{int}) = x\log(P_{exc})$ to the data with extracted slopes of 0.96 for exciton (X) and 1.587 for biexciton (XX), respectively. c) Time-resolved photoluminescence measurement of the exciton-like (X) and biexcitonic-like (XX) feature. Data are fit with a bi-exponential function with decay times $T_1 = 6.12$ ns for the exciton and $T_1 = 4.01$ ns for the biexciton features, in line with the expected dynamics of an exciton-biexciton pair. d) Time-trace of the spectral diffusion of the exciton and biexciton features. Each row represents a 10s integration time over a total 5 minute measurement window. Almost no spectral diffusion on the order of 10s was observed. Small jitter at around $t=250$ s is correlated on both exciton and biexciton lines, further hinting at their correlated nature.

4.6 Temperature dependent properties of the engineered single-photon emitters

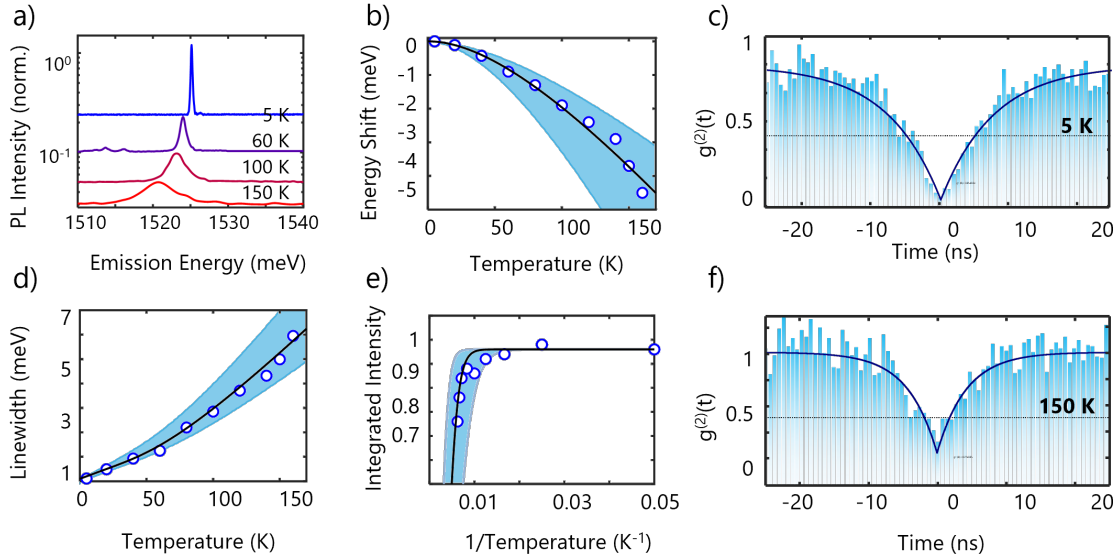


Figure 4.14: Temperature dependence of the single photon emitters up to 150 K a) Temperature evolution of a representative single-photon emitter from 5 K to 150 K. b) Single-photon energy as a function of temperature. Single-photon is redshifted due to decrease in bandgap energy which follows the Varshni's empirical equation. c) Second-order auto-correlation function at 5 K for the emitter seen in (a) d) Homogenous linewidth of the emitter as function of temperature. e) Arrhenius plot of the integrated intensity of the emitter as function of temperature. A quenching behaviour is observed at $T = 215$ K. Shaded region in b, e, and e demonstrate the range of recorded parameters for an ensemble of emitters. Open circles demonstrate measured data for a single emitter in the ensemble and the solid black lines are theoretical fit to the data. f) Second-order auto-correlation function at 150 K for the emitter seen in (a)

Previous observations of single-photon emitters in WSe₂ have been limited to cryogenic temperatures. The photoluminescence signal from the emitters tend to quench at temperatures about 20-30 K. Extending the working temperatures of single photon emitters to 80 K would enable the use of nitrogen cooled cryostats, and extending to temperatures of 200 K would enable the use of TE-cooled coolers with significantly higher cooling power. Each of these milestones would result in significant increase for potential

scaling of quantum technologies.

The main contributor to the quenching of the single-photon emission is the interaction of the defect-bound exciton with the phonon bath, which results in carrier escape from the confinement potential to the band-edge and disassociation of the defect-bound exciton. This effect would be more pronounced for shallow emitters with smaller confinement potential. As mentioned, the spectral range in which electron beam and strain-engineered single-photons appear is about 100 meV lower in energy than previous observations. This could indicate [23] that our single photon emitters also have a higher energy barrier and, therefore, higher thermal activation energy at higher working temperatures. Furthermore, previous studies have shown that non-radiative trap-assisted recombination can also influence the quenching factor at high defect densities [24]. Given that in our fabrication method, high-quality WSe₂ films with very low defect density are used, as evidenced by their negligible defect-band emission at cryogenic temperatures and the fact that we only introduce defects deterministically in locations with high strain, we expect our approach also mitigates quenching from non-radiative trap-states and further enhance the quantum yield and working temperatures of our emitters.

Figure 4.14a and f demonstrates the temperature dependence of the photoluminescence spectra of single-photon emitters from 5 K to 150 K. The single-photon emission retains its purity even up to 150 K as seen in Figure 4.14c, which is almost an order of magnitude higher than previous demonstrations, indicating that our emitters exhibit higher confinement potential that decouples the exciton from the lattice. We note that the PL signal could also be observed up to 210 K. However, the temperature control of the cryostat only allowed us to reliably maintain an increased temperature up to 150 K. Figure 4.14b tracks the center frequency of the emission as a function of temperature. Due to the decrease of bandgap with increasing temperature, the single-photon is redshifted to lower energies by about five meV. The Varshni-like equation [25] with the

form

$$E(T) = E(0) - \frac{\alpha T^2}{T + 170K} \quad (4.8)$$

is used to fit the emission energy versus temperature data. Here, α is associated with the relaxation of the lattice, and 170 K is determined from experimentally measured Debye temperature. Fit data reveals $\alpha = 5.3 \times 10^{-6} K^{-1}$ which is considerably smaller than previously measured numbers for native defects in WSe₂ grown using CVD techniques [26]. As expected, the higher confinement potential enabled via accurate positioning of the e-beam-engineered chalcogen defects within the strain site more strongly decouples the defect-bound exciton from the temperature dependence of the bandgap of the lattice compared to previous observations.

Next, we study the evolution of the homogeneous linewidth of the emitter as a function of temperature (Figure 4.14d) to understand the broadening mechanisms contributions from exciton-acoustic/optical phonon scattering. The data are fit with the equation

$$\gamma(T) = \gamma_0 + \alpha T + b[(e^{\frac{E_p}{kT}} - 1)]^{-1} \quad (4.9)$$

where the first term is the temperature-independent linewidth, the second term is the linear broadening contribution from acoustic phonon-exciton scattering, and the final term is the scattering from an optical phonon with activation energy of E_p following Bose-Einstein statistics. Our curve fitting analysis yields $\alpha = 15 \mu eV/K$ and $E_p = 20 meV$. The acoustic phonon rate measured in our work is about a factor of four smaller than the free-exciton in WSe₂. However, the optical phonon energy is identical to the free exciton, which strongly indicates that the same phonon scattering processes that affect pristine WSe₂ also play a critical role in broadening the linewidth of the single-photon emitters.

Finally, the total integrated counts of the single-photon emitter as a function of

temperature are shown in Figure 4.14e . A clear quenching behavior is seen at 215 K. The exponential quenching mechanism is indicative of a thermally activated escaping mechanism. Hence, the data fit with an Arrhenius model developed for depopulation of a two-level system. The integrated intensity will follow the equation:

$$I(T) = \frac{I_0}{1 + Re^{(\frac{-E_A}{kT})}} \quad (4.10)$$

Here, R is the ratio of the radiative (T_R) to non-radiative (T_{NR}) recombination lifetimes, and E_A is thermal activation energy that disassociates the defect-bound exciton. Our fit to the data achieves $R = 19$ and $E_A = 95 \text{ meV}$. Assuming that the nanosecond recombination lifetime of the single-photon emission is mainly due to radiative recombination, the quantum yield (Q_Y) of the single-photon emitter can be estimated as

$$Q_Y = \frac{T_R^{-1}}{1 + RT_R^{-1}}, \quad (4.11)$$

which for our fit yield Q_Y of 5%. To compare our result with previous demonstrations, we analyzed all studies that have previously reported temperature dependence of the integrated intensity of WSe₂ quantum emitters. Here, we emphasize that activation energy (E_A) is not a fudge factor and is proportional to the confinement potential of the emitter. We also note that the coefficient preceding the exponential term in the equation for quantum yield, in more rigorous models, depends on various electron/hole capture rates, capture cross-section, and radiative and non-radiative lifetimes [23]. Given that these parameters are all material-dependent, the validity of the fits for quantitative analysis of activation energies cannot be justified. However, plotting the best fits for activation energies extracted from literature still reveals an expected trend as shown in Figure 4.15, the quenching temperature (the point at which the integrated intensity starts to drop exponentially) is directly proportional to the energy difference between

the emission energy of the defect from the conduction band edge, which is also directly proportional to the confinement energy of the defect. Our work reports the highest activation energy reported to date for WSe₂, and as expected, our emitters can function at up to 215 K temperatures. Figure 4.16 provides a summary histogram of our measured yield, temperature dependent linewidth, and temperature dependent purity of this work. As discussed in the following chapters, combining our high working temperature emitters with photonic cavities can extend these working temperatures well into room temperature by utilizing Purcell enhancement.

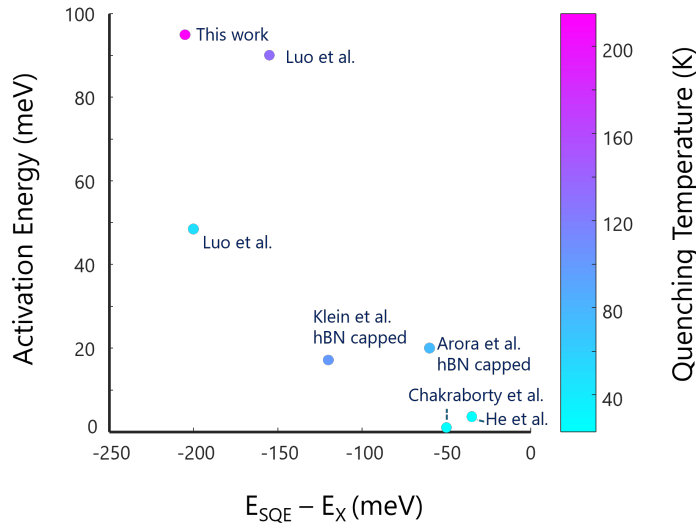


Figure 4.15: Estimated activation energy (E_A) of reported TMD-based single photon emitters as function of energy difference between defect emission and free-exciton. Quenching temperatures are color coded. Chakraborty et al. refers to reference [4], He *et al.* [21], Luo *et al.* [26], Klein *et al.* [27], and Arora *et al.* [28]

4.7 Discussion

Our analysis has verified that defects and strain are necessary to engineer single-photon emitters in WSe₂. However, the microscopic nature of the defect responsible for localizing the dark exciton remains elusive. Moreover, multiple defects could also

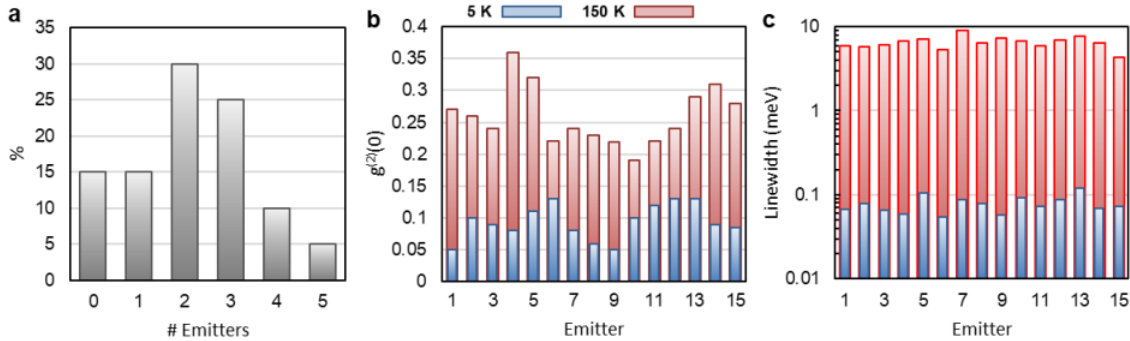


Figure 4.16: Statistics of single emitters across the ensemble a) Percentage of probed sites containing 0-5 emitters. b) Second-order correlation function, $g_2(0)$, measured at 5 K (blue) and 150 K (red). c) Homogeneous linewidth (γ) at 5 K (blue) and 150 K (red).

contribute to the experimental observation. Within the intervalley dark-exciton proposal, any valley-symmetry breaking defect that appears at an energetically favorable position, close to the conduction band edge, and has a probability of hybridizing with the dark exciton in locations of high strain could potentially be a candidate for single-photon emission. Previously, many point defects have been introduced as plausible defects for single-photon emission in WSe₂, including selenium vacancies [17], tungsten centered vacancies [29], oxygen interstitial [30], and anti-site defects [31].

Considering that the defects in this work were induced by e-beam irradiation a process whose resulting defect morphology has been extensively studied—we can narrow down the potential candidates through a systematic, ab initio approach. Research has shown that e-beam irradiation primarily leads to the formation of chalcogen and double chalcogen vacancies due to lower knock-off energy [15]. Additionally, prolonged exposure to a focused e-beam spot can destabilize the transition metal bond, causing the metal to migrate and create more complex vacancies, such as pore vacancies [32, 33]. In the case of WSe₂, rotational trefoil defect complexes have also been observed under e-beam irradiation [16]. Therefore, we selected five likely defect complexes to investigate: selenium single vacancy,

double vacancy, tungsten vacancy, pore vacancy, and trefoil vacancy. Given the common issues with bandgap underestimation in DFT, exciton binding energy uncertainties, and confinement potential variations, our focus is not on a quantitative comparison. Instead, we concentrate on the relative shifts between the conduction band and defect levels under strain, which can be evaluated using ab initio simulations.

Density-functional theory (DFT) calculations were conducted using the Synopsis QuantumATK [34] package, implementing the PerdewBurkeErnzerh (PBE) variant of the generalized gradient approximation [35] (PBE-GGA) exchange-correlation functional. The calculations and geometry optimizations utilized HGH pseudopotentials with Tier4 basis sets, $3 \times 3 \times 1$ Brillouin zone k-point sampling, a 200 Rydberg density mesh cutoff, and a maximum force constant of 0.2 eV/nm. This GGA-HGH Tier4 setup is widely recognized in the literature for studying the physics of 2D TMDs. Initially, the WSe₂ supercell was relaxed geometrically to the specified maximum force constant. Subsequently, depending on the defect complex size, a 5×5 or 7×7 supercell was constructed, followed by the removal of the appropriate atoms. The geometry was then re-optimized, with the supercell constrained in the in-plane direction to induce the target strain, allowing the defective supercell to reach its final configuration.

Figure.4.17 a-b, verifies our expected shrinkage of bandgap and reduction of E_c within the framework of DFT calculations. Figure 4.17c displays the behavior of selenium single-vacancy levels under biaxial tensile strain. For full simulation results, we refer readers to the supplementary material section of reference [36]. It is evident that these defect levels emerge at favorable energies near the conduction band and shift closer as strain is applied. However, selenium single and double vacancies are prone to passivation through oxidation [37]. Given that the single-photon emitters (SPEs) in this study, like those in previous research, remain functional after extended periods and temperature cycles, it is unlikely that these vacancies are the responsible defects. In contrast, tungsten

vacancies do not create energy levels near the conduction band, making them energetically unfavorable. Conversely, WSe₆ vacancy complexes, or pore vacancies, form nanopores similar to those observed in MoS₂ [32] and WS₂ [33] after geometry relaxation. These vacancies generate energy levels close to the conduction band and move closer with increasing strain (Figure 4.17d). This suggests that more complex vacancy structures, such as nanopores induced by e-beam irradiation, might be responsible for the SPEs observed at the e-beam irradiated sites in WSe₂. This implies that the morphology of the e-beam-induced defects might differ from previously observed native defects, potentially residing deeper within the bandgap.

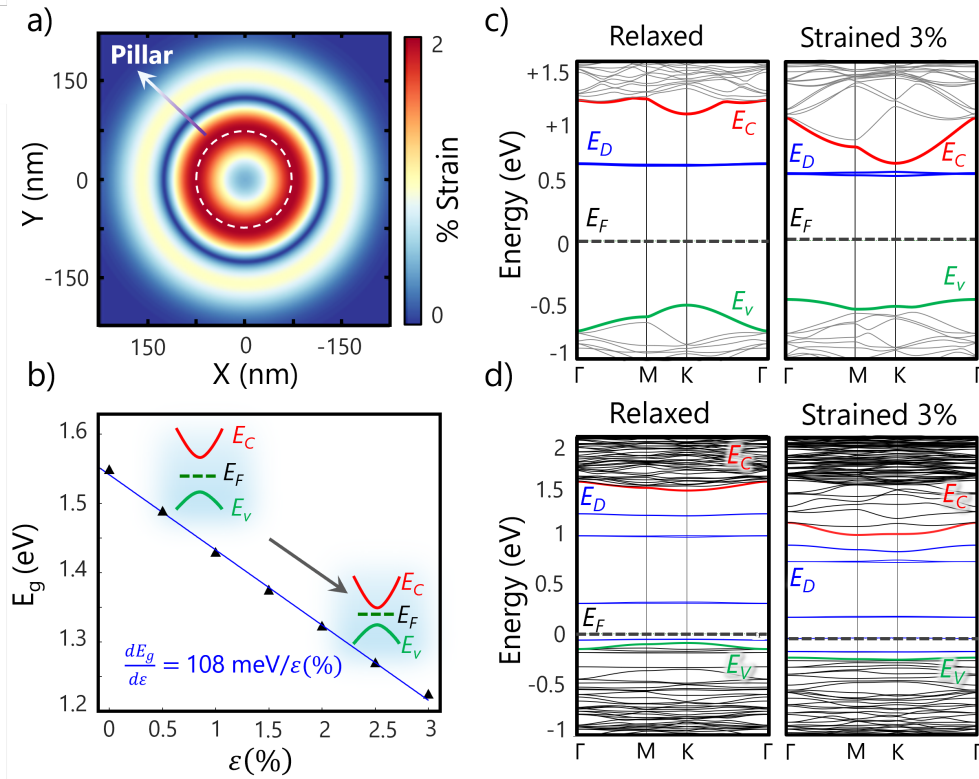


Figure 4.17: DFT Calculations of strained defect bandstructure a) Simulated strain profile at the nanopillar location. b) Bandgap variation as a function of applied biaxial tensile strain. The inset band diagram qualitatively illustrates the movements of the conduction band (E_C), valence band (E_V), and Fermi level (E_F) under strain. Notably, the conduction band exhibits a larger shift compared to the valence band. c) Evolution of the band diagram for a selenium vacancy under strain. E_D and the corresponding blue bands represent the localized defect levels. As strain is applied, the conduction band (E_C) and defect level (E_D) draw closer to each other. d) Evolution of the band diagram for the WSe₆ pore complex under strain. With strain, the energy gap between the conduction band and the nearest defect level diminishes. It is important to note that the Fermi level's position varies depending on the supercell size.

Bibliography

- [1] Y.-M. He, G. Clark, J. R. Schaibley, *et. al.*, *Single quantum emitters in monolayer semiconductors*, *Nature nanotechnology* **10** (2015), no. 6 497–502.
- [2] M. Koperski, K. Nogajewski, A. Arora, *et. al.*, *Single photon emitters in exfoliated wse_2 structures*, *Nature nanotechnology* **10** (2015), no. 6 503–506.
- [3] A. Srivastava, M. Sidler, A. V. Allain, *et. al.*, *Optically active quantum dots in monolayer wse_2* , *Nature nanotechnology* **10** (2015), no. 6 491–496.
- [4] C. Chakraborty, L. Kinnischtzke, K. M. Goodfellow, *et. al.*, *Voltage-controlled quantum light from an atomically thin semiconductor*, *Nature nanotechnology* **10** (2015), no. 6 507–511.
- [5] P. Tonndorf, R. Schmidt, R. Schneider, *et. al.*, *Single-photon emission from localized excitons in an atomically thin semiconductor*, *Optica* **2** (2015), no. 4 347–352.
- [6] S. Kumar, A. Kaczmarczyk, and B. D. Gerardot, *Strain-induced spatial and spectral isolation of quantum emitters in mono- and bilayer WSe_2* , *Nano Letters* **15** (2015), no. 11 7567–7573, [<https://doi.org/10.1021/acs.nanolett.5b03312>]. PMID: 26480237.
- [7] A. Branny, G. Wang, S. Kumar, *et. al.*, *Discrete quantum dot like emitters in monolayer $MoSe_2$: Spatial mapping, magneto-optics, and charge tuning*, *Applied Physics Letters* **108** (2016), no. 14 142101, [<https://doi.org/10.1063/1.4945268>].
- [8] J. Kern, I. Niehues, P. Tonndorf, *et. al.*, *Nanoscale positioning of single-photon emitters in atomically thin wse_2 .*, *Advanced materials (Deerfield Beach, Fla.)* **28** (2016), no. 33 7101–7105.
- [9] C. Palacios-Berraquero, D. M. Kara, A. R.-P. Montblanch, *et. al.*, *Large-scale quantum-emitter arrays in atomically thin semiconductors*, *Nature Communications* **8** (2017), no. 1 1–6.

BIBLIOGRAPHY

- [10] A. Branny, S. Kumar, R. Proux, and B. D. Gerardot, *Deterministic strain-induced arrays of quantum emitters in a two-dimensional semiconductor*, *Nature communications* **8** (2017), no. 1 15053.
- [11] Y. Luo, G. D. Shepard, J. V. Ardelean, *et. al.*, *Deterministic coupling of site-controlled quantum emitters in monolayer WSe₂ to plasmonic nanocavities*, *Nature Nanotechnology* **13** (2018), no. 12 1137–1142.
- [12] M. R. Rosenberger, C. K. Dass, H.-J. Chuang, *et. al.*, *Quantum calligraphy: writing single-photon emitters in a two-dimensional materials platform*, *ACS Nano* **13** (2019), no. 1 904–912.
- [13] H. Kim, J. S. Moon, G. Noh, *et. al.*, *Position and frequency control of strain-induced quantum emitters in WSe₂ monolayers*, *Nano Letters* **19** (2019), no. 10 7534–7539.
- [14] G. Moody, K. Tran, X. Lu, *et. al.*, *Microsecond valley lifetime of defect-bound excitons in monolayer wse₂*, *Physical review letters* **121** (2018), no. 5 057403.
- [15] H.-P. Komsa, S. Kurasch, O. Lehtinen, *et. al.*, *From point to extended defects in two-dimensional mos₂: Evolution of atomic structure under electron irradiation*, *Physical Review B* **88** (2013), no. 3 035301.
- [16] Y.-C. Lin, T. Björkman, H.-P. Komsa, *et. al.*, *Three-fold rotational defects in two-dimensional transition metal dichalcogenides*, *Nature communications* **6** (2015), no. 1 6736.
- [17] L. Linhart, M. Paur, V. Smejkal, *et. al.*, *Localized intervalley defect excitons as single-photon emitters in wse₂*, *Physical review letters* **123** (2019), no. 14 146401.
- [18] H. Moon, E. Bersin, C. Chakraborty, *et. al.*, *Strain-correlated localized exciton energy in atomically thin semiconductors*, *ACS Photonics* **7** (2020), no. 5 1135–1140.
- [19] A. V. Tyurnina, D. A. Bandurin, E. Khestanova, *et. al.*, *Strained bubbles in van der waals heterostructures as local emitters of photoluminescence with adjustable wavelength*, *ACS photonics* **6** (2019), no. 2 516–524.
- [20] T. P. Darlington, C. Carmesin, M. Florian, *et. al.*, *Imaging strain-localized excitons in nanoscale bubbles of monolayer wse₂ at room temperature*, *Nature Nanotechnology* **15** (2020), no. 10 854–860.
- [21] Y.-M. He, O. Iff, N. Lundt, *et. al.*, *Cascaded emission of single photons from the biexciton in monolayered WSe₂*, *Nature Communications* **7** (2016), no. 1 1–6.

BIBLIOGRAPHY

- [22] M. Bayer, G. Ortner, O. Stern, *et. al.*, *Fine structure of neutral and charged excitons in self-assembled in (ga) as/(al) gaas quantum dots*, *Physical Review B* **65** (2002), no. 19 195315.
- [23] E. Le Ru, J. Fack, and R. Murray, *Temperature and excitation density dependence of the photoluminescence from annealed inas/gaas quantum dots*, *Physical Review B* **67** (2003), no. 24 245318.
- [24] A. Chahboun, M. Vasilevskiy, N. Baidus, *et. al.*, *Further insight into the temperature quenching of photoluminescence from inas/ gaas self-assembled quantum dots*, *Journal of Applied Physics* **103** (2008), no. 8.
- [25] Y. P. Varshni, *Temperature dependence of the energy gap in semiconductors*, *physica* **34** (1967), no. 1 149–154.
- [26] Y. Luo, N. Liu, X. Li, *et. al.*, *Single photon emission in wse₂ up 160 k by quantum yield control*, *2D Materials* **6** (2019), no. 3 035017.
- [27] J. Klein, M. Lorke, M. Florian, *et. al.*, *Site-selectively generated photon emitters in monolayer MoS₂ via local helium ion irradiation*, *Nature Communications* **10** (2019), no. 1 1–8.
- [28] A. Arora, N. K. Wessling, T. Deilmann, *et. al.*, *Dark trions govern the temperature-dependent optical absorption and emission of doped atomically thin semiconductors*, *Physical Review B* **101** (2020), no. 24 241413.
- [29] S. Zhang, C.-G. Wang, M.-Y. Li, *et. al.*, *Defect structure of localized excitons in a wse₂ monolayer*, *Physical review letters* **119** (2017), no. 4 046101.
- [30] Y. J. Zheng, Y. Chen, Y. L. Huang, *et. al.*, *Point defects and localized excitons in 2d WSe₂*, *ACS Nano* **13** (2019), no. 5 6050–6059.
- [31] C. K. Dass, M. A. Khan, G. Clark, *et. al.*, *Ultra-long lifetimes of single quantum emitters in monolayer wse₂/hbn heterostructures*, *Advanced Quantum Technologies* **2** (2019), no. 5-6 1900022.
- [32] S. Wang, H. Li, H. Sawada, *et. al.*, *Atomic structure and formation mechanism of sub-nanometer pores in 2d monolayer mos 2*, *Nanoscale* **9** (2017), no. 19 6417–6426.
- [33] G. H. Ryu, A. France-Lanord, Y. Wen, *et. al.*, *Atomic structure and dynamics of self-limiting sub-nanometer pores in monolayer ws₂*, *ACS nano* **12** (2018), no. 11 11638–11647.
- [34] S. Smidstrup, T. Markussen, P. Vancraeyveld, *et. al.*, *Quantumatk: an integrated platform of electronic and atomic-scale modelling tools*, *Journal of Physics: Condensed Matter* **32** (2019), no. 1 015901.

BIBLIOGRAPHY

- [35] J. P. Perdew, K. Burke, and M. Ernzerhof, *Generalized gradient approximation made simple*, *Physical review letters* **77** (1996), no. 18 3865.
- [36] K. Parto, S. I. Azzam, K. Banerjee, and G. Moody, *Defect and strain engineering of monolayer WSe_2 enables site-controlled single-photon emission up to 150 K*, *Nature communications* **12** (2021), no. 1 3585.
- [37] J. Lu, A. Carvalho, X. K. Chan, *et. al.*, *Atomic healing of defects in transition metal dichalcogenides*, *Nano Letters* **15** (2015), no. 5 3524–3532.

Chapter 5

Photonic Integration of Quantum Emitters in 2D Materials

5.1 Rationale for 2D Integrated Quantum Light Sources

As outlined in Chapter 2, an ideal single-photon emitter must be able to excite a single photon in a well-defined single unique spatiotemporal mode with near-unity efficiency, high purity, and high indistinguishability.

Two main approaches exist for the photonic integration of deterministic quantum light sources. In the first approach, one can attempt to efficiently collect the light from the optical mode off the chip, generally using a high-NA objective, and then try to couple the collected light into a single-mode fiber, which can serve as the input into any arbitrary quantum circuitry. The state-of-the-art demonstrations in this approach are done using quantum dots embedded in the micro-pillar cavity, which can be collected to the first objective with efficiencies up to 60 % [1–3]. Unfortunately, this approach requires using bulk optics to collect light from the system, and even with advanced packaging techniques, such quantum light sources are typically limited to one source

per chip. Given that future quantum computers potentially require millions of qubits, the scalability of such approaches is an extremely challenging outstanding issue. In the second approach, one can integrate the single-photon source directly with a single-mode waveguide. If the integration process can be done in a scalable and foundry-compatible way, it is possible to integrate many emitters on a chip simultaneously, ideally with the same chip responsible for quantum information processing and detection, and enable genuinely scalable and stand-alone integrated quantum photonic circuitry. However, the single-photon host material must meet many engineering requirements to enable such integration.

First and foremost, a reliable and site-specific single-photon engineering method must be developed to create bright, pure, and indistinguishable emitters. For example, III-V quantum dots, considered state-of-the-art in terms of single-photon metrics, fail to meet this criterion as outlined in Chapter 2, given that their stochastic growth process makes it extremely difficult to align and integrate with the photonic waveguide. The next challenge is material growth and processing. Ideally, the single-photon sources must be integrated with a low-loss and mature photonic platform that can be utilized to build highly efficient photonic components such as phase shifters, directional couplers, splitters, MZIs, and grating couplers. This requires the development of a material growth or heterogeneous integration technique [4–6], such as flip-chip bonding, that is compatible with the emitter engineering and does not alter the spectral properties of the emitter in the process. This requirement becomes even more difficult to meet after introducing the next challenge. The emitter must be able to function close to surfaces.

In the simplest approximation, one can think of the single-photon emitter as a linear dipole in space. In order to couple the light from a single-photon emitter into a waveguide, the linear dipole must have the maximum overlap with the photonic mode and must be oriented correctly with respect to the polarization of the waveguide. This requirement,

in heterogeneous integration approaches, means that the emitter must function as close as possible to the photonic proximity of the photonic layer in order to achieve high coupling efficiency. Unfortunately, single photon emitters are usually very susceptible to surfaces. The charge-filling of interface states mainly dominates the Fermi level at the surfaces and interfaces of the material. In many cases, for example, the NV-centers in diamond, the interface states causes the quantum defect to transition into a new charge state incapable of luminescence. Even if the defect can exist with the correct charge state near the surface, interactions with trapped charges and interface states can become a detrimental source of dephasing and decoherence, hindering their functionality.

These stringent requirements have made on-chip integration of most of the known deterministic single-photon sources very difficult. However, the novel class of quantum defects in 2D material offers unique advantages in this regard. First, as shown in Chapter 4, single-photon emitters in WSe₂ can be site-specifically engineered down to 100 nm resolution. Furthermore, in recent years, other methods have been developed to create site-specific single-photon emitters in other 2D materials, such as hBN using electron-beam irradiation [7] and MoS₂ using helium-ion bombardment [8]. Quantum defects in 2D materials are among the few defects that can be site-specifically engineered.

However, the critical advantage of 2D materials is the ability to have functional defects at the surface. The 2D nature of these materials inherently means that all bonds are in-plane, and there are no dangling bonds or terminated interface states in the out-of-plane direction; 2D sheets interact via van der Waals interactions with their surroundings. This advantage allows defects in 2D materials to operate on the dangling-bond-free interface of the material with high isolation and long lifetimes, making them ideal for heterogeneous integration as they are capable of achieving the highest electronic/magnetic dipole proximity coupling strength with any exogenous fields. Furthermore, the atomic thickness of the 2D sheet translates to near-ideal photon extraction efficiencies as there is no light

lost to internal reflections in the material itself. Finally, the vdW forces that govern the interaction of the 2D sheets with their environment allow 2D material to be stacked on top of almost any materials using conventional transfer techniques without the common concerns for lattice matching. Combining all of these advantages, quantum defects in 2D materials present themselves as almost the ideal candidate for photonic integration.

5.2 Previous Integration Demonstrations for 2D Quantum Emitters

Attempts at photonic integration of quantum defects in 2D materials started almost as soon as these emitters were identified. Peyskens *et al.* [9] demonstrated coupling of WSe₂ single photon emitter with silicon nitride waveguides. In this approach, WSe₂ emitters were transferred on pre-fabricated silicon nitride waveguides. Relying on defects in the material and strain caused by draping of WSe₂ over the waveguide ridge, single-photon emitters were semi-deterministically created in the edge of the waveguide. However achieving high efficiency in this approach is challenging, given that the mode overlap of the waveguide with the emitter located at the top edge of the waveguide is minimal, and only a small portion of the light is coupled to the emitter. Similar approaches were also explored for both single photon emitters in hBN and WSe₂ [10]; however, again, due to the low coupling efficiency and random positioning of the dipole orientation, overall coupling efficiency was limited to 3-4 % in these approaches. Another challenge is minimizing the background emission of the photonic layer itself. In 2021, El Shaari *et al.* [11] demonstrated the deterministic coupling of hBN single photon emitters with SiN waveguides grown on top of the hBN using an optical image alignment technique. However, background emission from the silicon nitride itself spectrally overlaps

with the single-photon emission and reduced the overall purity. This brought another consideration for integration into the forefront, namely, the photonic layer growth should not only be compatible with the 2D material, but also the photonic layer itself should have minimized autofluorescence. Many single-photon emitters in 2D materials, like red (600 nm) and blue (440 nm) Single Photon Emitters (SPEs) in hBN, typically require hundreds of microwatts of non-resonant laser excitation power which can cause a considerable amount of background emission depending on the material for the photonic layer.

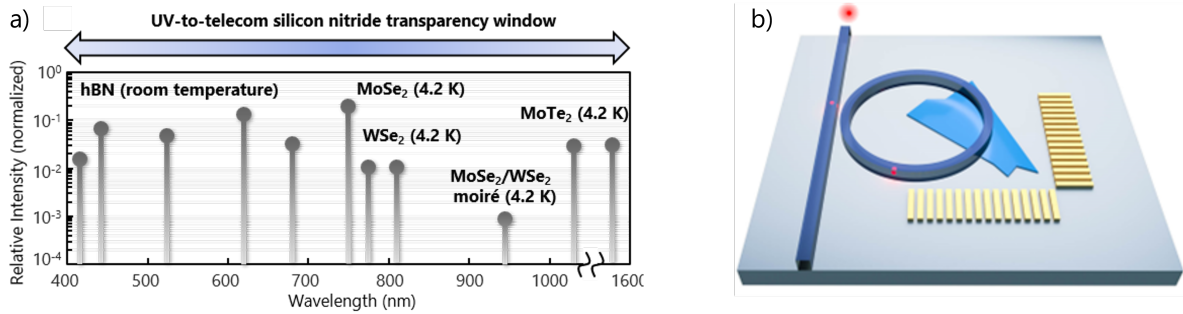


Figure 5.1: Universal platform for precision integration of 2D quantum emitters in silicon nitride photonics. a) The family of 2D materials, including hBN emitters at UV [7, 12] and visible [13] wavelengths, TMD emitters [9, 14, 15], and TMD heterostructures [16, 17], exhibiting a rich spectrum of quantum emitters spanning the ultraviolet-to-telecommunications wavelength transparency window of silicon nitride photonics. Height of each bar corresponds to reported intensity of each class of emitters. Grey data points are brightness corrected for the objective extraction efficiency, whereas blue data points are reported at the detector. b) Our ideal platform for deterministic integration of 2D quantum emitters. Single-photon emitters embedded in silicon nitride micro-ring resonators with precise positional and dipole alignment accuracy to achieve high Purcell enhancement.

5.3 The Ideal Integration Platform for 2D Materials

In this chapter, we aim to develop an ideal platform for integrating a 2D-based single-photon emitter that can overcome the challenges mentioned above. An ideal platform

for integration of 2D quantum emitters must:

- **Be transparent to a wide range of SPEs observed in the 2D materials family.** 2D single-photon emitters have been observed in various energies, from 440 nm hBN blue emitters to telecom-band emitters in MoTe₂. Amongst the photonic platforms, the silicon nitride transparency range perfectly fits the observed emitters (Figure 5.1a). Moreover, in the visible range, silicon nitride can be considered one of the most mature photonic platforms with a demonstration of low loss waveguides down to 0.1 dB m⁻¹ [18–20] and microring-resonators with an intrinsic quality factor up to 422 million [21].
- **Develop a 2D compatible, low-autofluorescence SiN recipe.** Stochastic and low-stress silicon nitride grown with both PECVD and LPCVD methods typically demonstrate background fluorescence in the visible range [22]. In our experience, these emissions are even present in silicon nitride obtained from different vendors. This emission has been attributed to Si-Si bonds in silicon nitride [23] and also band-edge transitions to K-centers [24]. It is critical to develop a recipe capable of quenching the background emission that can also be grown on 2D flakes while keeping the spectral properties of the emitter intact.
- **Integration with an on-chip cavity.** As we will discuss in the next section, even if a single-photon emitter is placed at the center of the waveguide with correct dipole moment orientation, given the finite mode overlap of the dipole moment with the mode of the waveguide and the presence of leaky modes, near-unity emission from the emitter into the waveguide is almost impractical. To mitigate this problem, one approach is to integrate the emitter with an on-chip cavity. The cavity, through Purcell enhancement, is not only capable of boosting the extraction efficiencies but

also can lead to increased indistinguishability. Hence, the emitter should be coupled to an on-chip cavity in an ideal integration platform (Figure 5.1b).

- **Deterministic and dipole-aligned integration.** To efficiently couple the emitter into the photonic mode of the cavity, the emitter’s position and emission dipole must be precisely aligned to the cavity. The following sections discuss an inexpensive and robust methodology to achieve such an alignment.

5.4 Engineering quantum defects in hBN

A critical advantage of hBN emitters is that they can function at room temperature due to their high confinement energy and isolation from band-edges. Given that in this project, in addition to conventional PL spectroscopy setup, an integrated photonic testing setup had to be developed that would interface with the confocal microscopy setup, we decided first to demonstrate room temperature integration of hBN quantum emitters with on-chip microcavities. Naturally, methods of engineering hBN single photon emitters had to be explored first.

Four classes of single-photon emitters have been observed in hBN. The first class, and probably the most studied, are the emitters appearing in the 800 nm wavelength that electron-paramagnetic-resonance (EPR) studies and density-function theory (DFT) calculations have converged on their origins and have assigned them to negatively charged boron defects. These emitters are typically engineered using neutron scattering; however, to our knowledge, all the observations of such defects have been from an ensemble of defects, and isolated V_B^{-1} defects have not been observed so far.

The second class of hBN emitters is the red emitters, appearing at a wide wavelength range of 550-630 nm. The origins of these defects are still under debate, and many studies have attempted to shed light on their microscopic configuration. The leading hypothesis

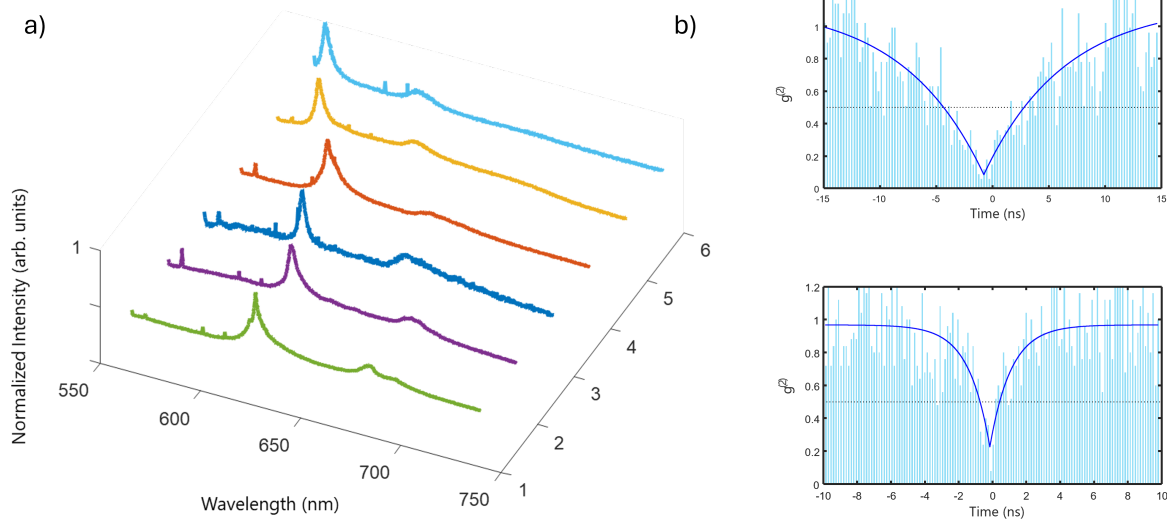


Figure 5.2: Red emitters in hBN. a) Representative PL spectra of plasma treated and thermally annealed activated red single-photon emitters in hBN. b) Representative second-order autocorrelation function g^2 of red-emitters demonstrating dip below 0.5 at zero time delay, evidencing single-photon emission.

has attributed these emitters to boron dangling bonds [25] and carbon-related impurities such as $V_B C_N^{-1}$ [26]. Site-specific engineering of these emitters has proven to be challenging. The most robust way to engineer these emitters has been through plasma treatment followed by thermal annealing [27, 28], which has been shown to considerably increase the isolated emitter density in hBN flakes. Our experiments utilized 10 minute O_2 plasma treatment at 100 W power with an oxygen flow of 0.3 sccm per minute, followed by rapid thermal annealing at 800 C in a forming gas environment. Figure 5.2a presents spectra of our plasma-treated and thermally-annealed hBN emitters. The phonon side-band at 60 nm redshifted from the zero-phonon line is one of the distinct features of these single-photon emitters. Figure 5.2b presents the representative second-order auto-correlation measurement on hBN red emitters. At room temperature, we typically observe average purities of 60-90 %. The rise time of the anti-bunching dip typically shows time constants on the order of 2-8 ns, consistent with previous observations of a lifetime of red

hBN emitters.

Similar to WSe₂ and TMDs, site-specific engineering methods have also been explored for hBN red emitters. hBN emitters typically present themselves near the edges or cracks in the flakes. Hence, a lot of effort has been focused on artificially creating hBN edges in small areas to localize the emitters. These efforts include chemical etching [29], laser irradiation [30], and ion irradiation [30] to deterministically induce structural damage in hBN, which is then can be followed by thermal annealing to allow the crystal lattice to reconstruct itself to some extent and stabilize the remaining optically active defects. Interestingly, nano-pillars were also successful, although with a lower yield than TMDs, in site-specific engineering of emitters in hBN [31]. However, we could not achieve any emitters using our nano-pillar engineering methodology described in the previous chapter.

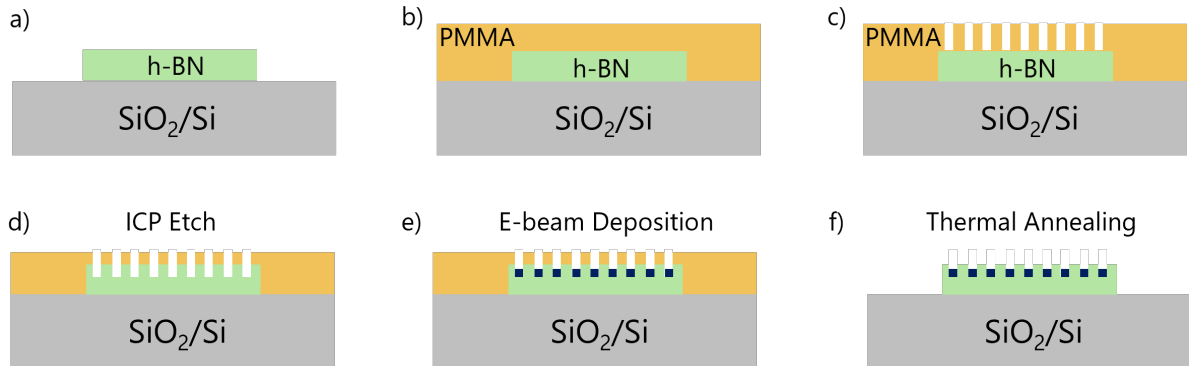


Figure 5.3: Nanopore engineering of visible hBN emitters. a) hBN flakes are exfoliated on SiO₂/Si chips. b) PMMA photoresist is spun on the substrate. c) Using electron beam lithography, nanometer array of pores are patterned in the PMMA. d) Inductively Coupled Plasma (ICP) etch using CHF₃/O₂ chemistry was utilized to etch pores into the hBN. e) A 1-nm carbon film can be deposited on the resist and the pores. Note that this step can be complimentary. f) After lift-off and photoresist strip, a thermal annealing step can be used to optically stabilize active emitters.

Inspired by the previous edge-creation methodologies and the fact that carbon impurities were a prime suspect for red emitters in hBN, we also developed a novel method to create site-specific single-photon emitters in hBN. Our method is based on etching small-diameter pores (down to 50 nm) in hBN flakes, followed by carbon e-beam deposition

and lift-off. This method is designed to mimic a cheap and accessible version of carbon-implantation. Figure 5.3 shows our process flow for this method. First, hBN flakes are exfoliated on top of SiO₂/Si chips. Next, optical flakes with thicknesses between 15-40 nm are identified using the optical contrast and color method. 80 nm thick polymethyl methacrylate (PMMA A4) e-beam photoresist is spun on the chips with a pre-exposure bake of 180 °C for 90 s. Electron-beam irradiation is utilized on a modified SEM (NPGS) system using a JOEL IT800SHL scanning electron microscope. Arrays of nanopores with a diameter of 50 nm up to 300 nm are irradiated with the base dose of 300 $\mu\text{C}/\text{cm}^2$ using an electron beam with an electron density of 10 pA/s and accelerating voltage of 30 keV. Next, the sample is developed in IPA/Acetone mixture for 22s, followed by a dehydration bake at 110 °C for 2 minutes. The sample is then loaded into an inductively coupled plasma (ICP) chamber and is etched for 4 seconds in CHF₃/O₂ environment. The etch rate of hBN and PMMA have been calibrated to avoid etching all the way through the hBN and PMMA. We typically etched about 10 nm of hBN in flakes with 15-40 nm thicknesses. After etching, PMMA was treated with oxygen plasma for 2 minutes at 50 W to avoid polymerization of PMMA during CHF₃ etch. In this step, we created two control samples; in one set of samples, PMMA was stripped away using acetone, and samples were thermally annealed at 800 C for 20 minutes in forming gas. The next set of samples was put aside for 1-nm carbon deposition in an electron deposition system with a graphite source, followed by lift-off.

Interestingly enough, the control samples demonstrated decent yield in creating red single photon emitters in hBN. Figure 5.4a-c presents one of the etched flakes in hBN. Representative spectra of these single-photon emitters is presented in Figure 5.4b. In Figure 5.4c, we correlate the position of the single-photon emitters with the position of the nanopores and their sizes. The red highlighted dots are the position of the nanopores, and the green dots demonstrate the position of observed single-photon emitters. Overall,

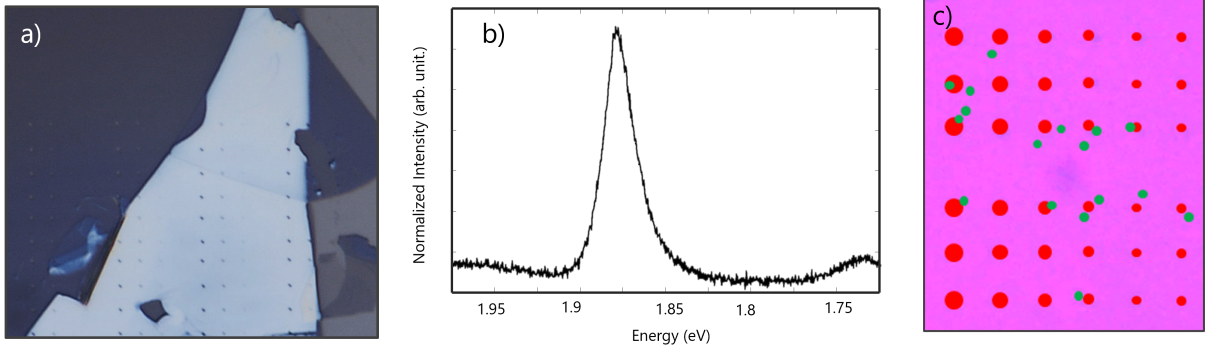


Figure 5.4: Nanopore engineering of visible hBN emitters results. a) Optical image of a processed hBN flake. Note that only the three largest rows of nanopores are visible within the image. b) Representative PL spectra of one of the engineered emitters. c) Position of measured single-photon emitters relative to the nanopores. Red dots denote the position of the pores and green dots are the position of the emitters.

amongst 36 etched sites, 12 sites demonstrated a single photon emitter within $3 \mu\text{m}$ distance from the nanopore. The pores with 150-100 nm diameter demonstrated a higher yield in single-photon emitter creation. These experiments are still ongoing, and further optimization is underway to see the effects of carbon deposition and provide further statistical significance to our approach. However, preliminary results seem very promising, as our method is an accessible and cost-effective way to create red emitters in hBN with positional accuracy in possibly sub-micron range. Finally, it is worth mentioning that, even though our method is semi-site specific, the best quality hBN emitters are currently found in plasma irradiated and annealed samples. Given this, for the integration of hBN emitters with on-chip cavities, we opted to use plasma and annealed samples.

The final class of hBN emitters is blue [7] emitters. These emitters were identified during cathodoluminescence measurements of hBN when the stationary electron beam, after some time, created new emission lines near 436 nm. Second-order correlation measurement proved the single-photon emission nature of these lines. A critical advantage of blue emitters in hBN is the fact that they seem to appear at a very narrow spectral range, within 2-3 nm spectral width around 436 nm. This is a unique property of these emitters,

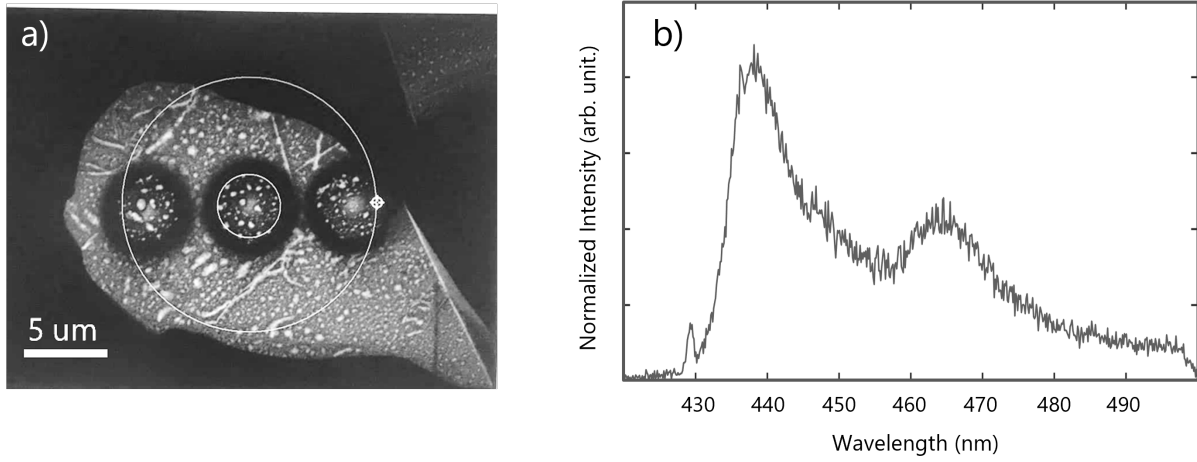


Figure 5.5: Electron beam engineering of blue emitters in hBN. a) Optical image of an irradiated hBN flake. The dark rings form around the center of irradiation and are only visible in SEM image. The SEM is centered on an irradiation spot. b) Representative PL spectra of one of the engineered emitters.

compared to other emitters in hBN, such as red emitters or WSe₂ emitters, which tend to appear at a wide-spectral range randomly. Theoretical studies are still underway to identify the microscopic nature of these emitters. We were also able to replicate these emitters at UCSB. Figure 5.5a demonstrates an irradiation array of electron beams on hBN. The electron beam dose was set at 10 nA with 30 keV accelerating voltage. Using a Nano Pattern Generation System (NPGS) on a modified SEM, we exposed 20 by 20 nm grids that are consistent of 3.14 nm linespaces (36 exposure points in the square) for dwell times between 0.1 s to 100 s. At roughly the threshold of 1s per exposure point, we could see a photoluminescence signal from blue emission lines centered at 436 nm at room temperature. The excitation was done using a 405 nm laser diode with excitation average power of 5 mW. Figure 5.5b demonstrates the representative spectra of these emitters measured in our group. We should note that while these emitters have the advantage that they appear at very narrow spectral ranges, and even though some degree of indistinguishability has been measured for them [32], the 436 nm energy is not an

ideal wavelength for quantum information processing as it is close to the absorption edge of silicon nitride. In the future, with further progress in quantum frequency conversion, these emitters might prove beneficial. However, due to this concern, we opted to focus on integrating red emitters in hBN with our silicon nitride cavities.

5.5 On-chip cavities for efficient on-chip coupling

In this section, we will discuss the rationale and motivation for using on-chip cavities to integrate quantum light sources into on-chip circuitry.

An isolated two-level system, once excited, decays back to the ground state through the spontaneous emission of a single photon. First, we revisit the physics of spontaneous emission for an isolated two-level system in a free-space vacuum. Fermi's golden rule can represent the rate of spontaneous emission for such a system [33]:

$$W = \frac{2\pi}{\hbar^2} |M_{12}|^2 g(\omega) \quad (5.1)$$

Here, M_{12} is the dipole transition matrix element between the two levels, and $g(\omega)$ is the photonic density of states. The photonic density of states of free-space modes can be represented as:

$$g(\omega) = \frac{\omega^2 V_0}{\pi^2 c^3} \quad (5.2)$$

Here, V_0 is a normalization factor that is used to normalize the number of available modes in an infinitesimal slice of momentum-space to the total volume. As seen shortly, this factor will be canceled out in derivation. The matrix overlap term for the interaction of the two-level field with the electric dipole of the vacuum field (E_v) can be written as:

$$M_{12} = \langle \rho \cdot E_v \rangle \quad (5.3)$$

where E_v can be calculated by normalizing the zero-point energy of the groundstate of the quantized electromagnetic field by its mode-volume, which can be defined as:

$$E_v = \sqrt{\left(\frac{\hbar\omega}{2\epsilon_0 V}\right)} \quad (5.4)$$

Calculating M_{12} and averaging over all configuration of the dipole with the three-dimensional space, we find:

$$M_{12} = \sqrt{\frac{\mu_{12}^2 \omega^3}{3\pi\epsilon_0 \hbar c^3}} \quad (5.5)$$

Finally, the rate (W) can be calculated found as

$$W = \frac{\mu_{12}^2 \omega^3}{3\pi\epsilon_0 \hbar c^3} \quad (5.6)$$

The critical observation here is that the mode-volume term that appeared in the free-space density of states term canceled out with the mode-volume in the transition-matrix term that was added to normalize the zero-point energy of the vacuum electric field. However, in the case of a single-mode cavity with small finite mode-volume V_0 , these terms will not cancel out.

Now, let's assume an isolated two-level system in a single-mode cavity with mode-volume (V_0). The emission rate can be estimated again using Fermi's Golden Rule. However, here, we must derive a new term for the photonic density of states.

By definition, if we assume our cavity has a single Lorentzian mode at an angular frequency of (ω_0) with a bandwidth of $\Delta\omega_0$. By definition of single-mode, the density of states must satisfy:

$$\int_0^\infty g(\omega) d\omega = 1 \quad (5.7)$$

Assuming the lorentzian shape of $g(\omega)$, then we can find:

$$g(\omega) = \frac{2}{\pi\Delta\omega_c} \frac{\Delta\omega_c^2}{4(\omega - \omega_0)^2 + \Delta\omega_c^2} \quad (5.8)$$

Assuming that the cavity is in resonance with the transition of the two-level system, we reduce this equation to:

$$g(\omega_0) = \frac{2}{\pi\Delta\omega_c} = \frac{2Q}{\pi\omega_0} \quad (5.9)$$

where Q is the quality factor of the cavity.

Similar to the free-space case, the transition matrix can be written as:

$$M_{12} = \frac{1}{3}\mu_{12}^2 E_v^2 \quad (5.10)$$

Where the factor $1/3$ is due to the normalization of the dipole in all three directions of space. Similar to before, E_v is represented as $\frac{\hbar\omega}{2\epsilon_0 V_0}$. Substituting the single-mode density of states and Fermi's golden rule, we arrive at the newly modified spontaneous emission rate for a two-level system emitting into a single-mode cavity.

$$W = \frac{2Qu_{12}^2}{\hbar\epsilon_0 V_0} \frac{1}{9} \frac{\Delta\omega_c^2}{4(\omega - \omega_0)^2 + \Delta\omega_c^2} \quad (5.11)$$

Comparing the rate of emission into cavity with the free-space emission rate, we arrive at the following ratio:

$$F = \frac{W_{cav}}{W_{free}} = \frac{3Q(\lambda/n)^3}{4\pi^2 V_0} \frac{\Delta\omega_c^2}{4(\omega - \omega_0)^2 + \Delta\omega_c^2} \quad (5.12)$$

Assuming resonance condition, F can be simplified as:

$$F = \frac{3Q(\lambda/n)^3}{4\pi^2V_0} \quad (5.13)$$

Factor F is the spontaneous emission enhancement factor, known as the "Purcell factor." For high-quality factor cavities with small-mode volume, large Purcell factors ($F \gg 1$) can be achieved, resulting in boosting the emission rate of the emitter well beyond its typical free-space emission rate. Looking back at the derivations, two main points should be emphasized. First, when deriving the density of states, given that the system is only allowed to interact with one photonic mode, the normalizing mode volume factor (V_0) is not relevant here. The density of the single mode is directly proportional to $\frac{dg(\omega)}{d\omega}$; hence, the higher the quality factor, the higher the density of states for the single mode. Note that since the mode volumes do not cancel out, the zero-point energy of the vacuum field carries the (V_0) factor into the Purcell term. This can intuitively understood as follows: for a single mode, the ground state of the quantized electromagnetic field, carries the finite zero-field energy (eigenvalue of the ground state of the harmonic oscillator). For a confined mode, the zero-field energy density is normalized by space. Hence, the higher the confinement, the higher the intensity of the zero-field energy density. Vacuum fluctuations (zero-field energy density) cause spontaneous emission in a free-space propagating mode and are normalized to all spaces. Once the mode is confined to a small mode volume of a cavity, the intensity of the vacuum fluctuations is increased, causing a boost in spontaneous emission.

While the two-level system inside the cavity has an enhanced emission rate into the cavity (W_{cav}), in most practical cavities, the system still can interact with a portion of free-space modes (leaky modes), depending on the design of the cavity. In the weak coupling limit, it could be assumed that the rate of emission to leaky modes remains unaffected and is equal to W_{free} , the free-space rate of emission before placing the system

in the cavity. Therefore, the total emission from the two-level system placed in the cavity in the presence of leaky modes can be approximated as

$$W_t = W_{free} + W_{cav} = W_{free} + FW_{free} = (1 + F)W_{free} \quad (5.14)$$

Finally, the total coupling efficiency (β), known as the beta factor, can be represented as:

$$\beta = \frac{W_{cav}}{W_t} = \frac{F}{F + 1} \quad (5.15)$$

As expected, given that the Purcell factor preferentially boosts the emission into cavity mode, in the presence of constant coupling to leaky modes, the coupling efficiency into the cavity is proportional to the Purcell factor. Evidently, near unity coupling efficiencies can be achieved for a significant Purcell factor. This is in stark contrast to the coupling efficiency of a linear dipole to a single-mode waveguide with TE fundamental mode. While it is still possible to achieve spontaneous emission boost through mode engineering, typically the coupling efficiency is inversely proportional to the effective mode area of the waveguide:

$$A_{eff} = \int \epsilon |E|^2 dS / |E(r_0)|^2, \quad (5.16)$$

which is a measure of the concentration of the mode's electric field over the cross-section of the waveguide. Evidently, to achieve near unity coupling, the effective mode should be minimized (high confinement) and centered exactly on the dipole. Given that confinement engineering of a single-mode waveguide would be limited by the refractive index of the waveguide layer and the cladding, it is very difficult to achieve theoretical coupling efficiencies above 70-80 %, even in the best-optimized platforms. However, with

the introduction of on-chip microcavities and leveraging the Purcell effect, a practical pathway can exist to achieve coupling efficiencies in excess of 99%, which is one of the main requirements of quantum photonic technologies.

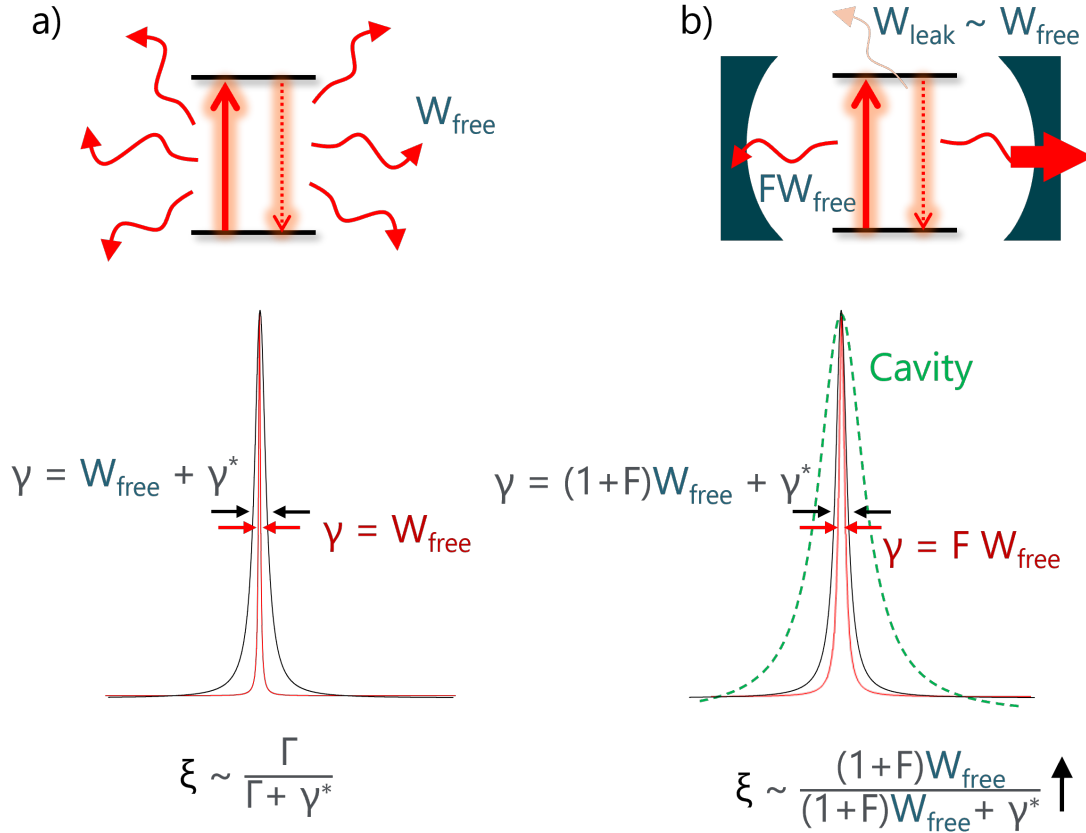


Figure 5.6: a) A two-level system with radiative rate of W_{free} and broadening (homogenous and inhomogenous) rate of γ^* will have an experimental linewidth larger than the intrinsic linewidth. b) A two-level system placed inside a cavity with Purcell Factor of F , will have total emission rate of $(1 + F)W_{\text{free}}$, the radiative linewidth is broadened while the broadening terms (γ^*) remain constant. Therefore, the experimental linewidth becomes closer to the intrinsic linewidth, demonstrating enhancement in the indistinguishability.

Furthermore, Purcell enhancement not only boosts coupling efficiency but also increases indistinguishability as seen in Figure 5.6. We will discuss indistinguishability in more detail in the next chapter by solving the Jaynes-Cummings Hamiltonian for a two-level system in a cavity. However, this can also be described in our current approach.

Indistinguishability, in the simplest terms, can be expressed as a lifetime limited degree of the linewidth of an emitter. An ideal emitter, due to Heisenberg's uncertainty, would have linewidth set by the spontaneous emission lifetime of the emitter defined as:

$$\Delta E = \hbar W_{free}/2 \quad (5.17)$$

However, the experimental decay rate of the phase can be increased by considering the non-radiative decay mechanism (W_{nrad}) and elastic-scattering mechanism causing pure dephasing (W_{deph}), yielding a total rate of

$$\Delta E = \hbar(W_{free} + W_{nrad} + W_{deph})/2 \quad (5.18)$$

Therefore, the ratio of the lifetime limited linewidth over the experimentally observed linewidth becomes:

$$\xi = \frac{W_{free}}{W_{free} + W_{nrad} + W_{deph}} \quad (5.19)$$

In the presence of Purcell enhancement, the rate of spontaneous emission is increased, while it can be generally assumed that the rate of dephasing and non-radiative terms will stay constant. Therefore,

$$\xi = \frac{W_{free} + W_{cav}}{W_{free} + W_{nrad} + W_{deph} + W_{cav}} = \frac{(1 + F)W_{free}}{(1 + F)W_{free} + W_{deph} + W_{nrad}} \quad (5.20)$$

Evidently, for high Purcell enhancement factors, indistinguishability can approach unity. In the next chapter, a more rigorous metric, the indistinguishability-efficiency ($\xi\eta$) byproduct, will be introduced and analyzed in-depth.

5.6 Low fluorescence 2D-compatible SiN development

As mentioned, standard stoichiometric Si_3N_4 has a strong background emission that overlaps with single-photon emission from multiple quantum defects in the 2D family [11, 34]. Figure. 5.7 presents photoluminescence spectra of a red single-photon emitter in plasma treated and thermally annealed hBN with 200 nm of PECVD low-stress nitride grown on top using a standard stoichiometric recipe. A 488 nm laser is used to excite the sample, and the excitation power is $200 \mu\text{W}$, below the saturation of the single-photon emitter. Almost 50 % of the integrated intensity at the zero-phonon lines stems from the background emission in the nitride.

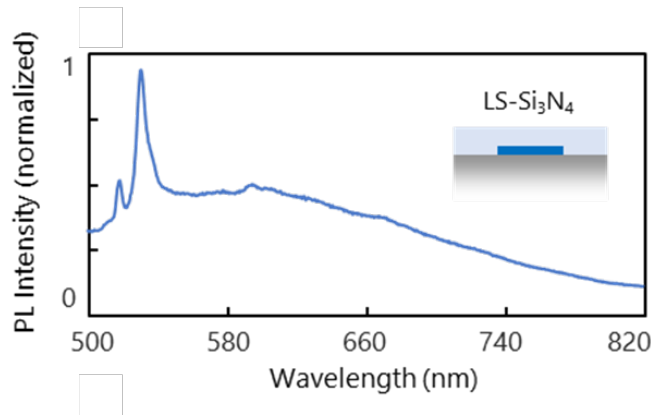


Figure 5.7: PL Spectra of visible hBN emitters under stoichiometric PECVD nitride.

The nature of this background emission has been previously attributed to Si-Si bonds. To circumvent this problem, we explored the growth of non-stoichiometric nitrogen-rich silicon nitride to minimize the Si-Si bonds. The PECVD silicon nitride growth relies on two main precursors of silane (SiH_4) and ammonia (NH_3) in the growth chamber in the presence of N_2 flow. For stoichiometric growth, the flow rates of silane, NH_3 , and N_2 are set to be 520 sccm, 18 sccm, and 980 sccm, respectively, yielding silane/ammonia ratio (R) of 29. All films were grown using a Vision 310 advanced vacuum PECVD system operating at $300 \text{ }^\circ\text{C}$ under 800 mTorr pressure. While maintaining the ammonia and

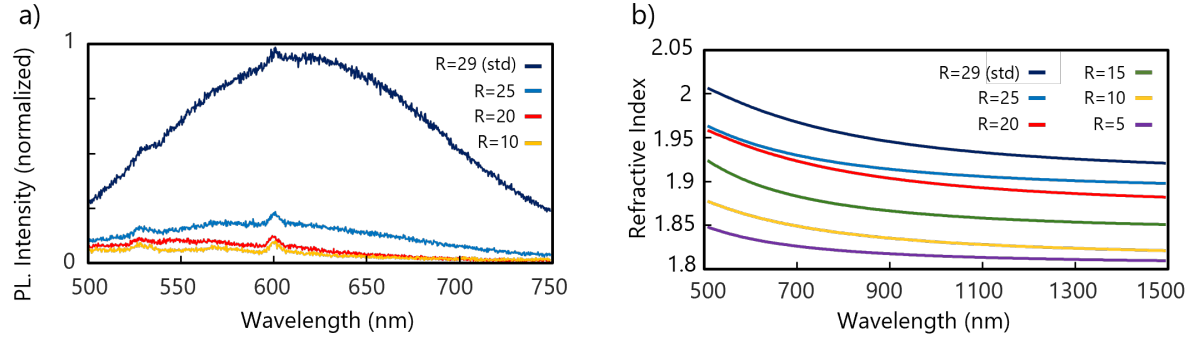


Figure 5.8: Non-stoichiometric SiN characterization. a) Background emission of silicon nitride as function of silane/ammonia ratio (R). At $R = 20$, the background emission is suppressed, enabling high-purity measurements of hBN quantum emitters. b) Refractive index of silicon nitride as function of R .

nitrogen flows, we reduced the silane flow from 520 sccm ($R=29$) to 90 sccm ($R=5$). During this growth, an iterative plasma of 30 W, 13.56 MHz for 8 seconds and 90 W, 187 kHz for 1.5 seconds was utilized. The plasma recipe did not detrimentally affect hBN films, and the SPEs had their spectral properties intact before and after growth.

Figure.5.8a displays the background emission of the SiN films grown with different silane/ammonia ratios. A clear quenching of the autofluorescence signal is observed at $R=25$. Figure.5.8b shows the measured refractive index of the SiN films in the visible range for different silane/ammonia ratios. With a decreasing R , the refractive index at 500 nm decreases from 2.01 (stoichiometric) to 1.86 ($R=5$). There is a cost-benefit analysis in quenching the background emission; we find that for $R=20$, a sufficient background level is achieved for the saturation power of hBN emitters only at the cost of slight reduction (2%) of the refractive index.

Furthermore, given that to achieve high-quality red emitters in hBN, a thermal annealing step is necessary, and the SiN needs to be able to sustain the rapid thermal annealing process while maintaining its low background emission. In previous studies, thermal annealing has been shown to lead to enhancing fluorescence signal even in nitrogen-rich films [11]. Here, by pre-conditioning the RTA chamber with nitrogen and

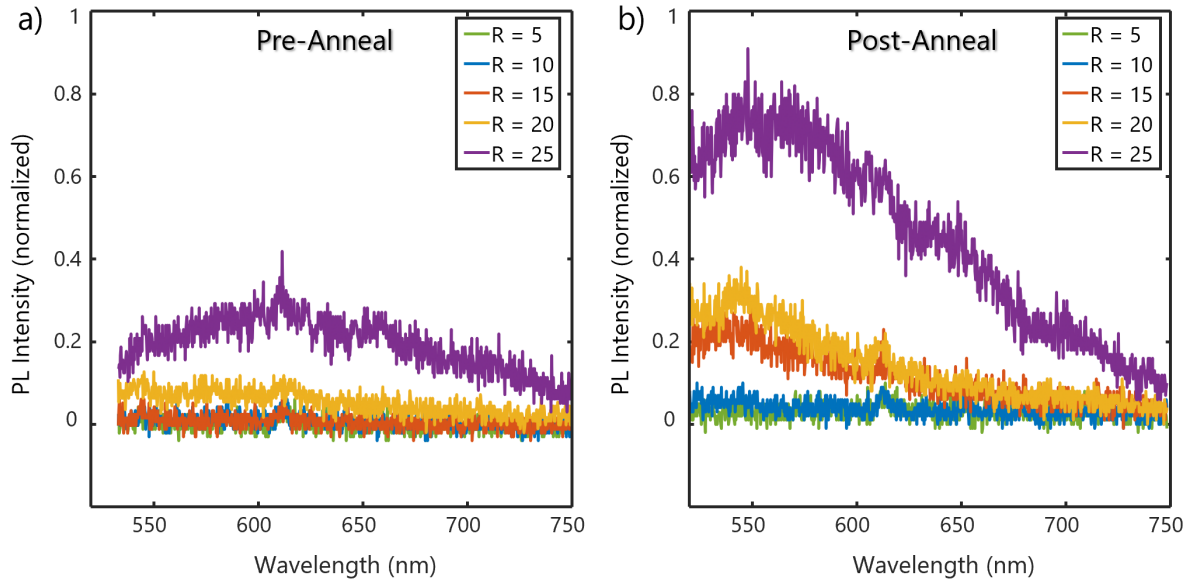


Figure 5.9: Non-stoichiometric SiN anneal at 1000 °C for 20 minutes . a) Background emission pre-anneal. b) Background emission post annealing.

oxygen at gas flow rates of 100 sccm and utilizing a 97 °C/minute ramp rate, we were able to minimize the background emission due to annealing up to 1000 °C temperature for 20 minutes. Figure 5.9 demonstrates the nitrogen-rich SiN photoluminescence emission pre and post-anneal. Interestingly, we observed that non-stoichiometric SiN films grown in nitrogen-rich conditions demonstrated less background emission activation after the annealing. For R ratios of < 15 , almost no background emission is observed even after annealing. Finally, Figure 5.10 demonstrates an hBN emitter before and after integration with our nitride where no observable background emission is present.

The ability to grow and anneal SiN thin films without background emission is a key challenge in developing an ideal photonic platform for the integration of 2D materials that was developed here.

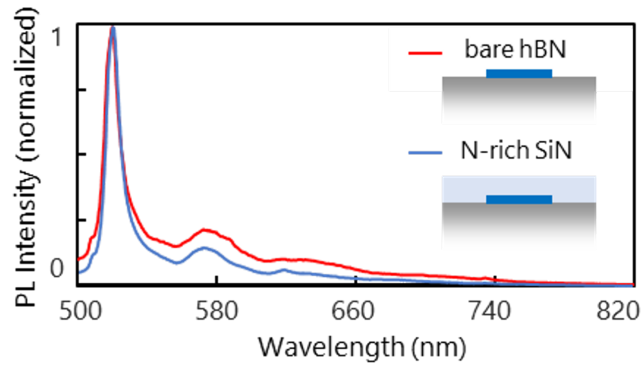


Figure 5.10: PL Spectra of visible hBN emitter before (red line) and after (blue line) integration with annealed non-stoichiometric nitrogen-rich nitride.

5.7 Microring Resonator Theory

In this section, we will discuss the design considerations for the integration of the 2D emitters with on-chip microring resonator cavities. Microring resonator is essentially a circular closed-loop waveguide that mimics Fabry-Perot-like cavities and can support standing wave optical modes, creating instructive interference and build-up of electric field in the cavity on supported modes and suppressing modes off-resonance through interference. Light can be coupled to or out of ring resonators by bringing another waveguide (bus waveguide) to the cavity and leveraging evanescent coupling. A bus waveguide and microring resonator create a notch filter whereby the ring-resonator allows coupling and build-up of specific wavelengths of light traveling through the bus waveguide that matches its resonance condition.

Figure 5.11 shows an illustrative sketch of a microring resonator and a bus waveguide. Assuming that light is traveling from left to right in the bus waveguide, the coupling region of the ring can be analyzed through coupled mode theory as follows. E_{o1} and E_{o2} denote the output field amplitude to the right of the coupling region in the bus waveguide and the ring resonator, respectively. Similarly, E_{i1} and E_{i2} denote the input

field amplitude to the left of the coupling region in the bus waveguide and the ring resonator. Assuming t represents the portion of the field amplitude of transmitted light through the bus-waveguide, and κ represents the portion of the field amplitude of the light coupled into the ring resonator, the following scattering matrix can be used to describe the coupled system. Note the κ and t must follow energy conservation such that $|\kappa^2| + |t|^2 = 1$.

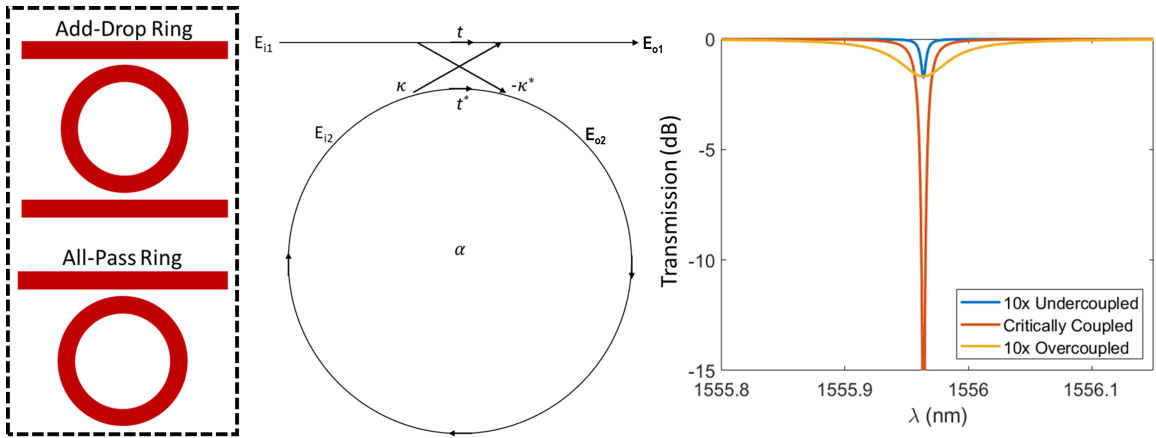


Figure 5.11: Schematic of an add-drop and all-pass ring resonator. The relevant coupling and transmission coefficients for an all-pass ring resonator are shown in the central panel. The different coupling regimes are illustrated in the simulated transmission spectra of an all-pass ring resonator that is 10x undercoupled, critically coupled, and 10x overcoupled.

$$\begin{bmatrix} E_{o1} \\ E_{o2} \end{bmatrix} = \begin{bmatrix} t & \kappa \\ -\kappa^* & t^* \end{bmatrix} \begin{bmatrix} E_{i1} \\ E_{i2} \end{bmatrix} \quad (5.21)$$

The gap and length of the coupling region can be controlled through the design and fabrication process and are the parameters that will set the coefficients t and κ . We will discuss briefly how ring-resonators can be designed with desired parameters using numerical simulations. Assuming that the circumference of the ring is $2\pi R$, and the normalized loss per length is α :

$$E_{i2} = e^{(-j\beta+\alpha)2\pi R} E_{o2} = E_{o2}\eta \quad (5.22)$$

where β is the propagation constant of the circulating mode ($2\pi n_{eff}/\lambda_0$), and we denote $e^{-\alpha 2\pi R}$ as η , the ring round-trip transmission factor.

Combining this equation with the second row of the matrix, we find:

$$E_{o2} = \frac{-\kappa^* E_{i1}}{1 - t^* \eta} \quad (5.23)$$

which can then be combined with the first equation in the matrix to find:

$$E_{o1} = tE_{i1} + \eta \frac{-\kappa^* E_{i1}}{1 - t^* \eta} = \frac{t - \eta(|t|^2 + |\kappa|^2)}{1 - t^* \eta} E_{i1} \quad (5.24)$$

For loss-less coupling, $t = \sqrt{1 - k}$, and the equation further is simplified to:

$$E_{o2} = \frac{t - |\eta|(\cos\phi + i\sin\phi)}{1 - t|\eta|(\cos\phi + i\sin\phi)} E_{i1} \quad (5.25)$$

where ϕ is the ring round-trip phase change ($-2\pi\beta L$). Finally, the transmitted power can be represented as:

$$|E_{o1}|^2 = \frac{t^2 - 2t|\eta|\cos\phi + |\eta|^2}{1 - 2t|\eta|\cos\phi + |\eta|^2 t^2} |E_{i1}|^2 \quad (5.26)$$

From this equation, it can be deduced that the resonance condition is met when the optical cavity length becomes an integer multiple of the wavelength of the light ($2\pi R = m\lambda_0 n_{eff}^{-1}$) resulting in $\cos\phi = 1$, and the equation becomes:

$$T = \frac{|E_{o1}|^2}{|E_{i1}|^2} = \frac{(t - |\eta|)^2}{(1 - t|\eta|)^2} \quad (5.27)$$

Three distinct scenarios are possible to describe the transmission behavior of the ring-

resonator and bus-waveguide system.

- For $t = |\eta|$, when the coupling coefficient is equal to round-trip loss in the ring, transmission equals $T = 0$. This causes full extinction of the light at the output due to destructive interference of the light incident on the ring and light out-coupling from the bus waveguide back into the ring resonator. As we can see, this causes the ring to have the maximum quality factor.
- For $t > |\eta|$, the system is said to be under-coupled. In this case, the extinction ratio is reduced, and only a portion of the light passing through the bus waveguide destructively interferes with the built-up field in the ring resonator. The quality factor of the ring is reduced depending on the difference between t and η .
- For $t < |\eta|$, the system is said to be over-coupled. Here, the portion of the light transmitted directly through the bus waveguide is less than the round-trip loss of the ring resonator. The built-up field in the cavity coupling into the output of the bus-waveguide partially interferes with incoming light power through the bus-waveguide. The quality factor and extinction ratio are less than the critical coupling conditions in this scenario as well.

The quality factor of the waveguide, defined as the ratio of the resonance angular frequency divided by the full-width half-maxima of the transmission dip ($\omega/\Delta\omega$), can be derived by finding the phases (ϕ_0) that result in $T=0.5$ from the equation 5.26. In this case, an analytical expression for Q can be defined as:

$$Q_{tot} = \frac{\omega_0}{\Delta\omega} = \frac{\pi n_g L \sqrt{t|\eta|}}{\lambda_{res}(1 - t|\eta|)} \quad (5.28)$$

where n_g is the group refractive index and λ_{res} is $2\pi c/\omega_0$,

A simpler expression for quality factor (Q_{tot}) can be found in regimes of low-loss or low-coupling. For the cases where $\sqrt{t|\eta|} \sim 1$:

$$Q_{tot}^{-1} = Q_i^{-1} + Q_c^{-1} = \frac{\gamma_0}{\omega_0 \tau_{rt}} + \frac{K}{\omega_0 \tau_{rt}} \quad (5.29)$$

where Q_i , Q_c , γ_0 , K , and τ_{rt} are intrinsic quality factor, coupling quality factor, intrinsic cavity loss per round trip ($2\pi R\alpha_p$), power coupling ratio ($|\kappa|^2$), and round-trip time ($2\pi Rv_g^{-1}$).

Another important metric of a ring resonator is the free spectral range, which describes the spacing between adjacent resonance wavelengths.

$$FSR = \frac{\lambda_0^2}{Ln_g} \quad (5.30)$$

where n_g is the group index.

5.8 Microring Resonator Design

In our application, the ring resonator is utilized differently than most photonic integrated circuit applications. Here, the microring resonator acts not as a filter but as a source. From the perspective of a source embedded in the ring resonator, the bus-waveguide resonator system acts as a bandpass filter. Suppose the zero-phonon line of the single-photon emitter is aligned with the resonance frequency of the microring resonator. In that case, spontaneous emission is enhanced by the Purcell effect, leading to efficient light funneling into the cavity mode, which then exits through the bus waveguide. Therefore, a critical criterion is to design the microring-resonator waveguide system in the over-coupled regime, where the single-photon light can be coupled out of the resonator efficiently and not be lost due to the intrinsic loss of the resonator.

The ratio of the light coupled into the ring that can then evanescently couple to the bus-waveguide can be expressed as $\eta_{out} = Q_{tot}/Q_c$. In an under-coupled regime, $Q_i < Q_c$ and $Q_{tot} \sim Q_i$; therefore, outcoupling efficiency would be less than unity. In the overcoupled regime, total quality would be dominated by Q_c as $Q_i > Q_c$ and outcoupling efficiency approaches unity. Note that η_{out} can always be maximized by arbitrarily reducing Q_c . However, the Purcell factor is linearly dependent on the quality factor and, therefore, not the best strategy. The best strategy is to have a microring resonator with the highest possible Q_c while maintaining an over-coupled regime. This requires that the intrinsic quality factor of the microring be consistently higher than the designed coupling quality factor to ensure the over-coupled operation. Finally, we note that two practical limits exist for higher bounds of the total quality factor. First, suppose the total quality factor exceeds the emitter's intrinsic quality factor. In that case, the system enters the so-called "bad-emitter" regime where only a portion of the linewidth of the emitter can spectrally couple to the cavity mode, reducing overall coupling efficiency. Another practical limit for high-quality factors is the possibility of the emitter-cavity system transitioning from a weak coupling regime to a strong coupling regime, which can result in a reduction of overall coupling efficiency. These two points will be discussed in more depth in the next chapter. Finally, the Purcell factor is inversely proportional to the mode volume of the cavity; therefore, minimum mode volume is desired. However, to achieve a ring resonator with a small mode volume, small bending radius is required, which can lead to a decrease in the intrinsic quality factor due to bending losses. Given that many processes can contribute to and dominate the intrinsic quality factor (Q_i) of the ring resonators, such as material absorption, surface-scattering, side-wall roughness scattering, and grain-boundary scattering, it is ideal to reduce the bend radius until Q_i begins to monotonically decrease.

To summarize, in designing a microring resonator to achieve the best overall coupling

efficiency ($\beta\eta$), the following design rules must be followed:

- The cavity must operate in over-coupled regime ($Q_{tot} \sim Q_c$)
- The cavity must have a high-quality factor to achieve a high Purcell factor. To achieve this, the intrinsic quality factor of the cavity (Q_i) must be as high as possible. However, the total quality factor should not be too high, which causes the system to enter a bad-emitter or strong coupling regime.
- The mode volume of the cavity must be as small as possible. This is achieved by finding the minimum possible bend-radius at which a desired Q_i is possible.

5.9 Photonic Component Simulations

First, we start by designing single-mode TE waveguides at a wavelength of 600 nm. It is critical for the waveguides to be single-mode as many on-chip quantum photonic technologies that rely on the interference of photons require well-defined spatiotemporal modes for the photons. Furthermore, for Purcell enhancement, as discussed previously, it is beneficial to minimize the photonic density of states by having a well-defined unique mode. Using the refractive index information measured for non-stoichiometric N-rich SiN, we performed numerical Finite Difference Eigenmode (FDE) simulations in Ansys Lumerical. SiN waveguides were defined inside SiO₂ cladding (3 μm buried oxide (box) on both top and bottom). The waveguide height was fixed at 100 nm, and the width of the waveguide was swept from 500 nm to 900 nm. Figure 5.12a demonstrates the effective index of available modes at each simulation frequency. Modes with an effective index below the cladding cannot propagate through the waveguide. The bottom of the Y-axis is set at the effective index of the cladding. It can be seen that for wavelengths below 630 nm, the waveguide can only support a single TE mode. Hence, the waveguide dimensions

were set for 100 nm height and 600 nm width for our simulations. Figure 5.12b shows the cross-section of the fundamental TE mode for the designed waveguides at a wavelength of 600 nm. Note that a single TM mode also exists in this wavelength, however, since it has a polarization vector perpendicular to the emitter, emitter cannot couple to this mode efficiently. From the emitter's perspective, this waveguide will function as a single-mode.

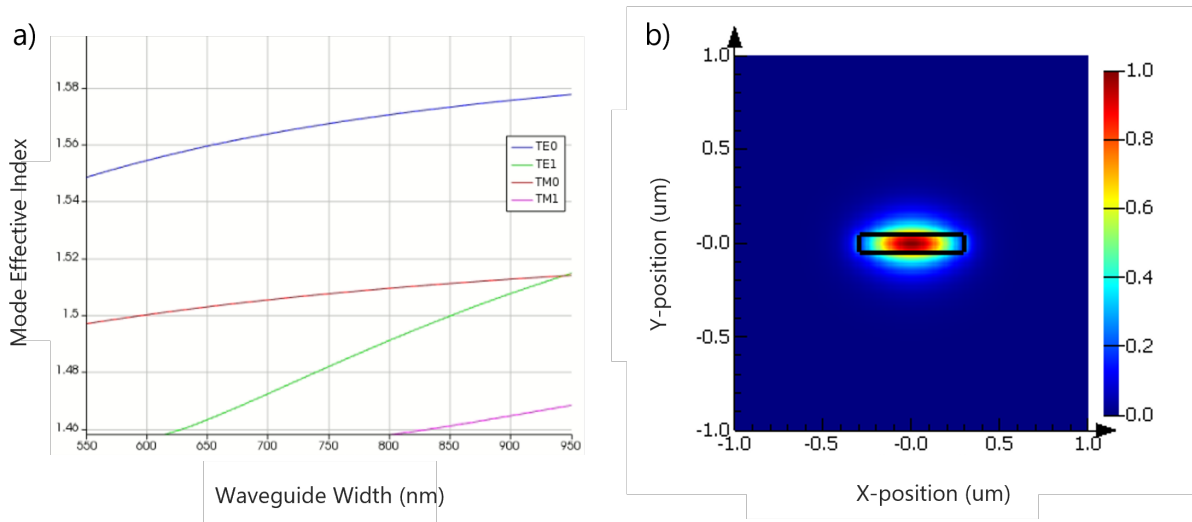


Figure 5.12: a) Mode effective index as function of width of the waveguide. Waveguide height is set at 100 nm. The bottom of Y-axis is set at SiO₂ refractive index. It can be seen that for waveguide width below 620 nm only the fundamental modes can propagate. b) Cross-sectional mode intensity profile of the fundamental TE mode for a waveguide with 600 nm width and 100 nm thickness

Next, the loss versus bend radius was calculated for the waveguide. As discussed in the previous section, estimating the bend loss is essential, given that it can set a limit on achievable intrinsic losses (Q_i) for the ring-resonator. Figure. 5.13 displays waveguide loss versus bend-radius calculated in Lumerical FDE simulations. Data was extrapolated using a quadratic function down to 10 μm . At around 15 μm bend radius, the loss becomes substantial with bend loss exceeding 1 dB/m. Hence, we limited the maximum bend radius to 30 μm with a predicted loss of 0.215 dB/m, considering that contributions from side-wall roughness scattering can also further degrade the intrinsic quality factor.

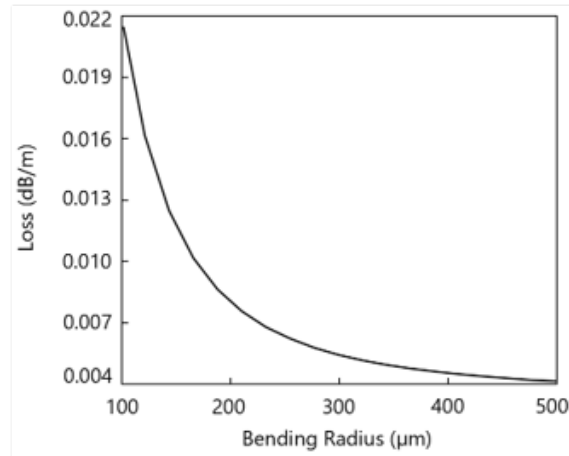


Figure 5.13: Calculated bend loss of the waveguide.

For the ring geometry, we decided to use a race-track design. In the race-track design, the coupling region is similar to a directional coupler, simplifying simulations for coupling coefficient and providing more control over the extent of bus-waveguide and ring-resonator coupling compared to pulley or point coupling approaches. As we discuss further in the following sections, to determine whether fabricated rings operate in over-coupled or under-coupled regimes, it is critical to fabricate identical devices but with sweeps in their coupling strength. In a race-track design, this could be simply achieved by extending the length of the coupling region where the two waveguides run parallel.

Figure.5.14 demonstrates the final design for the race-track microring resonator with a coupling length of $3 \mu\text{m}$. Our directional coupler simulations predict that the coupling length should provide about $\kappa^2 = 0.2$ coupling coefficient and coupling quality factors of about 10,000. Whether we achieve the same total quality factor in the experiments would depend on the intrinsic quality factor of the integrated system, which will be discussed in the result section of this chapter.

Finally, to extract light from the bus waveguide, we decided to pursue edge coupling rather than coupling using grating couplers. Given the randomness in the spectral distri-

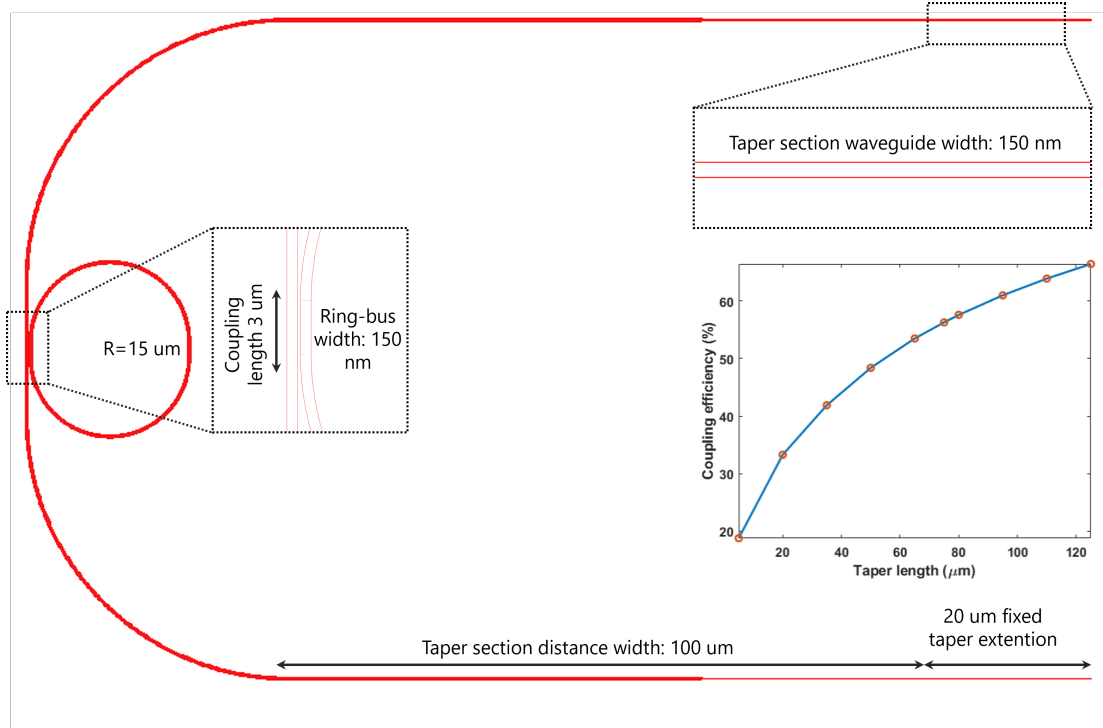


Figure 5.14: Final design of the ring resonator, bus-waveguide, and the edge taper. Waveguide width is set at 600 nm , coupling distance between waveguide and ring is $3 \mu\text{m}$ in this design. Distance between ring and the waveguide is fixed at 150 nm and only the coupling length is varied to tune the coupling coefficient of the system. Taper is $120 \mu\text{m}$ wide considering both the taper region and the fixed extension which was added to allow for error in dicing step. Width of the taper is 150 nm (Note that the value of 150 nm was chosen so that experimentally the taper width achieved 110 nm width. The optimized electron beam dose that yields the correct 150 nm gap for the waveguide and ring cross-section underexposes the tapered region and slightly wider taper was implemented in the design to achieve the design value.)

bution of red single photon emitters in hBN, grating couplers with their small bandwidth could severely limit the observable wavelength in the experiments. To efficiently couple light from the bus waveguide over a wide energy range, we used inverse taper as a spot-size converter to expand the waveguide mode into the cladding to reduce the effective index and to match the mode better with that of the fibers. The coupling efficiency of the fundamental TE mode to a fiber as a function of the taper length with a mode field diameter of $4.5 \mu\text{m}$ calculated using Lumerical FDTD is shown in the inset of Figure

5.14. Edge tapers are fabricated to be $120\ \mu\text{m}$ long with an end cross-section of $110\ \text{nm}$ width to ensure adiabatic mode transition with as little loss as possible, resulting in a simulated coupling efficiency of 66% at the SQE emission wavelength.

5.10 Integration Strategies

With the design of the ring-resonator and bus waveguides finalized, we now turn our attention to the integration strategies of the ring-resonator with respect to the single-photon emitter. As discussed previously, the single-photon emitter needs to achieve sufficient mode overlap with the waveguide to achieve efficient coupling. From a practical perspective, the emitter can be placed either on top, in the center, or at the bottom of the waveguide. Figure 5.15 displays all three configurations. We used numerical Finite Difference Time Domain (FDTD) simulations to calculate coupling efficiency in all three configurations. A linear dipole mode source with fixed power was placed at three different locations of the waveguide and was allowed to propagate through the device. A power monitor was placed $20\ \mu\text{m}$ away from the waveguide to measure the amount of uni-directional coupled power into the single mode of the waveguide. The distance from the power monitor to the mode source was swept to ensure the measured power demonstrated saturating behavior, eliminating the contribution from scattered light. Figure 5.15 demonstrates the coupling coefficient for three different types of emitters: hBN red emitters at 560-630 nm, WSe_2 emitters from 750-850 nm, and MoTe_2 emitters from 1350-1450 nm. As expected, the highest coupling coefficient can be achieved when the emitter is embedded in the center of the waveguide where the mode concentration is highest. However, as we discuss shortly in the fabrication section, placing the quantum emitter deterministically either at the top or center of the waveguide would require the 2D film to be etched away at the same process step where the ring-resonator is etched out of

the SiN. We found that experimentally, exposing the edges of hBN 300 nm away from the quantum defect causes the single-photon emitter to quench completely. We attribute this to the possibility of Fermi-level pinning at the edge of the hBN, which can cause the Fermi-level to be pinned to an energy level set by the charge-neutrality point of hBN's edge interface. Given that hBN in our experiment is an undoped wide bandgap semiconductor, 300 nm cannot sufficiently screen the potential at the edge from the quantum defect. Therefore, the Fermi level at the position of the defect is most likely very close to the Fermi level at the edge. Given that the quantum defect charge state can change based on the position of the Fermi-level, it is most likely that the defect undergoes a charge state transition that puts it in a dark state when hBN edges are exposed.

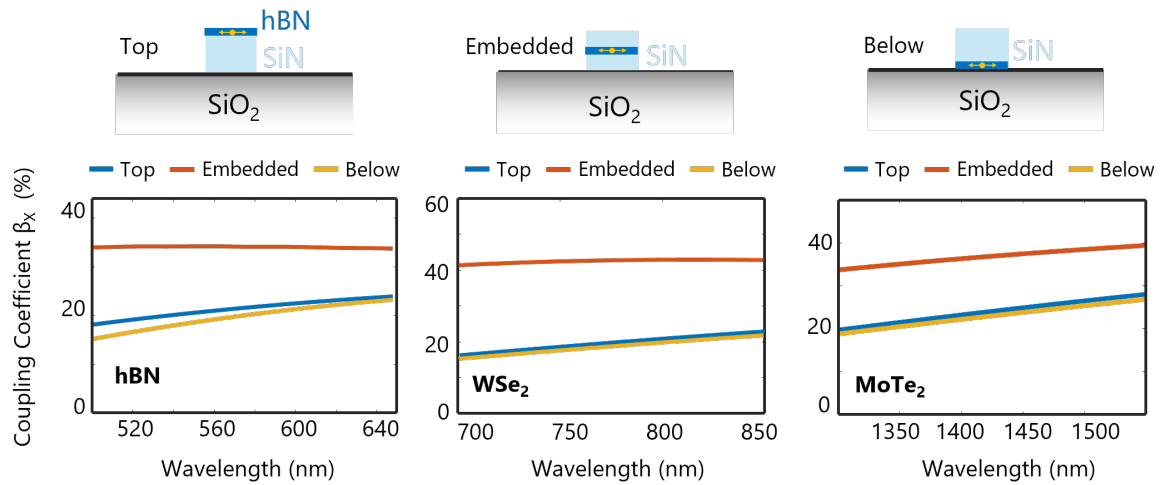


Figure 5.15: Simulated waveguide-emitter coupling efficiency (β) for 2D quantum emitters on top, within, or below the straight waveguide. A maximum of up to 40% coupling efficiency (summed over both waveguide propagation directions) is possible for each type of emitter.

Therefore, from practical experimental limits, we decided to embed the 2D films right below the surface of the waveguide. In the etch step, we can ensure that hBN edges are not exposed by under-etching the SiN by 3-5 nm. Although this configuration is not ideal, however, the Purcell enhancement from the cavity can boost the spontaneous emission

and compensate for the non-ideal coupling, albeit at the expense of a higher required quality factor. One of the main criteria that also contributed to choosing the waveguide height of 100 nm was that it allowed the mode to overlap more significantly with the bottom planes of the waveguide, achieving higher coupling rates.

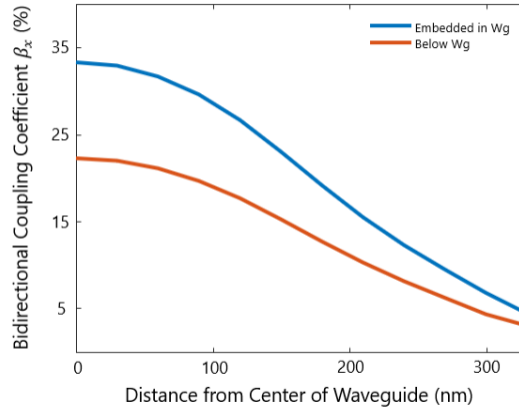


Figure 5.16: Emitter-waveguide coupling efficiency as a function of emitter misalignment from the center of the waveguide

Finally, the accuracy in the horizontal placement of the emitter in the waveguide is also critical. Figure. 5.16 shows the coupling coefficient as a function of horizontal displacement of the dipole mode from the center of the waveguide for both dipole embedded and dipole under the waveguide configurations. It can be seen that 150 nm and 200 nm misalignment can reduce the coupling coefficient in both configurations by almost 30 % and 50 %. Therefore, achieving sub-100 nm deterministic alignment accuracy is also critical to achieve efficient coupling. Here, we again emphasize that the Purcell effect can compensate for possible misalignment. However, this would also increase the required quality factors to achieve efficient integration. Utilizing a method that can embed the single-photon emitter at the center of a waveguide with high-mode concentration at the center and perfect alignment would reduce the burden on required quality factors to

achieve efficient integration,

5.11 Fabrication Process Flow

In this section, we will discuss the full fabrication process flow of our devices. The fabrication process for integrating 2D quantum emitters within SiN photonic structures is illustrated in Figure 5.17. Note that these process steps are for integrating emitters under the waveguide, as outlined in the previous section.

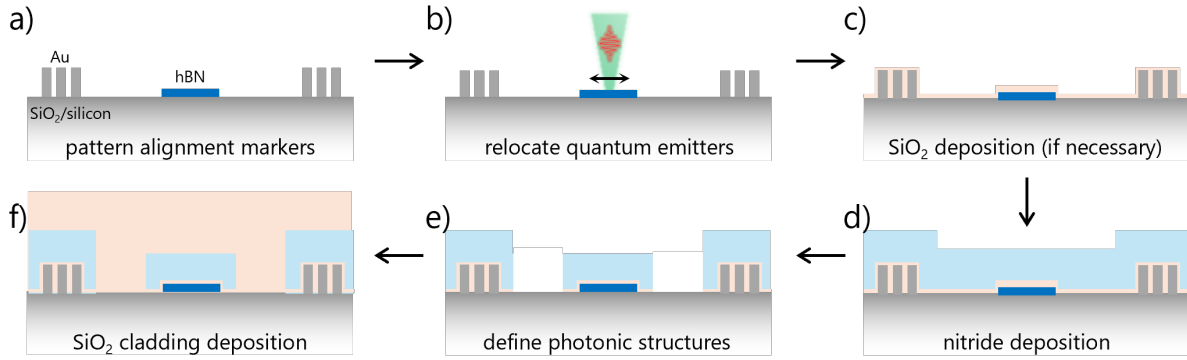


Figure 5.17: Photonic integration fabrication process flow. a) To position the flake with respect to the photonic structure, thin hBN flakes are exfoliated on PECVD SiN films with optional thickness (t_{opt}) that is either equal to full or one-half of the designed thickness of the waveguide for top or embedded flakes, respectively. Alternatively, to position the flake on bottom of the waveguide, hBN can be exfoliated directly on the SiO₂ substrate. Gold alignment markers are patterned with electron-beam lithography in close proximity to the flake. b) The position and dipole orientation of quantum emitters are determined by high numerical-aperture polarization-resolved microscopy and raster scanning the sample. c) Thin-film PECVD SiO₂ for protecting TMD flakes from damage during SiN PECVD. d) Deposition of remaining SiN, if necessary, to complete the photonic layer. e) Electron-beam lithography and ICP-RIE etching are used to define the photonic circuits. f) Final PECVD SiO₂ for the cladding layer.

First, using an all-dry visco-elastic transfer technique, 2D material flakes of hBN are transferred on top of 3- μm SiO₂/Si substrates and cleaned with a standard solvent clean recipe. Next, hBN is treated with a plasma step of 5-minute, 250 W in O₂ plasma (330 sccm), followed by a rapid thermal annealing step of 1000 °C in forming gas. Next, hBN

emitters with 5-15 nm thicknesses are identified using optical microscopy contrast. The size of the flakes needs to be less than the ring-bend radius so the flake does not interfere with another part of the cavity once it is integrated. Next, the candidate flakes are loaded in a custom-built room-temperature PL setup and are screened for single-photon emitters using a 532 nm laser and a 0.9 numerical aperture (NA) objective. Once flakes with suitable emitters in terms of brightness, linewidth, and purity are identified, a fine alignment mark array has to be fabricated close to the flake to align the ring resonator to the quantum emitters.

This is done using a conventional metal lift-off technique using PMMA photoresist. A layer of 80 nm PMMA is spun on the sample and baked for the 90s at 180 °C. Next, a tiny scratch mark was created next to the flake in the PMMA resist using an optical microscope and an electrical probe holder with a translational stage. This scratch mark serves as a rough alignment mark for us to fabricate the alignment mark array near the flake. Next, using electron beam lithography (Nabity NPGS SEM), the fine alignment mark structure (250 nm rectangle with 500 nm linespace) was exposed with a 30 keV electron beam and dosage of 10 pA. The sample was developed in IPA/water mixture with a 3:1 ratio for 22 seconds, followed by Ti/Au (5 nm / 15nm) e-beam metal deposition at 10^{-7} torrs. The lift-off was achieved by leaving the sample overnight in acetone, as seen in Figure 5.17a.

Next, the sample was returned to the lab, and the emitter was re-identified in the PL setup. Utilizing an open-loop piezoelectric stage (Thorlabs NanoMax MAX312D), the quantum emitter is centered under an excitation laser spot. This procedure can be done either manually or using an automated code. First, the stage is scanned in the x-axis and y-axis iteratively to find the maximum intensity of the emitter. After locating the maximum intensity point in the xy plane, the z-axis is adjusted to minimize the spot size based on the emitter's intensity. This process can be iteratively done until the emitter

attains maximum intensity at a given power below its saturation. Next, using a blue light imaging microscope, the sample is illuminated within the same setup, and the laser intensity is lowered to a point where it is barely observable. At this point, an optical image is taken using a standard CMOS camera while ensuring that the alignment marks and laser spot are in the camera's Field of View (FOV) ($70\ \mu\text{m}$ by $70\ \mu\text{m}$). Figure 5.18a demonstrates an example of such an image. Finally, 100 nm of N-rich non-stoichiometric silicon nitride is deposited on the chip with the recipe specified in the previous section as seen in Figure 5.17b.

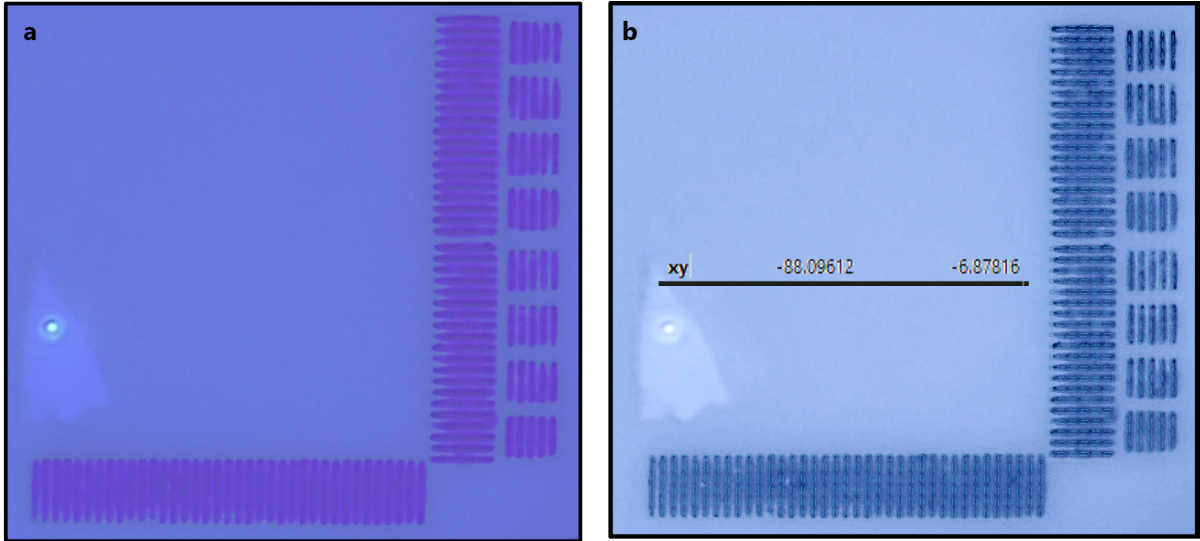


Figure 5.18: Optical images of the alignment process. a) Optical image during the re-identification process. The green laser spot denotes the SQE location. Note that the laser is attenuated using an additional notch filter, while the blue-light imaging is achieved by passing a white light source through a dichroic mirror. The camera is centered on the flake with the alignment marks in the field of view of the image. b) Processed image with corrections. The reference pattern of the alignment marks (dashed orange lines) is now overlaid with the alignment bars. The location of the defect with respect to the center of the first pattern is read and displayed on the image.

The optical images are then processed in Matlab using an edge detection code based on the "canny edge detection" technique. First, the edges of the fine-alignment bars are detected. Then, the image scale undergoes a matrix transformation until the mean

square error of the difference between the actual and the optically detected patterns is minimized. Afterward, the corrected image is overlaid with the pattern in K-Layout software, and the location of the center of the laser spot with respect to the center of the pattern is determined (Figure 5.18b). The pattern of the ring-resonator is then aligned to the image based on the measured emission dipole of the defect. The initial spacing of the fine-alignment metal bars was designed so that at least $2 \mu\text{m}$ spacing would exist between the alignment marks and the microring, ensuring no waveguide propagation loss due to the metal.

The key step in our dual-step alignment process is using both X and Y alignment bar arrays that are visible to the FOV of the microscope. This allows for a sufficient amount of identified edges along both the X- and Y-axis that can be used to correct for barrel distortions in the image.

To define the waveguide structure, a 200 nm layer of HSQ was spun on the sample and was baked for 4 minutes at 80°C . Using electron-beam lithography (Nabity NPGS SEM, 30 keV electron beam, 10 pA beam current), the HSQ was exposed with the base dosage of $600 \frac{\mu\text{C}}{\text{cm}^2}$. The sample was then developed in 25% TMAH for 33 seconds. Note that the second mask is aligned with respect to the identified position of the emitter so that the emitter is at the center of the microring resonator in a position with correct dipole orientation. Next, an inductively coupled plasma tool was utilized to define the photonic structures using a typical nitride etch recipe of CHF_3/O_2 (40/10 sccm) with RF source bias of 50 V.

Finally, a $1 \mu\text{m}$ PECVD SiO_2 layer was grown on top of the final sample to serve as a cladding layer and shield the structures from the environment. The sample is then diced at the waveguide taper region to provide optical access to enable edge coupling.

Figure.5.19 demonstrates the full fabrication flow for the emitter presented in the section. Figure 5.19a represents the re-identification process of the emitter, Figure 5.19b

shows the alignment of the emitter with respect to the ring-resonator. Note that the the emission dipole of the resonator is measured as seen in Figure 5.19e. Image of the final device, after growth of nitride, e-beam lithography, and ICP-etch step is shown in Figure 5.19c that demonstrates near perfect alignment of the emitter. Furthermore, the PL spectra of the emitter before and after all the fabrication steps remain unperturbed as seen in Figure 5.19d and the emitter still shows clear antibunching behaviour as seen in the result of the second-order correlation measurements (Figure 5.19d).

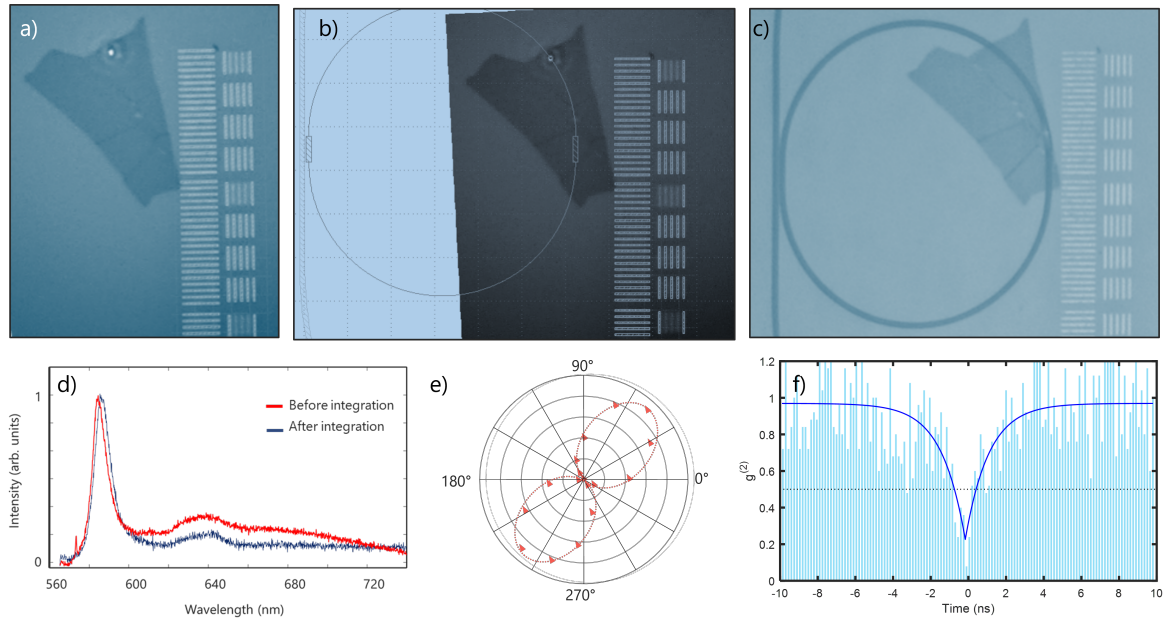


Figure 5.19: Alignment process. a) Optical image of a sample after fine-alignment mark array deposition. b) Alignment of the corrected optical image and the layout of the resonator. c) Final fabricated device. d) PL Spectra of the emitter before and after integration. e) Measured emission dipole of the emitter. f) Second-order auto-correlation function of the emitter after all the fabrication steps.

5.12 Experimental Setup Overview

Figure.5.20 is a schematic illustration of the optical setup used in the experiments. The main laser source is a continuous-wave 532 nm green laser diode. A dichroic mirror

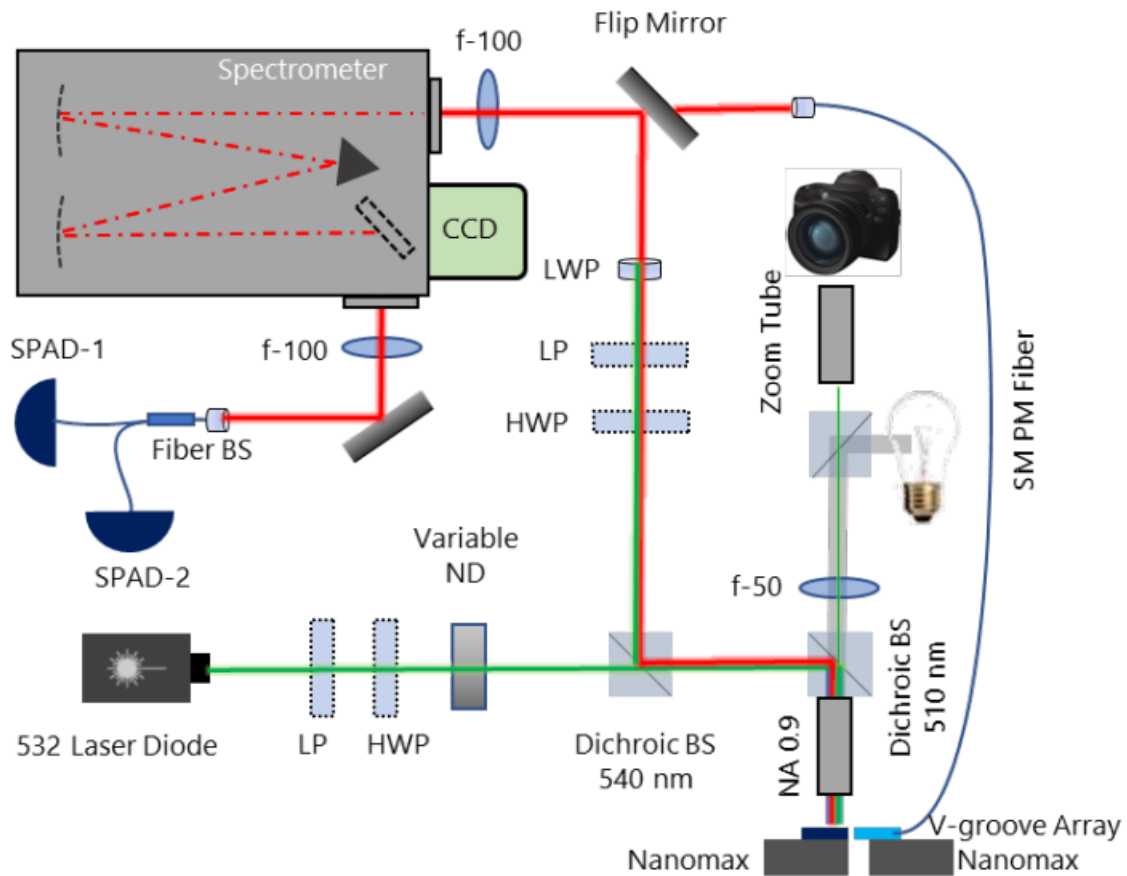


Figure 5.20: Optical Setup Schematic

at 540 nm is used to separate excitation and collection paths. In addition, a 600 nm long-pass spectral filter was used further to extinguish the excitation laser in the collection path. A second dichroic mirror at 510 nm separates the camera and white light path from the excitation/collection path. Using a second dichroic not only doubles the signal collection efficiency from the sample, but it is also necessary to minimize the chromatic aberrations in the optical images used for the alignment process in this study. An infinity-corrected 0.9 NA dry objective with a 1 mm working distance is used for spectroscopy. A low profile (1.4 mm total height) customized v-groove array (4x PM460-HP OZ Optics) is used for the edge coupling. The low-profile v-groove fiber array enables

us to collect light from the edge while simultaneously exciting the SQE with the 0.9 NA objective. A superluminescent diode (Thorlabs SLD635T) was coupled on and off the chip using a two-channel single-mode v-groove PM460-HP fiber array to characterize the microring resonator transmission spectrum. Second-order autocorrelation measurements with continuous-wave excitation were performed by passing the collected emission through the side-slit of the spectrometer (Princeton instruments HRS-500) using a 300 groove/mm grating set at the center ZPL wavelength. The filtered light was sent into a multimode fiber beamsplitter and fed into two single-photon avalanche detectors (Excelitas SPCM-AQRH-13-FC) through two optical circulators to minimize optical cross-talk between the detectors. The electrical signals from detectors (350 ps timing resolution) were analyzed using a Swabian Time Tagger Ultra photon counting module (8 ps timing resolution).

5.13 Microring Resonator Characterization

First, microring resonators without embedded single-photon emitters were characterized to assess the total quality factor, cavity regime (over-coupled or under-coupled), and intrinsic quality factors. Typically, microring resonators are characterized by transmission measurements, which sweep the input frequency of the laser and measure the transmitted power. In these measurements, the quality factors of the cavity can be measured with a resolution as low as the linewidth of the laser. Unfortunately, given that we did not have a tunable laser at the energy range of interest, we relied on an alternative method to characterize the cavities. Here, we used a broad-band superluminescent diode (SLED, 638 nm center wavelength, 5 nm FWHM) to characterize the transmission spectrum of the microresonators. The SLED emission is first coupled into a single-mode v-groove fiber array (4-PM-460HP with 127 μ m spacing) and then launched into the ex-

posed facets of the tapered waveguides. The second part of the waveguide is then used to read out the response of the photonic chip and send it to the spectrometer. Figure 5.21a shows an optical image of the device under test.

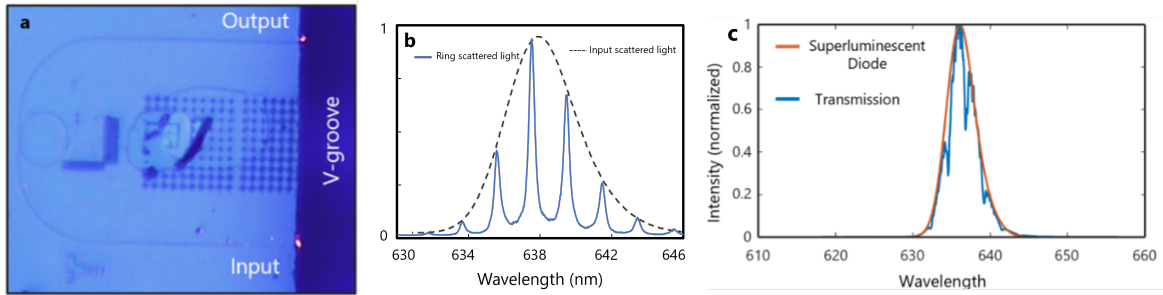


Figure 5.21: Microring resonator characterization. a) Optical image of a device under test. The input port is used to launch a broadband superluminescent diode into the waveguide. Light is collected from the output port. b) Dashed black line is the scattered light from the waveguide when objective is centered on the input waveguide. The dashed black line represents the SLED spectrum. The blue line represents scattered light from the ring-resonator. c) The transmission spectrum of the superluminescent diode collected from the top waveguide is indicated by the blue curve, and the raw spectrum of the superluminescent diode is shown by the orange curve for reference. Dips in the transmission correspond to the resonances of the microresonator. The normalized microresonator transmission and reference spectra are fit using the presented theoretical model to determine the microresonator response.

The edge-coupling experiment was conducted using the same PL confocal microscopy setup. In order to measure the spectrum of the SLED, the PL objective was centered on the input port of the waveguide. The scattered light from the waveguide was collected by the setup and was sent to the spectrometer. Similarly, if the objective is centered on the ring resonator, the built-up light in the ring is scattered into the collection path and can be imaged by the spectrometer. Finally, if the objective is centered on the bus waveguide's output port, the microring resonator's transmission spectrum can be imaged. Figure 5.21 displays the results of all the three scenarios. The quality factor of the ring can be characterized in two ways. Either the built-up field in the ring can be measured with the Lorentzian function to measure their FWHM, or it can be calculated by fitting

the dips in the transmission spectrum of the SPED. We note that the transmission spectrum can also be measured by introducing the light collected from the output port of the waveguide back into the collection path.

To find the normalized transmission spectra, the measured transmission spectra can be normalized by the spectrum of the SLED. As discussed in the previous section, the extinction ratio and the quality factor of the resonances can be derived based on the transmission coefficient (t) and the roundtrip-loss coefficient (η) as follows:

$$T = \frac{|E_{o1}|^2}{|E_{i1}|^2} = \frac{(t - |\eta|)^2}{(1 - t|\eta|)^2} \quad (5.31)$$

$$Q_{tot} = \frac{\omega_0}{\Delta\omega} = \frac{\pi n_g L \sqrt{t|\eta|}}{\lambda_{res}(1 - t|\eta|)} \quad (5.32)$$

By deriving t and η , the intrinsic quality factor and coupling quality factor can then be calculated using:

$$Q_i^{-1} = \frac{\gamma_0}{\omega_0 \tau_{rt}} \quad (5.33)$$

$$Q_c^{-1} = \frac{K}{\omega_0 \tau_{rt}} \quad (5.34)$$

However, note that equation 5.31 has two distinct solutions depending on whether $t > |\eta|$ (under-coupled condition) or $t < |\eta|$ (over-coupled condition). This yields two sets of different Q_c and Q_i depending on the over/under-coupled condition for which the system is solved. Hence, first, it is imperative to establish whether the system is under or over-coupled.

We fit the data of over twenty samples in three fabrication runs to establish a baseline for our microresonators. From our Lumerical simulations, for our designed race-track lengths of 3 μm , a κ^2 value of 0.18 is extracted at the 635 nm wavelength. Figure

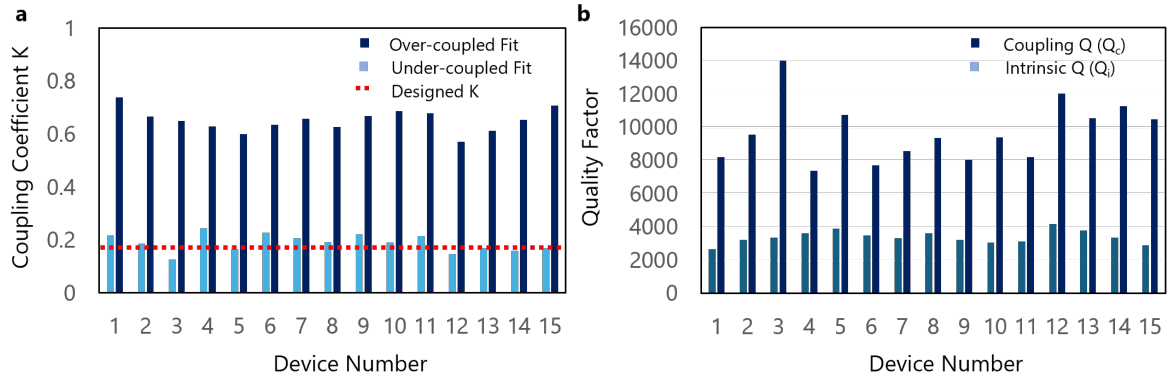


Figure 5.22: Fit to the theoretical model. a) Coupling coefficient (K) extracted from fitting the normalized transmission plots with under-coupled and over-coupled assumptions of the theoretical model. The undercoupled fit closely matches the designed coupling coefficient extracted from the Lumerical simulations. b) Extracted coupling and intrinsic quality factors with the under-coupled assumption. The coupling quality factor average is $Q_c = 9690$ with a standard deviation of 1834. The intrinsic quality factor average is $Q_i = 3560$ with standard deviation of 393.

5.22a presents the average extracted κ^2 values for our rings under over-coupled and under-coupled conditions. The under-coupled condition closely matches the Lumerical simulations, supporting our assessment that all fabricated devices are operating in the under-coupled regime. Figure 5.22b represents the extracted Q_c and Q_i of over ten measured devices for the microring with three μm coupling region length, which is the same configuration for which we fabricated the integrated devices. The rings' average total quality factor Q_t was measured at 2200, coupling quality factor Q_c was averaged at 9700, and the average intrinsic quality factor Q_i was 3560. While the coupling quality factor was about the expected range, the intrinsic quality factor was lower than our expectation. Scanning Electron Microscopy (SEM) imaging reveals substantial sidewall roughness presence at the edges of the waveguide. The increased roughness is potential because the ICP CHF_3/O_2 etch recipe is not optimized for N-rich silicon nitride, which will require further optimization.

5.14 Integrated System Results

Finally, we turn our attention to the characterization of microring resonators with hBN single photon emitters embedded in them. Figure 5.19a displays the flake where the laser (green spot) is centered on the single-photon emitter. Figure 5.19b-c shows the same emitter integrated with the microring resonator after fabrication with sub-50 nm placement accuracy. Figure 5.19d shows the PL spectrum of the single-photon emitter after integration (excitation and collection from the top) and Figure 5.19e demonstrates the emission dipole orientation of the emitter. Note that the dipole is aligned perfectly to the fundamental TE mode of the ring resonator. The PL spectrum after integration does not show any background emission or alteration to the spectral property of the emitter after the entire fabrication process, evidencing that our process is compatible with 2D materials.

Next, in the same setup, a fiber array silicon v-groove is aligned to expose facets of the bus waveguide. The output of one of the fiber ports is collimated and introduced to the collection path as outlined in the experimental setup section. Next, the emitter is excited with a 532 nm laser from the top. However, light is collected from the bus waveguide. Figure 5.23 shows the PL spectra from the integrated hBN single photon emitter centered at 610 nm. The solid red line is the emission collected from the top objective, and the blue line is the light collected from the bus waveguide, which shows the resonator modes imprinted on the ZPL emission spectrum separated by a free-spectral range of 2 nm. This evidences that light out of the bus waveguide is the out-coupled light from the cavity and not scattered light. The loaded quality factor of the integrated resonator is averaged to 700.

We note that a sharp decrease of the total quality factor before (2200 average) and after (integration) was expected in the configuration where hBN is placed under the

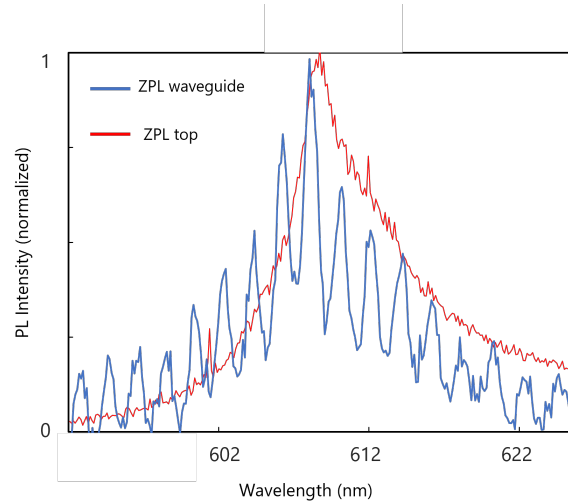


Figure 5.23: ZPL of the emitter observed from the output port of the waveguide using an aligned fiber array (blue line) and from the top collection (red line). A factor of ten reduction of the ZPL linewidth is observed (from 7.2 nm down to 0.72 nm) as expected from the bandwidth of the microresonator. The peak intensity of the ZPL is misaligned from the nearest cavity resonance by ~ 0.35 nm.

waveguide. Given the finite thickness of the hBN (5-15 nm for our flakes), this inevitably creates a step-like feature in the microring resonator, as illustrated in Figure 5.24a. The additional scattering from this step can significantly decrease the intrinsic quality factor of the waveguide. This can be seen from imaging the ring resonator when the SLED diode is injected from one of the ports into the bus-waveguide ring resonator. As seen from Figure 5.24b, while the red scattered light is visible throughout the waveguides due to usual side-wall scattering, inside the ring at the edges of the flake, a high level of red light scattering is observed, which shows significant leakage of the light from the cavity. Figure 5.24c demonstrates the loaded quality factor as a function of the hBN thickness of several integrated devices. Experimentally, for flakes with a thickness exceeding 30 nm, Q_{tot} decreases by one order of magnitude. Given that hBN emitters tend to have narrower linewidth and brighter emission in thin but multilayer flakes, this result confirms a necessary design tradeoff for resonator integration. We concluded that emitters with linewidth as low as 3-4 nm could often be found in flakes with 10-15 nm thicknesses,

which can demonstrate quality factors up to 1500.

We corroborated these measurements with further numerical simulations. The theoretical simulations of the intrinsic quality factor of the ring-resonator with an incorporated hBN step covering one-quarter of the waveguide as a function of hBN thickness are shown in Figure 5.24c. Normalizing the theoretical intrinsic quality factors (Q_{sim}) by measured intrinsic quality factor average of the experimental unloaded devices (Q_i) aligns very well with experimental observations (blue-dashed line), which further confirms that reduced quality factor is due to scattering from the steps created by hBN. A possible mitigating strategy is to place the hBN on the waveguide. However, as discussed previously, the exposed hBN interface caused the emitters to quench, likely due to the transition into a dark charge state resulting from Fermi-level pinning. Therefore, further investigations into the passivation of the hBN edges are required to alleviate this problem and allow integration with minimal reduction in the total quality factor.

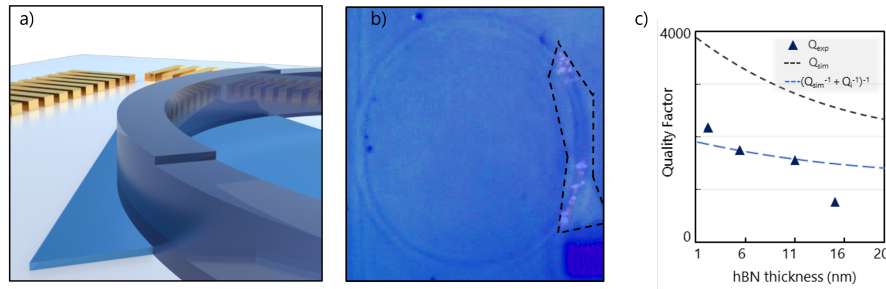


Figure 5.24: a) Illustration of the step in the ring due to the presence of the hBN underneath. b) Visible camera image of scattering of the 638 nm superluminescent diode. The edge of the flake is denoted by the dashed black lines. Increased scattering is observed from the edge of the flake under the ring waveguide. c) Theoretical (lines) and experimental (points) resonator quality factor as a function of the integrated hBN flake thickness. It is assumed the flake covers 25% of the ring in the simulations. The Black dashed line represents the theoretical simulations, which do not consider the intrinsic loss due to the flake and absorption in the guiding medium. The Blue dashed line represents the theoretical simulations corrected with the experimental intrinsic quality factor.

5.15 Spectral Purcell Factor

Next, in order to determine the coupling efficiency, we evaluate the Purcell enhancement in our devices. Here, we need to make a clear distinction. As described earlier, the Purcell effect in the spontaneous emission rate boost is only valid for the so-called "good-emitter" regime. In the good-emitter regime, the cavity linewidth (κ) is larger than the single-photon linewidth (γ); therefore, the emitter spectrally fully overlaps with the cavity mode, and the total rate of the emitter is enhanced. However, for many cases, like room temperature emitters in hBN, the zero-phonon line is significantly broader than the intrinsic radiative line due to phonon-induced dephasing. In cases where the linewidth of the single-photon is broader than the cavity linewidth ($\gamma > \kappa$), the system transitions to the so-called "bad-emitter" regime. In the bad-emitter regime, only a portion of the emitter's light spectrally overlaps with the cavity. This causes the traditional Purcell factor (defined as total emission rate enhancement) to reduce by a factor of $F\kappa/\gamma$ where the κ/γ factor heuristically represents the ratio of radiated power from the single-photon emitter. Therefore, in the bad emitter regime, it is difficult to characterize the Purcell enhancement by calculating the ratio of the lifetime of the emitter before and after integration. However, in the bad-emitter regime, Purcell factor and coupling efficiency can be defined in terms of the spectral power of the emitter, $F_s(\lambda) = I_{cav}(\lambda)/I_{fb}(\lambda)$ and $\beta_s = F_s(\lambda)/(1 + F_s(\lambda))$ where $I_{cav}(\lambda)$ and $I_{fb}(\lambda)$ are the spectral intensities of the emitter in the cavity mode and in the free-space respectively. Using the spectral definition of the Purcell factor effectively negates the κ/γ factor. It allows for enhancing the portion of the single-photon light that is resonant with the cavity to be quantified regardless of the emitter-cavity regime [35]. Note that, irrespective of the emitter-cavity regime, $\beta_s(\lambda_0)$ quantifies the enhancement at the emission wavelength of λ_0 , while integration over wavelength determines the total β .

To extract the spectral coupling efficiency and Purcell factor, we follow a similar process to that of references [36–38], namely, the spectral intensity of the emitter before integration is estimated and compared to the spectral intensity of the emitter in the cavity mode. To achieve an accurate estimate, all the possible system losses have to be accurately accounted for. The spectral Purcell enhancement can then be expressed as:

$$F_s(\lambda) = \frac{\eta_{ob}\eta_{top}}{\eta_{out}\eta_{facet}\eta_{side}} \frac{I_{cav}^{ccd}}{I_{fb}^{ccd}} \quad (5.35)$$

where η_{ob} , η_{top} , η_{out} , η_{facet} , η_{side} , I_{fb}^{ccd} , and I_{cav}^{ccd} are respectively the portion of the light collected by the top objective, efficiency of the top collection path, microring out-coupling efficiency, facet-loss, side-path collection efficiency, spectral intensity of the light measured on the CCD from the top objective, and spectral intensity measured from the waveguide output port at the CCD.

5.16 System Efficiency Calibration

In this section, we discuss the procedure to calibrate the system efficiencies. First, the waveguide facet loss (η_{facet}) can be estimated by injecting the SLED diode at 638 nm into the input port of the waveguide and measuring the power right at the output port: the transmitted and injected power ratio results in twice the facet loss. Our devices measured an average facet loss of 17.5 dB per facet. The side-path collection efficiency (η_{side}) can then be quantified by measuring the intensity of the red laser right at the output facet of the waveguide and comparing it to the red laser intensity before the entrance-slit of the spectrometer.

The top path collection efficiency (η_{top}), defined as the efficiency after the first objective up to the entrance slit of the spectrometer, can be quantified by reflecting a red laser

off of a mirror placed on the sample stage and measuring the reflected light intensity after the objective and comparing it to the intensity of the laser at the entrance slit of the spectrometer. The microring-resonator outcoupling efficiency (η_{out}), as discussed in previous chapters, can be quantified as the ratio of Q_{tot}/Q_c which is calculated for each device based on the measured quality factors.

To estimate the objective collection efficiency (η_{ob}), We use Lumerical FDTD to estimate the percentage of dipole emission upwards towards the objective. The far-field projection is integrated over a cone corresponding to the objective's NA. The simulations are performed with a dipole source embedded underneath the SiN with a three micron-thick SiO₂ cladding layer. We used two ways to integrate the power in the structure's far field. The first method integrates the electric field intensity over the objective's acceptance angle and then normalizes the result to the total transmitted power of the dipole emitter going through the monitor. The second method integrates the Poynting vector in the far field over the solid angle and then normalizes it to the total power emitted from the dipole source. For 610 nm wavelength, the collection efficiency of the objective is 10.3% and 13.2% using method one and method two, respectively. For 750 nm wavelength, the calculations result in 13.3% and 13.8% of the light captured by the objective from the two calculation methods.

5.17 Spectral Purcell Factor and Coupling Factor Estimates

After deriving the system loss's, the spectral Purcell factor for the device in Figure.5.23 was measured to be 0.86 ± 0.15 , which corresponds to $\beta_s = 46 \pm 4\%$ at the resonance. Theoretically, given that our mode volumes are on the order of $30(\lambda/n)^3$,

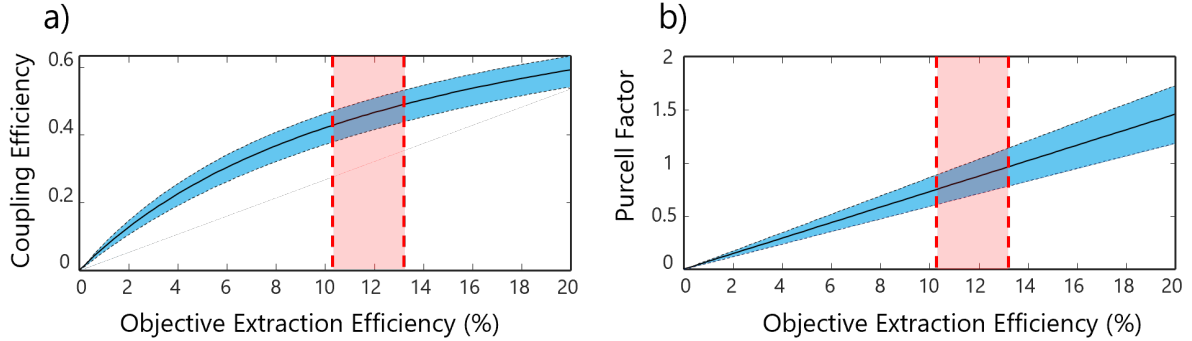


Figure 5.25: Coupling efficiency and Purcell factor estimation as a function of objective collection efficiency. The error bound has been extracted from the standard deviation in the Q_c values. The red region represents the estimated objective extraction efficiencies using Lumerical for hBN (610 nm).

spectral Purcell factor of ~ 1.7 was predicted. However, the lower Purcell factor can be attributed due to possible small positional misalignment and dipole orientation inaccuracies. The Purcell factor error bars was extracted from the standard deviation error in extraction of Q_c and lower and higher bound estimates for objective extraction efficiency as seen in Figure 5.25. Note that even though we have achieved a modest Purcell factor ~ 1 , this results demonstrate that nearly half of the emission from the single photon is coupled to the cavity mode. As seen in Figure 5.15 for the configuration of an emitter embedded below the waveguide, numerical simulations only yield about $\sim 20\%$ coupling efficiency.

To demonstrate the universality of our method with other 2D-materials, we also integrated monolayer WS_2 with our microring-resonators. Monolayer and bilayer TMDs are more sensitive to fabrication processes, especially those involving active ions and plasma. While it is possible to integrate single-photon emitters in TMDs with our microring resonators, given that our photonic integrated experiments were limited to room temperature, we chose to demonstrate the compatibility of our platform, by coupling the bilayer WS_2 exciton with our cavity. Figure 5.26a) demonstrates the Photoluminescence

spectra of the light coupled out of the output waveguide while the WS_2 is excited from the top. Resonances of the cavity are clearly imprinted on top of the exciton signature. As discussed in the previous section, the majority of the loss in the ring after integration is due to scattering at the step site due to the embedding of the 2D-materials below the waveguide. However, for bilayer WS_2 , this step-like feature is only ~ 2 nm. Therefore, the reduction of the quality factor of the ring resonator after integration is less significant compared to multilayer hBN. In our experiments, we achieved integrated quality factor of 2400 for the device seen in Figure 5.26a, resulting in $\beta_s = 63 \pm 4\%$ and spectral Purcell factor of $F_s = 1.44 \pm 0.25$ (Figure 5.26b-c).

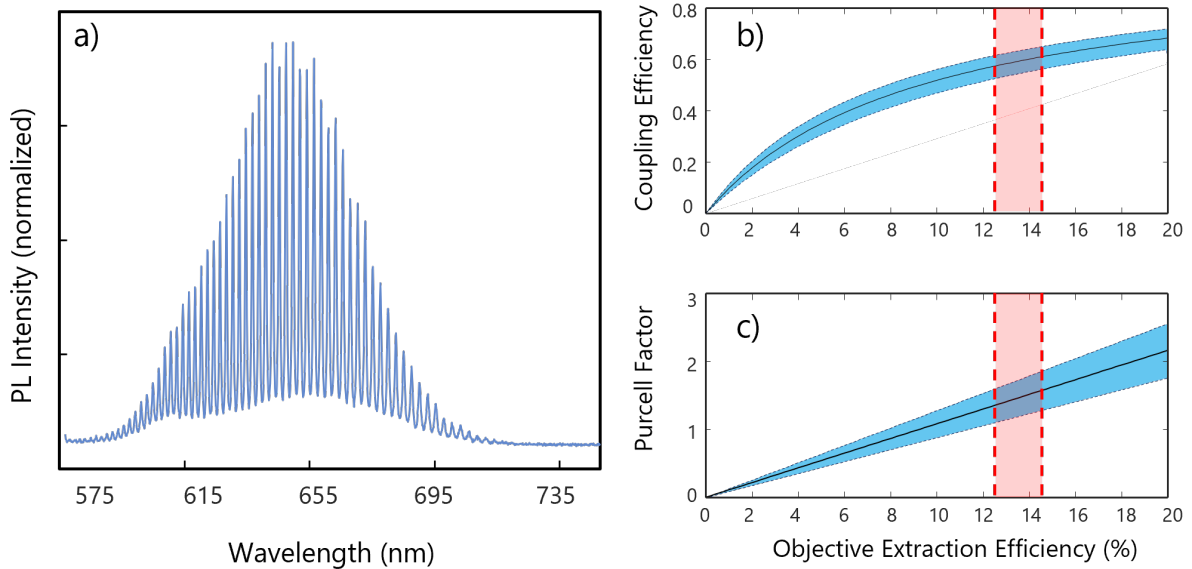


Figure 5.26: a) PL Spectra of the WS_2 integrated microring resonator measured from the output of the bus-waveguide. b-c) Coupling efficiency and Purcell factor estimation as a function of objective collection efficiency. The error bound has been extracted from the standard deviation in the Q_c values. The red region represents the estimated objective extraction efficiencies using Lumerical for WS_2 (640 nm)

5.18 Conclusion and Outlook

In this chapter, we introduced a straightforward approach for deterministically aligning and orienting SQEs in 2D materials to microresonators with a route toward high coupling efficiency. Already, this approach achieves 46% coupling efficiency into the resonator at the emitter ZPL resonance, which is an order of magnitude higher than waveguide coupling for hBN. System-wide efficiency approaching 10% can be attained in the near term with modest improvements to the microresonator Q and its design for over-coupling. The platform and methods developed in this work can serve as a crucial advancement towards future demonstrations of on-chip 2D quantum emitter integration with high extraction efficiency, brightness, and indistinguishability. In the next chapter, by exploring SiN microresonators embedded with other SQEs with narrow linewidths, such as WSe₂ and simultaneous integration of the ring resonator with electrical devices, we explore new opportunities for on-demand and site-controlled SQEs with silicon-based photonics for chip-scale quantum information applications.

Bibliography

- [1] X. Ding, Y. He, Z.-C. Duan, *et. al.*, *On-demand single photons with high extraction efficiency and near-unity indistinguishability from a resonantly driven quantum dot in a micropillar*, *Physical Review Letters* **116** (2016), no. 2 020401.
- [2] H. Wang, Y.-M. He, T.-H. Chung, *et. al.*, *Towards optimal single-photon sources from polarized microcavities*, *Nature Photonics* **13** (2019), no. 11 770–775.
- [3] N. Maring, A. Fyrrillas, M. Pont, *et. al.*, *A versatile single-photon-based quantum computing platform*, *Nature Photonics* **18** (2024), no. 6 603–609.
- [4] M. Davanco, J. Liu, L. Sapienza, *et. al.*, *Heterogeneous integration for on-chip quantum photonic circuits with single quantum dot devices*, *Nature communications* **8** (2017), no. 1 889.
- [5] A. Chanana, H. Larocque, R. Moreira, *et. al.*, *Ultra-low loss quantum photonic circuits integrated with single quantum emitters*, *Nature Communications* **13** (2022), no. 1 7693.
- [6] H. Larocque, M. A. Buyukkaya, C. Errando-Herranz, *et. al.*, *Tunable quantum emitters on large-scale foundry silicon photonics*, *Nature Communications* **15** (2024), no. 1 5781.
- [7] C. Fournier, A. Plaud, S. Roux, *et. al.*, *Position-controlled quantum emitters with reproducible emission wavelength in hexagonal boron nitride*, *arXiv preprint arXiv:2011.12224* (2020).
- [8] J. Klein, M. Lorke, M. Florian, *et. al.*, *Site-selectively generated photon emitters in monolayer MoS₂ via local helium ion irradiation*, *Nature Communications* **10** (2019), no. 1 1–8.
- [9] F. Peyskens, C. Chakraborty, M. Muneeb, *et. al.*, *Integration of single photon emitters in 2d layered materials with a silicon nitride photonic chip*, *Nature communications* **10** (2019), no. 1 4435.

BIBLIOGRAPHY

- [10] C. Errando-Herranz, E. Schöll, R. Picard, *et. al.*, *Resonance fluorescence from waveguide-coupled, strain-localized, two-dimensional quantum emitters*, *ACS photonics* **8** (2021), no. 4 1069–1076.
- [11] A. W. Elshaari, A. Skalli, S. Gyger, *et. al.*, *Deterministic integration of hbn emitter in silicon nitride photonic waveguide*, *Advanced Quantum Technologies* **4** (2021), no. 6 2100032.
- [12] A. Gale, C. Li, Y. Chen, *et. al.*, *Site-specific fabrication of blue quantum emitters in hexagonal boron nitride*, *ACS Photonics* **9** (2022), no. 6 2170–2177.
- [13] G. Grosso, H. Moon, B. Lienhard, *et. al.*, *Tunable and high-purity room temperature single-photon emission from atomic defects in hexagonal boron nitride*, *Nature Communications* **8** (2017), no. 1 1–8.
- [14] H. Zhao, M. T. Pettes, Y. Zheng, and H. Htoon, *Site-controlled telecom-wavelength single-photon emitters in atomically-thin MoTe_2* , *Nature Communications* **12** (2021), no. 1 6753.
- [15] Y. Luo, G. D. Shepard, J. V. Ardelean, *et. al.*, *Deterministic coupling of site-controlled quantum emitters in monolayer WSe_2 to plasmonic nanocavities*, *Nature Nanotechnology* **13** (2018), no. 12 1137–1142.
- [16] H. Baek, M. Brotons-Gisbert, Z. Koong, *et. al.*, *Highly energy-tunable quantum light from moiré-trapped excitons*, *Science advances* **6** (2020), no. 37 eaba8526.
- [17] H. Zhao, L. Zhu, X. Li, *et. al.*, *Manipulating interlayer excitons for ultra-pure near-infrared quantum light generation, 2022, 2205.02472. arXiv preprint server. <https://arxiv.org/abs/2205.02472> (October 24, 2022)* (2022).
- [18] B. Li, W. Jin, L. Wu, *et. al.*, *Reaching fiber-laser coherence in integrated photonics*, *Optics Letters* **46** (2021), no. 20 5201–5204.
- [19] J. Liu, G. Huang, R. N. Wang, *et. al.*, *High-yield, wafer-scale fabrication of ultralow-loss, dispersion-engineered silicon nitride photonic circuits*, *Nature communications* **12** (2021), no. 1 2236.
- [20] K. Alexander, A. Bahgat, A. Benyamini, *et. al.*, *A manufacturable platform for photonic quantum computing*, *arXiv preprint arXiv:2404.17570* (2024).
- [21] M. W. Puckett, K. Liu, N. Chauhan, *et. al.*, *422 million intrinsic quality factor planar integrated all-waveguide resonator with sub-MHz linewidth*, *Nature Communications* **12** (2021), no. 1 934.
- [22] J.-F. Lelievre, J. De la Torre, A. Kaminski, *et. al.*, *Correlation of optical and photoluminescence properties in amorphous Si_3N_4 thin films deposited by pecvd or uv-cvd*, *Thin Solid Films* **511** (2006) 103–107.

BIBLIOGRAPHY

- [23] M. Wang, D. Li, Z. Yuan, *et. al.*, *Photoluminescence of si-rich silicon nitride: Defect-related states and silicon nanoclusters*, *Applied physics letters* **90** (2007), no. 13.
- [24] I. Parkhomenko, L. Vlasukova, F. Komarov, *et. al.*, *Origin of visible photoluminescence from si-rich and n-rich silicon nitride films*, *Thin Solid Films* **626** (2017) 70–75.
- [25] M. E. Turiansky, A. Alkauskas, L. C. Bassett, and C. G. Van de Walle, *Dangling bonds in hexagonal boron nitride as single-photon emitters*, *Physical Review Letters* **123** (2019), no. 12 127401.
- [26] N. Mendelson, D. Chugh, J. R. Reimers, *et. al.*, *Identifying carbon as the source of visible single-photon emission from hexagonal boron nitride*, *Nature Materials* (2020) 1–8.
- [27] Z.-Q. Xu, C. Elbadawi, T. T. Tran, *et. al.*, *Single photon emission from plasma treated 2d hexagonal boron nitride*, *Nanoscale* **10** (2018), no. 17 7957–7965.
- [28] M. Kianinia, B. Regan, S. A. Tawfik, *et. al.*, *Robust solid-state quantum system operating at 800 k*, *Acs Photonics* **4** (2017), no. 4 768–773.
- [29] N. Chejanovsky, M. Rezai, F. Paolucci, *et. al.*, *Structural attributes and photodynamics of visible spectrum quantum emitters in hexagonal boron nitride*, *Nano Letters* **16** (2016), no. 11 7037–7045.
- [30] S. Choi, T. T. Tran, C. Elbadawi, *et. al.*, *Engineering and localization of quantum emitters in large hexagonal boron nitride layers*, *ACS applied materials & interfaces* **8** (2016), no. 43 29642–29648.
- [31] N. V. Proscia, Z. Shotan, H. Jayakumar, *et. al.*, *Near-deterministic activation of room-temperature quantum emitters in hexagonal boron nitride*, *Optica* **5** (2018), no. 9 1128–1134.
- [32] C. Fournier, S. Roux, K. Watanabe, *et. al.*, *Two-photon interference from a quantum emitter in hexagonal boron nitride*, *Physical Review Applied* **19** (2023), no. 4 L041003.
- [33] A. M. Fox, *Quantum optics: an introduction*, vol. 15. Oxford University Press, USA, 2006.
- [34] A. Senichev, S. Peana, Z. O. Martin, *et. al.*, *Room-temperature single-photon emitters in silicon nitride*, in *2021 Conference on Lasers and Electro-Optics (CLEO)*, IEEE, 2021.

BIBLIOGRAPHY

- [35] H. Kaupp, C. Deutsch, H.-C. Chang, *et. al.*, *Scaling laws of the cavity enhancement for nitrogen-vacancy centers in diamond*, *Physical Review A* **88** (2013), no. 5 053812.
- [36] C. Li, J. E. Froch, M. Nonahal, *et. al.*, *Integration of hBN quantum emitters in monolithically fabricated waveguides*, *ACS Photonics* **8** (2021), no. 10 2966–2972.
- [37] S. Kim, N. M. H. Duong, M. Nguyen, *et. al.*, *Integrated on chip platform with quantum emitters in layered materials*, *Advanced Optical Materials* **7** (2019), no. 23 1901132.
- [38] M. Gould, E. R. Schmidgall, S. Dadgostar, *et. al.*, *Efficient extraction of zero-phonon-line photons from single nitrogen-vacancy centers in an integrated gap-on-diamond platform*, *Physical Review Applied* **6** (2016), no. 1 011001.

Chapter 6

Outlook for Turnkey Quantum

Diodes

In the previous chapters, we introduced two critical technological advancement for 2D-based quantum emitters. Namely, the ability to create site-specific single photon emitters in WSe₂ and a SiN-based photonic platform for efficient on chip integration of 2D-based quantum emitters. In this chapter, we will discuss how these two advancements pave the way for the realization of a true turnkey quantum source. First, through theoretical study, we identify and evaluate the required performance targets of our cavity-emitter for applications in quantum photonic technologies. Then, we will discuss our progress in solving one of the final hurdles to scalable realization of on-chip quantum emitters, namely moving away from bulk optics required for optical pumping and exploring simultaneous integration of cavity-embedded single-photon emitters with on-chip electrical diodes.

6.1 Figure of Merit for Cavity-Emitter Systems

In the previous chapter, the main focus of our integration was on leveraging Purcell enhancement to increase the on-chip coupling efficiency. We also briefly discussed that the Purcell enhancement can also lead to increased indistinguishability by increasing the radiative rate of the system while maintaining the broadening rate of the system. However, for photonic quantum technologies that rely on interference of two photons, a key system benchmark is to know the probability of two-photon interference within a deterministic clock cycle. Answering this question first requires the knowledge of deterministic creation of each photon, captured in the total source efficiency (η), and also the knowledge of the ability of interference between two photons, captured in indistinguishability (V). Therefore, it is critical to study system-wide efficiency and indistinguishability together, and define efficiency-indistinguishability product (ηV).

The total efficiency of our integrated system can be expressed as:

$$\eta = \eta_{qe}\beta\eta_{out}, \quad (6.1)$$

where η_{qe} , β , and η_{out} are the quantum efficiency of the emitter (probability of emitting a photon per pulse cycle), coupling efficiency into the cavity photonic mode, and extraction efficiency of the coupled light in the cavity into the bus waveguide [1, 2]. Maximizing ηV is a multi-variable problem because the individual components of efficiency and indistinguishability cannot be adjusted independently. For instance, while a high Q results in a larger β and V , for large Q , the cavity-emitter system can enter the bad-emitter regime where the linewidth of the cavity is smaller than the emitter itself. In this case, only a portion of the ZPL will couple into the microring resonator, and η will begin to decrease as result. Generally, the linewidth of the emitter sets a practical upper bound for the loaded Q . While this can imply that SQEs with the narrowest linewidth are more

suitable for cavity integration, the SQE quantum efficiency η_{qe} also plays an important role in the emitter-cavity design. For instance, η_{qe} for WSe₂ is estimated [3, 4] to be only $\sim 1 - 5\%$ compared to up to 87% reported for hBN [5]. Therefore, to optimize the cavity design with high $\eta \times V$ for different 2D emitters, a holistic approach must be considered.

In this section, we will explore the solutions to a modified Jaynes-Cummings Hamiltonian [6, 7] considering state-of-the-art 2D quantum emitters interacting with a cavity.

Here, we follow the solutions to the master equation for a dielectric nanophotonic waveguide evanescent interacting with a cavity-emitter system following the approach of Peyskens *et al.* [7]. The density matrix in the rotating framework will follow:

$$\begin{aligned} \frac{d\rho}{dt} = & -i\Omega[pS_+ + p^\dagger S_-, \rho] + \frac{\gamma_p}{2} (2p\rho p^\dagger - p^\dagger p\rho - \rho p^\dagger p) \\ & + \frac{\gamma_e}{2} (2S_- \rho S_+ - S_+ S_- \rho - \rho S_+ S_-) + \frac{\gamma^*}{2} (2S_z \rho S_z - S_z S_z \rho - \rho S_z S_z) \end{aligned} \quad (6.2)$$

Here, have assumed the emitter with angular frequency of (ω_e) is in resonant with the cavity mode. The spin operators are defined as:

$$S_- = |g\rangle \langle e| \quad (6.3)$$

$$S_+ = |e\rangle \langle g| \quad (6.4)$$

$$S_z = \frac{1}{2}(|e\rangle \langle e| - |g\rangle \langle g|) \quad (6.5)$$

The three decay rates γ_p, γ_e , and γ^* are defined as total cavity decay rate (including both intrinsic and out-coupling), emission rate of the emitter into lossy modes, and pure

dephasing rate of the emitter. The emitter-cavity coupling term is defined as:

$$\Omega = \sqrt{\frac{\omega_c}{2\hbar\epsilon_0}} |P_d| \cos\theta_d \left(\frac{1}{\sqrt{V_c}} \right), \quad (6.6)$$

where the V_c is cavity mode volume, P_d is the dipole moment term, and θ_d is the misalignment between dipole of the emitter and the polarization axis of the cavity. The relationship between emitter spontaneous emission rate and dipole moment interaction strength was derived in the previous chapter. Assuming a medium with refractive index (n_d), we can represent:

$$|P_d| = \sqrt{\frac{3\pi\epsilon_0\hbar c^3\Gamma}{n_d\omega_e^3}}, \quad (6.7)$$

and therefore,

$$\Omega^2 = \frac{3\pi c^3}{2n_d\omega_c^2} \cos(\theta)^2 \frac{\Gamma}{V_c}$$

Assuming that the two level system is initially in the excited state and the cavity has no photons, the system can be described by three basis states:

$|1\rangle = |g, 0\rangle$, $|2\rangle = |g, 1\rangle$, $|3\rangle = |e, 0\rangle$, which follow the following rate equations:

$$\frac{d\rho_{22}}{dt} = -2\Omega \text{Im}(\rho_{23}) - \gamma_p \rho_{22} \quad (6.8)$$

$$\frac{d\rho_{33}}{dt} = 2\Omega \text{Im}(\rho_{23}) - \gamma_e \rho_{33} \quad (6.9)$$

$$\frac{d\text{Im}(\rho_{23})}{dt} = -\frac{\gamma_p + \gamma_e + \gamma^*}{2} \text{Im}(\rho_{23}) + \Omega\rho_{22} - \Omega\rho_{33} \quad (6.10)$$

Here, we assume resonant excitation and cryogenic temperature operation, which implies that the pure dephasing term (γ^*) can be neglected when compared with intrinsic

emission rate into the cavity (γ_p) and lossy modes (γ_e). The coupled system can be solved for $\rho_{22}(t)$ to find the single photon coupling efficiency as:

$$\eta = \kappa \int_0^\infty dt \rho_{22}(t) = \frac{\kappa}{(\gamma_e + \gamma_p)(1 + 0.25\gamma_e\gamma_p\Omega^{-2})}. \quad (6.11)$$

Indistinguishability has also been derived within this framework [8]. In the weak-coupling limit for bad cavity ($\gamma_p > \gamma_e + \gamma^*$) indistinguishability can be defined as:

$$V = \frac{\gamma_e + R}{\gamma_e + R + \gamma^*} \quad (6.12)$$

and in the good cavity limit ($\gamma_p < \gamma_e + \gamma^*$) it can be defined as:

$$V = \frac{\gamma_e + \frac{\gamma_p R}{\gamma_p + R}}{\gamma_e + \gamma_p + R}, \quad (6.13)$$

where

$$R = \frac{4\Omega^2}{\gamma_e + \gamma_p + \gamma^*}. \quad (6.14)$$

Relating the decay rates in terms of cavity parameters, we have:

$$\gamma_c = \frac{\omega_c}{2Q_i} \quad (6.15)$$

and

$$\kappa = \frac{\omega_c}{2Q_e} \quad (6.16)$$

Finally, to capture the dynamics of the system close to the bad-emitter regime, we have applied a heuristic correction factor (ζ) to the cavity-emitter coupling rate (Ω), expressed as:

$$\zeta = \frac{\kappa + \gamma_e}{\kappa + \gamma_e + \Gamma}, \quad (6.17)$$

which accounts for partial coupling of the emitter into the cavity due to spectral mismatch [6].

6.2 Cavity Requirements for useful 2D SQEs

State-of-the-art demonstration of integrated single photon emitters in III-V quantum dots have achieved ηV factors up to 3% for dots emitting on-chip [9] and 78% for quantum dots embedded in nanopillar cavity emitting off-chip [10]. In our opinion, reaching on-chip ηV above 90% can make 2D quantum emitters systems truly competitive compared with state-of-the-art sources. Therefore, we aim to answer the question that, given the state-of-the-art demonstration of 2D-quantum emitters in the last five years, what are the cavity requirements that can make these emitters truly competitive.

First, to determine the loaded quality factors needed for high ηV factors, we assume, for now, that the intrinsic quality factors of the cavities can be extremely high (10^8), and the cavity quality factor is purely dominated by the coupling quality factor (Q_c). In addition, we assume emitters can be integrated via a deterministic approach which can yield $\cos(\theta_d) = 1$, meaning it achieves near-ideal placement and orientation between electric field and polarization axis of the mode. Lastly, assuming the emitter is resonantly excited, the emitter quality factor is defined using ($Q_e = \frac{\omega_c}{2\gamma_e}$). The total emitter decay rate, $\Gamma = \gamma_e \eta_Q$ where η_Q is the emitter's quantum efficiency, assuming no additional pure dephasing is present. For hBN and WSe₂ emitters, the parameters below have been extracted from literature [4, 5]

Figure 6.1 demonstrates the result of the simulation as function of quality factor and mode volume of the cavity. The vertical dashed line sets the boundary of the bad-emitter regime, in which the total quality factor exceeds the emitter quality factor Q_e determined from its linewidth. The horizontal dashed line indicates the mode volume for

Material	λ_0 (nm)	τ (ns)	γ^* (MHz)	η_Q	n_d	Q_i .
hBN	600	1.2	150	0.87	2.1	10^8
WSe ₂	800	10	2000	0.05	4.2	10^8

Table 6.1: Material properties and parameters used in the calculation of single photon extraction efficiency as a function of the cavity loaded quality factor, and the cavity volume normalized by the modal volume. Where λ_0 represents the free-space wavelength of the emitter, τ represents the emitter lifetime, η_Q represents the quantum efficiency, n_d represents the materials refractive index, and Q_i representing the intrinsic quality factor.

our demonstrated PICs. As expected, with smaller mode volume, both higher efficiency and indistinguishability is possible. However, while generally higher Q results in higher indistinguishability, for ultra-high Q's (Q's higher than the emitter's linewidth), the extraction efficiency, indistinguishability, and their byproduct begins to rapidly decrease. Figure 6.2a demonstrates a slice cut of ηV for both hBN and WSe₂ single photon emitters as a function of the total quality factor at the $V_c = 30(\lambda/n)^3$. For $Q \sim 16000$, existing hBN emitters at cryogenic temperatures can reach ηV factors up to 90%. This is mainly due to the higher reported quantum efficiency and closer to lifetime limited linewidth for hBN emitters. However, as shown in Figure 6.2a, existing WSe₂ emitters can also obtain ηV factors exceeding 90% provided they can be integrated with cavities with loaded Q exceeding 10^5 . While Purcell enhancement can compensate for emitters with intrinsically low quantum efficiency and indistinguishability, this comes with a great cost of required Purcell factor.

In the former analysis, we assumed the cavity is purely in the over-coupled regime by assuming an ultra high intrinsic quality factor. However, this is rarely the case. Next, we calculated the highest attainable ηV factor for both WSe₂ and h-BN emitters as function of the intrinsic quality factor of the platform. Figure 6.2b, demonstrates the results. For intrinsic quality factors approaching 10^6 , which is already achievable for different SiN waveguide aspect ratios, it is possible to integrate 2D quantum emitters with ηV factors

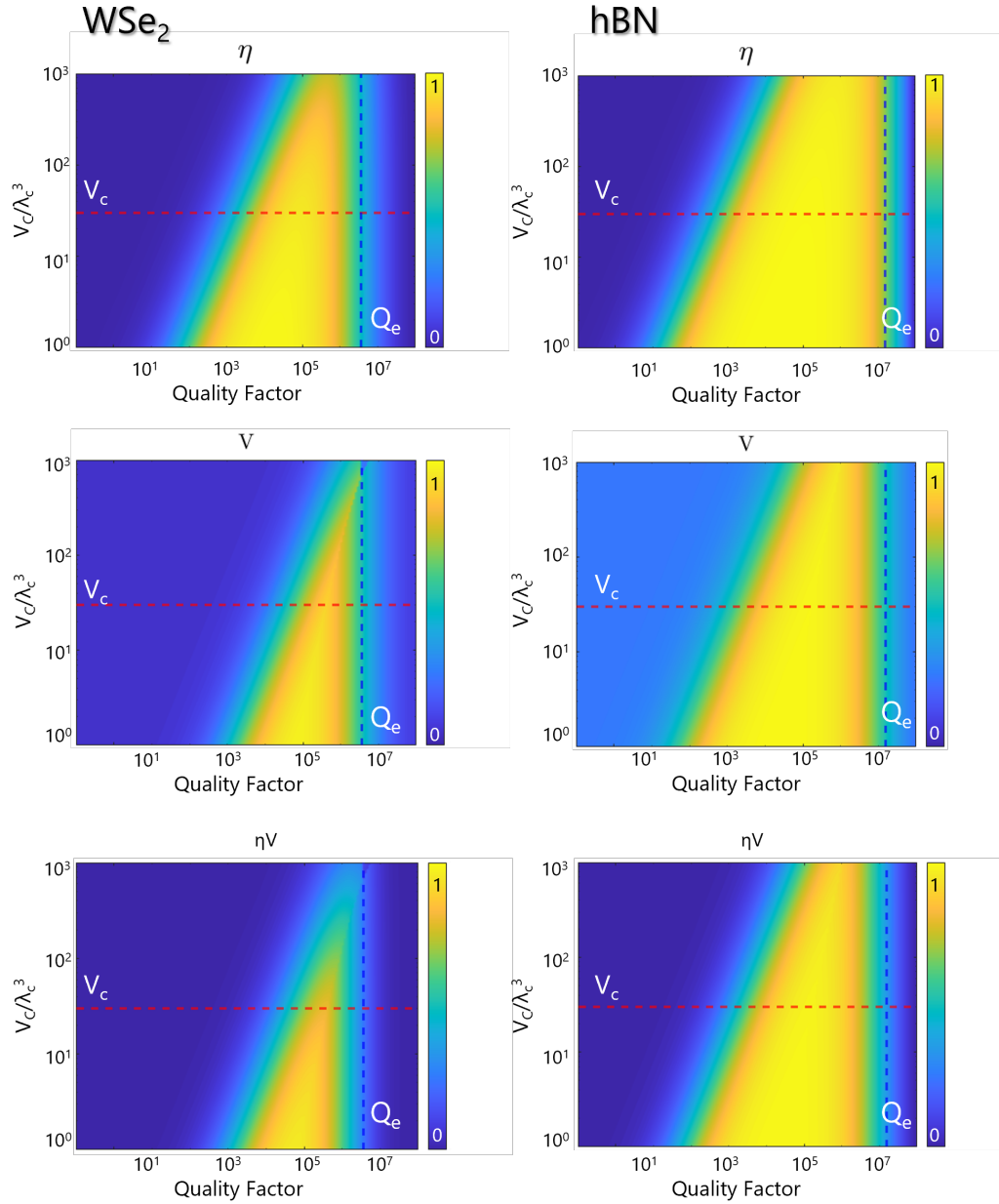


Figure 6.1: System efficiency η (emission of photons into the bus waveguide), indistinguishability (V), and system efficiency indistinguishability product ($\eta \times V$) as a function of the loaded quality factor of the cavity and the cavity volume normalized by the mode volume.

exceeding 80%. Our demonstration was limited by the low intrinsic quality factor of the integrated system which stemmed from scattering from inevitable step-like features at

the edge of the 2D-flake. In the future, it is vital to explore other integration strategies, such as top integration after passivating the hBN edges that can allow for deterministic integration while maintaining high quality factors.

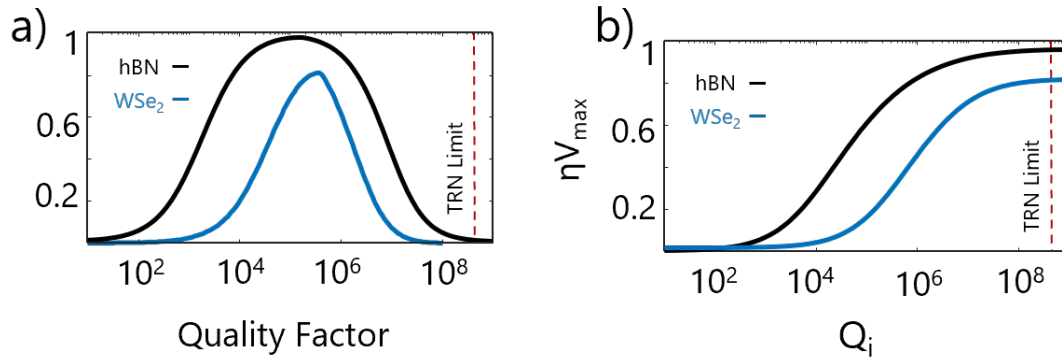


Figure 6.2: a) Total system efficiency-indistinguishability figure of merit $\eta \times V$ as a function of loaded Q at the minimum achievable mode volume for hBN and WSe_2 emitters in the visible wavelength. The intrinsic linewidth and total dephasing rate are taken from previous resonant fluorescence studies to be 50 MHz and 150 MHz (for hBN [11]) and 100 MHz and 2 GHz (for WSe_2 monolayers [12]), respectively. b) Maximum figure of merit $\eta_{max} \times V$ achievable for each class of emitters as function of the intrinsic quality factor of the SiN platform

6.3 The Need for Electrical Excitation for Scalable On-chip Sources

Our previous result shows that with a pragmatic improvements in the intrinsic quality factor of integrated SiN platform, on-chip single photon emitters with competitive benchmarks can be realized in the near future. In this section, we aim to address one of the final obstacles to realization of true turnkey single-photon emitters.

With the introduction of site-specific methods of engineering arrays of defects in WSe_2 and hBN, as demonstrated in chapter 4, and also development of the low autofluorescence 2D compatible photonic platform for 2D SQEs, an important next step is to create arrays

of many integrated quantum emitter devices as illustrated in Fig. 6.3.

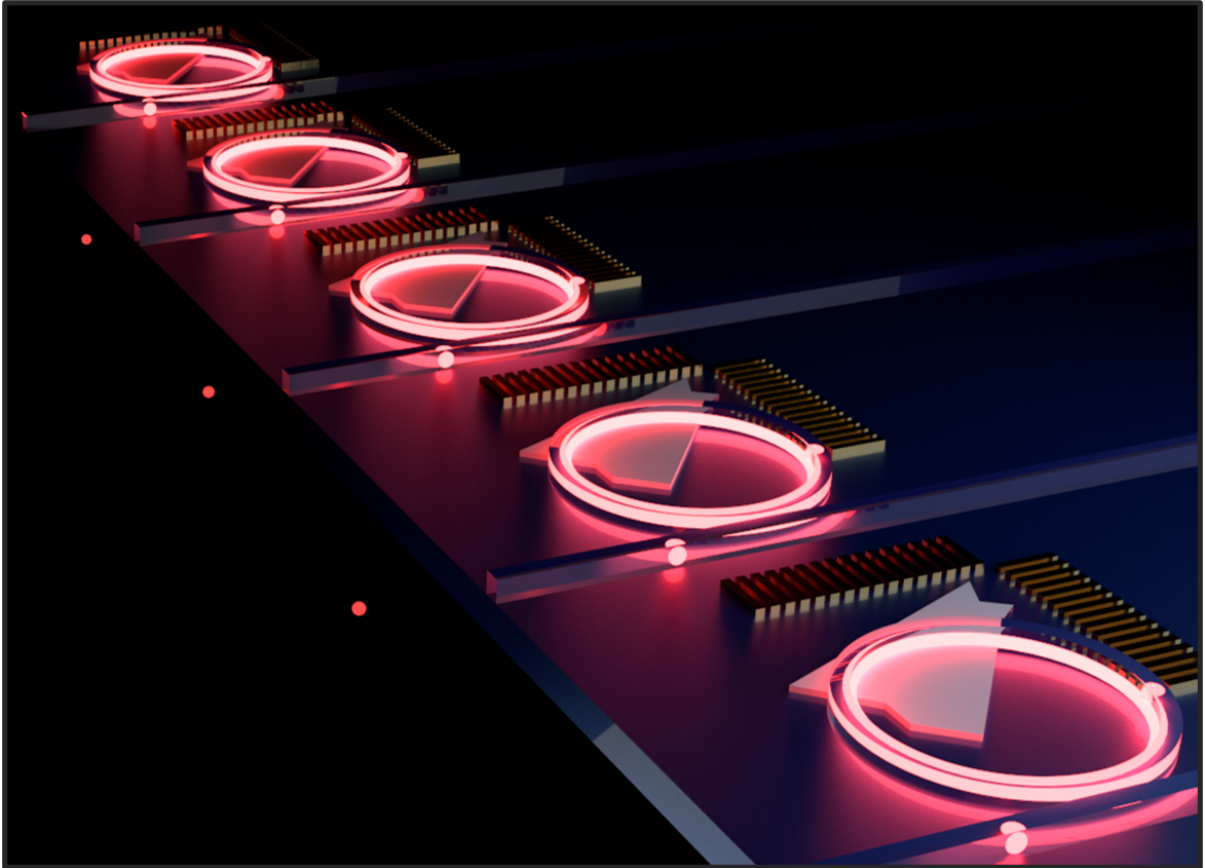


Figure 6.3: Illustration of arrays of on-chip cavity-coupled 2D-based single-photon emitters.

One major limitation for practical use of single-photon emitters (SPEs) is the requirement of optical pumping with a pulsed laser for on-demand single-photon emission. The requirement of bulk optics not only limits the scalability of optically pumped sources, but it also prohibits compact form factors that are needed for field deployable systems such as ground and space-based communication networks using room temperature emitters [13]. Alternatively, embedding solid-state emitters directly in diode structures can enable electrical pumping, thereby eliminating the need for bulky optical instrumentation. For example, electroluminescent III-V QDs integrated within p-i-n junctions in micro-pillar cavities can emit single photons [14, 15]; however, the extraction efficiency

is typically $< 50\%$ due to the stochastic formation of QDs during growth. Additionally, QD diodes have not been integrated with silicon-based photonic waveguides, and electrical pumping degrades the quality of the emitted light. As such, turn-key, quantum light-emitting diodes (QLEDs) with high efficiency and optical quality has remained a sought-after goal for advancing quantum photonic sources. [16, 17].

We hypothesize that by leveraging our site-specific fabrication methods, we will be able to deterministically position the SPEs in the intrinsic region of an electrostatically-doped lateral p-i-n junction. Our proposed device is compatible with our existing photonic integration process, allowing the intrinsic region to be coupled into the photonic mode of a microring resonator to enable efficient photon extraction efficiency and a boost in indistinguishability through the Purcell effect, thereby enabling a gigahertz pulsed, photonically integrated QLED.

6.4 Distinctions Between Electrical and Optical Excitation Method

To understand the working principles of a potential single-photon diodes, it is critical to establish the differences between the microscopic mechanism of electrical and optical excitation methods.

With optical excitation, a laser pump promotes an electron in the ground state of the defect to the excited state. This process could happen with either sub-bandgap or above-bandgap excitation (Figure 6.4a-b). In electroluminescence, however, the electron and holes are injected into the vicinity of the defect from the conduction and valence band edges of the n-type and p-type p-i-n junction (Figure 6.4c). The electron/hole are captured by the defect and promote it to its excited state where it eventually returns to

the ground state either by emitting a photon or phonons, the proportion of which would depend on the quantum efficiency of the defect.

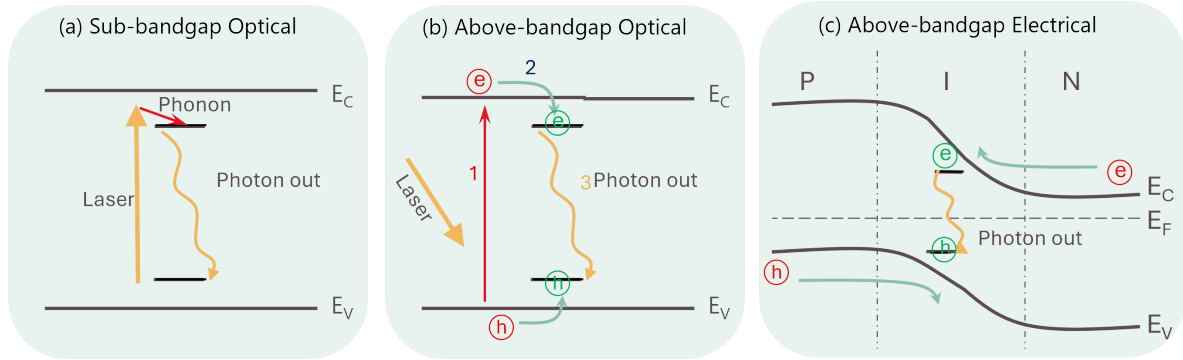


Figure 6.4: Excitation modalities of quantum defects. a) Sub-bandgap optical excitation through phonon-assisted absorption. b) Above-bandgap optical excitation. c) Above-bandgap electrical excitation. Excess carriers are injected near the defect in a p-i-n junction and radiatively recombine

In order to generate electroluminescence from a specific charge state of a defect, that defect must have either a higher or lower thermodynamically stable charge state and, depending on the electronic configuration, is supplied by the adequate concentration of electrons and holes to maintain the cyclic process. For example, in above-bandgap excitation, the charge state of the defect changes as additional charges are added or removed. This inevitably starts a cyclic process for the defect as exemplified by the case of color centers in widegap semiconductors, such as NV^- centers [18]. The fact that the defect has to undergo a change in charge state in electrical excitation is a critical distinction between the two excitation modalities with important consequences.

In the single-particle picture, the defect is usually treated as a single recombination center where, by subsequently capturing excess electrons and holes, it attempts to bring the local charge distribution back to equilibrium. However, in a single particle picture, the change in the electronic state of the defect due to its altered charge state is not accounted for, which not only results in large miscalculations in electron/hole recombination rates [19], but also is completely unable to predict luminescent properties based

on ab-initio results. The importance of understanding the cyclic process of electroluminescence has come to light only in recent years. Amongst 2D material SPEs, defects in TMDs have shown that they are capable of electroluminescence [20, 21]; however, the underlying microscopic process of electroluminescence has yet to be understood. For instance, it is unknown which higher/lower charge states are involved in the process or whether the cyclic process is limited by hole or electron injection. Understanding the electronic structure, cyclic process of luminescence, and the appropriate modeling of this microscopic process is essential to designing single photon emitting diodes with these hosts.

6.5 Lateral Tunable P-I-N Geometry for Simultaneous Electrical and on-chip Integration

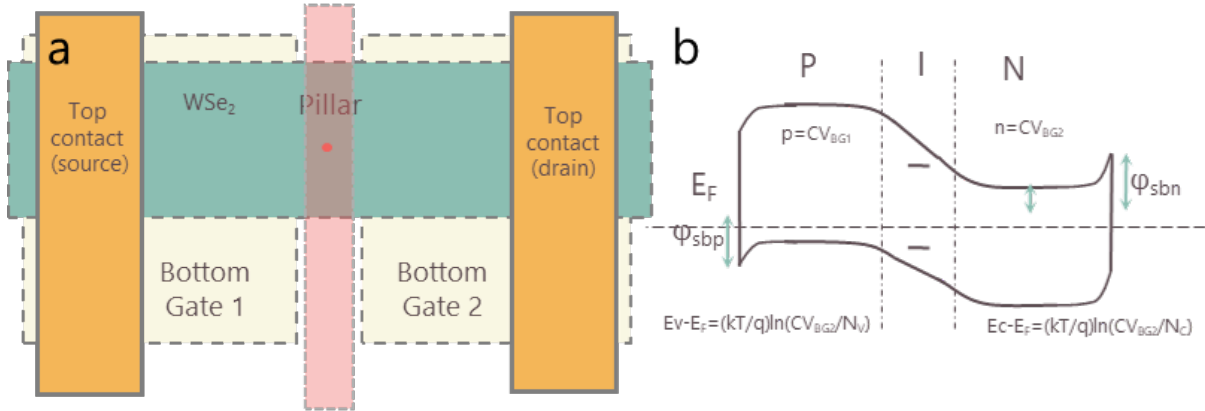


Figure 6.5: Band diagram of a tunable P-I-N single-photon emitter diode. a) Architecture of the proposed single-photon emitter. b) Band-diagram of the device.

We aim to demonstrate a truly turn-key and scalable on-chip quantum LED via simultaneous electrical and photonic-cavity integration of quantum defects in 2D TMDs. With a single defect engineered to reside in the intrinsic region, depending on the doping

concentration of the adjacent junctions and the forward bias voltage, an arbitrary concentration of each minority charge carriers can be injected into the vicinity of the defect. This should allow us to excite any electrically triggerable luminescent defect without being restricted by electron or hole capture rates.

Heterojunctions based on TMDs are highly configurable, since they can be fabricated laterally, and instead of using static dopants to form p-type and n-type regions, the electrostatic back gates can be used to create reconfigurable p and n regions with tunable carrier concentration [22, 23]. The two major advantages of such device geometry (Figure 6.5) over other proposed or demonstrated devices are: (1) the lateral configuration allows a waveguide to be integrated with the defect in the intrinsic region, making this device one of the only possible geometries that can allow on-chip electrically triggered sources, and (2) the dynamical tuning of carrier concentration would simultaneously enable luminescence and Stark tuning of the SPE. Hence, using the device architecture, it would be possible to create an electrically triggered p-i-n diode with a site-specific quantum defect being embedded in the intrinsic region and coupled with an on-chip microcavity. The back gates can be used not only to induce charges necessary for the diode operation, but they can also tune the SPE into resonance with the microcavity, providing Purcell enhancement and improved brightness and indistinguishability. This device allows all the essential components of the ideal single photon emitter to be integrated together.

Creating a functional device requires multiple technological and theoretical gaps to be addressed. First, a better understanding of the electroluminescence (EL) process in TMDs, the charge states involved, the recombination rates, and the internal quantum efficiencies is required. We also need to engineer pulsed QLEDs with frequencies up to the inverse lifetime of the emitters. Upon benchmarking the performance, then a compatible on-chip photonic cavity architecture must be integrated with the device without compromising electrical and optical performance. Therefore this proposal is organized in

three objectives.

6.6 Full Diode Fabrication Flow and Contact Engineering

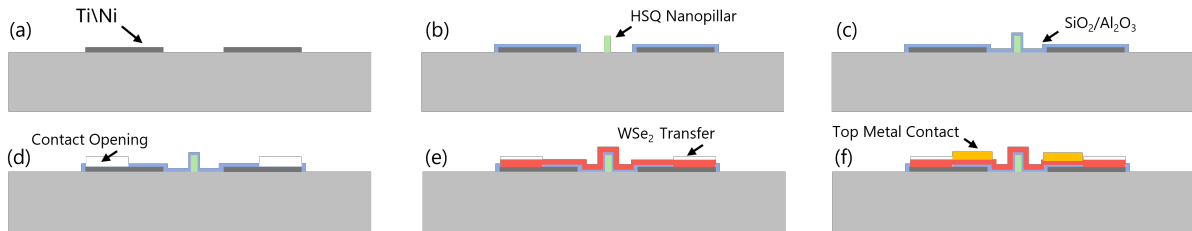


Figure 6.6: Overview of diode-only SPE device.

In this section we will discuss the fabrication details of the P-I-N based single-photon diode. Given the complexity of the total fabrication process, we aimed to initially fabricate the single-photon diodes without photonic integration. This allowed us to first understand and improve the electrical aspects of the single-photon diode before attempting the full integration attempt.

First, using electron-beam lithography (JOEL 6300FX) utilizing 55 nm of single-layer PMMA followed by e-beam metal evaporation of a 10 nm/20nm/10nm stack of Titanium, Gold, and Nickel and lift-off process, we defined the bottom gate electrodes (Figure 6.6a). Here, titanium is used as wetting layer, while high atomic number of gold allows us to align the subsequent layers in e-beam lithography steps. Use of nickel proves essential as it enables a low-leakage dielectric interface between Ni/SiO₂/Al₂O₃ for the gate stacks. The spacing between the back-gates were swept from 200 nm up to 1 μm to study the effect of increased intrinsic region.

In the next step, we defined the nanopillar arrays at the center of the backgates. Here, we utilized a 5% HSQ solution that would yield about 80 nm of SiO₂ after subsequent

anneal. The HSQ was irradiated with e-beam to create nanopillars with radius of 100 nm as illustrated in Figure 6.6. Figure 6.7a demonstrates the darkfield image of the device after bottom gate and nanopillar fabrication. Next, the gate-dielectric was deposited using Atomic Layer Deposition (ALD). Prior to deposition, a brief 2 minute oxygen plasma was used to activate the surface of nickel on the bottom electrodes. An 8-nm SiO_2 followed by 20 nm of Al_2O_3 was deposited using ALD. The use of SiO_2 capping layer along with Nickel was critical in achieving low-leakage dielectric with leakage levels down to femtoamps. Finally, using direct laser lithography (MLA Heidelberg) followed by MIKZ-300 and BHF dip, contact pads are stripped of the gate-oxide and are opened for electrical connection. The image of the device after pad openings is illustrated in Figure 6.7b.

In the next step, WSe_2 monolayers were transferred and draped over the active region of the device using viscoelastic transfer method. In the final step, using a bilayer SF8 and SPR955 resist recipe and direct laser lithography, the pattern for final source drain contacts is opened. 4-nm nickel and 65 nm platinum were deposited in high vacuum condition ($\sim 10^{-7}$ torr) followed by lift-off in cold NMP solution. Figure 6.7 demonstrates the optical image and SEM image (Figure 6.7 of the final fabricated device).

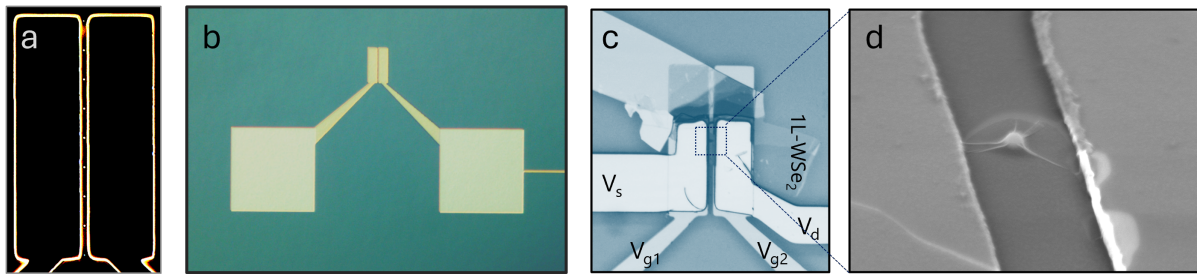


Figure 6.7: Optical and scanning electron microscope of fabricated devices. a) Dark-field image of the nanopillar array at the intrinsic region of the diode. b) Bottom gate structure before 2D integration. c) Fully fabricated diode after monolayer WSe_2 transfer and top contact deposition. d) Scanning electron microscope image of the monolayer WSe_2 at the intrinsic region of the device. Monolayer WSe_2 can be seen draping over the nanopillar.

6.7 Preliminary Result of Fabrication Prior to Integration

A major challenge in the device fabrication was lowering the current leakage from the dielectric stack. Directly depositing Al_2O_3 on conventional Ti/Au metal stacks resulted in poor and leaky interfaces. Utilizing a thin layer of nickel on top of the metal gate stack, performing a short two minute oxygen plasma ash prior to ALD of the gate oxide, and utilizing an 8-nm SiO_2 buffer layer in ALD prior to depositing the Al_2O_3 layer were all essential steps in allowing us to reach leakage currents on the order of 1.25×10^{-6} $\text{fA}/\mu\text{m}^2$ for fields on the order of 1.2 Mv/cm . Figure 6.8 displays the I-V characteristic of a test capacitance with $400 \mu\text{m}^2$ area. Finally, Figure 6.8b presents the PL spectra of WSe_2 single photon emitter after the full-fabrication flow, measured at the site of the nano-pillar shown in Figure 6.7d, displaying sharp emission lines as expected.

6.8 Discussion

Unfortunately, the final quantum electro-optical measurements of the fabricated devices are still an on-going project at the time of writing of this thesis. However, given that the tunable P-I-N junction quantum LEDs are a relatively new conceptual device, limited only to 2D community, in this section we will describe our measurement protocol for full characterization and operation of such devices.

To investigate the microscopic mechanism of EL in TMDs, we propose a novel electrical testbed and benchmarking criteria that, coupled with ab initio calculations, would allow us to determine the optimized parameter space for EL in our defects.

In the first test, both electrostatic gates are shorted, and their bias is swept from negative to positive voltages. In this regime, the device essentially becomes either a PP

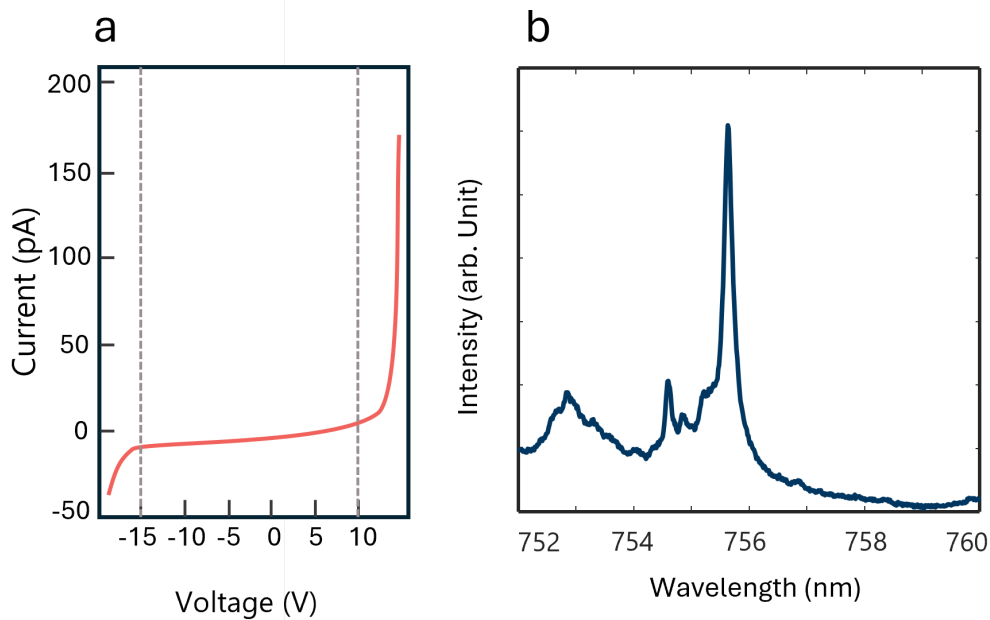


Figure 6.8: Preliminary results of the fabricated diodes. a) Characterization of gate dielectric leakage current for a $400 \mu\text{m}^2$ capacitor. b) PL Spectra of the intrinsic region of the device at a nano-pillar location displaying sharp features.

or NN junction (acting like an NMOS/PMOS), whereby the intrinsic region, due to its short width ($< 200 \text{ nm}$), fails to completely screen the potential in the N or P regions and the Fermi-level in the intrinsic region would be closely tied to the gate biases. At this point, the emitters are excited optically and the photoluminescence is used to measure the emission intensity, lifetime, and linewidth as a function of the Fermi-level. The Fermi-level is estimated through capacitive accumulated charge and these data capture the emitters' PL property as a function of different charge states. The thermodynamic transition levels between different charge states can be calculated accurately from ab initio methods and compared with experimental data to narrow down the suspected defects underlying single-photon emission. Furthermore, identifying the correct charge states and the range of Fermi-level energies at which the defect would maintain its charge state is critical information that can be later used to bias the QLEDs with correct parameters.

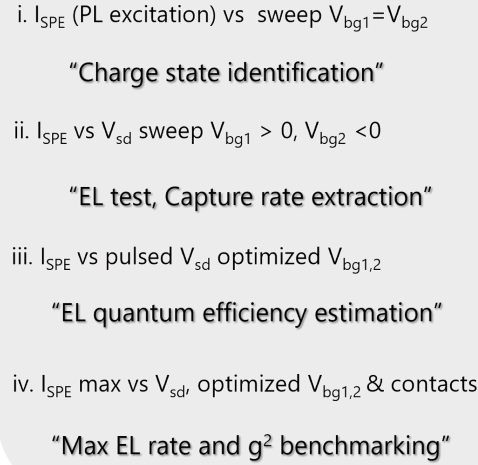
- 
- i. I_{SPE} (PL excitation) vs sweep $V_{\text{bg1}}=V_{\text{bg2}}$
“Charge state identification”
 - ii. I_{SPE} vs V_{sd} sweep $V_{\text{bg1}} > 0, V_{\text{bg2}} < 0$
“EL test, Capture rate extraction”
 - iii. I_{SPE} vs pulsed V_{sd} optimized $V_{\text{bg1,2}}$
“EL quantum efficiency estimation”
 - iv. I_{SPE} max vs V_{sd} , optimized $V_{\text{bg1,2}}$ & contacts
“Max EL rate and g^2 benchmarking”

Figure 6.9: Benchmarking procedure for defect-based single-photon diodes

Next, the position of the SPE can be identified using PL spectroscopy, then the laser is turned off, and the SPE can be tested for EL. In this mode of operation, we will operate the device as a p-i-n junction. Initially, a constant drain-source voltage is applied (ensuring the emitter remains below saturation), and the voltage of the P and N gates are separately swept. The emitter EL intensity as a function of gate voltages is then extracted at different drain-source voltages from below saturation to above saturation. As discussed earlier, given the cyclic nature of the EL process, both electron capture and hole capture events are required. This would lead to two different carrier capture mechanisms, which can restrict the EL process and lead to early saturation of the emitter’s intensity. By sweeping the charge density in both the P and N regions separately, we can accurately control the injection rate of each type of minority charge carrier to the defect and model and extract the capture rate of both electrons and holes [24] Knowing the capture rates of both electrons and holes, we can also estimate the relative positions of electronic states involved with respect to the band edges, which is essential information that can further

narrow the list of possible defects involved in the EL process. We emphasize that separate estimation of capture rates of electrons and holes is only possible using EL and is distinct from the typical PL intensity vs. laser power saturation plots, which cannot be used to estimate separate electron and hole capture rates.

Finally, we can turn to assessing the EL Quantum Efficiency. Previous studies have estimated the internal quantum efficiency for WSe₂ defects using Arrhenius models [3, 4]; however, to our knowledge, the electrical quantum efficiency of WSe₂ emitters, defined here as the probability of having a single photon emission per electrical pulse, has not been investigated before. After finding the optimal biases for gates and source-drain of the device, we will perform pulsed electrical excitation to estimate the internal efficiency of the emitters. Initially, the excitation will be configured to have a long delay between pulses to minimize the device's charging and discharging effects. Furthermore, protocols for pulse engineering similar to QD LED devices should be followed [25, 26], setting the DC component of the pulse just below the turn-on of the QLED diodes, voltage height set to just below saturation voltage, and increasing the pulse width until the second-order correlation function, $g^2(0)$, begins to monotonically increase with the pulse width, indicating the start of multi-photon events in each excitation cycle. Electrical internal quantum efficiency can then be estimated by accounting for the collection efficiency and system losses following the process similar to references [25, 26]. The overall process to find the optimized operation parameter space for QLEDs and their benchmarking is summarized in Figure 6.9.

Bibliography

- [1] M. Gould, E. R. Schmidgall, S. Dadgostar, *et. al.*, *Efficient extraction of zero-phonon-line photons from single nitrogen-vacancy centers in an integrated gap-on-diamond platform*, *Physical Review Applied* **6** (2016), no. 1 011001.
- [2] N. Thomas, R. J. Barbour, Y. Song, *et. al.*, *Waveguide-integrated single-crystalline gap resonators on diamond*, *Optics express* **22** (2014), no. 11 13555–13564.
- [3] Y. Luo, N. Liu, X. Li, *et. al.*, *Single photon emission in wse_2 up to 160 k by quantum yield control*, *2D Materials* **6** (2019), no. 3 035017.
- [4] K. Parto, S. I. Azzam, K. Banerjee, and G. Moody, *Defect and strain engineering of monolayer wse_2 enables site-controlled single-photon emission up to 150 k*, *Nature communications* **12** (2021), no. 1 3585.
- [5] N. Nikolay, N. Mendelson, E. Özelci, *et. al.*, *Direct measurement of quantum efficiency of single-photon emitters in hexagonal boron nitride*, *Optica* **6** (2019), no. 8 1084–1088.
- [6] H. Kaupp, C. Deutsch, H.-C. Chang, *et. al.*, *Scaling laws of the cavity enhancement for nitrogen-vacancy centers in diamond*, *Physical Review A* **88** (2013), no. 5 053812.
- [7] F. Peyskens, C. Chakraborty, M. Muneeb, *et. al.*, *Integration of single photon emitters in 2d layered materials with a silicon nitride photonic chip*, *Nature communications* **10** (2019), no. 1 4435.
- [8] T. Grange, G. Hornecker, D. Hunger, *et. al.*, *Cavity-funneled generation of indistinguishable single photons from strongly dissipative quantum emitters*, *Physical review letters* **114** (2015), no. 19 193601.
- [9] P. Schnauber, A. Singh, J. Schall, *et. al.*, *Indistinguishable photons from deterministically integrated single quantum dots in heterogeneous $gaas/si_3n_4$ quantum photonic circuits*, *Nano letters* **19** (2019), no. 10 7164–7172.

BIBLIOGRAPHY

- [10] H. Wang, J. Qin, X. Ding, *et. al.*, *Boson sampling with 20 input photons and a 60-mode interferometer in a 1 0 14-dimensional hilbert space*, *Physical review letters* **123** (2019), no. 25 250503.
- [11] A. Dietrich, M. Doherty, I. Aharonovich, and A. Kubanek, *Solid-state single photon source with fourier transform limited lines at room temperature*, *Physical Review B* **101** (2020), no. 8 081401.
- [12] S. Kumar, M. Brotóns-Gisbert, R. Al-Khuzheyri, *et. al.*, *Resonant laser spectroscopy of localized excitons in monolayer wse₂*, *Optica* **3** (2016), no. 8 882–886.
- [13] G. Moody, V. J. Sorger, D. J. Blumenthal, *et. al.*, *2022 roadmap on integrated quantum photonics*, *Journal of Physics: Photonics* **4** (2022), no. 1 012501.
- [14] Z. Yuan, B. E. Kardynal, R. M. Stevenson, *et. al.*, *Electrically driven single-photon source*, *science* **295** (2002), no. 5552 102–105.
- [15] Y. Arakawa and M. J. Holmes, *Progress in quantum-dot single photon sources for quantum information technologies: A broad spectrum overview*, *Applied Physics Reviews* **7** (2020), no. 2.
- [16] A. J. Shields, *Semiconductor quantum light sources*, *Nature photonics* **1** (2007), no. 4 215–223.
- [17] I. Aharonovich, D. Englund, and M. Toth, *Solid-state single-photon emitters*, *Nature photonics* **10** (2016), no. 10 631–641.
- [18] D. Y. Fedyanin and M. Agio, *Ultrabright single-photon source on diamond with electrical pumping at room and high temperatures*, *New Journal of Physics* **18** (2016), no. 7 073012.
- [19] A. Alkauskas, C. E. Dreyer, J. L. Lyons, and C. G. Van de Walle, *Role of excited states in shockley-read-hall recombination in wide-band-gap semiconductors*, *Physical Review B* **93** (2016), no. 20 201304.
- [20] S. Schwarz, A. Kozikov, F. Withers, *et. al.*, *Electrically pumped single-defect light emitters in wse₂*, *2D Materials* **3** (2016), no. 2 025038.
- [21] C. Palacios-Berraquero and C. Palacios-Berraquero, *Atomically-thin quantum light emitting diodes*, *Quantum confined excitons in 2-dimensional materials* (2018) 71–89.
- [22] J. S. Ross, P. Klement, A. M. Jones, *et. al.*, *Electrically tunable excitonic light-emitting diodes based on monolayer wse₂ p–n junctions*, *Nature nanotechnology* **9** (2014), no. 4 268–272.

BIBLIOGRAPHY

- [23] B. W. Baugher, H. O. Churchill, Y. Yang, and P. Jarillo-Herrero, *Optoelectronic devices based on electrically tunable p–n diodes in a monolayer dichalcogenide*, *Nature nanotechnology* **9** (2014), no. 4 262–267.
- [24] S. M. Sze, Y. Li, and K. K. Ng, *Physics of semiconductor devices*. John Wiley & sons, 2021.
- [25] T. Heindel, C. Schneider, M. Lermer, *et. al.*, *Electrically driven quantum dot-micropillar single photon source with 34% overall efficiency*, *Applied Physics Letters* **96** (2010), no. 1.
- [26] A. Schlehahn, A. Thoma, P. Munnely, *et. al.*, *An electrically driven cavity-enhanced source of indistinguishable photons with 61% overall efficiency*, *APL Photonics* **1** (2016), no. 1.

Chapter 7

Outro

This thesis aimed to establish a novel platform for on-chip single-photon generation with defects in 2D materials. A scalable CMOS-compatible on-chip integrated single-photon source has been one of the primary missing links in quantum photonics, and it has become clear that to solve this challenge, new materials, new physics, and new fabrication processes need to be explored.

In Chapter 4, we studied the microscopic physics of WSe₂ emitters and uncovered the role of defect-bound dark-excitons in the microscopic dynamics of WSe₂ single photon emitters. Over the past couple of years, new studies [1, 2] have provided additional proof and insight into this new mechanism of single-photon emission. Understanding the role of these defect-bound excitons in TMDs allowed us to develop a novel site-specific emitter fabrication method by employing simultaneous strain engineering and electron-beam irradiation to create arrays of single-photon emitters with high purity, record-breaking working temperatures, and sub-100 nm positioning accuracy. The ability to fabricate arrays of deterministic single-photon emitters on chip using traditional cleanroom and lithography techniques is one of the first demonstrations of its kind and paved the way for future scalable on-chip single-photon emitters using 2D materials.

However, it was critical to develop an efficient method to integrate 2D-SPEs with photonic waveguides to create truly on-chip single-photon emitters while improving their brightness and indistinguishability. In Chapter 5, we developed a 2D CMOS-compatible low-autofluorescence SiN platform and demonstrated that by integrating single-photon emitters in microring cavities, leveraging cavity Purcell enhancement, single photons could be efficiently coupled to a photonic waveguide. This work achieved nearly 46% coupling efficiency—an almost order-of-magnitude increase in coupling efficiency compared to previous achievements. In Chapter 5, we also discussed how these cavity-integrated systems could be further optimized by increasing the intrinsic quality factor of the low-autofluorescence SiN to demonstrate figure of merits exceeding the state-of-the-art demonstrations in quantum dot systems while retaining a fully scalable approach.

While the progress in the 2D single-photon emitter field has been tremendous, with demonstrations of new emitters with Fourier limited linewidths and partial indistinguishability [3, 4], room temperature operation of emitters in hybrid heterostructures [5], and identification of spin-photon interfaces in 2D single photon emitters [6], the realization of commercially viable 2D based sources still faces several challenges. Most crucially, the CMOS-compatible wafer-scale growth of high-quality 2D-TMDs on insulating substrates needs to progress further. However, given the current investments from the commercial semiconductor sector, such as TSMC and Intel, in CMOS-compatible growth of 2D-based devices, and recent demonstrations in large-area growth of TMDs [7], the solution to this problem seems to be imminent. Even then, significant steps are still needed to increase the performance metrics of 2D-based emitters. The true limits of indistinguishability of 2D-based emitters still need to be explored. Given that 2D emitters have been identified in a variety of spectral bands, most experiments rely on non-resonant excitation to probe 2D SPEs, which inherently introduce linewidth broadening due to acoustic-phonon scattering and, in the case of TMD-based emitters, also cause significant

inhomogeneous broadening due to stray electric fields by excess charge carriers. In the future, more efforts should focus on resonant or phonon side-band excitation of 2D-based emitters with tunable lasers to quantify the true linewidth and indistinguishability limit of emitters fabricated with different engineering techniques. Furthermore, the resonant excitation techniques should be complemented with integration in high-Q optical cavities to assess the boost in indistinguishability in the presence of a cavity.

In Chapter 6, we discussed the opportunities in electrically triggered 2D-based single-photon emitters. As argued, 2D-based emitters may be one of the only possible platforms that would simultaneously allow electrical single photon diodes to integrate with on-chip microring resonators. Overall, electrical excitation of isolated defects is relatively new and uncharted territory for 2D materials. Given the ability to tune the electronic properties of 2DMs with electrostatic gating combined with the ability to integrate them in ultrathin heterostructures, 2DM emitters can become a testbed for novel concepts in this domain. For instance, resonant electrical excitation of isolated defects through a reverse-biased tunnel diode has never been demonstrated in any platform; such a device could enable electrical excitation of near-indistinguishable photons by minimizing acoustic-phonon relaxation of carriers into the electronic structure of the defect. Finally, electrical integration can also be exclusively used to tune and stabilize the optical properties of the emitter. Simultaneous integration of 2D emitters embedded in a reverse bias junction and an optical cavity, similar to a state-of-the-art demonstration of III-V quantum dots [8], can truly boost the performance of 2D-based devices.

In 2019, when I started working on the subject, 2D-based single-photon emitters were a new phenomenon with many unanswered questions about the microscopic physics and feasibility of these emitters for any practical applications. It has been a thrilling and humbling experience to be part of the 2D community that has developed this field in recent years. I would like to extend my gratitude one last time to my wonderful friends

and advisors, Professor Galan Moody and Professor Kaustav Banerjee.

Bibliography

- [1] P. Hernández López, S. Heeg, C. Schattauer, *et. al.*, *Strain control of hybridization between dark and localized excitons in a 2d semiconductor*, *Nature communications* **13** (2022), no. 1 7691.
- [2] A. N. Abramov, I. Y. Chestnov, E. S. Alimova, *et. al.*, *Photoluminescence imaging of single photon emitters within nanoscale strain profiles in monolayer wse₂*, *Nature Communications* **14** (2023), no. 1 5737.
- [3] A. Dietrich, M. Bürk, E. S. Steiger, *et. al.*, *Observation of fourier transform limited lines in hexagonal boron nitride*, *Physical Review B* **98** (2018), no. 8 081414.
- [4] C. Fournier, S. Roux, K. Watanabe, *et. al.*, *Two-photon interference from a quantum emitter in hexagonal boron nitride*, *Physical Review Applied* **19** (2023), no. 4 L041003.
- [5] N. Fang, Y. Chang, S. Fujii, *et. al.*, *Room-temperature quantum emission from interface excitons in mixed-dimensional heterostructures*, *Nature Communications* **15** (2024), no. 1 2871.
- [6] A. Gottscholl, M. Kianinia, V. Soltamov, *et. al.*, *Initialization and read-out of intrinsic spin defects in a van der waals crystal at room temperature*, *Nature materials* **19** (2020), no. 5 540–545.
- [7] Y. Xia, X. Chen, J. Wei, *et. al.*, *12-inch growth of uniform mos₂ monolayer for integrated circuit manufacture*, *Nature Materials* **22** (2023), no. 11 1324–1331.
- [8] N. Somaschi, V. Giesz, L. De Santis, *et. al.*, *Near-optimal single-photon sources in the solid state*, *Nature Photonics* **10** (2016), no. 5 340–345.